UNIVERSITÀ DEGLI STUDI DI TRIESTE

XXXII CICLO DEL DOTTORATO DI RICERCA IN SCIENZE DELLA TERRA E MECCANICA DEI FLUIDI

Finanziatore / Funding Agency:
PO FRIULI VENEZIA GIULIA - FONDO SOCIALE EUROPEO 2014/2020

Inferring the lithospheric thermal structure from satellite gravimetry

Settore scientifico-disciplinare:
GEO/10 GEOFISICA DELLA TERRA SOLIDA

DOTTORANDO
ALBERTO PASTORUTTI

COORDINATORE
PROF. PIERPAOLO OMARI

SUPERVISORE DI TESI
PROF. CARLA BRAITENBERG

ANNO ACCADEMICO 2018/2019

UNIVERSITÀ DEGLI STUDI DI TRIESTE

XXXII CICLO DEL DOTTORATO DI RICERCA IN SCIENZE DELLA TERRA E MECCANICA DEI FLUIDI

Finanziatore / Funding Agency:
PO FRIULI VENEZIA GIULIA - FONDO SOCIALE EUROPEO 2014/2020

Inferring the lithospheric thermal structure from satellite gravimetry

Settore scientifico-disciplinare:
GEO/10 GEOFISICA DELLA TERRA SOLIDA

DOTTORANDO
ALBERTO PASTORUTTI

COORDINATORE
PROF. PIERPAOLO OMARI

SUPERVISORE DI TESI
PROF. CARLA BRAITENBERG

ANNO ACCADEMICO 2018/2019

Contents

Extended abstract

This doctoral dissertation is aimed at obtaining regional surface heat flow estimates on stable continental lithosphere from satellite-derived global models of the Earth static gravity field, using variations in crustal thickness as a gravity-derived thermal constraint.

The heat transported across the Earth surface, arising from its cooling interiors, senses a wide assortment of phenomena, from near-surface paleoclimatic perturbations (Majorowicz and Wybraniec, 2011) to the driving forces of plate tectonics and mantle dynamics (Cooper et al., 2017). Surface heat flow is sensed with in situ measurements of temperature and conductivity, usually in boreholes. This implies that heat flow is a costly observable, highly depending on logistic and financial constraints, on previous exploration interest and on availability of data. The collection and maintenance of a global database is an ongoing effort, spanning multiple decades (Lee and Uyeda, 1965; Hasterok and Chapman, 2008).

Different components superimpose on the surface heat flow signal. Over continents, at regional scales (from 100 km onwards), most of the static signal can be explained by a partition between a 'basal heat flow' (through the crust-mantle boundary) and a crustal radiogenic component, i.e. the result of radioactive decay occurring in the crust (Jaupart et al., 2016). The generation of continental crust through magmatic differentiation significantly enriched the upper portions of the lithosphere with radioactive elements, among which uranium, thorium, and potassium account for almost the total heat production. These are highly mobile trace elements, and their concentration alone does not directly affect petrophysical quantities by a significant amount (Hasterok et al., 2017).

Therefore, the indirect estimation of radioactive heat production is a non trivial task. However, other petrogenetic processes concur in affecting sensible quantities (e.g. seismic velocities, density). Empirical relationships from velocity and/or density to heat production have developed and tested satisfactorily (Rudnick and Gao, 2003; Vilà et al., 2010; Hasterok and Webb, 2017). In addition, multi-observable modelling (e.g. Mather et al., 2018; Afonso et al., 2019) is regularly employed to improve the understanding on the subsurface distribution of temperature and thermal parameters, exploiting their effect on directly sensed quantities (e.g. topography, gravity, seismic, and electromagnetic observations).

The gravity field is particularly sensitive to variations in crustal thickness, arising from the significant density contrast at the Moho (a global average of 485 kg m^{-3} according to Tenzer et al., 2012b, of 448 ± 187 kg m^{-3} according to Sjöberg and Bagherbandi, 2011, to name two). Compared with the problematically sampled heat flow, gravity data benefits from a much more uniform coverage, instead. While high resolution terrestrial data suffers from the same data availability issues that affect heat flow, models derived from satellite gravimetry missions provide an unprecedented spatial homogeneity in sampling and in data quality. The global gravity models (GGMs) derived from the European Space Agency Gravity field and steady-state Ocean Circulation Explorer mission (GOCE, Floberghagen et al., 2011) provide a ppm-level accuracy for g with a resolution of about 70 km at the Earth surface (Brockmann et al., 2014; Kvas et al., 2019a), enough to resolve geological structures in the crust and upper mantle (Peral et al., 2018). These kind of models, together with other geophysical constraints, have already shown promising results in global crustal thickness modelling (e.g. Eshagh et al., 2011; Reguzzoni and Sampietro, 2015) and in regional thermal modelling (Bouman et al., 2015).

This basis provided the motivation to perform an assessment on how satellite gravity data can contribute to thermal modelling. I devise and test a strategy to constrain the crustal radioactive heat production (RHP) using gravity-derived Moho depths and the available heat flow data (Gosnold, 2011), with the aim of overcoming the issues with heat flow interpolation over areas devoid of measurements. This strategy relies on gravity data reduction, the content of chapter 2, in order to isolate the Moho undulation signal, and on a thermal forward model, which was developed ad-hoc. Moho signal isolation is part of the general topic of signal separation in the observed static gravity field, i.e. stripping the effect of an assumed mass distribution to isolate an anomalous potential, usually attributed to the enquired phenomenon (Mikuška et al., 2007; Sjöberg, 2013; Aitken et al., 2015; Tenzer and Chen, 2019, to name a few). Uncertainties in the a-priori masses, such as unmodelled spatial variability in density, accumulate in the reductions and are propagated to the reduced data and to the inversion results. Incomplete and inexact geological knowledge cannot be avoided, thus a perfect data reduction is unrealistic.

Therefore, an uncertainty-aware signal isolation process, i.e. a process providing error estimates alongside its reduced gravity data, is a necessary step in estimating confidence of the inversion results, in statistical terms. In chapter 2 of this dissertation I deal with this issue, presenting the results of a Monte Carlo error propagation (Aster et al., 2013) of a global reduction for lithospheric masses (from the terrain correction to the lithosphere-asthenosphere bound-

ary). The experiments results are preceded by a brief introduction on gravity corrections (revolving on the ellipsoid-referenced disturbances defined by Vajda et al., 2008) and on the adopted spectral-domain forward modelling method (a layer-wise arrangement of the code by Wieczorek and Meschede, 2018). The chapter is complemented by a series of validation tests against spatial-domain forward modelling of test mass distributions. The tested strategy, albeit relying on a simplified uniform model of error distribution, proved fit for purpose at the target resolution (maximum degree and order of 280, aimed at data reduction of satellite-only models) and may be easily scaled to more complex schemes.

An application test in Central-Eastern europe, across the Trans-European Suture Zone is presented in chapter 3. It integrates a combined satellite-only GGM, data reductions including a mixed spatial- and spectral-domain forward modelling scheme (to include the regional sediment thickness model by Tesauro et al., 2008 in the global reductions), and available heat flow measurements (Gosnold, 2011). It resulted in a 3D lithospheric model of temperature and thermal parameters, fitting available data and providing added information respect to the structure of the lithosphere. The modelled thermal regime is coherent with what geological inference expects and with other models of the area, keeping into account the limitations of a method which relies on as little a-priori data as possible, by design. The model is accompanied by a sensitivity test of the results to the crustal thickness estimate —to quantify the role of the information inverted from gravity. The gravity-derived Moho is benchmarked against existing crustal models in the area, obtained through different methods (Grad et al., 2009; Pasyanos et al., 2014; Reguzzoni and Sampietro, 2015). Since no prior information on density-to-RHP relationship was included, the output data was also used to independently test the relationship proposed by Hasterok and Webb (2017). Albeit complicated by wide uncertainties, a satisfying overlap between the two data fits was observed.

Original contribution

The gravity-geothermal integrated technique described and applied in chapter 3 is based on the thermal model described in the supplementary chapter A and shares part of the strategies devised for the gravity data reduction, presented in chapter 2. A first proof-of-concept with a 1D analytical model was presented at the 2016 ESA Living Planet Symposium (Pastorutti et al., 2016), and a set of results was the subject of an oral communication I gave at the 2017 EGU General Assembly (Pastorutti and Braitenberg, 2017).

Those first tests, which were applied along a south-north transect from the Western Alps to the Upper Rhine Graben, were then extended to the more complex thermal numerical modelling scheme described in this dissertation (chapter 3 and appendix A). Afterwards, the iterative radioactive heat production fitting strategy was devised, its details presented as a poster at 2018 EGU General Assembly (Pastorutti and Braitenberg, 2018).

The integrated application, in the form presented in this chapter 3, was further enhanced with an in depth discussion of its results and of the rationale for the choice of parameters. It also benefited of a revised gravity data reduction scheme, developed in parallel with the experiments of chapter 2 and exploiting its results (albeit in a mixed spatial-spectral, regional-global scheme, as described in section 3.2). This application, edited in a suitable manuscript form, was submitted to Geophysical Journal International on February 26, 2019.

The paper: "A geothermal application for GOCE satellite gravity data: modelling the crustal heat production and lithospheric temperature field in Central Europe" (Pastorutti and Braitenberg, 2019) has been accepted for publication in Geophysical Journal International on July 25, 2019, following peer review. The paper *version of record* is available online at doi: 10.1093/gji/ggz344.

As mentioned in the 'Data Availability' statement of that paper, the data sets of the results are available as an open data repository (doi: 10.5281/zenodo.3358901). That repository includes: a volume of temperature, pressure, radioactive heat production, thermal conductivity, and density of the lithosphere in the study area; a Matlab/Octave function to extract 2D sections and 1D vertical plots of physical properties from the volume (as shown in Fig. 3.17 and 3.18); gravity input data and applied reductions; and the inverted Moho depth.

The gravity data reduction / signal isolation scheme and the uncertainty propagation experiments, presented in chapter 2, were developed during a 12-month visiting period at TU München, at the *Ingenieurinstitut für Astronomische und Physikalische Geodäsie* (IAPG), under the supervision of Prof. Roland Pail. It has been the subject of an oral presentation at 2019 EGU General Assembly (Pastorutti et al., 2019c) and two posters (Pastorutti et al., 2019a; b).

Acknowledgements

Some concise acknowledgements paragraphs may not be enough to convey how this journey, as any other doctoral project, would not have been possible without the support, scientific and not, of many people.

Above all, I thank my supervisor Prof. Carla Braitenberg, for her precious guidance through these years. The foundations of this project stemmed from an enthusiastic chat on the potential of GOCE-derived gravity for geothermal applications, which took place at the end of April 2015: back then, I was just enquiring for a master thesis topic. Trying to enquire the temperature field meant getting out of the 'comfort zone' of gravity and delving deep into thermal modelling – an exciting journey between geoscience specialities. My utmostly sincere gratitude for giving me this opportunity.

I ought to extend my gratitude to the all Tectonophysics and Geodynamics section, first and foremost to Dr. Ildiko' Nagy, to whom I wish the best for her retirement. I would then like to thank Dr. Magdala Tesauro, for feedback on the thermal segment of this project and on a preliminary manuscript. Yet as importantly, I thank all the lab mates in this wing of *Palazzina C*, for all the opportunities for discussion, prolific arguing, and mutual advice through the last years, both in the office and remotely, when scattered abroad: Francesca, Tommaso, Federico, Luigi, Marco, and anyone I may have forgotten. I may have learned as much from 'collateral collaborations' as I have from this thesis' work, spacing from tidal analysis to Central African basins in the timespan of a cup of coffee.

Spending a year in München has been a fundamental milestone and an unprecedented experience for me. Although the work carried out there was of utmost importance in shaping this final work, I should not forget the sheer extent of possible opportunities I did not explore while still there. Surely I must

regret not making the best out of such an opportunity to become proficient in German …

My sincere thanks go to Prof. Roland Pail, for his availability, and to the rest of the academic staff and colleagues at the Institute, for the pleasant working atmosphere throughout all my stay, from the frantic room search in the first weeks, to landing the first proper room in July ’18 (vielen Dank Martin!), up to what had then become a familiar setting and routine.

This journey took me through new, exciting, challenges, with level of professional independence (and consequent responsibilities) which I had never encountered before. I may say it has been stressful and rewarding in equal measure. I cannot take all the merit for that, it is not a project one can carry alone: non posso ignorare il naturale supporto e l’infinita pazienza dei miei genitori in tutti questi anni. Nemmeno va tralasciato il fondamentale e invisibile contributo dei miei più cari amici.

The ESF-funded EUSALP-area bound fellowship also meant frequent reporting, a good deal of wading through paperwork, and all the uncertainty that results from being among the first recipients of what was then a new founding source. Thus my gratitude also goes also to Valentina Demontis, UniTS Doctoral Registrar’s Office, for her help in dealing with my countless questions and forwarding those that were still unclear to the relevant funder’s offices.

My gratitude to Prof. Mehdi Eshagh and Dr. Roman Pašteka, referees to this final dissertation, for their availability and advice. I would also like to thank Dr. Derrick Hasterok and an anonymous reviewer for providing fruitful comments on a manuscript, which greatly improved its quality and have been an invaluable feedback, especially on the project segments I was less familiar with.

Funding Financial support was provided by Region Friuli Venezia Giulia (Italy) through an European Social Fund co-funded 3-year PhD fellowship (HEaD FP1687011001), under the program 'PO Friuli Venezia Giulia - Fondo Sociale Europeo 2014/2020'. The same funding source also supported a 12-month visiting period at the Institute of Astronomical and Physical Geodesy (IAPG) of the Technical University of Munich, under the supervision of Prof. Roland Pail, which I gratefully thank for his availability. Financial support for the abroad period was also supplemented by an International Mobility Scholarship, from resources of the University of Trieste.

Data, software, computational resources All the maps were drawn with the Generic Mapping Tools (GMT, Wessel et al., 2013) and the GMT/Matlab toolbox (Wessel and Luis, 2017). As thoroughly further in this thesis, the gravity forward modelling relied both on SHTOOLS (Wieczorek and Meschede, 2018) and Tesseroids (Uieda et al., 2016). Part of the computations involved in this research benefited of resources provided by the Leibniz Supercomputing Centre (www.lrz.de) and conceded by IAPG during my stay there, for which I express my gratitude. I acknowledge and thank all the producers of data cited in this work.

1. Introduction and motivation

The thermal structure of Earth's interior, the heat transport mechanisms involved and the heat flow observed near its surface are parameters of utmost importance in understanding the phenomena involved in geodynamics and the underlying driving forces. Temperature is also a parameter of direct interest in the exploitation of heat, as a source of geothermal energy or as a critical factor in hydrocarbon system modelling.

Direct measurements are technologically limited to the first kilometres of depth, and carrying them out is a costly task. Therefore, the spatial distribution of samples is uneven and often biased towards areas of anomalously high surface heat flow (Mareschal and Jaupart, 2013). The collection and maintenance of the publicly available data is an ongoing effort, spanning multiple decades (Lee and Uyeda, 1965).

For these reasons most of the knowledge on the thermal structure of the subsurface relies on the integrated analysis of indirect proxies, such as the petrologic information inferred from xenoliths, data inferred from seismological observables, and other physical or chemical quantities for which a temperature dependence is known (Fischer et al., 2010; Vilà et al., 2010; Afonso et al., 2013a).

Satellite-derived gravity models have already shown promising results in integrated geophysical modelling of regional heat flow (Bouman et al., 2015). The resolution and spatial homogeneity of the data obtained by the European Space Agency Gravity field and steady-state Ocean Circulation Explorer mission (GOCE, Floberghagen et al., 2011; van der Meijde et al., 2015) suggest that it may be a suitable tool in continental-scale thermal estimates.

While the temperature field in the solid Earth and the measured gravity field are not related by any direct physical law, mass distributions sensed by gravity can be a controlling factor for the temperature distribution at depth. The temperature-density and temperature-velocity relationships provide satisfactory insights in the thermal state of the mantle (Priestley and McKenzie, 2006; Cammarano et al., 2011), but the crust is dominated by the heterogeneous distribution of heat produced by decay of radioactive elements (Jaupart et al., 2016), superimposed with the dynamic effects of transients (i.e. when thermal equilibrium has not yet been reached) and non-conductive heat transfer mechanisms: advection and fluid circulation.

The gravity field anomalies due to variations in crustal thickness are among

the largest signals sensed by satellite-borne gravity measurements. The observation error in satellite-only GOCE-based gravity models propagates to a theoretical ± 0.2 km uncertainty in Moho determination, ignoring the much larger error contribution due to non-exact density distribution models (Braitenberg et al., 2011; van der Meijde and Pail, 2020). Satellite-derived gravity (synthesised from global models or in the form of on-orbit gradiometry data) has been extensively employed in the last decade in inverse modelling of crustal thickness and density, at regional and global scales. The non-uniqueness of gravity inversion is usually overcome by integration of different geophysical observables.

A variety of methods have been developed to achieve this: through combination of models, e.g. Eshagh et al. (2011) combined the seismological CRUST2.0 model (Bassin et al., 2000) with the gravimetric inversion of EGM08 global gravity model (Pavlis et al., 2012), Reguzzoni and Sampietro (2015) used a mean-depth constrain based on geological provinces; or by constraining the a-priori parameters of gravity inversion using seismic estimates (where available) as ground truth for depths and density contrasts, e.g. resorting to iterative forward modelling (Ebbing et al., 2006), cross-validation (Uieda and Barbosa, 2017), and grid-searching for maximum correlation (Zhao et al., 2020). Joint analysis of satellite gravity products and seismological models has been proven useful to assess the crust-mantle density contrast, as in the work by Eshagh et al. (2016), which exploited the GOCE gradiometry data.

Therefore, estimating the crustal contribution to the surface heat flow by assuming a 'standard heat production' and scaling it with crustal thickness is tempting. Nevertheless, available evidence suggests against such a simple relationship (Mareschal and Jaupart, 2013; Alessio et al., 2018). However, crustal thickness variations on their own successfully isolate tectonothermal age groups, terranes, and geological provinces. An example of this was shown in Grad et al. (2009), through spatial filtering of their European Plate Moho model at different wavelengths.

Hence, the strategy devised in this dissertation stems from the assumption that in contiguous areas of similar crustal thickness, interpreted as contiguous geological provinces, consistent thermal parameters can be expected –provided that both the crustal thickness modelling and the thermal analysis are carried out at the same spatial scale. The fundamental hypothesis is that the 'thermal omission error' due to the unmodelled short-wavelength variability in thermal characteristics should be smaller when this local dependence of heat production on crustal thickness is included.

Motivated by these premises, the **core objectives** of the research hereby presented are the following:

1. the **definition of a thermal modelling scheme** to implement and test the strategy outlined in the previous paragraphs. In order to do so, I need to set up a thermal 'forward operator' (i.e. a solver for the steady state heat equation), an iterative fitting strategy for the radioactive heat production, and the parametrisation of the thermal volumes.

2. the **application of a gravity inversion procedure** for regional estimates of crustal thickness, which is the gravity-derived quantity that constrains the thermal – the other constrain being the sparsely sampled surface heat flow.

3. the **signal isolation** of the gravity effect of crust-mantle boundary undulations from the gravity signal as provided in a chosen satellite-only gravity model.

In chapter 2, the gravity reduction scheme is defined and tested using the globally available LITHO1.0 model (Pasyanos et al., 2014). It is accompanied by a brief introduction on the definition of the gravity functionals and the adopted ellipsoid-referenced corrections. In addition to providing the means for the gravity reductions, then utilised in the thermal application, it also includes a spectral assessment of the modelled corrections and a strategy for error propagation of uncertainties in the depths and densities of the input models.

In chapter 3, an application of the aforementioned thermal strategy is presented: a test on a study area in central-eastern Europe, crossing the Trans-European Suture Zone, a diffuse boundary between the young lithosphere of the European Plate and the Russian Platform. Coherently with the objective of assessing the performance of the satellite-only gravity model in providing suitable thermal results, external a-priori information is kept to a reasonable minimum. I assessed how a strategy based on crustal thickness (inverted from the global gravity model data) and the available surface heat flow measurements can provide a joint estimate of crustal heat production. Trough interpolation of this heat production estimate I filled in those crustal columns which are devoid of surface heat flow measurements and provide a complete model of temperature at depth – added information that surface heat measurements alone can not provide.

2. Signal isolation: data reduction and uncertainty budget

Chapter summary

In order to perform geophysical inversions on the static gravity field, a signal separation procedure is required, i.e. the effect of an a-priori mass distribution must be removed, isolating an anomalous field (e.g. Tenzer et al., 2009a; 2012a; Sjöberg, 2013; Aitken et al., 2015, and references therein). The observed field stripped of the forward-modelled attraction of these "known masses" constitutes the input of inverse gravity modelling. Any distribution of anomalous masses that results in the isolated field is a solution to the inverse problem. Common reductions include the well-known terrain correction, i.e. landmasses and bathymetry (Hinze, 2003; Hinze et al., 2005), which can be further refined by stripping the effect of subsurface density variations (Vajda et al., 2008).

Uncertainties in the a-priori masses, such as unmodelled spatial variability in density, accumulate in the reductions and are propagated to the reduced data and to the inversion results. Incomplete and inexact geological knowledge cannot be avoided, thus a perfect data reduction is unrealistic. Therefore, an uncertainty-aware signal isolation process, i.e. a process providing error estimates alongside its reduced gravity data, is a necessary step in estimating confidence of the inversion results, in statistical terms. Error information is required in order to perform multi-observable integrated modelling (e.g. Afonso et al., 2013b), comparisons (e.g. Root et al., 2017), or assimilation of geophysical models (e.g. to assemble large scale maps from local studies, see Tesauro et al., 2008; Grad et al., 2009; Molinari and Morelli, 2011).

The procedure and experiments described in this chapter were designed for local Moho inverse modelling, using global satellite-only gravity field models. They were applied in the gravity-constrained thermal modelling strategy described in this thesis, in chapter 3. The forward-modelling experiments presented in this chapter include corrections for the terrain effect (solid topography, water, and ice), sediments and other intra-crustal density variations, and inhomogeneities in the lithospheric mantle.

Uncertainty was quantified through Monte Carlo error propagation (Aster

et al., 2013), resulting in a population of randomly perturbed reduction fields (according to a set of parameter uncertainty assumptions). Results include the probability density function of these reductions, from which the global spatial distribution of the standard deviation was computed.

2.1. Definition and computation of data reductions

2.1.1. No-topography gravity disturbance

In order to isolate the gravitational signal due to an unknown mass distribution, a technique known as "stripping" is employed (Vajda et al., 2008; Tenzer et al., 2009a). It consists in computing the gravitational effect of a "known mass" model, as inferred by other investigations, and removing it from the observed signal. The gravimetric inverse problem is therefore formulated in terms of an anomalous gravity field resulting from the enquired mass/density distribution.

Following the recommendations in Hackney and Featherstone (2003) and Vajda et al. (2007), the formulation hereby presented is based on gravity disturbances, to avoid the "Secondary Indirect Topographic Effect" that arises when the topographic correction is applied to gravity anomalies (Meurers, 2017). Recalling the definition of gravity disturbance from Hofmann-Wellenhof and Moritz (2006), section 2.12: it is defined as the difference in magnitude between the observed gravity vector $\boldsymbol{g}$ and the normal gravity vector $\boldsymbol{\gamma}$, at the same point P of geocentric geodetic coordinates (h, λ, ϕ):

$$\delta g(h, \lambda, \phi) = |\boldsymbol{g}(h, \lambda, \phi)| - |\boldsymbol{\gamma}(h, \lambda, \phi)| \tag{2.1}$$

where $\boldsymbol{g}$ is the gradient of the potential ∇W and $\boldsymbol{\gamma}$ is the gradient of the normal potential ∇U. By "geocentric geodetic coordinates" we refer to "ellipsoidal coordinates" (Hofmann-Wellenhof and Moritz, 2006), with h ellipsoidal height, ϕ geodetic latitude, and λ geodetic longitude. This follows from the definition of normal and disturbing potential, respectively U and T:

$$W(h, \lambda, \phi) = U(h, \phi) + T(h, \lambda, \phi) \tag{2.2}$$

in which W and U can be decomposed in an attraction (gravitational) and a centrifugal component each, denoted with Φ (Eq. 5 and 13 in Barthelmes, 2013).

$$\underbrace{W_a(h, \lambda, \phi) + \Phi(h, \phi)}_{W} = \underbrace{U_a(h, \phi) + \Phi(h, \phi)}_{U} + T(h, \lambda, \phi) \tag{2.3}$$

To isolate the contribution of the anomalous density distribution we must remove the effect of a reference density model, against which anomalous densities

are referred (in terms of density contrasts). Following the strategy of Vajda et al. (2006), we can define a reference density model composed of two regions: one inside the reference ellipsoid, such as to generate the external normal potential, and one between the reference ellipsoid and the "ellipsoidal topography", i.e. the "topography reckoned from the ellipsoid". As demonstrated by them, the gravity disturbance obtained by removing the effect of such a reference model is rigorously related with the "gravitational attraction of the anomalous density distribution inside the entire Earth" (Vajda et al., 2006). Omitting most of the derivation, for which I refer the reader to the contents in Vajda et al. (2006), I report here the following decomposition of the attraction potential W_a:

$$W_a(h, \lambda, \phi) = V^E(h, \lambda, \phi) + V^{ET}(h, \lambda, \phi) \tag{2.4}$$

where V^E is the normal potential (U_a in Eq. 2.3), due to the masses inside the reference ellipsoid, and V^{ET} is the potential due to the masses between the ellipsoid and the topography. Each of the potentials in Eq. 2.4 is further decomposed, in the contribution of a reference density and in the contribution of the anomalous density distribution (in respect to the chosen reference). Therefore, omitting the position arguments (h, λ, ϕ), the following is obtained:

$$W_a = V_R^E + \delta V^E + V_R^{ET} + \delta V^{ET} \tag{2.5}$$

where the terms with the subscript R (V_R^E and V_R^{ET}) denote the potentials due to the reference density contribution and the terms preceded by δ (δV^E and δV^{ET}) denote the potentials due to the anomalous density contribution. Recalling that $W_a - V_R^E$ (equivalent to $W_a - U_a$) is the disturbing potential T, Eq. 2.5 can thus be rewritten as:

$$T = \left(\delta V^E + \delta V^{ET}\right) + V_R^{ET} \tag{2.6}$$

The sum of δV^E and δV^{ET} is the potential of the anomalous density distribution in the whole Earth δV, so the Eq. 2.6 can be further rearranged to:

$$T - V_R^{ET} = \delta V \tag{2.7}$$

Vajda et al. (2006) proposed the notation T^{NETC} for $T - V_R^{ET}$, the NETC acronym standing for "No Ellipsoidal Topography of Constant density". Taking the vertical derivative of T^{NETC} (applying the differential operator $-\partial/\partial h$, along the ellipsoidal normal), the "NETC gravity disturbance" is obtained:

$$\delta_g^{NETC} = -\frac{\partial T^{NETC}}{\partial h} = -\frac{\partial \delta V}{\partial h} \equiv \delta A \tag{2.8}$$

where δA is the attraction of the anomalous density distribution. The NETC gravity disturbance can be computed for each point gravity disturbance δg using the following:

$$\delta_g^{NETC} = \delta_g - A_R^{ET} \tag{2.9}$$

here A_R^{ET} is the forward-modelled attraction of the Earth topography of reference density.

The process that has been just described is conceptually akin to computing and removing a "complete Bouguer correction" (Hinze, 2003; Mikuška et al., 2006) to gravity observations. There are, however, some methodological discrepancies in the various definitions (see LaFehr and Nabighian, 2012, ch. 5; Hinze et al., 2013, ch. 6.3). The method and terminology hereby presented should prevent confusion, providing a gravity quantity (δ_g^{NETC}) which is formally related to the unmodelled density distribution, i.e. the component that was not accounted for in the reference model.

2.1.2. Corrections to the gravity disturbance

Following the definitions used by Vajda et al. (2008) and Tenzer et al. (2009a), we classify the corrections to the gravity disturbance as topographic, bathymetric, and stripping. They are fundamentally further refinements to the reference density model. The topographic correction is computed with a reference density for both solid and liquid topography, i.e. for the strict sense topographic surface of land masses and for the surface of water bodies, both in respect to the reference ellipsoid. The bathymetric correction consists in the removal of the effect of water density, expressed as contrast against the reference topographic density. All further corrections (e.g. ice, sediments, crustal and mantle inhomogeneities...) go under the name of stripping – they are computed as contrasts against reference, similarly to the bathymetric correction (Hammer, 1963).

In regard to the masses below the reference ellipsoid, the reference densities are the ones of a model which results in the adopted normal potential, in concordance with the normal potential decomposition of Eq. 2.4. A radially-stratified model of the interior, such as the PREM (Preliminary Reference Earth Model, Dziewonski and Anderson, 1981), should satisfy this condition (C. Tscherning and Sünkel, 1981). Note that, in the adopted configuration, the 'radial stratification' is actually defined by shells with a constant distance from the reference ellipsoid.

Stripping a set of *known masses* (i.e. a-priori density distribution models) is often aimed at signal isolation. For example, *mantle gravity anomalies* (e.g. Mooney and Kaban, 2010; Kaban et al., 2014) are obtained by stripping the "crustal effect", i.e. by correcting for a crust model (e.g. CRUST1.0, Laske et al., 2012). Starting from the NETC gravity disturbance introduced in the previous section (2.1.1), corrections can be applied for ice, sediments, crustal heterogeneities. The disturbance obtained after those corrections equals to a model Earth without topography above the ellipsoid and a reference-density (*normal*) crust inside the ellipsoid, down to the crust-mantle interface. In the

unlikely case we had a perfect density model for these above-Moho masses, this reduced gravity would be equal to the attraction of anomalous densities in the mantle and core.

The work by Tenzer et al. (2009a) is an example of a similar application: they compiled and presented a set of global maps of the gravity disturbance (obtained from the EGM08 global gravity model, Pavlis et al., 2012)– corrected for the CRUST2.0 model (Bassin et al., 2000). They also provided a crust reduction not depending on a-priori density models, using a decorrelation analysis between the crust–reduced disturbance and the Moho undulations. A further development of that analysis is presented in Tenzer et al. (2012b). Tenzer et al. (2009a) also provided a global map of ellipsoid– versus geoid–referenced topography and bathymetry corrected gravity disturbance. Differences reach upwards to ± 14 mGal over continents, with a morphology highly correlated to geoidal undulations, as expected. The methodology of Tenzer et al. (2009a) is the basis of the later work by Tenzer and Chen (2019), which extended the forward modelling from CRUST2.0 to LITHO1.0 (Pasyanos et al., 2014).

Signal isolation is also addressed using spectral separation, such as the source-depth theory developed by Bowin (1983): Li et al. (2017) applied it to the inversion of GOCE gradients, in order to separate the integrated effect of mantle, crust and sediments in the Tibetan plateau. It was also used, similarly, by Afonso et al. (2019) to remove the contribution of density anomalies under 410 km in their *LithoRef18* global density model. However, as Kaban et al. (2004) pointed out, considerable overlap in long wavelengths between shallow and deep sources warrants caution in doing so.

In crustal thickness modelling, signal isolation is obtained by concurrently correcting for masses in the upper crust (sediments included) and in the upper mantle —as it has been done to obtain the global model GEMMA (Reguzzoni et al., 2013; Reguzzoni and Sampietro, 2015). Most of global crustal density models are constrained by seismic data (e.g. Laske et al., 2012; Pasyanos et al., 2014; Szwillus et al., 2019), either completely or for the most part, and are constrained mainly in terms of velocity. Reliance on assumed velocity-density conversions is therefore required. Mantle stripping is affected by the same issues, and no ready-made velocity conversions of seismic models are available, as observed by Tenzer et al. (2015), requiring again to resort to conversion schemes (e.g. Sebera et al., 2018; Liu et al., 2018). At mantle conditions, density conversion from velocity models (e.g. Simmons et al., 2010; Schaeffer and Lebedev, 2013) require modelling the concurring effect of temperature, pressure and composition on the elastic parameter — which means carrying out comprehensive thermodynamic modelling (Connolly, 2005; Connolly, 2009). These issues area dealt in detail in section 2.3.

The atmospheric correction has a range of −0.04 to 0.18 mGal at the Earth

surface (Tenzer et al., 2009b). Owing to its small value (3 orders of magnitude smaller than the effects of lithospheric mass inhomogeneities), it is often not considered for solid Earth signal isolation (e.g Tenzer and Chen, 2019).

2.2. Forward modelling method

2.2.1. Spectral–domain forward modelling

Forward modelling the gravity field resulting from a mass distribution involves integrating its gravitational effects, thus evaluating the so called *Newton integral* (Hofmann-Wellenhof and Moritz, 2006):

$$W = -G \int_{v'} \frac{\rho(r')}{|r - r'|} dv' \tag{2.10}$$

where G is the gravitational constant and $r - r'$ is the distance from an element of mass of volume v' at r', with $dm' = \rho dv'$.

Common methods to do so are either *spatial–domain* or *spectral–domain* forward modelling methods (Kuhn and Featherstone, 2005).

In spatial–domain methods, the direct integration of masses is computed: volumes are decomposed (*discretised*) in elementary bodies for which a solution to the Newton integral exists. There are analytical formulas available for special cases (e.g. point masses, prisms Nagy et al., 2000; 2002, or polyhedra Tsoulis, 2012; Benedek, 2016), while numerical approximations are more commonly employed for general solutions (e.g. spherical tesseroids Heck and Seitz, 2007; Uieda et al., 2016). Numerical methods, in addition, are less time consuming in equivalent cases, e.g. by resorting to FFT, Taylor series expansion, or Gauss–Legendre cubature (see Grombein et al., 2013, and references therein).

Spectral–domain forward modelling, on the other hand, is based on the spherical harmonic (SH) series expansion of the Newtonian kernel (Rummel et al., 1988; Blakely, 1996; Root et al., 2015; Wieczorek, 2007). In methods of this kind, coefficients of the resulting potential (or its derived functionals) are obtained from the mass distribution. To assure convergence of the SH series, modelling is typically performed outside the *Brillouin sphere*, i.e. a sphere encompassing all the field-generating mass, concentric with the spherical coordinate system (Moritz, 1980a). Spectral–domain methods are commonly adopted for global computations, where they are considered less time consuming than spatial–domain methods, at least for degrees less than about 1000 (Kuhn and Featherstone, 2005). Computing higher maximum degrees of the SH series expansion, points inside the Brillouin sphere, and rugged topography are three factors that influence issues of numerical accuracy and divergence of spectral

forward modelling methods (Hu and Jekeli, 2015; Hirt and Kuhn, 2017). Combined spectral/spatial methods have been recently employed with success to obtain very high resolution synthetic gravity models (Hirt et al., 2019).

The experiments described in this chapter were designed by taking into account the highest resolution available from satellite-only global gravity models – which defined the maximum degree – and the comparable (albeit lower) resolution of global density models to compute reductions (as described in the following section 2.3). In addition, error assessment through random perturbation of the input models, the aforementioned Monte Carlo uncertainty propagation technique (described in section 2.4), requires a large number of forward iterations. Therefore, I resorted to spectral–domain methods, using the method by Wieczorek (2007), as implemented in the SHTOOLS code (Wieczorek and Meschede, 2018).

Wieczorek (2007) provides a method for calculating the potential due to the topography, using a technique analogous to the cartesian ("flat-Earth") method by Parker (1973). For its detailed description, I refer to the derivation of Eq. 6–12 in Wieczorek and Phillips (1998). It is similar to a wider family of spherical-harmonics based solution to the volume integral, based on the binomial series expansion method, which Root et al. (2015) defined as "Fast Spectral Methods" (FSMs).

Consider the case with a relief $h(\lambda, \theta)$ ($\theta = 90° - \phi$, colatitude), referenced to a spherical interface of radius D, with density $\rho(\lambda, \theta)$ radially constant between h and D, ρ considered negative when $h < 0$. Expressing the potential W at a reference radius R_0 as a sum of spherical harmonic functions, we get:

$$W(r, \lambda, \theta) = \frac{GM}{r} \sum_{l=0}^{l_{max}} \sum_{m=-l}^{l} \left(\frac{R_0}{r}\right)^l C_{lm} Y_{lm}(\lambda, \theta) \tag{2.11}$$

where G is the gravitational constant, M the total mass, r calculation radius. Y_{lm} denotes the real spherical harmonics:

$$Y_{lm}(\lambda, \theta) = \begin{cases} \overline{P}_{lm}(cos\theta) \cos m\lambda & \text{if } m \geq 0 \\ \overline{P}_{l|m|}(cos\theta) sin|m|\lambda & \text{if } m < 0 \end{cases} \tag{2.12}$$

with $\overline{P}_{lm}$ the normalized associated Legendre polynomial.Note that this notation, which is the one that Wieczorek (2007) adopted, differs from the one more commonly used in geodesy and geophysics (e.g. Hofmann-Wellenhof and Moritz, 2006). Here, the order-wise sum over m (the innermost sum) is performed starting from $-l$. This results in a more compact notation: the spherical harmonics coefficients are denoted only by C_{lm}, instead of the usual "C_{lm}" and "S_{lm}". As defined by the two cases of Eq. 2.12, positive-order coefficients would be usually noted with C_{lm} and negative-order ones would be usually noted with S_{lm}.

Therefore, the formula for C_{lm}, on which the forward modelling of the relief is based, can be expressed in this form (Wieczorek, 2007):

$$C_{lm} = \frac{4\pi D^3}{M(2l+1)} \sum_{n=1}^{l+3} \frac{(\rho h^n)_{lm}}{D^n\, n!} \frac{\prod_{j=1}^{n}(l+4-j)}{(l+3)} \tag{2.13}$$

where the $(\rho h^n)_{lm}$ denotes the spherical harmonics of the relief times density, obtained from:

$$(\rho h^n)_{lm} = \frac{1}{4\pi} \int_{\lambda,\theta} [\rho(\lambda,\theta) h^n(\lambda,\theta)]\, Y_{lm}(\lambda,\theta) d(\lambda,\theta) \tag{2.14}$$

M in Eq. 2.13 denotes the total mass, as in Eq. 2.11. The relief h is expressed in respect to radius D. Eq. 2.13 includes a Taylor series expansion of the power of the relief $(\rho h^n)_{lm}$. If the sum is carried out up to its upper bound of the sum, $l+3$, it provides an exact solution. However, the number of terms grows linearly with l. Therefore, a truncation value n_{max} is typically chosen, under the assumption that higher terms become more and more smaller (Wieczorek, 2007). As observed by Balmino et al. (2012) (for Earth topographic potential) and Hirt and Kuhn (2017) (for the Moon case), this holds true only outside of the Brillouin sphere. Monotonic decrease in variance terms is not guaranteed for adimensional degree variances on the reference sphere: when a certain degree is reached, "the energy of succeeding terms is larger than of the previous" (Hirt and Kuhn, 2017). They found this phenomenon to become significant around degree 1000 —way above this experiment objective, which is limited by the maximum degree of satellite-only potential models (less than 300 as of March 2019).

The convergence of expansions of this kind has been rigorously studied by Sun and Sjöberg (2001), among others. For a maximum degree $l = 360$, a n_{max} of 2 was shown to already provide less than 1 % error —in the case of topography. Large deviations from the reference radius (e.g. in modelling deep and/or thick layers) may result in convergence problems, which can be mitigated by reducing the reference radius accordingly, as was shown later by Root et al. (2015). For this reason, the experiments described in this section included a test against a spatial–domain benchmark. It is described in more detail in section 2.2.2.

Wieczorek (2007) notes that the potential (Eq. 2.11) so obtained is valid only at $r > (D + h)$, i.e. outside the maximum radius of the relief —this arises from the derivation of Eq. 2.13, which is omitted here.

2.2.2. Layer–wise modelling

The forward modelling method by Wieczorek (2007), which was just described in section 2.2.1, provides the potential due to relief against a reference sphere.

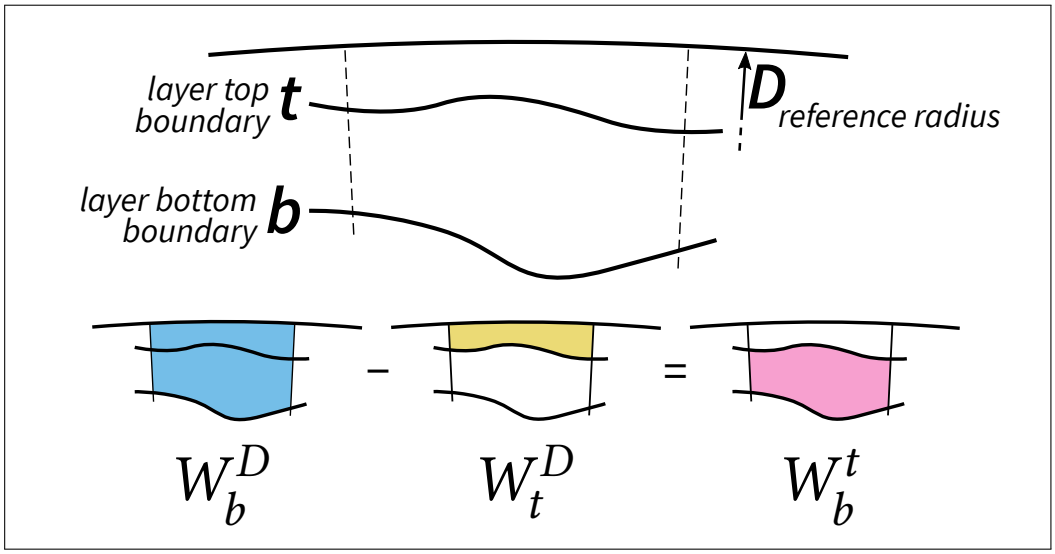

Figure 2.1.: Sketch for the potential of a layer bounded by surfaces b and t, as expressed in Eq. 2.15.

In order to model the gravity effect of a *layer*, I devised a strategy based on superposition of two relief-against-sphere potentials, which is described hereafter. Defining a *layer* as a volume of radially constant density $\rho(\lambda, \phi)$, bound by two surfaces expressed by geocentric radii $t(\lambda, \phi)$ and $b(\lambda, \phi)$, respectively top and bottom, its resulting potential (W_b^t) is equal to the following difference:

$$W_b^t = W_b^D - W_{top}^D \tag{2.15}$$

where subscripts denote the bottom boundary, superscripts denote the top boundary and D is the radius of the reference sphere (from Eq. 2.13). Therefore, the potential of a layer with two arbitrary bounding surfaces can be forward modelled by computing the difference between two reliefs referred to the same sphere, W_b^D and W_t^D. A graphical representation of this difference is shown in Fig. 2.1.

A pitfall of this strategy is that Eq. 2.11 needs to be evaluated twice, including the series expansion of Eq. 2.13. Other strategies with a similar aim have been developed (e.g. Novák and Grafarend, 2006) and avoid this issue. Nevertheless, the implementation by Wieczorek and Meschede (2018) was preferred here, since it could be readily integrated in the random modelling scheme — their Fortran functions are provided as F2PY–wrapped Python modules (Peterson, 2009).

A potential source of issues is the depth of the modelled mass distribution, in terms of distance from the reference sphere: we are not in the same conditions that topographic effect modelling operates in. Sun and Sjöberg (2001), assessing the convergence issues of spherical harmonics methods based on the binomial

expansion, observed that isostatic studies require much higher truncation numbers than terrain forward modelling. They argued that this arises due to the much larger differences between isostatic roots and the compensation depth (e.g. 100 km), compared to topography and the reference radius (about 9 km of maximum topography). This issue was also addressed by Root et al. (2015), who proposed an improved *fast spectral method* (Rummel et al., 1988; Novák and Grafarend, 2006) in order to model crustal and upper mantle regions. They devised an "error mitigation strategy" which consists in lowering the reference sphere to model the deeper layers. By doing so, they obtain results inside a ± 4 mGal difference range from spatial–domain forward modelling.

Compared with the mean Earth radius ($R = 6371$ km), a 40 km deep crust–mantle boundary accounts for about 6 thousandths of R. When modelling the underlying lithospheric mantle, a 300 km lithosphere–asthenosphere boundary reaches about 4.7 % of R. This means that the layers modelled in the following experiments are likely to incur in the issues that have been just described. Therefore. D has been lowered accordingly for each modelled layer, setting it at the shallowest modelled depth.

Care must be paid to the sign of density, which is provided on the same grid as the top and bottom boundaries. The relief-times-density product (ρh in Eq. 2.14) is negative for reliefs below the reference sphere (radius D). Since in this setup all the boundary surfaces lie at radii less than D, by design, we must reverse the sign of the input density map.

2.2.3. Spectral domain transform

Transforming a generic function f in its spherical harmonic coefficients f_{lm} goes under the name of Global Spherical Harmonic Analysis, GSHA (Sneeuw, 1994). It implies performing the following integration (Eq. 8 in Wieczorek, 2007):

$$f_{lm} = \frac{1}{4\pi} \int_{\lambda,\theta} f(\lambda, \theta) Y_{lm}(\lambda, \theta) d(\lambda, \theta) \tag{2.16}$$

which was already presented in Eq. 2.14, for the specific case of the relief-density product. When f is provided as a grid of discrete points, the integral of Eq. 2.16 can be evaluated numerically. For these tests we utilised $n \times 2n$ grids (expressed as latitude times longitude) compliant to Driscoll and Healy (1994) sampling theorem. Grids of this kind are also known as "equally spaced". For such grids, the numerical solution to Eq. 2.16 is obtained through along–latitude FFT first, then by integration over longitude for each degree and order (Sneeuw, 1994; Wieczorek, 2007). The transform on a $n \times 2n$ Driscoll and Healy (1994) grid is exact if f is band-limited to a maximum degree of $n/2 - 1$.

2.2.4. Power spectrum and correlations between functions

For the degree l of spherical harmonic coefficients f_{lm}, the *degree variance* is defined as:

$$S_{ff}(l) = \sum_{m=-l}^{l} f_{lm}^2 \tag{2.17}$$

The degree variances spectrum, $S_{ff}(\boldsymbol{l})$ with $\boldsymbol{l} = (1, \ldots, l_{max})$, provides a metric of the average power per harmonic degree (Rapp, 1982; Wieczorek, 2007; Hirt and Rexer, 2015b).

Comparison between the coefficients of two functions, f_{lm} and g_{lm} may be performed by computing their cross-correlation:

$$S_{fg}(l) = \sum_{m=-l}^{l} (f_{lm} \;\; g_{lm}) \tag{2.18}$$

which is usually expressed in a normalised form (e.g. Phillips and Lambeck, 1980; Rapp, 1982; Rexer et al., 2016), multiplying it with the factor $[S_{ff}(l) \cdot S_{gg}(l)]^{-\frac{1}{2}}$. Note that while Eq. 12 in Wieczorek (2007) omits it, this normalisation factor is applied by the *SHAdmitCorr* routine in SHTOOLS (Wieczorek and Meschede, 2018).

2.3. Input mass distribution models

2.3.1. Terrain correction

To model the solid topography, bathymetry (ocean, lakes) and ice, I adopted the Earth2014 model (Hirt and Rexer, 2015b). It comprises data from SRTM (SRTM v4.1 continental topography by Jarvis et al., 2008, SRTM30 PLUS v9 bathymetry by J. J. Becker et al., 2009), Bedmap2 (Fretwell et al., 2013), and GBT v3 (Bamber et al., 2013). It is the base of the extensively used `dV_ELL_Earth2014` topographic potential model (Rexer et al., 2016). In order to model an ellipsoid–referenced terrain correction (NETC, as described in section 2.1.1) and to keep consistency with the subsurface stripping corrections applied afterwards, the already available potential model was not used. Instead, I forward modelled an ad-hoc topographic potential, using the Earth2014 shape model (i.e. relief provided as geocentric radii) as input.

Uncertainty propagation on the terrain correction was not among the objectives of these experiments, therefore it was not carried out. However, this ad-hoc modelling setup would enable to do so easily, e.g. if required in further developments.

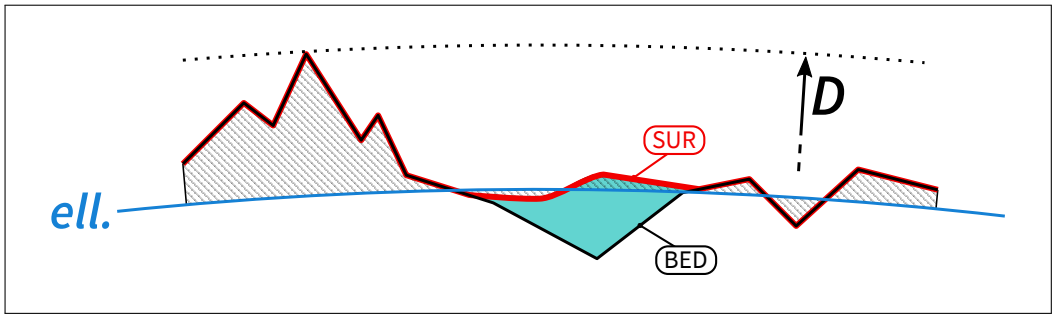

Figure 2.2.: Terrain correction: sketch of the solid topography and ocean bathymetry stripping. The hatched area ▨ covers the layer–volume of solid topography, between the reference ellipsoid (*ell.*) and the SUR surface. The teal-coloured area ■ represents the layer–volume of ocean bathymetry stripping, between the BED and SUR surfaces. Note that SUR and BED coincide onshore. D: reference radius. For a description of surfaces, see Tab. 2.2.

Potential forward modelling of the Earth2014 relief grids was partitioned in solid topography, ocean bathymetry, lake bathymetry, on-shore ice, off-shore ice, and on-lakes ice. Each unit was modelled as a distinct layer, with its own forward modelling call. *Solid topography* is defined by the SUR surface, the topmost surface in Earth2014, which includes the top surface of ice masses and of all bodies of water. The layers are summarised in Tab. 2.1, along with their densities and the defining top and bottom surfaces. The general scheme of layers arrangement is sketched in Fig. 2.2, showing the modelling of solid topography and ocean stripping as an example.

The boundary surfaces extracted from Earth2014 data are described in Tab. 2.2. Discrimination between ocean and lake bathymetry, and between on-shore and off-shore ice was performed using the "mask grid files" provided with the model, which include land type flags.

In order to obtain an exact number of samples nodes along latitude and longitude, all the grids were resampled to a 0.08° by 0.08° equally spaced grid ($n \times 2n$, as described in section 2.2.3), using a modified Akima piecewise cubic Hermite interpolation—a Matlab–specific implementation of Akima (1974)—which successfully avoided local artefacts and overshoots. The original grids in Hirt and Rexer (2015b) are provided with a 1 min and 5 min spacing, the latter being a box–mean downsampled version of the former. To ease the computational requirements, the 5 min version was used here, justified by the much lower target resolution of our terrain forward model ($l_{max} = 280$, resulting in a half–wavelength resolution of about 0.64°) This resulted in slight upsampling, from 5 min (equal to $0.08\overline{3}°$) to 0.08°.

The *complete terrain correction* was then computed by summing the gravity

effect of all the forward modelled masses. Expressed in terms of correction to the gravity disturbance (the *attraction of the Earth topography* A_R^{ET} in Eq. 2.9), it results in the following:

$$A_R^{ET} = -\frac{\partial}{\partial h}(W^{\mathrm{SUR}}_{\mathtt{GRS80}} + W^{\mathrm{SUR}}_{\mathtt{BED\_OCEANS}} + W^{\mathrm{SUR}}_{\mathtt{BED\_LAKES}} + \\ + W^{\mathrm{TBI}}_{\mathtt{ICEbot\_onshore}} + W^{\mathrm{TBI}}_{\mathtt{ICEbot\_offshore}} + W^{\mathrm{TBI}}_{\mathtt{ICEbot\_onlakes}}) \quad (2.19)$$

in which the terms refer to the labels in Tab. 2.1.

Table 2.1.: Terrain correction scheme: summary of the layers and their defining surfaces and densities. *Layer:* density of the modelled mass. *Ref.:* reference density for stripping corrections. *Contrast.:* layer density minus reference density. `GRS80`: GRS80 ellipsoid in geocentric radius (Moritz, 1980b; 2000). For a description of surfaces, see Tab. 2.2.

	Boundary surfaces		**Density [kg m^{-3}]**		
Layer name	**Top**	**Bottom**	Layer	Ref.	Contrast
Solid topography	`SUR`	`GRS80`	2670		
Stripping of					
ocean bathymetry	`SUR`	`BED_OCEANS`	1030	2670	−1640
lake bathymetry	`SUR`	`BED_LAKES`	1000	2670	−1670
on-shore ice	`TBI`	`ICEbot_onshore`	915	2670	−1755
off-shore ice	`TBI`	`ICEbot_offshore`	915	1030	−115
on-lakes ice	`TBI`	`ICEbot_onlakes`	915	1000	−85

2.3.2. Lithospheric density model

These experiments rely on the LITHO1.0 model by Pasyanos et al. (2014), which expands on the results of CRUST5.1 (Mooney et al., 1998), CRUST2.0 (Bassin et al., 2000) and CRUST1.0 (Laske et al., 2012). Pasyanos et al. (2014) provide a global model of the lithosphere, from the topography to the base of lithospheric mantle (lithosphere–asthenosphere boundary, LAB), parametrized vertically in a series of 'geophysical layers'. Horizontally, these layers are discretised on a icosahedron–based tessellation, which results in an average arc-distance of about 1° between points. The following physical properties are provided in each of the layers, for each of the depth-columns defined by the model nodes: compressional wave velocity (V_P), shear wave velocity (V_S), and density (ρ). In each node, the properties inside each layer are constant in the radial direction.

Thickness and properties of the crust and lithospheric mantle in LITHO1.0 are the result of a targeted–grid–search based inversion of surface wave dispersion

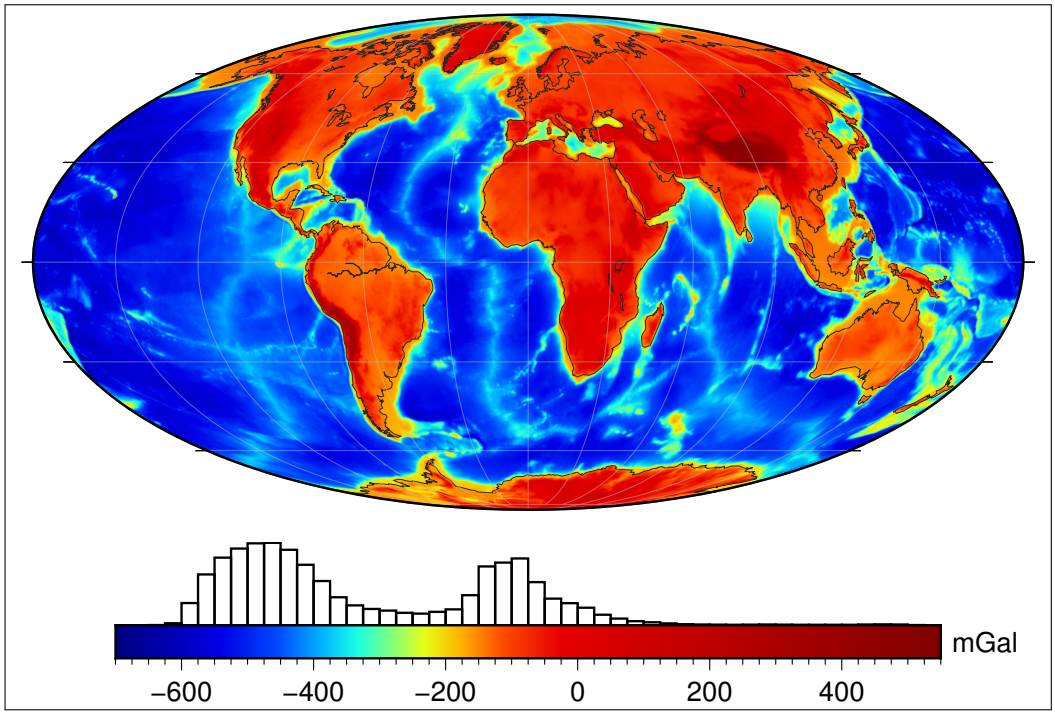

Figure 2.3.: Radial component of the terrain correction, corrections included. It is expressed as positive downwards (i.e. the attraction of solid topography is positive). The histogram over the colour scale is equal-area normalised, using a spherical approximation (cosine-of-latitude weighting).

Table 2.2.: Description of the input surfaces utilised in the terrain correction, as extracted from Earth2014. Text between quotes is from Table 1 in Hirt and Rexer (2015b). Land type flag description from the Earth2014 *readme* file (Hirt and Rexer, 2015a).

Surface	Description
SUR	"Lower interface of the atmosphere" i.e. surface of the continental topography, lakes, oceans and ice sheets. Unmodified from Earth2014 data.
BED_OCEANS	"Bedrock, planet without water and ice" masked by land type flag equal to 2 (ocean bathymetry).
BED_LAKES	"Bedrock, planet without water and ice" masked by land type flag equal to 3, 4 (inland lakes) or 8 (ice covered lake).
TBI	Topography, including ice, without liquid water. Unmodified from Earth2014 data.
ICEbot_onshore	TBI minus ice thickness, masked by land type flag equal to 5 and 6 (ice cover).
ICEbot_offshore	TBI minus ice thickness, masked by land type flag equal to 7 (ice shelf).
ICEbot_onlakes	TBI minus ice thickness, masked by land type flag equal to 8 (ice covered lake).

maps. Their starting model is based on the data in CRUST1.0 (Laske et al., 2012), an updated version of the sediment model by Laske and Masters (1997), an updated crustal thickness from undisclosed 1D seismic profiles (active source and receiver function studies), the lithospheric thickness by Pasyanos (2005), the upper mantle velocity from LLNL-G3Dv3 (Simmons et al., 2012), pure–gravity based crustal thickness in Antarctica (Block et al., 2009) and in other locations lacking seismic data (undisclosed). The lithospheric thickness in Pasyanos (2005) was in turn constrained by continental heat–flow based estimates by Artemieva (2006) and oceanic lithospheric cooling (Turcotte and Schubert, 1982).

As the authors of LITHO1.0 point out, it would be naive to assume that the model resolves the complicated lateral and vertical inhomogeneities of the lithosphere. They aimed at "a consistent, defensible, and updatable model that is compatible with observed data and can capture some of the geophysical community's collective understanding of the Earth" (Pasyanos et al., 2014). In the context of these experiments, LITHO1.0 provides a global, readily accessible model of density in sediments, crystalline crust, and lithospheric mantle. It provides a model at a nominal resolution which is comparable with the resolving

Table 2.3.: Average (**Avg.**) and standard deviation (**SD**) of thickness and density of the layers from LITHO1.0 (Pasyanos et al., 2014). SEDS: sediments, CRUST: crystalline crust (basement to Moho), LID: lithospheric mantle (Moho to LAB). See Tab. 2.4 for the statistics on aggregated layers.

	Thickness* [km]		Density† [kg m^{-3}]	
Layer	**Avg.**	**SD**	**Avg.**	**SD**
SEDS 1‡	0.62	0.61	1978	98
SEDS 2‡	2.21	1.23	2341	84
SEDS 3‡	3.10	2.33	2558	139
CRUST 1	5.63	6.36	2719	122
CRUST 2	6.49	1.23	2820	84
CRUST 3	9.06	4.20	2966	85
LID	81.9	62.0	3317	31

* Weighted by the cosine of latitude of each grid node, to account for the convergence of meridians.

† Density average is also weighted by thickness.

‡ Average of nodes with non-zero sediment thickness.

Table 2.4.: Average and standard deviation of thickness and density of grouped layers from LITHO1.0 (Pasyanos et al., 2014). See Tab. 2.3 for the non-grouped layers and notes on computation. Standard deviations ($1 \cdot \sigma$) are shown in parentheses.

Layer			
SEDS 1 SEDS 2 SEDS 3	SEDS 1.00 (1.56) km 2128 (182) kg m^{-3}	SEDS + CRUST 22.1 (15.8) km 2827 (82) kg m^{-3}	whole lithosphere 104.0 (67.7) km 3213 (91) kg m^{-3}
CRUST 1 CRUST 2 CRUST 3	CRUST 21.2 (15.6) km 2856 (76) kg m^{-3}		
LID			

power of geophysical inversion based on satellite–only global gravity models.

Compiling the available data in a global model of the crust and/or lithosphere is still a challenging task, requiring the retrieval, harmonisation and gridding of a huge assortment of data sets. The recent global crustal thickness by Szwillus et al. (2019) was also considered as an alternative crustal model, due to two features that are particularly relevant for these data reduction experiments: (1) the transparency in its construction, since the input data is disclosed and accessible (Mooney, 2015) and the methods are reproducible; (2) the estimation of uncertainty is described and its grids are provided: they could be employed in a realistic error propagation scheme to the forward modelled gravity field.

Nevertheless, while LITHO1.0 is lacking in those two aspects, it was still adopted as our reference density model, owing to: (1) its integration with a global sediment thickness model; (2) its seismic multi–observable nature, which takes advantage of the sensitivity to discontinuities of controlled–source and receiver functions, from prior models, and the sensitivity to "bulk Earth properties" —from which density can be derived— of surface waves; (3) its relative independence from gravity data: aiming at preventing any circular reference (i.e. correcting gravity data with models which were inverted from gravity), full independence would be ideal. While LITHO1.0 is not free from local gravity–based *fill-ins* (in Antarctica and other undisclosed locations), the inversion starting models and inversion strategy of Pasyanos et al. (2014) is predominantly based on seismic data. It is for this particular reason that multi–observable models that include global gravity models among their input data were left out, such as the recent *LithoRef18* model (Afonso et al., 2019).

In summary, LITHO1.0 is a reasonable compromise model, fit for this methodological test, albeit affected by the aforementioned pitfalls. It must be noted that the procedure hereby described could be easily scaled to different global models and to more refined uncertainty data, as further described in section 2.4.

The three properties provided in LITHO1.0 (V_P, V_S, and ρ) are not independently estimated quantities: the starting model reflects the reference values and parameter relationships defined by the "primary crustal types" and their variants, from CRUST5.1 (Mooney et al., 1998) and the following version (as mentioned above). The V_S/V_P ratio in the crust is unmodified from CRUST1.0 data. The Poisson's ratio (see e.g. Sheriff, 2002) in the lithospheric mantle, from which the V_S/V_P can be derived, is fixed to 0.26. Density in the lithospheric mantle ("LID" layer) is provided as a constant value (3300 $\mathrm{kg\,m^{-3}}$). The extraction of a velocity-converted density in the LID is the subject of the following section (2.3.3).

Regarding data uncertainty, no space–wise error information is provided, neither any information on data quality (e.g. distance to data or sources of the starting model). These experiments therefore resorted to a simplified error

model, which is described in section 2.4.

The 'water' and 'ice' layers were discarded, since Earth2014 (Hirt and Rexer, 2015b) relies on updated and revised data. Therefore, the top of the solid–Earth layers of LITHO1.0 (starting from the first sedimentary layer) has been re-referenced to Earth2014 bedrock (BED surface, see Tab. 2.2 and Hirt and Rexer, 2015a).

As already mentioned for the terrain correction, this data also needs to be gridded in a format compatible with the chosen gravity forward modelling: an equally spaced $n \times 2n$ grid, consistent with Driscoll and Healy (1994) sampling theorem. Triangulation from the original tessellated data to geographic coordinates was performed using the *Stripy* package (Moresi and Mather, 2019b; Moresi et al., 2019) and *litho1pt0* (Moresi and Mather, 2019a), a Python interface to LITHO1.0.

2.3.3. Velocity–density conversion in the lithospheric mantle

Density in LITHO1.0 (Pasyanos et al., 2014) lithospheric mantle (LID layer) is provided constant at 3300 kg m^{-3}. V_P and V_S are both provided, but with a Poisson ratio (σ) fixed at 0.26. The V_S/V_P ratio is directly related to σ (Sheriff, 2002):

$$\frac{V_S}{V_P} = \sqrt{\frac{0.5 - \sigma}{1 - \sigma}} \tag{2.20}$$

This results in a V_S/V_P ratio in LITHO1.0 lithospheric mantle of about 0.57.

Therefore, a velocity-to-density conversion was set up, based on assumptions on composition and thermodynamic modelling. In order to define this strategy, a trade-off was needed between uniform velocity-density scaling (i.e. with a constant ratio) and detailed modelling of mineralogical phases, which goes beyond the scope of these experiments.

The basis for the conversion is the compositional model by Griffin et al. (2009). As they argued, there is a broad relation between the lithospheric mantle composition and the tectonothermal age of the overlying crust. Therefore, I have grouped the crustal types from CRUST1.0 (Laske et al., 2012) in a simplified two-member model of LID composition. The result of this partition is shown in Fig. 2.4. The two members are *archon* (Arc_1) and *tecton* (Tc_1), the code from Griffin et al. (2009) shown in parentheses. They represent a simplified but realistic discrimination between 'young' (Phanerozoic) and 'old' lithospheric mantle (e.g. protons, shields, cratons).

Phase equilibria were modelled with the Perple_X program (Connolly, 2005; Connolly, 2009), adopting the hp02ver thermodynamic data base (Holland and Powell, 1998; Ghiorso et al., 2002), which is a comprehensive chemical model for silicates in the lithosphere, appropriate for depths less than 440 km. I extracted

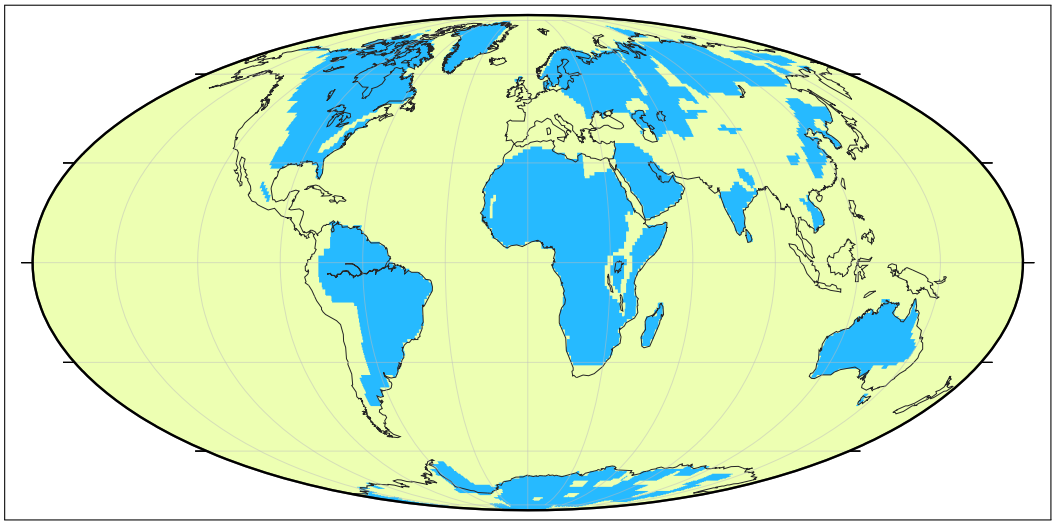

Figure 2.4.: Two-member tectonothermal age partition of the lithospheric mantle, derived from the crustal types by Laske et al. (2012). **Light green**: 'young' lithosphere (Phanerozoic, with *tecton* composition), **blue**: 'old' lithosphere (protons, shields, cratons, with *archon* composition).

V_S and ρ in the pressure range of interest (up to the maximum LAB depth, 300 km) and then fitted a $\rho(P, V_S)$ linear interpolator on the data. Pressure values were computed as purely lithostatic pressure, by depth-integration of the density of the overlying layers and of the constant 3300 kg m^{-3} lithospheric mantle density (prior to conversion). The conversion curves on the pressure-velocity field are shown in Fig. 2.5.

Since the whole lithospheric mantle is originally defined in bulk columns, Moho to LAB, it was sliced depth-wise prior to velocity conversion. While in LITHO1.0 V_S does not change depth-wise inside a layer, this slicing allowed for a finer discretisation of pressure: inside each slice, the value at the slice midpoint was adopted. This slicing operation follows the same depth discretisation that was adopted for the reference density model, as described in the next section 2.3.4. Conversion results, condensed after slicing using a thickness-weighted average, are shown in Fig. 2.7.

It must be noted that this conversion strategy was set up to enable propagation of lithospheric mantle inhomogeneities, as sensed by a model that provides only velocities. I deemed a constant velocity-to-density scaling factor as an excessive simplification, since it would have ignored the lateral variations due to tectonothermal ages and the radial ones due to pressure dependence. Still, since the main objective of these experiments is to assess a modelling method for global reductions and propagation of their uncertainties, comprehensive thermochemical modelling was left out.

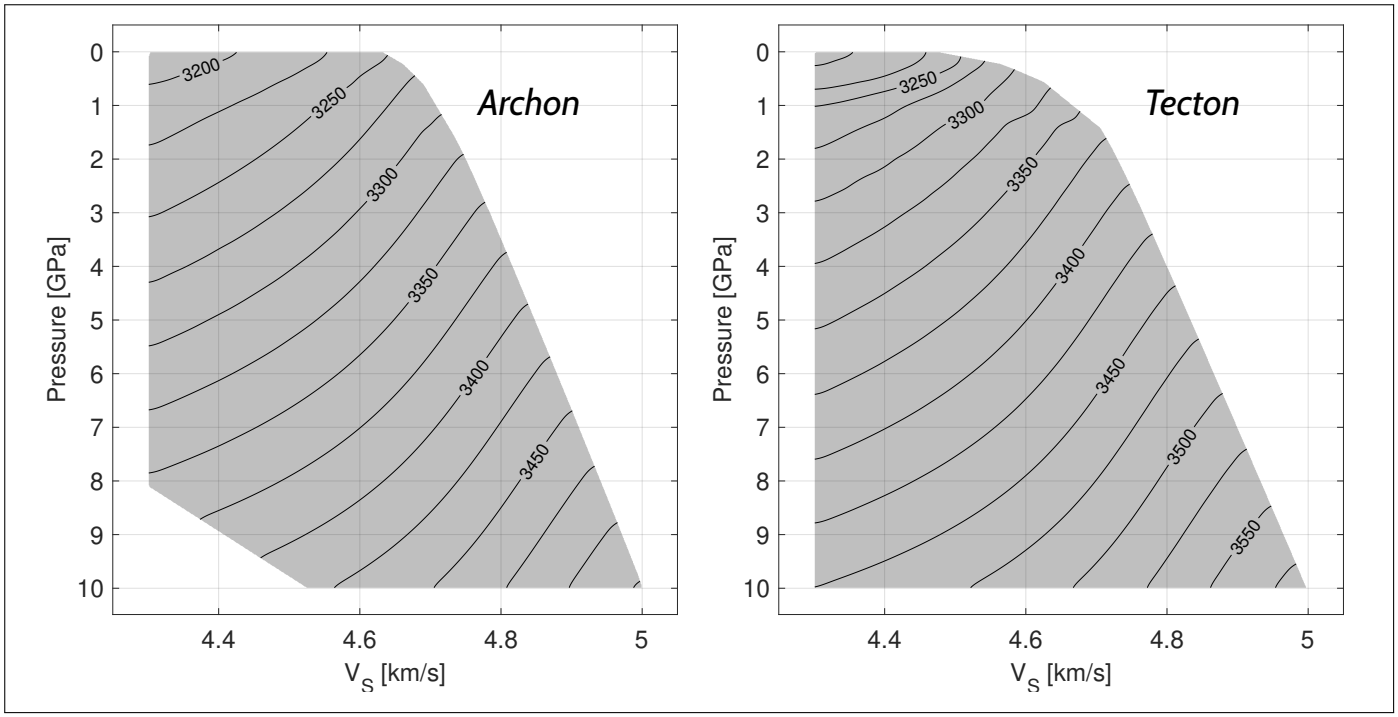

Figure 2.5.: Pressure and shear wave velocity (V_S) density conversion curves for the two-member lithospheric mantle composition model. Density is plotted with contours, the gray-filled area shows the bounds of the modelled domain.

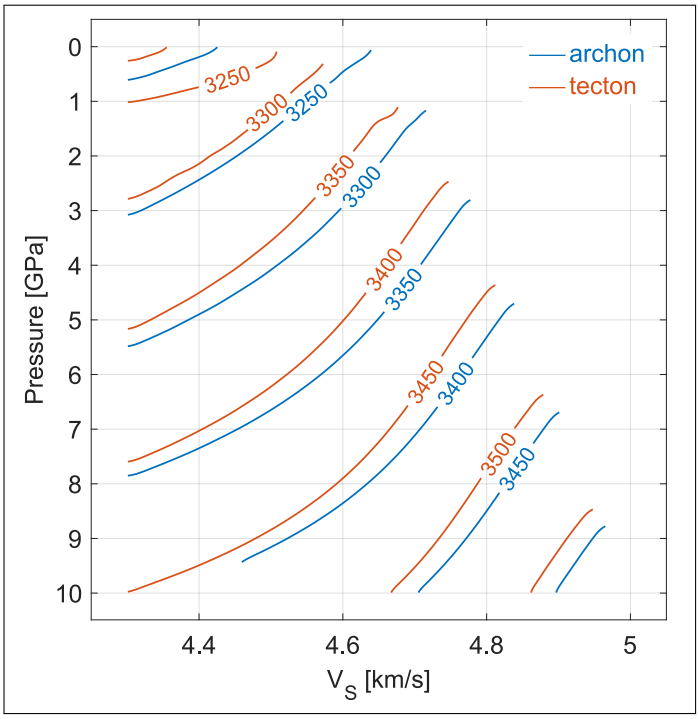

Figure 2.6.: The density conversion solutions for the two-member composition model (as shown in Fig. 2.5), plotted overlaid on the same pressure-velocity field.

2.3.4. Reference densities: layered normal Earth

As described in section 2.1.1, the attraction of 'anomalous masses' inside the planet is defined against the normal gravity (Eq. 2.5 and following). By assuming that the normal gravity arises from a 'reference Earth' with ellipsoidal stratification and with no lateral inhomogeneities, we can express any density refinement to the normal gravity model as a contrast against this 'normal density reference'. As mentioned in section 2.1.2 and as discussed by Vajda et al. (2008), this should be satisfactorily approximated by reference earth models.

For all the sub-topography (i.e. sediments to lithospheric mantle) forward modelling performed here, a 'normal density reference' was built, defined by a discretely layered reference column. The boundaries between layers in this column define a set of concentric shells, referred to the reference ellipsoid. The modelled layers in LITHO1.0 were 'sliced' according to these shells: in other words, an intersection was performed between the top/bottom boundaries defining each LITHO1.0 layer and the reference shells boundaries (see Fig. 2.9). By doing so, each layer of the input model was divided in a number of *layer-slices* equal to the number of reference shells it intersects. In each layer-slice the density contrast was expressed as the difference between the density prescribed by the model at those coordinates and the density of the reference shell covering

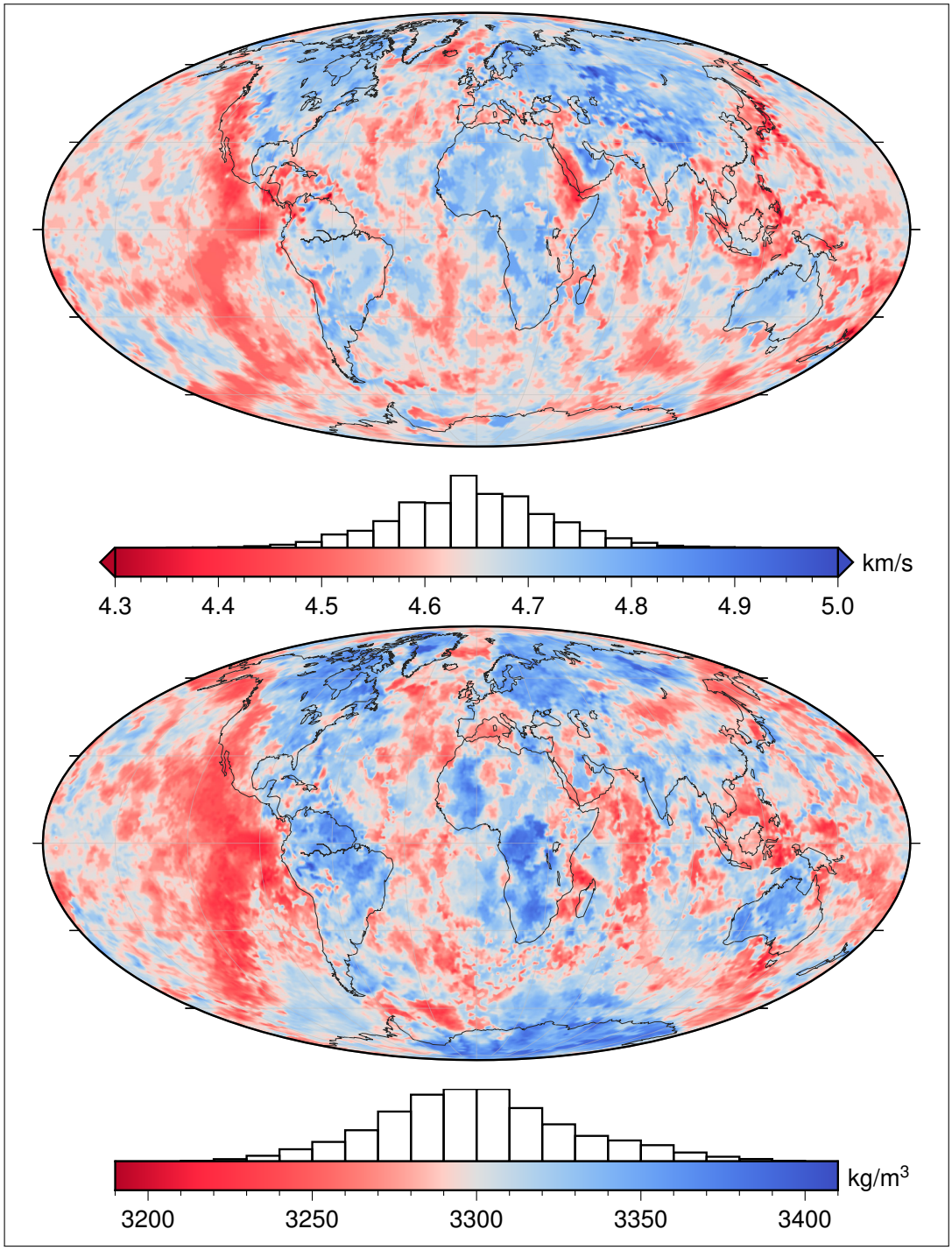

Figure 2.7.: **Top:** shear wave velocity (V_S) in the lithospheric mantle (LID), from LITHO1.0. **Bottom:** lithospheric mantle average (bulk) density, obtained by velocity to density conversion.

that depth range.

In order to build a reference density column, the density in each reference shell was computed by globally averaging the densities in the input model in the depth range defined by the shell. Averages were weighted for the portion of shell occupied by each layer of the model (e.g. if in a specific grid node, in the 10 to 18 km depth range, the first kilometre is occupied by the layer 'SEDS3' and the remainder by 'CRUST1', the average density is computed accordingly) and for the cosine of the latitude of each grid node (to account for the convergence of parallels in a regular grid, in a spherical approximation). The first reference shell extends from the Earth2014 bedrock (BED) to the first reference depth, 10 km. In this slice, the average density of LITHO1.0 data is equal to 2681 kg m^{-3}, only 11 kg m^{-3} more than the adopted 2670 kg m^{-3} constant density topography. For consistency with the terrain correction, the first reference shell density was kept at 2670 kg m^{-3}.

The maximum modelled depth was set to set to 410 km, to account for the thickest lithosphere in LITHO1.0, 320 km and a buffer for any additional depth introduced by the uncertainty-modelling perturbations. The volume between the bottom of the lithosphere and the maximum modelled depth was filled-in with a 'reference asthenosphere' with a density of 3300 kg m^{-3}. This a reference value which, albeit plausible (e.g. Bormann, 2002), is not directly constrained by the input data in any way - it is akin to the usual 2670 kg m^{-3} adopted for the terrain correction (Hinze, 2003). As discussed afterwards (section 2.5), any unmodelled sub-lithospheric density variation shows up in the refined gravity residuals (superimposed with all the omissions in the input 'known masses' of the lithosphere). The 'normal density reference' obtained in this way (average LITHO1.0 densities and 'asthenosphere fill-in') is presented in Fig. 2.8 (black line) and in Tab. 2.5. The depth-density curve from the *ak135* model (Kennett et al., 1995; Montagner and Kennett, 1996) is plotted alongside (blue line, the data was sourced from the NMSOP-2 manual Bormann, 2002, which provides it in a tabular form). The *ak135* model is also plotted as the average density in the same discrete depth intervals of the LITHO1.0-based density reference.

The density reference built using the LITHO1.0 densities is considerably lower than *ak135*, especially in the 18 to 210 km depth range. This arises from both omissions in the model and the constant 3300 kg m^{-3} 'asthenosphere fill-in' – if *ak135* was used as a fill-in instead, areas of thin lithosphere would contribute in raising the average. Nevertheless, this strategy was preferred since, by doing so, the gravity maps of forward modelled masses (in terms of contrast) and the GGM with applied reductions are not overwhelmed by the signal of thickened lower density crustal keels reaching in an high density upper asthenosphere resulting from *ak135* global average, which is sensibly biased by the predominance of oceanic lithosphere in the Earth.

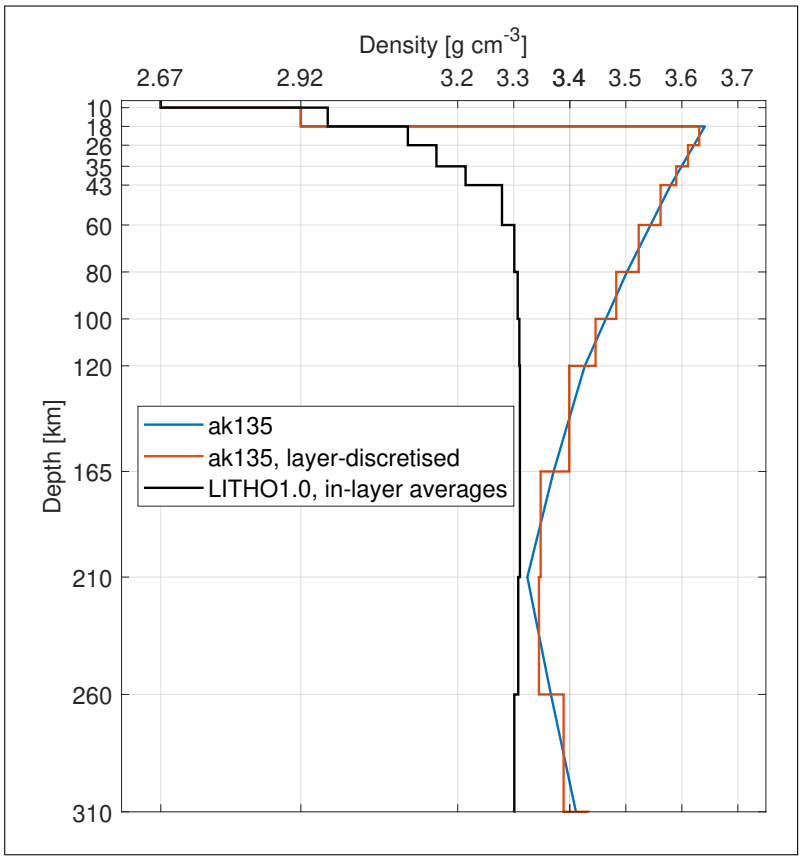

Figure 2.8.: **Blue**: input depths and densities from the *ak135* Earth reference model (Kennett et al., 1995), set at 2.67 g cm^{-3} at less than 10 km. **Orange**: constant density reference layers obtained by averaging the *ak135* model in discrete depth intervals. **Black**: constant density reference layers obtained by averaging the *LITHO1.0* (Pasyanos et al., 2014) model in the same discrete depth intervals of the orange curve. The layer-discretised densities are shown in Tab. 2.5.

Table 2.5.: Average densities of the *ak135* Earth reference model, obtained by interpolation in discrete depth intervals, and average densities derived from the *LITHO1.0* global data, computed inside the same depth intervals). See also Fig. 2.8.

Depth [km]	**Density [g cm^{-3}]**	
	ak135	*LITHO1.0*
0	2.670	2.670
10	2.920	2.968
18	3.631	3.111
26	3.611	3.162
35	3.590	3.214
43	3.562	3.279
60	3.523	3.301
80	3.483	3.307
100	3.446	3.310
120	3.399	3.311
165	3.348	3.311
210	3.345	3.308
260	3.389	3.301
310		

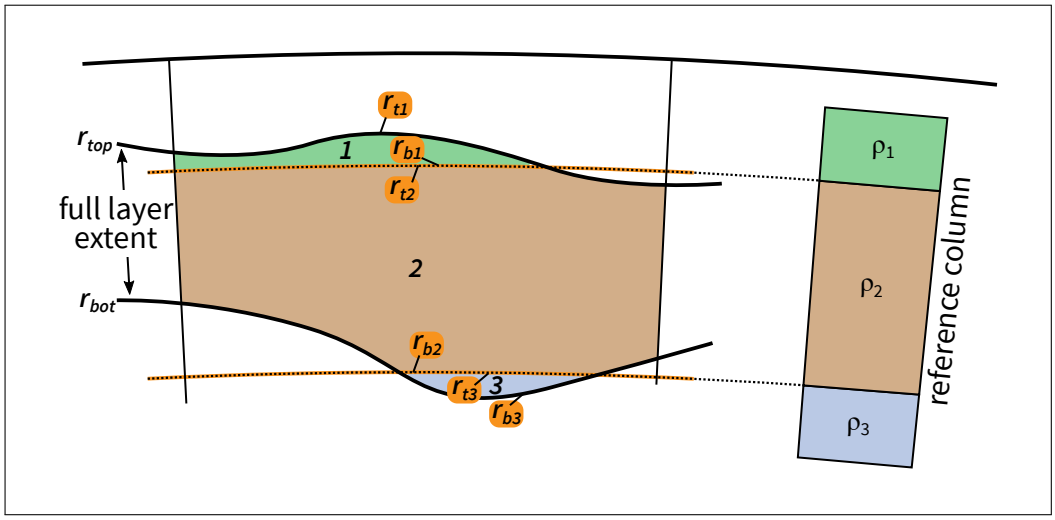

Figure 2.9.: Sketch describing the 'slicing' of layers according to a reference density model (a concentric depth-wise succession of constant density shells). The input, non-partitioned, layer is defined by top and bottom surfaces r_{top} and r_{bot}, expressed as radius. The portion of layer in the i-th reference shell is expressed as separate top and bottom sub-surfaces r_{ti} and r_{bi}. Where no part of the layer intersects a reference shell, i.e. where there is no mass to model, the two surfaces coincide.

2.4. Assessment of uncertainty

Uncertainty in the 'known masses' input data was estimated using Monte Carlo error propagation (Aster et al., 2013, chapter 2.6). Depths of the boundaries, defining the layers in LITHO1.0, and the density grids associated with each layer were randomly perturbed according to a set of error assumptions, obtaining a population of input mass models. The gravity field of each of these mass models was forward modelled using the spectral layer-wise method described in this chapter, therefore obtaining a population of resulting gravity fields. To extract a metric of the spatial distribution of uncertainty and its magnitude, I then computed the standard deviation of the vertical component of gravity at each grid node of the ensemble of globally synthesized grids.

2.4.1. Error model

As described in section 2.3.2, LITHO1.0 is provided with no information on uncertainty, nor on the spatial variability of data resolution. At the time of setting up and running this uncertainty assessment, the only crustal scale models providing spatial error information were regional extent Moho depth models: e.g. Grad et al. (2009) and Artemieva and Thybo (2013) for the European plate, Steffen et al. (2017) in Greenland, Van der Meijde et al. (2013) in South America,

to name a few.

In the design of this uncertainty assessment experiment, it was therefore decided to apply a spatially uniform error model for the depths and densities in the input mass model. The error on depth of the layer interfaces was modelled proportionally with the depth of each grid node, with a standard deviation of 5 % of depth and a normal error density function. The error on density was similarly modelled, with a normal distribution with a standard deviation of $100\,\mathrm{kg\,m^{-3}}$.

It should be noted that the method proposed and tested here can be easily scaled to more complex error models. Both the recent availability of global models with uncertainty information provided (e.g. Szwillus et al., 2019) and the possibility of global harmonisation of an ensemble of the aforementioned regional models leave plenty of room for further development.

2.4.2. Implementation

The forward modelling of each randomly perturbed mass model is independent from the other random draws – in other words, Monte Carlo uncertainty propagation is an 'embarrassingly parallel' problem (see e.g. Kontoghiorghes, 2005, chapter 15). Therefore, the computation was carried out concurrently, using the *multiprocessing* Python module.

The output of each forward modelling run, comprising the separated gravity effect of each slice of each input layer, adds up quickly in terms of memory requirement. Since the statistic we are interested in is the standard deviation at each grid node, a partition scheme was set up: the variance (σ^2) and average of the output at each grid node is computed in 100-draw blocks and the individual outputs of each draw are then discarded. The standard deviation of a variable X_i, partitioned in a set of g partitions, each obtained from k draws, is the following (Chan et al., 1982; Pebay, 2008):

$$\sigma(X_1, \ldots, X_{g\cdot k}) = \sqrt{\frac{k-1}{gk-1}\left(\sum_{j=1}^{g} V_j + \frac{k(g-1)}{k-1}\mathrm{Var}(E_j)\right)} \tag{2.21}$$

Where E_j is the mean and V_j is the variance computed inside each partition. $\mathrm{Var}(E_j)$ denotes the variance of the partition-averages.

Choosing the number of necessary random draws requires a trade-off between insufficient sampling of the error density function (due to low values) and computation time. Empirical assessment of the behaviour of number of draws against quality of the estimation would be possible – e.g. excessively low number of draws show an unrealistic short wavelength noise, arising from the uncorrelated perturbations of depth and density between adjacent grid nodes.

The attenuation of this phenomenon with rising number of draws could be, in theory, assessed. It was left aside due to computational time constraints, since it would have required a significant number of full-scale uncertainty propagation model runs. A value of 5000 draws was heuristically chosen, instead, observing no anomalous behaviour in the power of the higher degree and orders.

2.5. Global reductions: results and discussion

2.5.1. Maps of the forward modelled corrections and reduced NETC

The input gravity map (GGM, Fig. 2.10 top), the terrain-corrected disturbance (Fig. 2.10 bottom), and all the further refinements for lithospheric masses (the bottom maps in figures 2.11 through 2.16) are expressed as gravity disturbances (δg). δg, being a difference of a vector magnitudes, is a scalar by definition (Eq. 2.1). The forward-modelled gravity corrections (the top maps in figures 2.11 through 2.16), on the other hand, are the first-order derivative of the gravity potential arising from the modelled 'known masses'. Being a three-component vector, only its vertical component g_z is plotted – being the most significant. Both the disturbances and the g_z component of the corrections were synthesized on a global $n \times 2n$ grid at 10 km over the GRS80 ellipsoid. The spherical harmonic expansion of the attraction of the modelled masses was truncated at $l_{max} = 300$ (the maximum degree and order of the input GGM).

The colour scales were adapted to the range of values of each map, but no colour scale normalisation has been applied (i.e. there is no contrast enhancement using colour scale "stretching"). Minimum and maximum values of the scales were set to the 0.001 and 0.999 quantile of the plotted values, respectively. By doing so, extreme values are clipped and do not skew the scale excessively. Quantiles were computed using cosine-of-latitude weighting. The actual minimum and maximum values are always printed below each map, along with the global average and standard deviation (both appropriately weighted for latitude). The perceptually uniform 'viridis' colour scale (N. Smith and van der Walt, 2015) was used.

In the case of the forward modelled effect of the crystalline crust ('CRUST, g_z', top map of Fig. 2.12), the minimum values of some features are more than 1000 mGal lower than the average value. For the sake of map clarity, the colour scale minimum was clipped at an higher value. The same map is plotted with the full range in Fig. 2.13. The explanation for this behaviour is discussed afterwards.

An histogram accompanies each map, to provide a qualitative assessment

of the data distribution. The vertical scale, which is omitted for clarity, represents linear bin counts, after cosine-of-latitude weighting. A global equal-area Mollweide projection was adopted in all maps.

List of the presented maps

- Global gravity model: the gravity disturbance from the combined satellite-only GOCO06s model (Kvas et al., 2019a). *[Fig. 2.10, top]*
- NETC disturbance, obtained by applying the terrain correction (Fig. 2.3) to the global gravity model. *[Fig. 2.10, bottom]*
- Sediment correction: cumulative effect of the layers SEDS1, SEDS2, and SEDS3. Sediment corrected NETC disturbance. *[Fig. 2.11]*
- Consolidated crust correction: cumulative effect of the layers CRUST1, CRUST2, CRUST3. Whole-crust (sediments and consolidated crust) corrected NETC disturbance. *[Fig. 2.12]*
- Consolidated lithospheric mantle correction: effect of the LID layer. Whole-lithosphere (sediments, consolidated crust, lithospheric mantle) corrected NETC disturbance. *[Fig. 2.14]*
- Correction for the first 80 km, including a constant density asthenosphere fill-in, and 0-80 km corrected NETC. *[Fig. 2.15]*
- Correction for the first 310 km, including a constant density asthenosphere fill-in, and 0-310 km corrected NETC. *[Fig. 2.16]*

The gravity disturbance from the input global gravity model, the effect of sediments, consolidated crust, and lithospheric mantle, and three selected reduction stages of the NETC disturbance (only terrain correction, first 80 km, first 310 km) are also accompanied by histograms with separate counts for nodes over oceans and continents (i.e. above-sea-level landmasses). These histograms are in Fig. 2.17, 2.18, and 2.19, respectively. A brief discussion on the contents of these maps and histograms is provided in subsections 2.5.1.1 through 2.5.1.4.

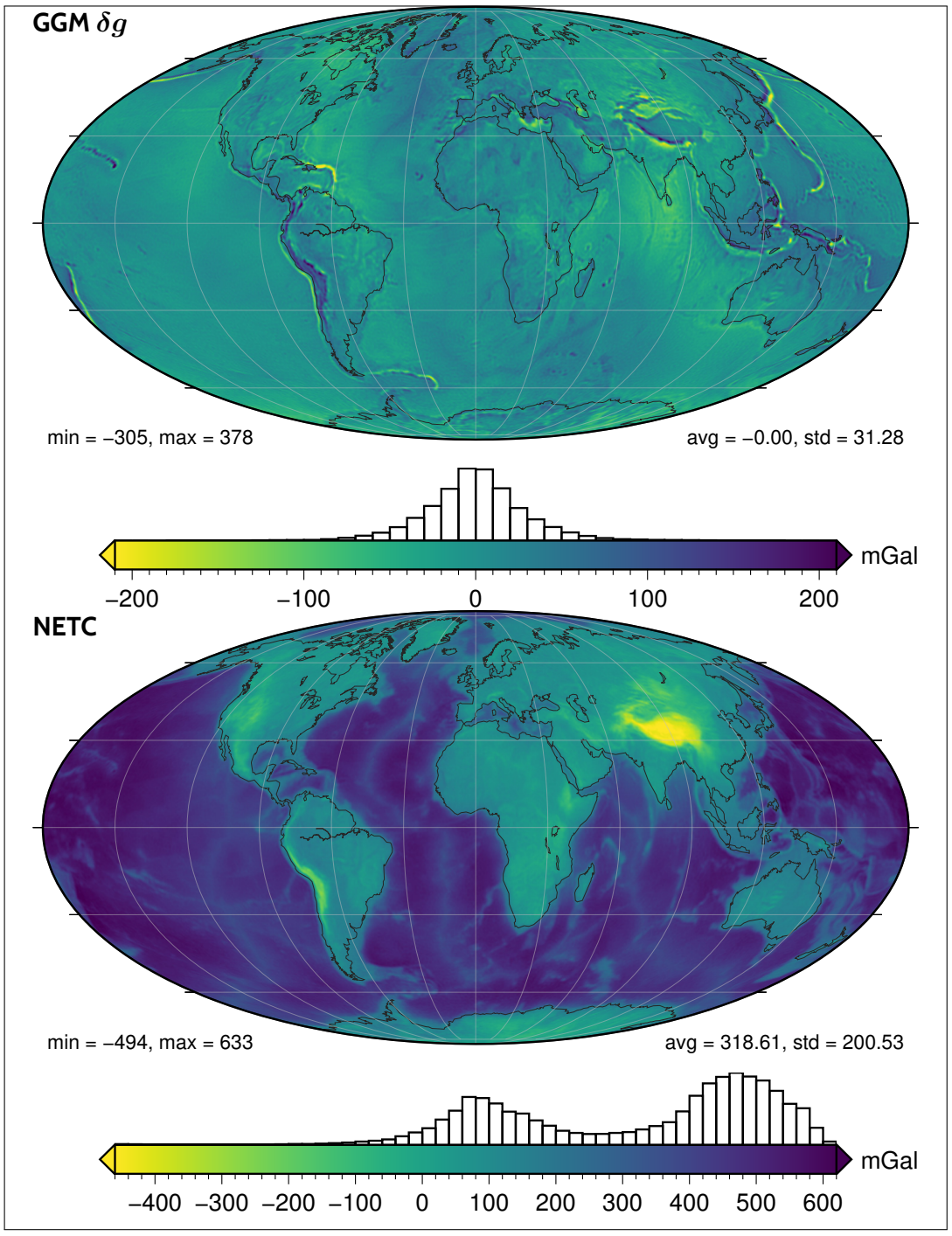

Figure 2.10.: Top: GGM. Gravity disturbance of the input global gravity model: the combined, satellite-only, GOCO06s model (Kvas et al., 2019a). **Bottom: NETC.** No Ellipsoidal Topography corrected gravity disturbance, resulting from applying the forward-modelled Earth2014 (Hirt and Rexer, 2015b) data (shown in Fig. 2.3) to the GGM.

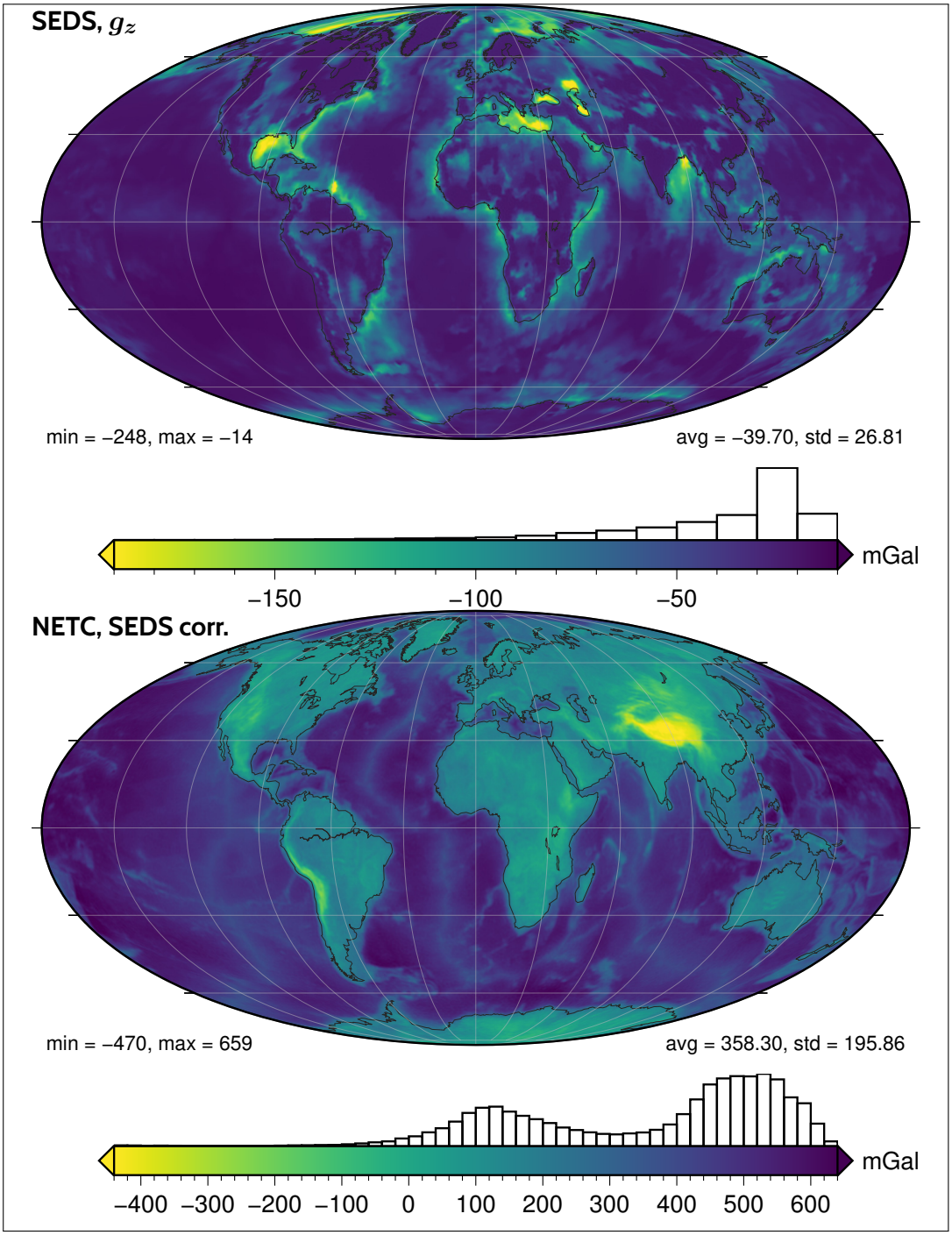

Figure 2.11.: Top: SEDS, g_z. Vertical component of the forward-modelled effect of the three sediments layer in LITHO1.0. **Bottom: NETC, SEDS corrected.** The NETC δg (Fig. 2.10 bottom) corrected for the effect of sediments.

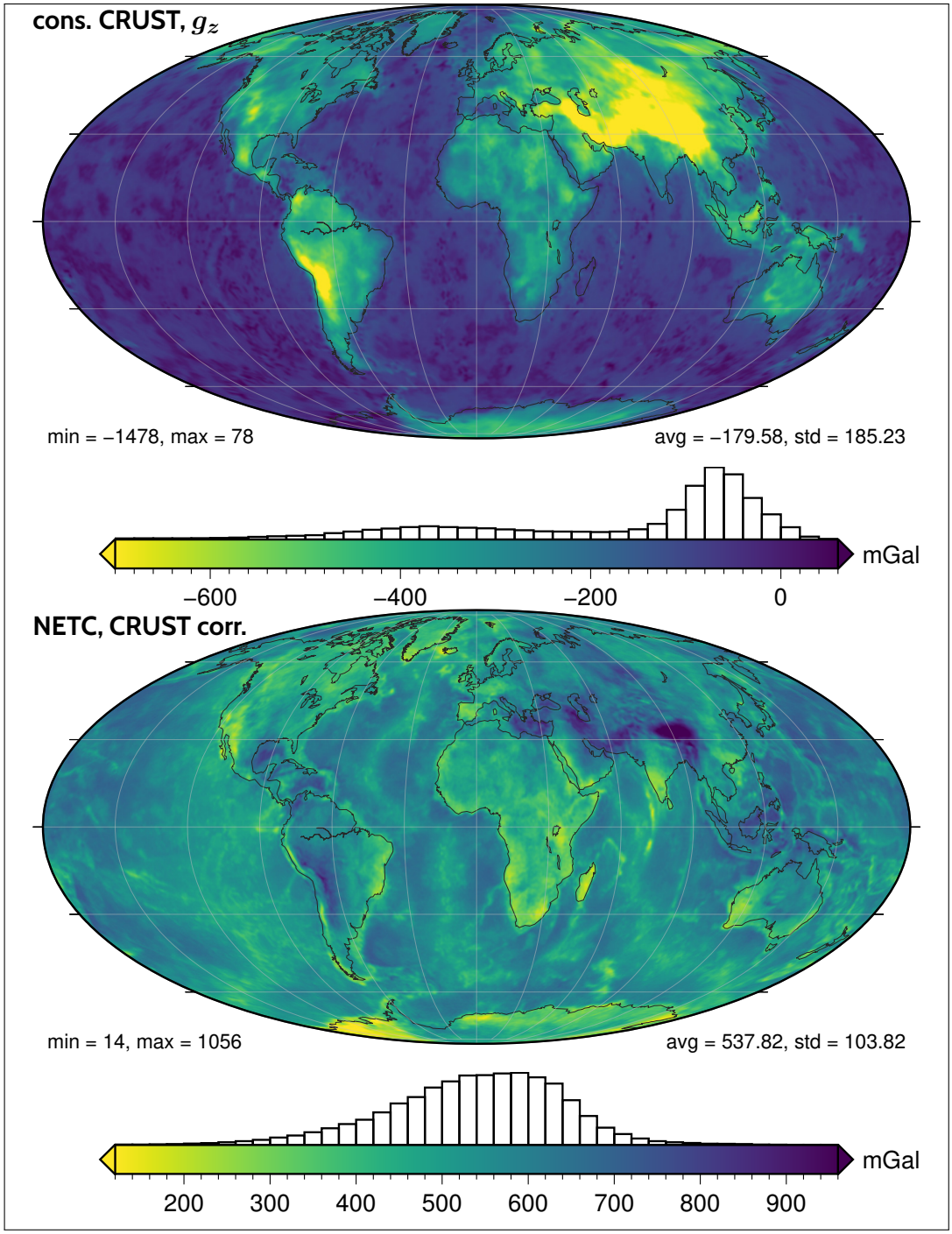

Figure 2.12.: Top: consolidated CRUST, g_z. Vertical component of the forward-modelled effect of the three consolidated crust layer in LITHO1.0. The minimum value of the colour scale was clipped at −700 mGal. A map covering the full extent is shown in Fig. 2.13. **Bottom: NETC, whole-crust corrected.** The NETC δg (Fig. 2.10 bottom) corrected for the cumulative effect of sediments and consolidated crust (i.e. for the *whole crust*).

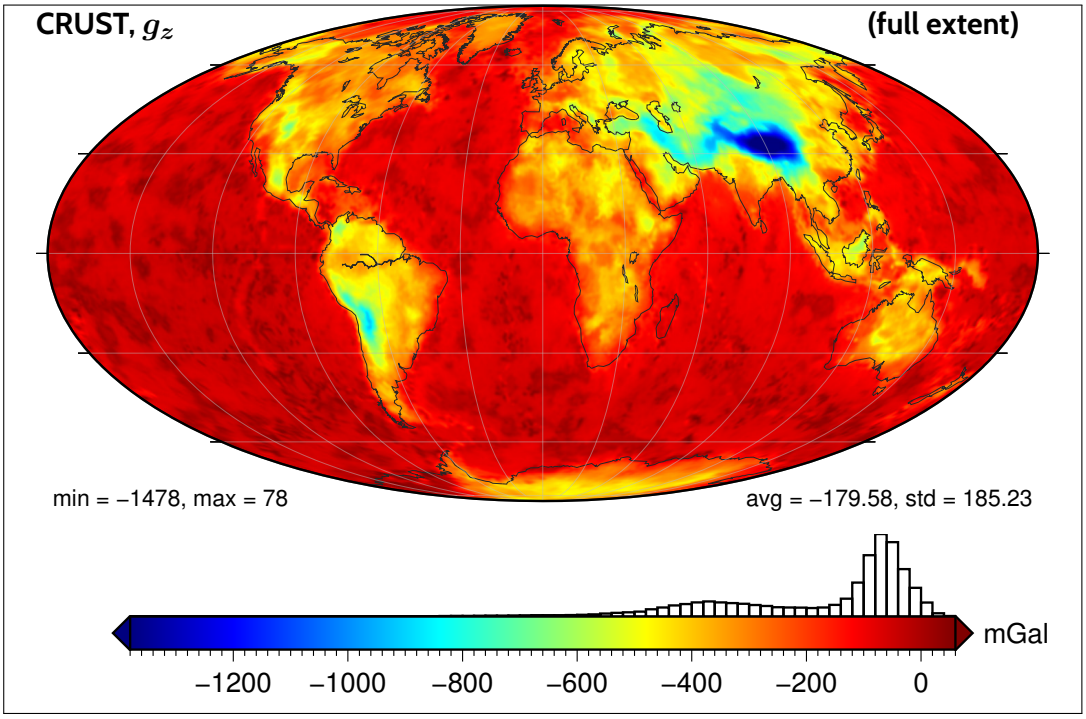

Figure 2.13.: CRUST, g_z. Vertical component of the forward-modelled effect of the three consolidated crust layer in LITHO1.0. This is the same quantity plotted in the top map of Fig. 2.12. Here a different colour scale is used and the full extent of values is plotted, without clipping the most negative values.

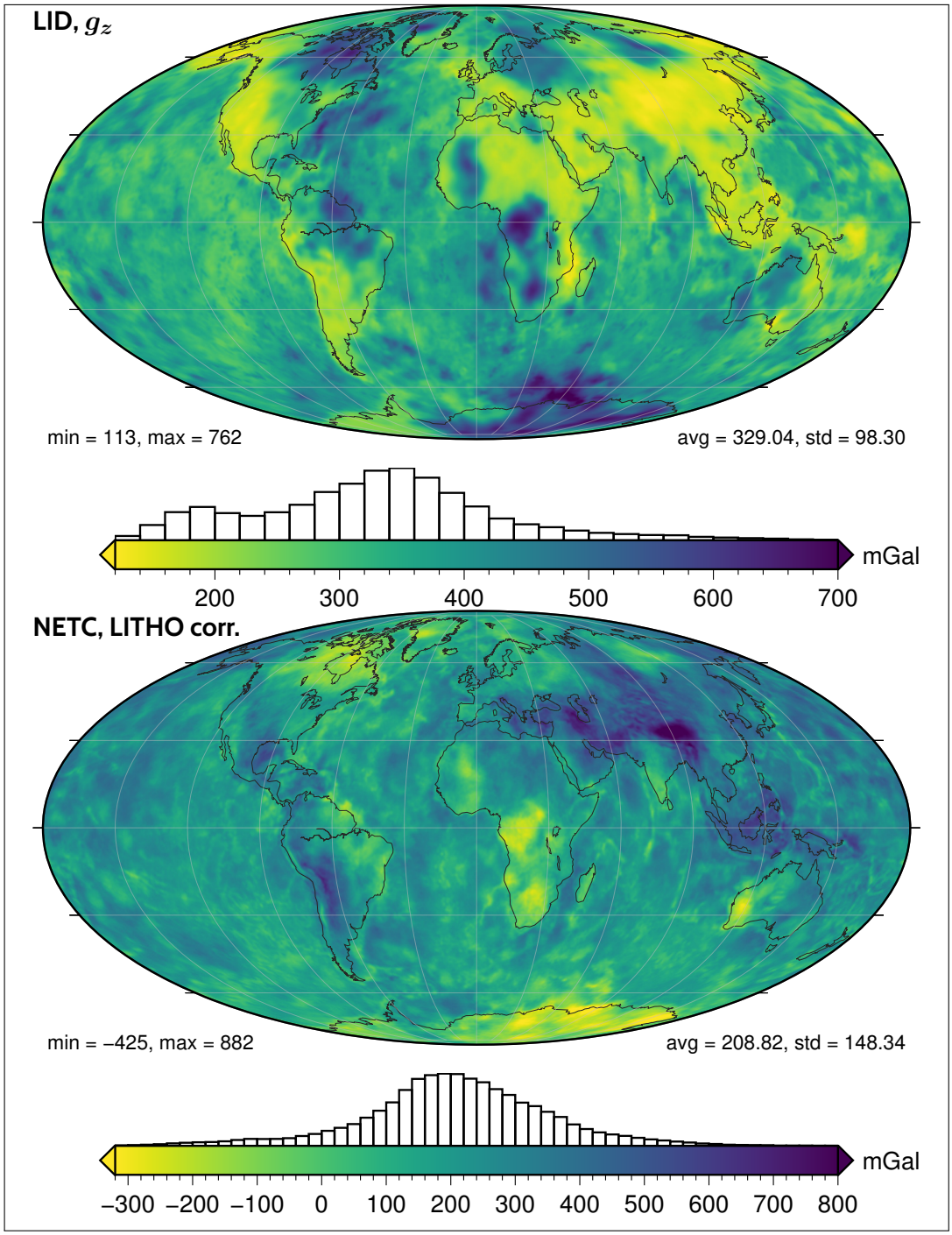

Figure 2.14.: Top: LID, g_z. Vertical component of the forward-modelled effect of the lithospheric mantle, the 'LID' layer in LITHO1.0. **Bottom: NETC, whole-lithosphere corrected.** The NETC δg (Fig. 2.10 bottom) corrected for the cumulative effect of the whole lithosphere: sediments, consolidated crust, lithospheric mantle.

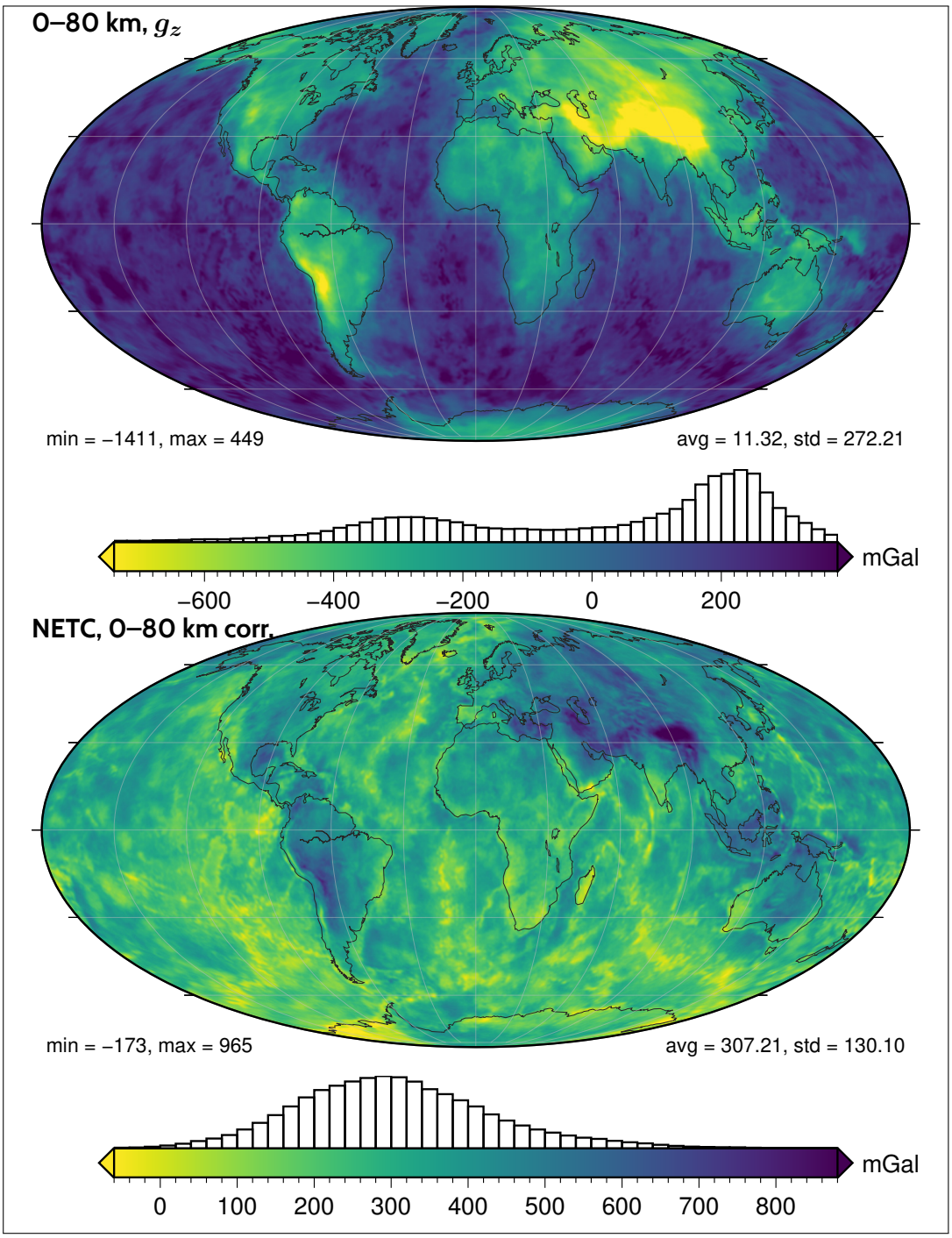

Figure 2.15.: Top: first 80 km, g_z. Vertical component of the forward-modelled effect of the first 80 km of depth. This includes sediments, consolidated crust, lithospheric mantle, and a reference-density (3300 kg m^{-3} asthenosphere. **Bottom: NETC, first 80 km corrected.** The NETC δg (Fig. 2.10 bottom) corrected for the cumulative effect of the first 80 km of depth.

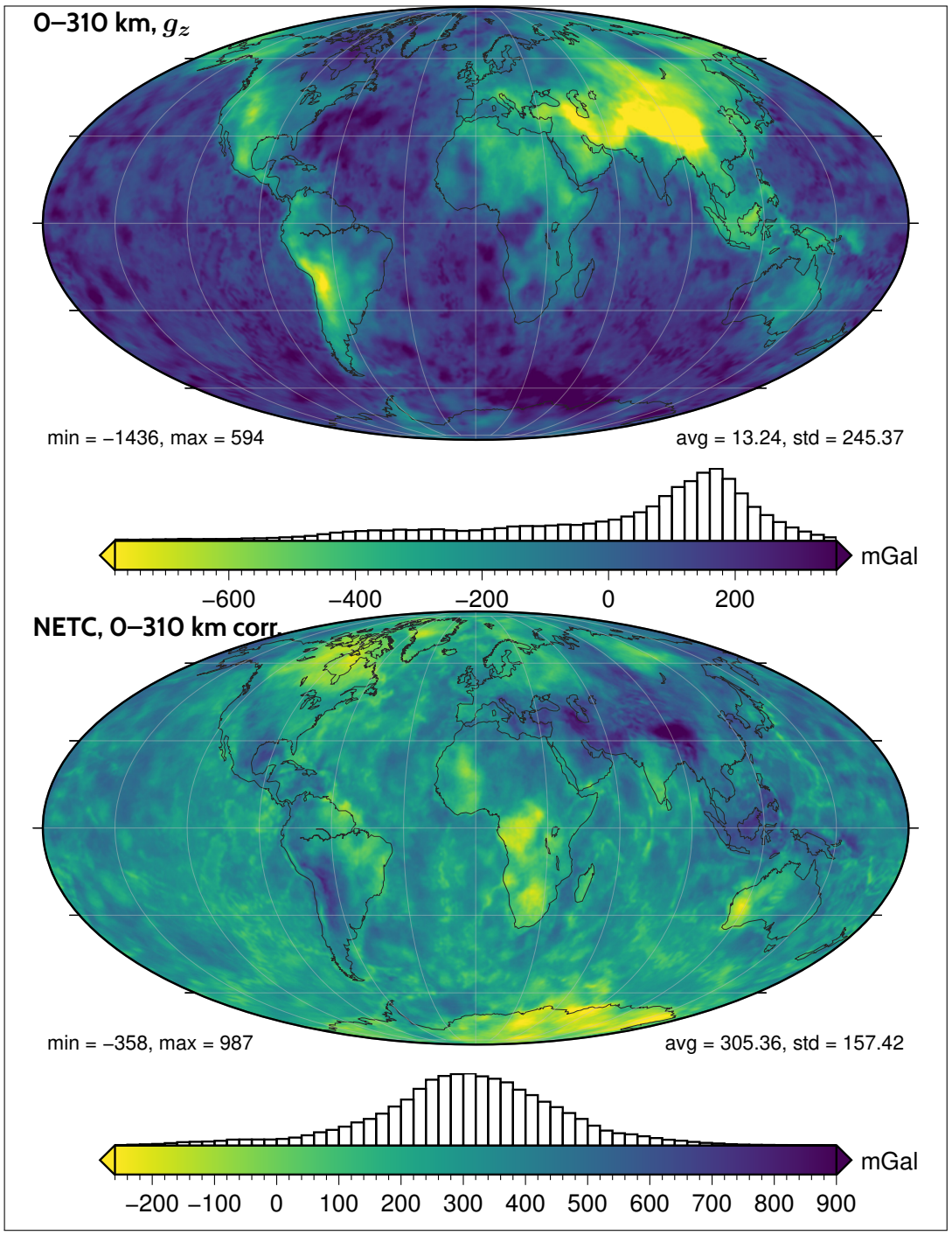

Figure 2.16.: Top: first 310 km, g_z. Vertical component of the forward-modelled effect of the first 310 km of depth. This includes sediments, consolidated crust, lithospheric mantle, and a reference-density (3300 kg m^{-3} asthenosphere. **Bottom: NETC, first 310 km corrected.** The NETC δg (Fig. 2.10 bottom) corrected for the cumulative effect of the first 310 km of depth.

Albeit a thorough geophysical interpretation would require an inversion of the refined disturbances obtained here, their meaning in a solid-earth modelling framework can be qualitatively described.

2.5.1.1. Sediments correction

The sediment-corrected NETC disturbance (Fig. 2.11, bottom) shifts the uncorrected NETC (i.e. the disturbance corrected for a constant density topography: Fig. 2.10, bottom) towards positive values – in other words, it corrects for the mass deficit introduced by the fill-in of basins. Note that the sediment density prescribed by the three SED layers in LITHO1.0 is always lower that the reference densities. Apart for areas of very thick sediment cover, the domain of sediments is in the first reference shell, for the most part (up to 10 km depth, 2.67 g cm^{-3} reference). The sediment-corrected NETC retains the bimodal distribution which already characterises the NETC, likely arising from the ocean-continent dichotomy of the terrain correction (Fig. 2.3) – this can be also seen by comparing the histogram of Fig. 2.17 (input GGM disturbance) with the top histogram of Fig. 2.19 (simple NETC).

When this kind of correction is applied in the context of inverse modelling of the crustal thickness (e.g. Tenzer and Chen, 2014, Eshagh et al., 2017, and the application example here, in chapter 3), it prevents mapping the intra-crustal mass deficit to an excessively deep Moho – i.e. by explaining a negative residual gravity disturbance with the negative mass anomaly that a deepened crustal keel provides.

2.5.1.2. Crust correction

The whole-crust correction (Fig. 2.12, top) shows a different pattern. The signal of the correction is consistently negative over continental crust. It is spread out on a distribution which reaches −1478 mGal on the Himalayan range. As expected, the extreme values are observed under the areas with the deepest Moho: e.g. the aforementioned Himalaya, the Andes, the Zagros belt. More localised thickening (e.g. Alps and Dinarides) does not reach similar values, it however results in local minima. Note that the average thickness of the whole crust in the input model is equal to 22.1 km (Tab. 2.4). Since the reference density model (Fig. 2.8) is based on the average densities of the input model, a rule-of-thumb for interpreting this result is that any crustal mass under that average depth results in a negative crustal correction. This simple interpretation disregards lateral variations in density, which are the reason for the negative crustal signal even in some oceanic areas, where LITHO1.0 prescribes less than average densities.

Compared to the average density (shell-wise), localised crustal thickening is an outlier respect to the average of the deeper reference shells (e.g. below 50 km) – therefore, relatively few nodes with crustal density at high depths cannot shift the average density of deep shells by much. The consequence is that deep crustal keels result in large density contrast, thus large forward modelled gravity corrections. To preserve clarity in the colour-scale representation of less extreme values (i.e. those in the −400 to +79 mGal range), the range in the top map of Fig. 2.12 is clipped at −700 mGal. The full range is plotted in Fig. 2.13, with a different colour map.

A bi-modal distribution, superposition of an ocean and a continent member, can be identified - the continent distribution showing a much wider dispersion (histogram in Fig. 2.18). The gravity effect (g_z) in all grid-nodes over continents is consistently negative, with an average of −406.9 mGal and a standard deviation of 179.2 mGal. Over oceans, part of the signal distribution lies over positive values – the average there is −92.19 mGal and values are less spread out (σ = 87.5 mGal). Mixing between the modelled signal oceanic and continental masses is unavoidable, due to the effect of distant masses and upward continuation. In addition, we must keep in mind that modelling only the effect of the crust neglects the other masses in the same reference shells: the lithospheric mantle and the asthenosphere, of higher density. This mis-compensation results in a significant bias towards negative values, which results in a negative global average – therefore even areas with little to no contribution to the crustal correction are negative-shifted, such as the thin, relatively dense, oceanic crust. This is the rationale for the "up to a maximum depth" shell-wise corrections (Fig. 2.15 and 2.16), discussed in the following section 2.5.1.4.

The *whole-crust corrected NETC* – the NETC disturbance refined for the sedimentary and crustal masses – is shown in the bottom map of Fig. 2.12. The local minima of the NETC in areas of high topography are over-compensated by the crustal correction (we may say 'over-corrected'), resulting in the largest values in the distribution (above about +700 mGal). Quality assessment of LITHO1.0 data is beyond the objectives of these tests, as is inversion of the input gravity models to improve the data quality – which has been shown to provide promising results (see e.g. Sjöberg and Bagherbandi, 2011). Anyway, this over-correction results in a residual-NETC that deviates from what could be expected from isostatic equilibrium. Such a positive residual may arise due to two different sources: the densities and/or thickness provided in LITHO1.0 may be erroneous, or the observed gravity signal and the estimated depth of boundaries (such as the Moho) may be influenced by non-isostatic effects (as defined by Bagherbandi and Sjöberg, 2012). Isostatic compensation may be also reached at depths higher than the crust-mantle boundary (Martinec, 1994). Without excessive speculation, the actual situation can be expected to be a

superposition of the two 'culprits': part a 'known-mass-model error', part non-isostatic effects. It follows that the better the known-mass-model, the better the assessment of compensation mechanism, and vice versa.

2.5.1.3. Lithospheric mantle correction

The forward-modelled correction for the lithospheric mantle (LID) is shown in Fig. 2.14, top. The whole range of resulting values is positive, ranging from 113 to 762 mGal, with a global average of 329 mGal. This implies that the density of the lithospheric mantle is consistently higher than the average density of the reference slices, at least when evaluated cumulatively. The oceans-continents partitioned stacked histogram (bottom plot of Fig. 2.18) highlights the two superimposed distributions: oceans (average 344 mGal) and continents (average 288 mGal). The latter presents a tail towards positive values, which skews the average, and a mode at around 180 mGal. A strong degree of mixing between the contribution of continental and oceanic masses can be expected, due to the large footprint of the attraction of deep masses, upward-continued at 10 km of ellipsoidal height.

However, no strong ocean-continent dichotomy can be identified, neither in the spatial distribution or in the histograms: the lithospheric thickness is mostly unrelated to the surface topography, the dominant pattern being instead defined by deep cratonic keels, areas of younger continental lithosphere, and oceans. The contribution of the oceanic lithospheric mantle to this correction is small, due to its small relative thickness.

The whole-lithosphere corrected NETC is shown in the bottom map of Fig. 2.14. The lithospheric mantle correction shifted the average from 537 mGal (crust-corrected disturbance) to 209 mGal, thus at least partially compensating the large positive residuals of the former. However, areas of high topography and thick crustal roots are not accompanied by lithospheric thickening, which instead occurs over cratons. Therefore, the higher mountain ranges still account for all the localised values on the high end of the range (more than 600 mGal) – their aforementioned 'crustal over-correction' is only partially compensated by the opposed-sign LID correction.

Cratons all lie towards the negative end of the residual disturbance. Cold cratonic keels, denser than average (see the V_S-converted density map in Fig. 2.7), should result in a positive gravity signal that removes the cratonic 'signature' in the lithosphere-free NETC disturbance – assuming there is no influence on the sub-lithospheric densities. This could also be an 'over-correction', in this case biased towards too high densities assigned to the lithospheric mantle underneath cratons. The mineralogical differences of cratonic lithosphere result in a 'compositional signature' (see e.g. Simmons et al., 2010), which implies

sensible petrophysical differences, including the velocity to density relationship and the Poisson's ratio (Guerri et al., 2015). Therefore, this over-corrected result suggests that different parameters in the conversion setup (section 2.3.3), resulting in lower densities, may be required to correctly reduce the gravity signal of cratons.

2.5.1.4. Shell-wise corrections

The forward-modelled corrections and the subsequent reductions to the disturbance described until now aim at removing the effect of a known-mass distribution up to a layer boundary: the basement separating sediments and consolidated crust, the Moho separating crust and mantle, the lithosphere-asthenosphere boundary.

Supposing a perfect known-mass model was employed, each resulting corrected gravity disturbance would contain only the attraction of masses below the chosen layer boundary: the corrected volumes above it would be effectively 'filled' by a density equal to the one in the *normal Earth* we are reducing our data to. Since reference densities are defined using global shell-wise averages, a consequence of this approach is that the forward modelled corrections are biased towards the modelled masses (e.g. the lower density crust), therefore the corrected gravity disturbance is biased towards the unmodelled masses (e.g. the higher density asthenosphere under oceans, at depths occupied by crust elsewhere).

By forward-modelling masses up to a maximum depth, instead of an undulating layer boundary, zero-average corrections are obtained (provided that reference densities are equal to the global average density in the reference shells). This is achieved by summing the separate gravity contribution of layers in slices up to a chosen deepest shell. This is easily implemented, since the innermost iteration of forward modelling already occurs, for each layer, in separated layer 'slices' (as described in section 2.3.4). A 'reference asthenosphere' (3300 kg m^{-3}) fills in the non-modelled volume (i.e. not provided in LITHO1.0) between the bottom of the lithosphere and the chosen maximum depth. As previously described, it was also accounted for when calculating the average densities in the reference shells.

Two shell-wise correction and corrected NETC are provided: a 'shallow' one down to 80 km, in Fig. 2.15, and a 'deep' one down to 310 km, in Fig. 2.16. The former contains all crustal masses, and part of the lithospheric mantle and reference asthenosphere. The latter also covers all the lithospheric mantle.

Both the forward-modelled corrections present consistently positive values over oceans, which were absent in previous figures. The global average of the forward-modelled correction is offset from zero (+11.32 mGal for the first

80 km and +13.24 mGal, for the first 310 km). The largest off-average contribution comes from the first slice (topography to 10 km depth), which accounts for +10 mGal – this is due to the difference between the actual LITHO1.0 average density in that slice (2681 kg m^{-3}) and the imposed reference density ((2670 kg m^{-3}), as described in section 2.3.4. Zero-offsets up to ±1.5 mGal are observed in the other shells.

The global averages of both the first-80 km and first-310 km corrected NETC is positive, at 307 and 305 mGal, respectively. Due to the small deviation from zero-average of the applied corrections (a direct consequence of the reference density model), the average of these shell-corrected NETC is almost the same average as the 'simple' NETC (Fig. 2.10 bottom: average of 319 mGal). However, the distribution of values in these reduced disturbances changed, as the histograms in Fig. 2.19 show: the bin count density function is transformed from the ocean-continent bimodal shape of the 'simple NETC' (top panel, oceanic average: 419 mGal, continental average: 58.7 mGal) to the single-mode distributions of the first-80 km and first-310 km corrected NETCs (middle and bottom panel). The difference between correcting down to 80 km and 310 km lies in the contribution of the thickest lithospheric masses: cratonic keels, which are still missing in the first 80 km. It is only after including the forward-modelled shells down to 310 km that the continental distribution become symmetrical, covering the most negative disturbance values of the observed range.

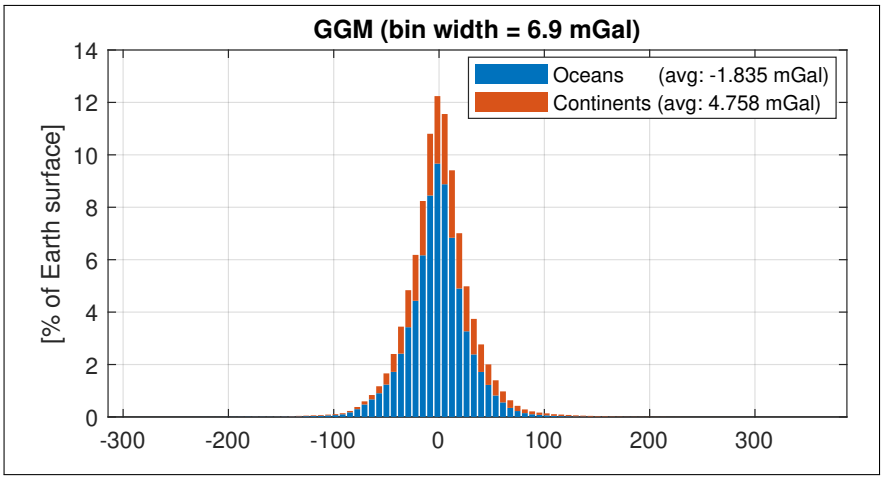

Figure 2.17.: Histograms of gravity disturbance of the input global gravity model: the combined, satellite-only, GOCO06s model (Kvas et al., 2019a). Nodes over oceans (blue) and continents (orange) are counted separately. Their bars are plotted stacked.

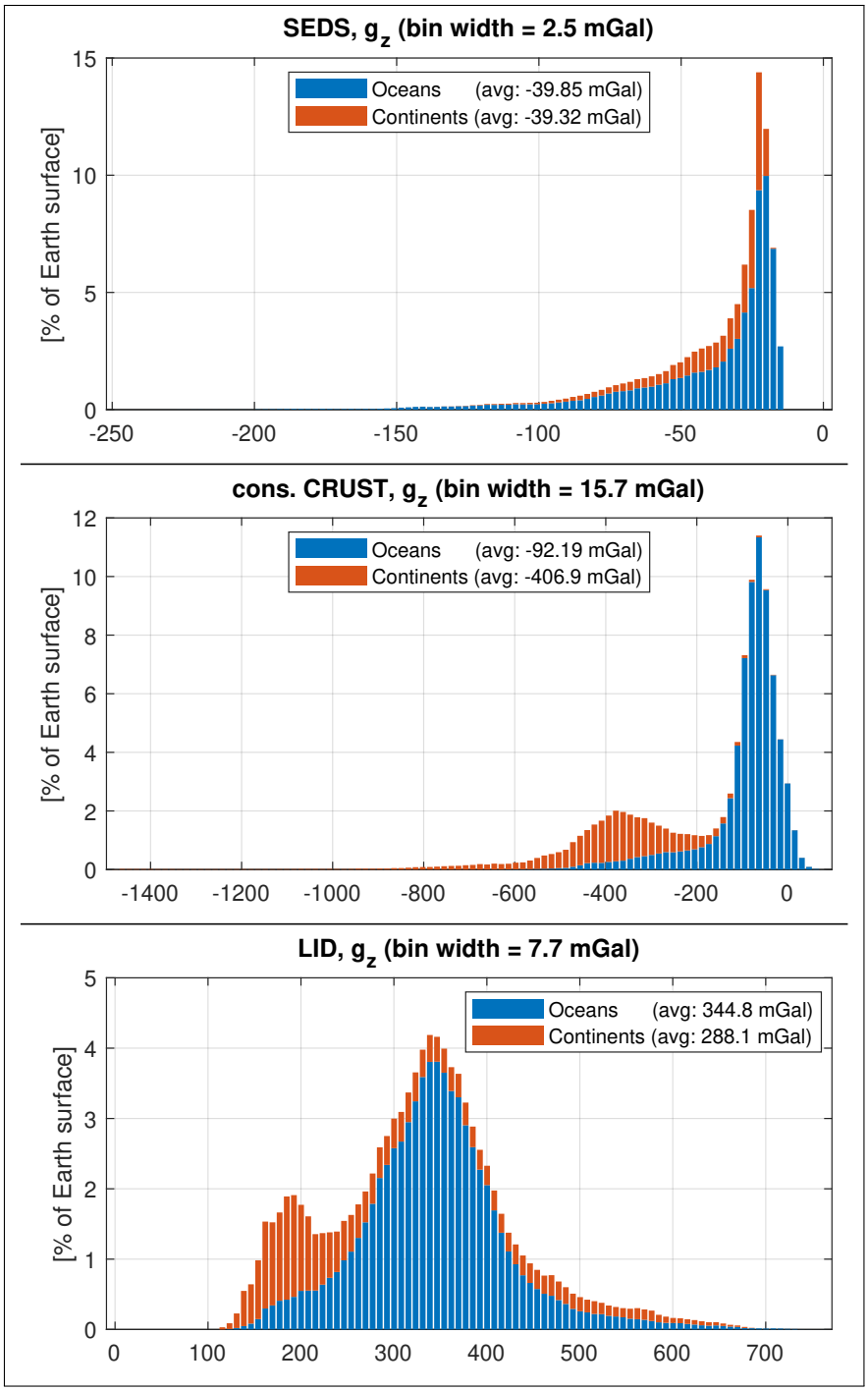

Figure 2.18.: Histograms of the forward modelled effect of sediments ('SEDS', Fig. 2.11, top), consolidated crust ('cons. CRUST', Fig. 2.12, top), and lithospheric mantle ('LID', Fig. 2.14, top). Nodes over oceans (blue) and continents (orange) are counted separately. Their bars are plotted stacked.

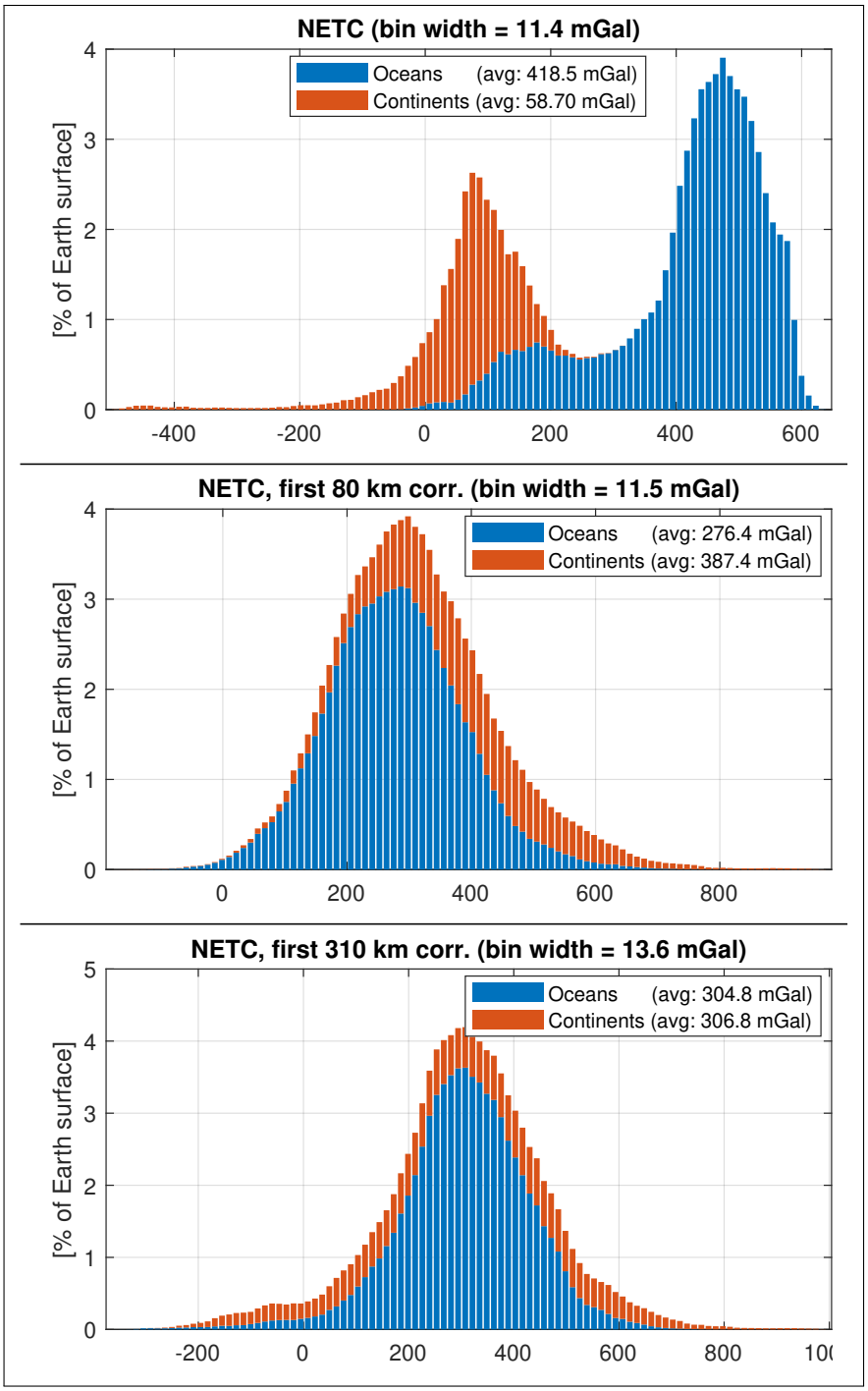

Figure 2.19.: Histograms of the NETC disturbances, from the top plot: after the simple terrain correction (Fig. 2.10 bottom), after correcting for the first 80 km (Fig. 2.15 bottom), after correcting for the first 310 km (Fig. 2.16 bottom). Nodes over oceans (blue) and continents (orange) are counted separately. Their bars are plotted stacked.

2.5.2. Spectral domain comparison

In addition to the synthesized grid of the modelled corrections and reduced disturbances, I resort to the spectra of degree variances (section 2.2.4, Eq. 2.17) and degree cross-correlation (Eq. 2.18) to compare the energy level of the corrections in different spectral bands. Degree variances and cross correlation were computed up to l_{max} 280.

Fig. 2.20 shows the degree variances of the attraction of the forward-modelled corrections against the degree variances of the GGM disturbance. The power density of the former become less than the latter (the GGM) at degree l 35 for sediments, 97 for the consolidated crust, and 72 for the lithospheric mantle. The power of the modelled terrain correction is always higher than the one of the GGM disturbance and of all the modelled LITHO1.0 layers.

The degree variances of the shell-wise corrections are plotted in Fig. 2.21, where the spectra of the GGM and TC are kept for reference. The degree variance of both these corrections becomes less than the one of the GGM at SH degree 138, a different pattern respect to the isolated layer-wise effect.

All the corrections, except sediments, exceed the power of the GGM disturbance at the lowest degrees. Sometimes truncation of global models at low degrees is employed as a low-pass filter to pursue isolation of sub-lithospheric or sub-crustal signals (Deschamps et al., 2001, e.g. Simmons et al., 2010). Such a significant contribution of crustal and lithospheric corrections warrants caution in doing so, as pointed out by Kaban et al., 2004. The magnitude of uncertainties involved (discussed in section 2.5.3) and the effects of mass under- and over-correction, as described when discussing the reduced disturbances (section 2.5.1) further corroborate this interpretation.

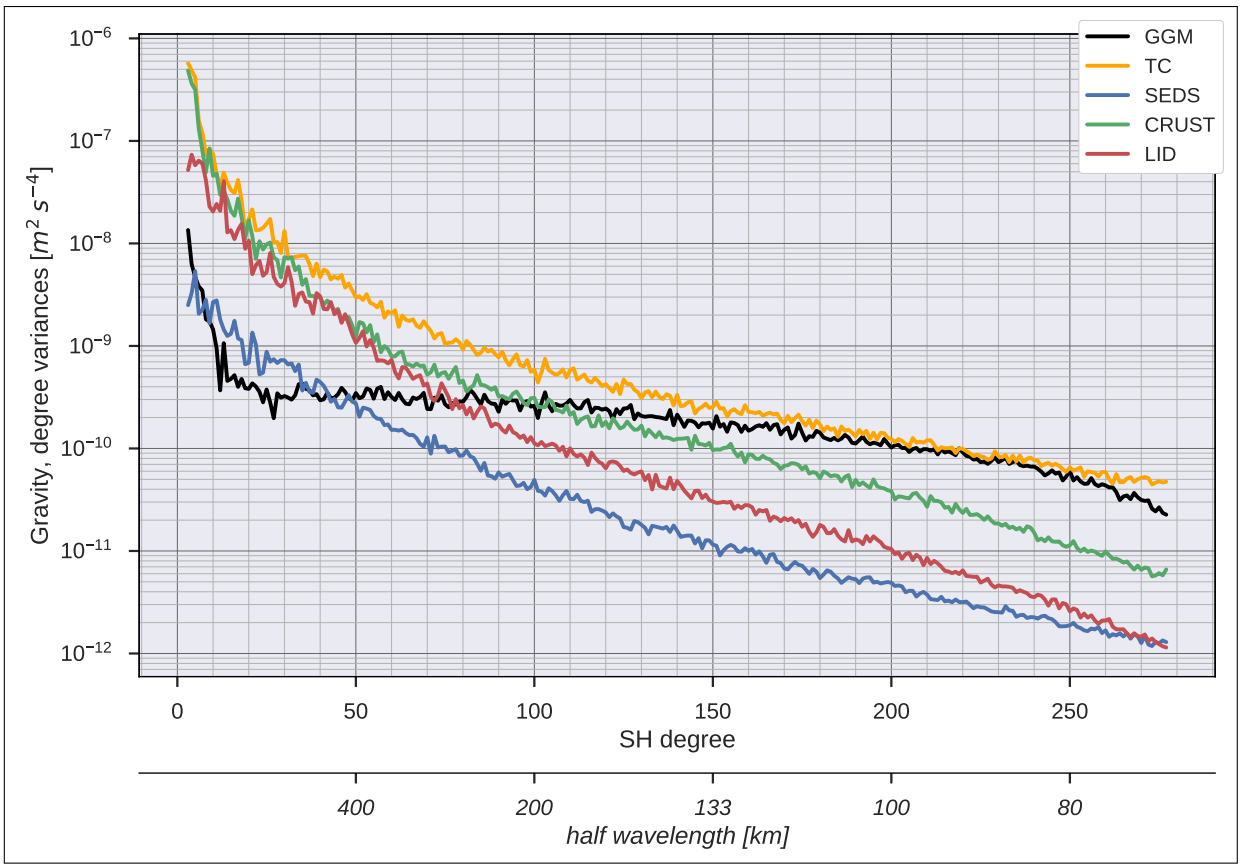

Figure 2.20.: Degree variance spectra of the spherical harmonics coefficients (for gravity) of: **GGM:** δg of the global gravity model GOCO06s, **TC:** NETC terrain correction, including ice and water stripping, **SEDS:** sediment layers effect, **CRUST:** consolidated crust layers effect, **LID:** lithospheric mantle effect. The half wavelength scale is provided for the Earth surface, along the equator.

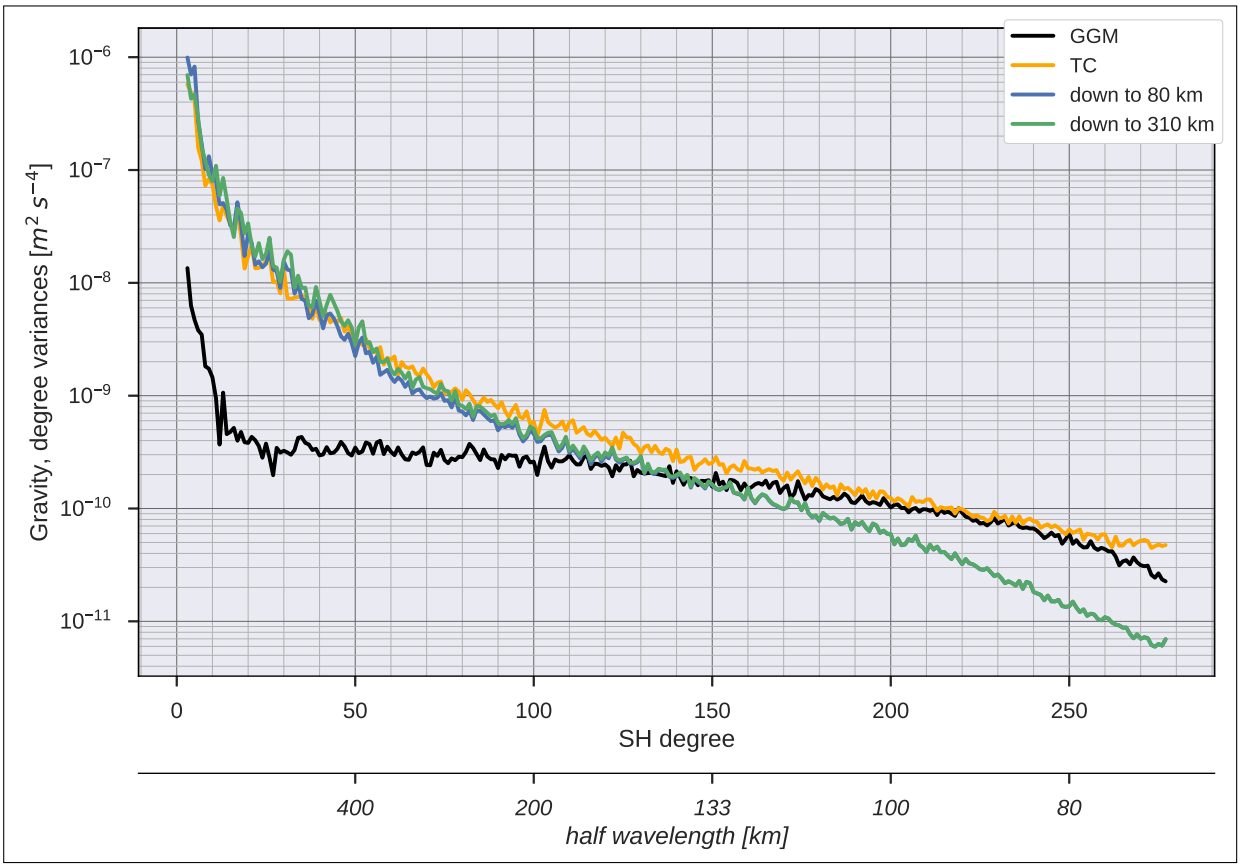

Figure 2.21.: Degree variance spectra of the spherical harmonics coefficients (for gravity) of the two shell-wise reductions (shown in Fig. 2.15 and 2.16, top). **GGM:** δg of the global gravity model GOCO06s, **TC:** NETC terrain correction, including ice and water stripping.

Degree cross-correlation (CC), as expressed in Eq. 2.18, are commonly employed for spectral cross-validation between gravity models (e.g. Rexer et al., 2016) or between a gravity model and topography (Wieczorek, 2007; Hirt et al., 2012). Here, in Fig. 2.22, the input GGM disturbance is cross-correlated with the forward-modelled corrections: the terrain correction (top panel); the effect of sediments, the whole crust (sediments and consolidated crust), and the whole lithosphere (whole crust and lithospheric mantle).

By doing so I aimed at getting a metric on how much the input signal is 'explained', thus reduced by, each correction. The top panel of Fig. 2.22 shows the degree-cross correlation between the terrain correction and the input disturbance. An almost constant CC, at +0.75, is observed from SH degree 20 onwards: this reproduces a common finding in topographic evaluation (Hirt et al., 2012; Hirt et al., 2010) of gravity models on Earth. Topography is generally considered as the dominant source of gravity signal at short scale (Forsberg and C. C. Tscherning, 1981).

There is a loss in spectral power towards the higher degrees, which becomes noticeable from about l =230 onwards. This decline is a direct consequence of the lower signal-to-noise ratio that satellite-only GGM solutions can provide at these short wavelengths. In the case of the model adopted here (GOCO06s Kvas et al., 2019a), the system of normal equations used to combine the input data (GOCE, GRACE, LEO orbits, and SLR) impose a Kaula regularization (Pail et al., 2010) from degree and order 150 onwards – a compromise between energy content in less accurately estimated high degrees and otherwise increasing GGM errors. Loss of signal at high degrees is therefore not unexpected, and should be accounted for when applying reductions and formulating inverse problems on the reduced gravity quantities. Failing to do so would map the omitted short wavelength gravity signal to the anomalous mass distribution sought for, resulting in artefact arising from the difference in formal resolution between input model and reductions.

Loss of terrain-gravity correlation occurs also at low degrees (less than 10), where they are usually attributed to deep density inhomogeneities (Kaban et al., 2004) not associated with an expression in surface topography.

Correlations between the input GGM and the forward-modelled masses from LITHO1.0 (middle and bottom panel of Fig. 2.22) are much smaller and decay to non-correlation at lower degrees. Both the whole-crust and whole-lithosphere corrections do not result in CCs higher than 0.2 above SH degree 60 (equal to an half wavelength of about 330 km, 3 arc–degrees). The sediments correction alone still correlates (more than the 0.2 threshold adopted here) up to SH degree 110 (equal to an half wavelength of about 180 km, 1.6 arc–degrees). The chosen threshold, albeit arbitrary, discriminates a spectral band with consistently non-zero GGM-correction correlation from the uncorrelated higher degrees. The

effective bandwidth so obtained are less than the 1 arc–degree discretisation LITHO1.0 is provided in.

The sign of CCs above degree 10 is consistently positive for the whole-crust and whole-lithosphere corrections, from SH degree 3 to the upper bound of their effective bandwidth. Such a correlation does not necessarily imply compensation of topography by the modelled masses – it is observed despite the over-correction behaviour observed for the forward-modelled crust masses (section 2.5.1.2). Correlation coefficients are negative for most of the degrees of the sediment correction, a pattern which can be speculated as resulting from correlation between basins and low topography.

The pattern of the shell-wise corrections CCs (bottom panel of Fig. 2.22) is coherent with the whole-lithosphere cross-correlation, with the same effective bandwidth (there is effectively no short-wavelength energy added by the asthenosphere fill-in). Relatively strong correlation, of alternating sign, is observed in the 1–10 SH degree range, where TC-GGM correlation is low. This may indicate that part of the low-degree field is, at least in part, due to the longest wavelengths of lithospheric structures, superimposed to the contribution of lower masses.

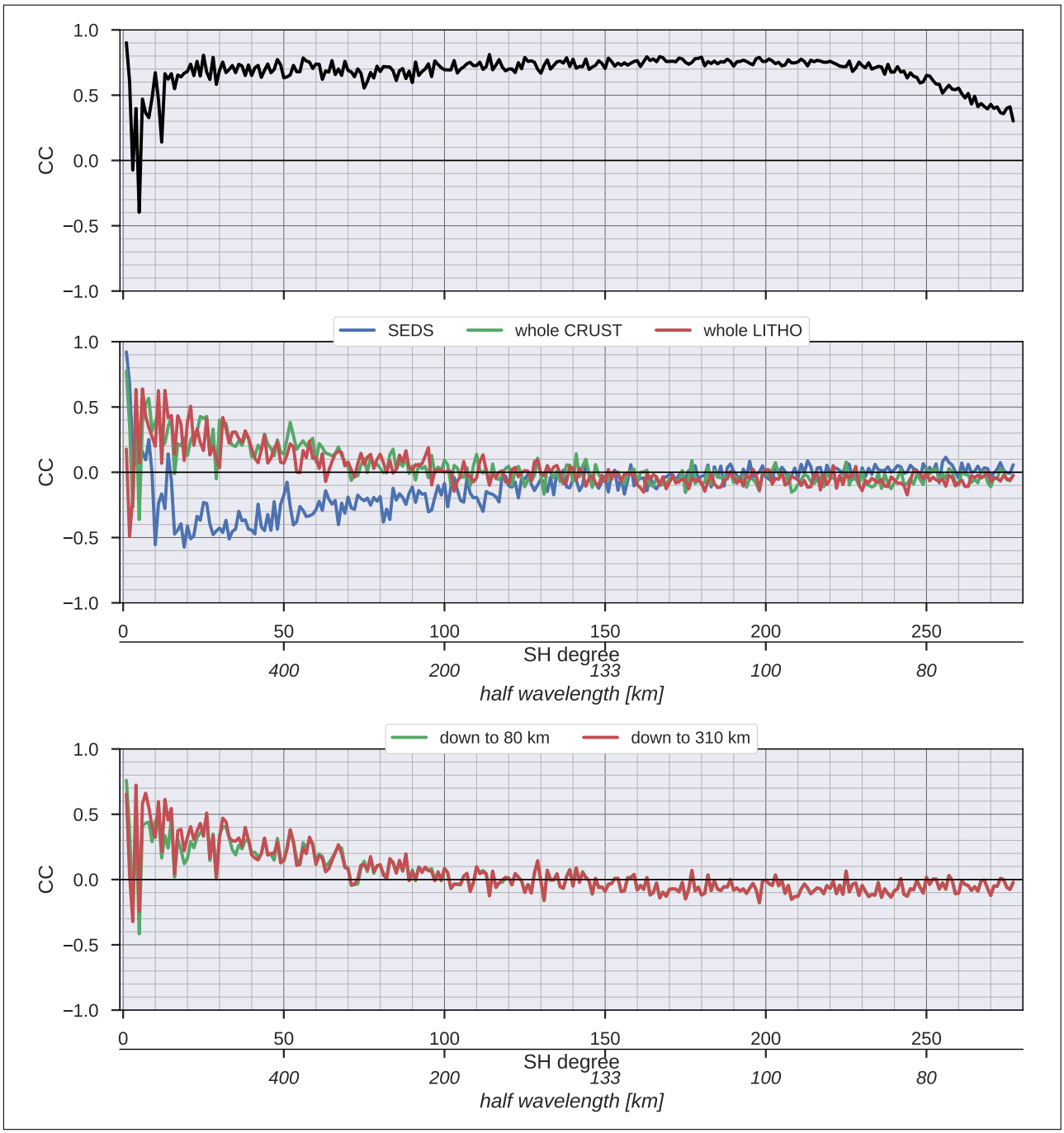

Figure 2.22.: Degree correlation coefficients (**CC**, S_{fg} of Eq. 2.18) between the δg of the global gravity model GOCO06s and the forward-modelled corrections. Top panel: terrain correction. Middle panel: **SEDS:** sedimentary layers, **whole CRUST:** consolidated crust and sedimentary layers, **whole LITHO:** whole crust and lithospheric mantle. Bottom panel: shell-wise correction, up to 80 and 310 km, including fill-in asthenosphere.

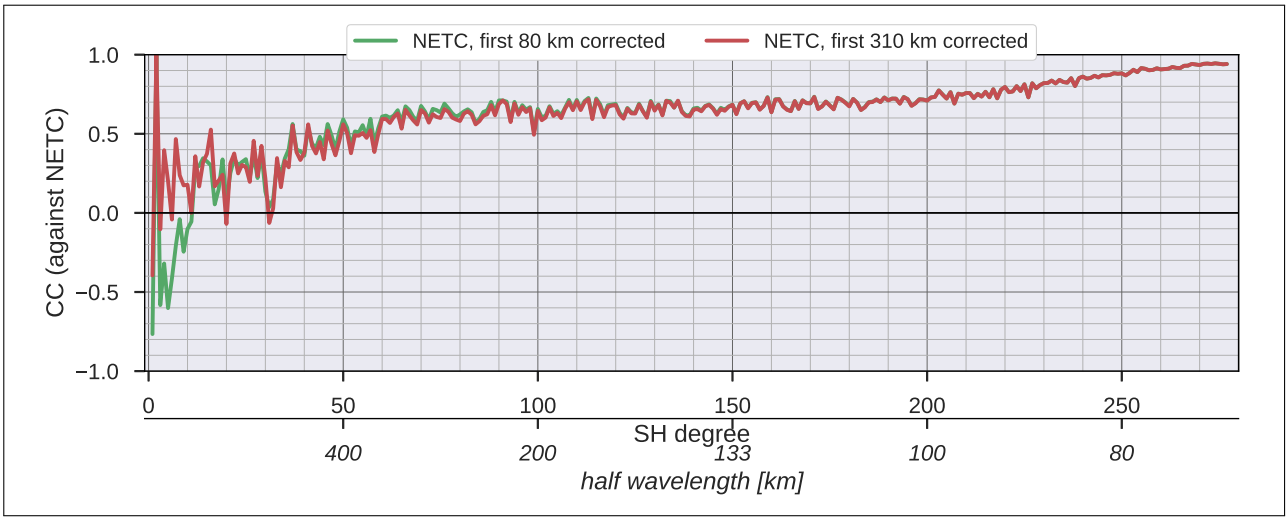

Figure 2.23.: Degree correlation coefficients (**CC**, S_{fg} of Eq. 2.18) between the terrain-correction only NETC disturbance and shell-wise corrected no-topography disturbances.

A different type of degree correlation coefficients is plotted in Fig. 2.23: the NETC disturbance corrected for the first 80 km shell (Fig. 2.15, bottom) and the NETC disturbance corrected for the first 310 km shell (Fig. 2.16, bottom) are cross-correlated with the non-corrected NETC (Fig. 2.10, bottom).

We can interpret the NETC before any further correction (i.e. only TC applied, Fig. 2.10) as the attraction of masses compensating the topography, plus a superposition of non-isostatic signals (deep masses, mantle flow) – this is the well known (Vening Meinesz, 1931) isostasy hypothesis, albeit formulated for refined gravity disturbances, instead of gravity anomalies. Therefore, perfect compensation by the forward-modelled masses would imply that a refined no-topography disturbance (e.g. for the crust, or for the first 80 km) should correlate less with the original disturbance – part of its signal being compensated by a correction of opposing sign.

On the contrary, high correlation values are the consequence of non-complete compensation of the topography-stripped signal, due to omission of the compensating bodies in the input 'known mass' model (e.g. a wrong Moho depth) and under-/over-correction due to erroneous density estimates, as it has been discussed when describing the output maps (section 2.5.1). Non-correction can be also attributed to compensation at deeper depths or superposition of non-isostatic effects.

It must be noted that the global bias in average gravity that a 'wrong' reference density model introduces is confined to the zero-degree term which is not part of the correlations computed here.

Correlation coefficients are steady at around +0.7 between degree 70 and 200,

a spectral band with no meaningful signal contained in the input models (as previously mentioned). Above degree 200 the coefficients increase, reaching almost complete correlation at the high end of the spectrum – as discussed before, here the input GGM signal is attenuated, most of the power spectral density being due to the applied terrain correction.

The lowest CC values are observed in the degrees below 30. The first 80 km corrected disturbance shows negative CC in that range, supposedly the consequence of the observed over-correction of high topography, already evident in the crust-corrected maps. The different pattern of the first 310 km corrected disturbance can be attributed to the long-wavelength contribution of thick cratons, which lack a well-identifiable signature in the simple NETC.

2.5.3. Propagated uncertainty

The results of the reduction uncertainty propagation scheme, as described in section 2.4, are presented in terms of standard deviation (σ) of the ensemble forward-modelling results for each grid node. Three global maps of correction-standard-deviation are plotted in Fig. 2.24, from the top: sediments (SEDS1, SEDS2, SEDS3), consolidated crust (CRUST1, CRUST2, CRUST3), and lithospheric mantle (LID).

A direct consequence of the simple uniform uncertainty model is the direct proportionality between uncertainty and the thickness of the modelled layers. Dependence of depth-uncertainty with the depth of layer boundaries and the 100 kg m^{-3} standard deviation of density uncertainty, add up. The consequence is that the deeper and thicker a layer, the larger its contribution to uncertainty in a given location.

The scatter plots of Fig. 2.25 present this proportionality pattern, which however deviates from simple linearity. The patterns are complicated by the concurrent contributions of : (1) different composing layers (in the case of sediments and crust, 3 layers each), (2) lateral variations in density in each layer, (3) different contrast respect to the reference density in each shell of the reference model, (4) large footprint of deep and far-field masses, especially in areas of sharp lateral contrasts (e.g. ocean margins). The LID layer, which is characterised localised bodies with high contrast (cratonic keels at large depths and patches of shallow dense lithospheric mantle in oceans), deviates from linear proportionality more significantly than the sediments and crust.

To avoid over-representation of nodes at high latitudes, the markers in the scatter plots of Fig. 2.25 were obtained by re-sampling the layer thickness and uncertainty maps on the regularly-spaced global grid (2 arc–degree spacing) by J. H. Davies (2013).

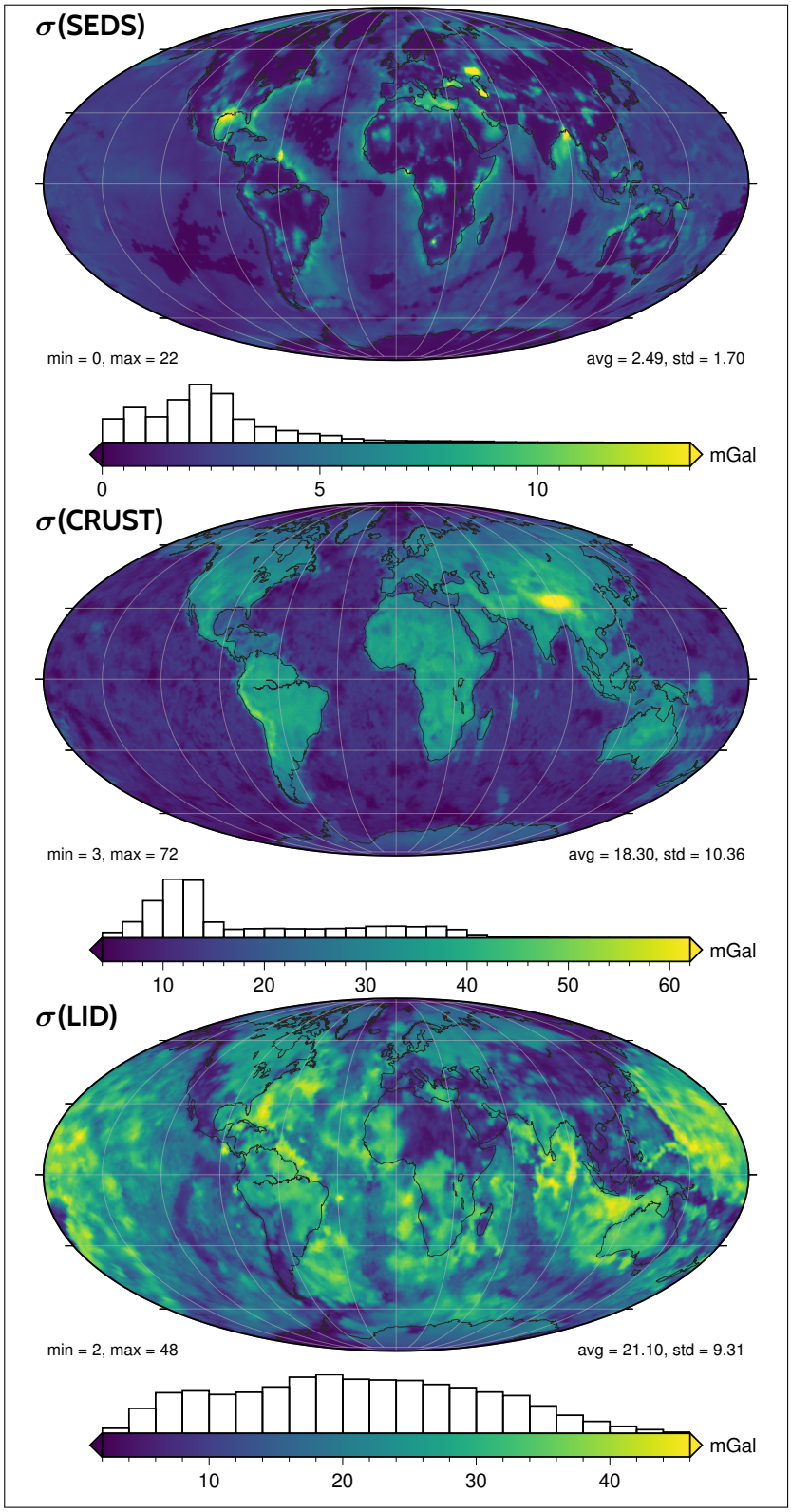

Figure 2.24.: Propagated uncertainties of sediments (SEDS), consolidated crust (CRUST), and lithospheric mantle (LID), expressed with the standard deviation (σ) in each grid-point in the ensemble of forward-modelled models in the Monte Carlo uncertainty propagation scheme.

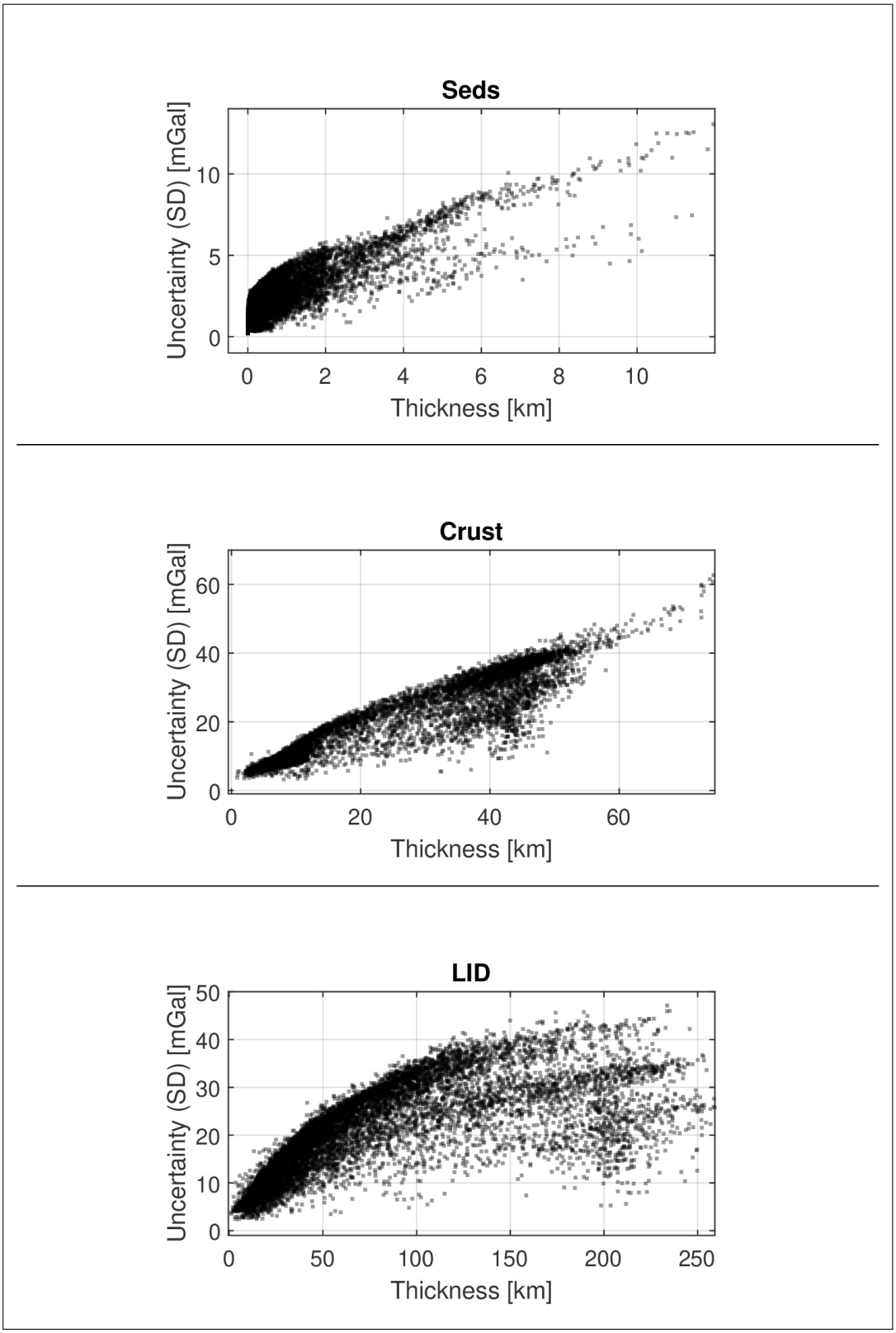

Figure 2.25.: Layer thickness versus propagated uncertainty (SD, one standard deviation) scatter plots.

The spatial distribution of uncertainty values and their surface-weighted probability density function – as plotted in the histograms beneath the maps (Fig. 2.24) and in Fig. 2.26 – bears a qualitative similarity with the histograms of the forward-modelled corrections, especially for the partition pattern of oceans and continents.

The average standard deviation for the sediment correction is 2.5 mGal (oceans: 2.7 mGal, continents: 1.9 mGal), with tails reaching values over 10 mGal only directly above thick sedimentary basins. The uncertainty in crust correction is an order of magnitude larger, with a marked ocean-continent dichotomy. Due to the thickness-uncertainty relationship, discussed before, larger values are observed over thicker crust, therefore all the higher part of the range is covered by nodes on above-sea-level landmasses (global average: 18.3 mGal, oceans: 13.0 mGal, continents: 32.1 mGal). Unsurprisingly, the crustal correction uncertainty reaches its largest values in the same regions where the crustal correction itself has its extremes: chiefly, the Himalaian range (up to 72 mGal). The uncertainty of the lithospheric mantle correction loses most of the ocean-continent dichotomy, since the layer itself is not strongly correlated with surface topography. While the maximum value is less than the one of σ(CRUST), the average is higher (21 mGal) and there is less dispersion, due to the lithospheric mantle effect lacking any localised 'outliers'.

Taking into account a $\pm 2\sigma$ range (covering the 95 % of the values, under the normally distributed error imposed here) and crustal thickness modelling as a potential application (e.g. the case involved in chapter 3), the uncertainty introduced by the sediment correction remains relatively small if compared to other contributions. For a 'rule-of-thumb' assessment, I adopt the first-order term of the attraction of a spherical Bouguer shell ($A = 4\pi G\rho H$, Vaníček et al., 2001) as an approximated conversion between the uncertainty range and an 'equivalent Moho depth' (arranged as $\Delta H = 4\sigma(A)/(4\pi G\Delta\rho)$). Using a $+485\,\mathrm{kg\,m^{-3}}$ crust-mantle contrast (Tenzer et al., 2012b), a 10 mGal 4σ range results in a uncertainty interval of about 245 m. For comparison, Grad and Tiira (2012) reports an 85 % confidence interval of ±2 km for a 20 km thick crust, ±4 km for a 60 km thick crust (for receiver functions on the well-surveyed European Plate). Note, however, that this error estimate disregards the uncertainties introduced by the gravity inverse problem.

The crustal and lithospheric-mantle correction, on the other hand, are a significant source of error. Adopting the same Bouguer-shell conversion, the average 4σ of the crustal correction over continents (128 mGal) results in about 3150 m of equivalent-Moho uncertainty range (again, this accounts only for the contribution of reductions).

Finally, it should be reiterated how the depth- and density-error models (described section 2.4.1) rely on a set of a strong assumptions, due to their

simplicity. As already mentioned, this proposed strategy could be easily scaled to complex error models, based on data availability of sources and their associated error (e.g. due to different geophysical observables and inversion methods). Still, there are biases that could affect such a kind of estimate, regardless of the error model. Two main issues suggest caution in the interpretation of uncertainty: systematic errors arising from modelling approximations, which propagate to a systematic "error on the uncertainty", and assumptions on the covariance between uncertainty at different grid nodes: if absence of spatial covariance (the case of this experiment) is indeed excessive, over optimistic smoothing may severely underestimate errors in areas where abrupt changes in geological features are expected.

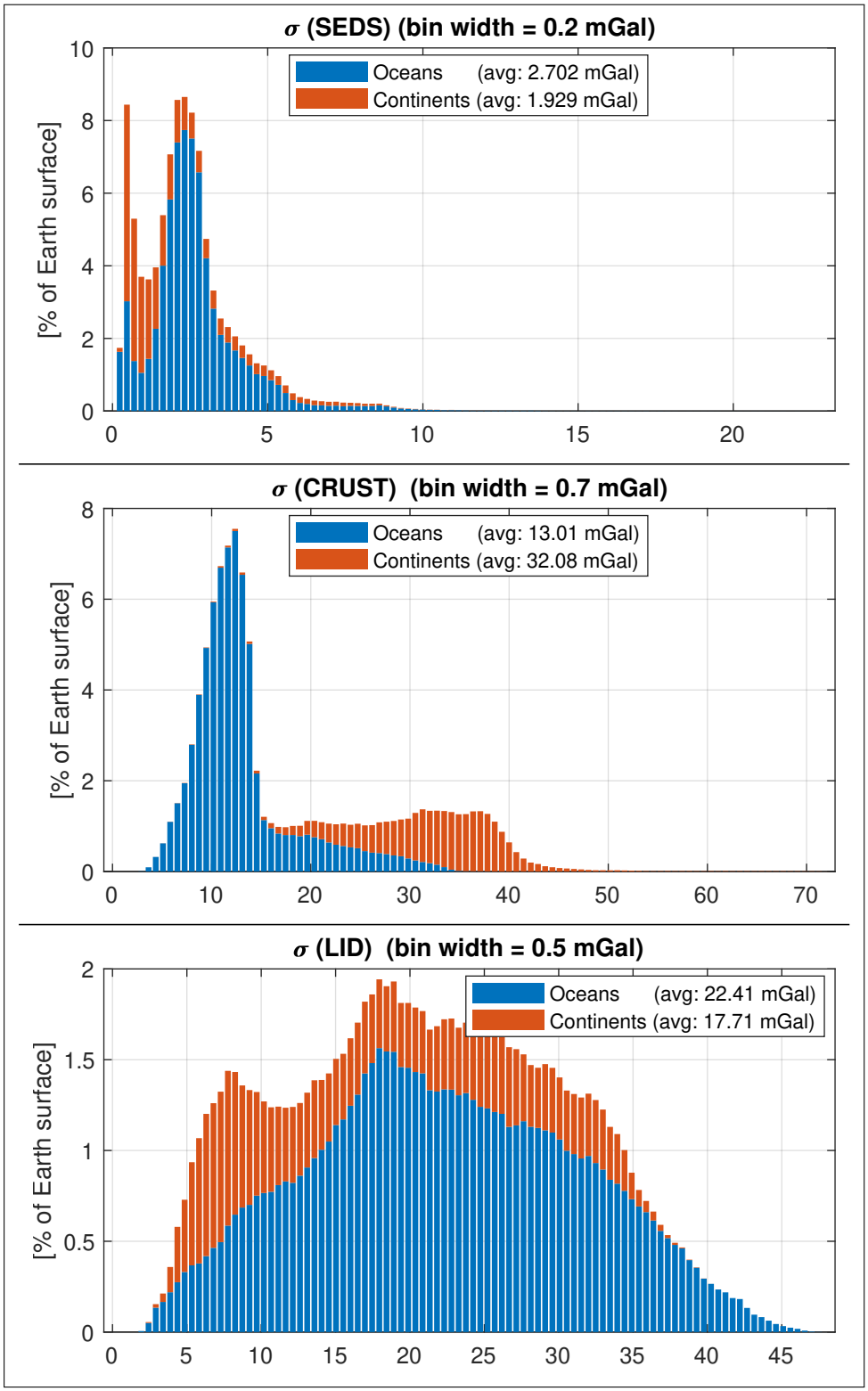

Figure 2.26.: Histograms of the propagated uncertainties (σ) of the corrections: sediments (SEDS), consolidated crust (CRUST), and lithospheric mantle (LID). The respective maps are shown in Fig. 2.24. Nodes over oceans (blue) and continents (orange) are counted separately. Their bars are plotted stacked.

2.6. Conclusions

In this chapter I have presented a method for fast forward modelling of mass distributions in the lithosphere, relying on a layer-wise modelling strategy based on Wieczorek (2007) spherical harmonics formulas. Forward modelled gravity corrections to the gravity disturbance, aimed at stripping gravity measurements, were computed for the complete terrain effect (according to the rock, water, and ice Earth2014 model by Hirt and Rexer, 2015b) and for the sediments, crust and lithospheric mantle (according to the LITHO1.0 model by Pasyanos et al., 2014).

In order to perform velocity-to-density conversion in the lithospheric mantle (where LITHO1.0 does not provide the spatial distribution density), thermodynamic modelling was performed with Perple_X (Connolly, 2005) on a simplified two-member global compositional model (Griffin et al., 2009).

Reductions were modelled as density contrasts against an ad-hoc reference density model, discretised in concentric shells respect to the GRS80 ellipsoid. The reference density in each shell was computed according to LITHO1.0 densities and a reference constant-density asthenosphere fill-in. By doing so, the biases that exist between the input density model and commonly adopted reference earth models (e.g. ak135) were not propagated to the forward modelled corrections. This involved partitioning each layer according to the 'reference-slices' and modelling the 'sliced' gravity effect separately. This procedure also provided novel grouped statistics on the average depth and densities of LITHO1.0 layers (Tab. 2.4).

The forward-modelled corrections were applied to the combined satellite-only global gravity model GOCO06s (Kvas et al., 2019a; b). They are presented as global maps of gravity effect of the modelled layers (i.e. attraction of the modelled masses) and of the incrementally corrected gravity disturbance of the global gravity model. In addition to layer-wise corrections (grouped in sediments, consolidated crust, and lithospheric mantle), two selected 'shell-wise' corrections are included. The 'shell-wise' corrections, instead of modelling masses up to the bottom boundary of the bottom-most layer, include all the modelled layers plus the fill-in asthenosphere up to a constant ellipsoidal depth. Biases due to the non-modelled volumes are therefore avoided. The residual gravity disturbance obtained from such corrections could be employed in inverse modelling of lithospheric and sub-lithospheric 'anomalous masses' respect to the model used for correction and the fill-in reference asthenosphere.

Maps are accompanied by histograms with constant-area weighted counts. Global averages have also been provided, separated for nodes over oceans and continents, enabling a quantitative separation of the already apparent ocean-continent dichotomy in the modelled layers. The corrections obtained highlight some of the issues regarding the 'known-masses' model LITHO1.0, particularly

regarding isostatic compensation of topographic masses. Two aspects, over-correction in areas of very thick crust and non-modelled compositional effects of cratonic keels, could be identified and are briefly discussed.

A spectral-domain assessment of the modelled quantities was also performed. Degree cross-correlation coefficients between the input gravity model and the obtained corrections were computed. Leaving isostatic analysis in the spectral domain aside – it would call for a more rigorous analysis (e.g. McKenzie and Fairhead, 1997; Kaban et al., 2004) – the assessment performed here provided an useful estimate on the effective bandwidth of the LITHO1.0 model, which decayed to near-zero correlation coefficients at spherical harmonics degrees less than what its 1 arc–degree nominal resolution could provide. This finding suggests that localised assessment of degree cross-correlations (e.g. with multitaper spectral estimation, such as the method by Wieczorek and Simons, 2007) could provide interesting metrics on the actual resolution of global crust/lithosphere models with undisclosed data sources.

Cross-correlation of the terrain correction with the input global gravity, an assessment that has been already performed for other GGMs and terrain models (e.g. Hirt et al., 2012), reminded of the loss of spectral power that satellite-only GGMs have at higher degrees – this calls for adequate attenuation of the forward-modelled solid-Earth reductions.

Propagation of errors in the depth of layer boundaries and layer densities was carried out with a Monte Carlo technique (Aster et al., 2013), a parallel computation scheme and a memory-lean partition strategy. It has proven successful in providing a propagated uncertainty estimate, quantified with the standard deviation of the correction values in each node of the synthesized global gravity maps. The input error model that has been adopted is based on a simple depth-dependent error in depth estimation and in a fixed standard deviation value for the normally-distributed error in density. Anyway, the method that I have devised may be easily scaled to more complex models of the spatial distribution of errors, based on quality and availability of data (such as in the regional model by Molinari and Morelli, 2011) and/or a geostatistics-based estimation of variance (e.g. Szwillus et al., 2019). Error covariance between nearby nodes is also an aspect that warrants further investigation.

This chapter is accompanied with a supplementary section (2.A), in which the adopted spectral-domain forward modelling method is compared with spatial-domain forward modelling, in a set of synthetic test cases.

2.A. Testing the method against spatial–domain forward modelling

Modelling setups such as the one employed in this chapter are commonplace, with different technical choices being dictated by application requirements. However, I decided to supplement these modelling experiments with a set of direct comparison tests aimed to assess: 1) the behaviour of the layer–wise modelling (section 2.2.2), since it is an "off-label" use of the single-relief forward modelling method by Wieczorek (2007); 2) the difference in results against a spatial domain modelling method, given the well known issues with limited bandwidth of spectral domain methods (Hirt and Kuhn, 2014).

A rigorous assessment of the convergence of the layer–wise arrangement adopted in this work is not available at the moment. Therefore, an heuristic test was devised to assess if such a strategy was fit for these experiments purpose, i.e. mGal level accuracy at comparatively low degrees (limited by satellite-only gravity models). As it is shown later, the satisfactory results of the direct comparison and the larger magnitude of the contribution of uncertainty of geophysical models were enough to support leaving any more rigorous analysis to further development.

2.A.1. Synthetic model: "four blocks test"

A synthetic mass distribution was defined, made up of four 2×2 degree "blocks", each 1 km thick. Set on a sphere with radius equal to WGS84 semi-major axis (6378.137 km), two blocks rise above it, the remaining two below it, arranged in a checker board fashion. The bodies above the sphere radius have a density of $+1\,\mathrm{g\,cm^{-3}}$, those below have a density of $-1\,\mathrm{g\,cm^{-3}}$. The resulting relief map is plotted in Fig. 2.27, zoomed in on the area covered by the blocks (centred on 47 °N, 47 °E). The grid covers the whole globe and contains no other masses. Owing to the limited bandwidth requirement of the input grids for the spectral method (section 2.2.3), the original square-wave shaped relief map was low-pass filtered with a Gaussian kernel (impulse response equal to $e^{-1/2}$ at 4°). All the three forward modelling methods tested employ a 0.0625°×0.0625° equally spaced global grid.

A section along the 48 °N parallel is plotted in Fig. 2.28, which shows the three ways in which the mass distributions have been expressed:

a) **one relief**, input for the unmodified spectral-domain method of Wieczorek (2007). The reference sphere radius D is set equal to the zero-relief sphere radius (6378.137 km). The input density is set uniform everywhere:

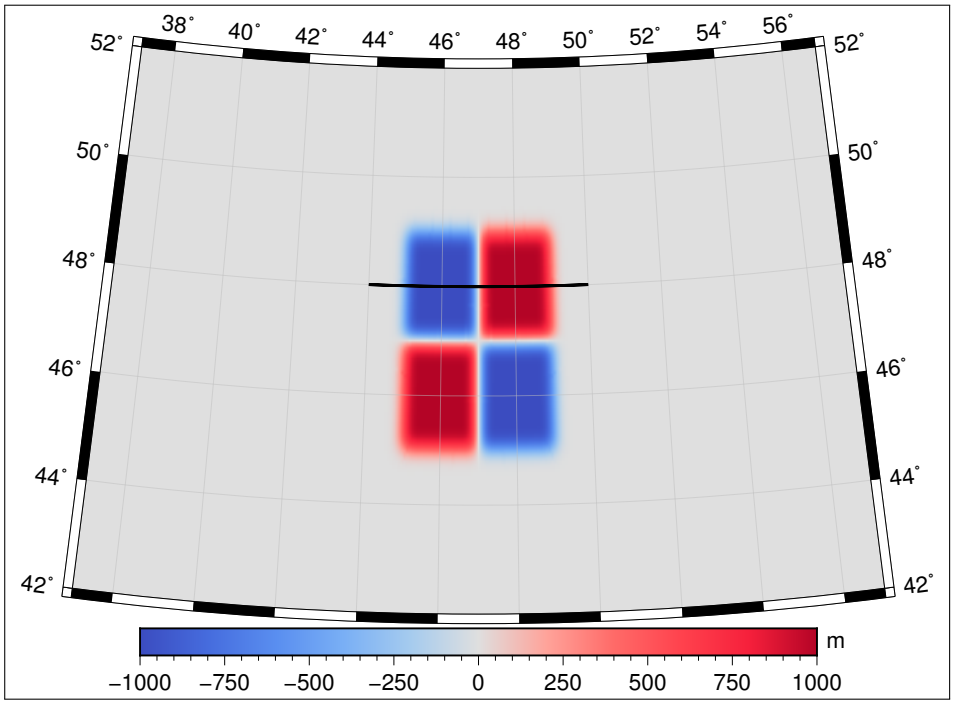

Figure 2.27.: Relief map of the synthetic mass distribution ("four blocks test") used to compare the three modelling methods. Heights (and depths) are expressed in respect to a reference sphere with radius equal to 6378.137 km (semi-major axis of WGS84). The black line along the 48 °N parallel denotes the profile shown in Fig. 2.28.

its effect is negative in areas with negative relief, due to the ρh product (Eq. 2.14).

b) **layer-wise** setup: positive- and negative-relief volumes are modelled as two separate layers. The reference sphere radius D is set equal to the highest relief. The aforementioned zero-relief sphere serves as the bottom boundary for the positive relief layer and as the top boundary for the negative relief one. Input density is positive above zero (red fill) and negative below (blue fill) – as mentioned in the strategy description, density signs are then reversed in the forward-modelling function, since height in respect to D is negative.

c) spatial-domain **tesseroids** discretisation: the relief was turned into discrete spherical tesseroids, sized with the same grid spacing as the input grid and centred on the grid nodes (*grid registration*). Forward modelling was carried out with the Tesseroids code (Uieda et al., 2016; Uieda, 2017).

Four blocks test, g_z grids Figure 2.29 shows the results and direct comparison between spectral-domain (method **a)**) and spatial-domain (method **c)**). The

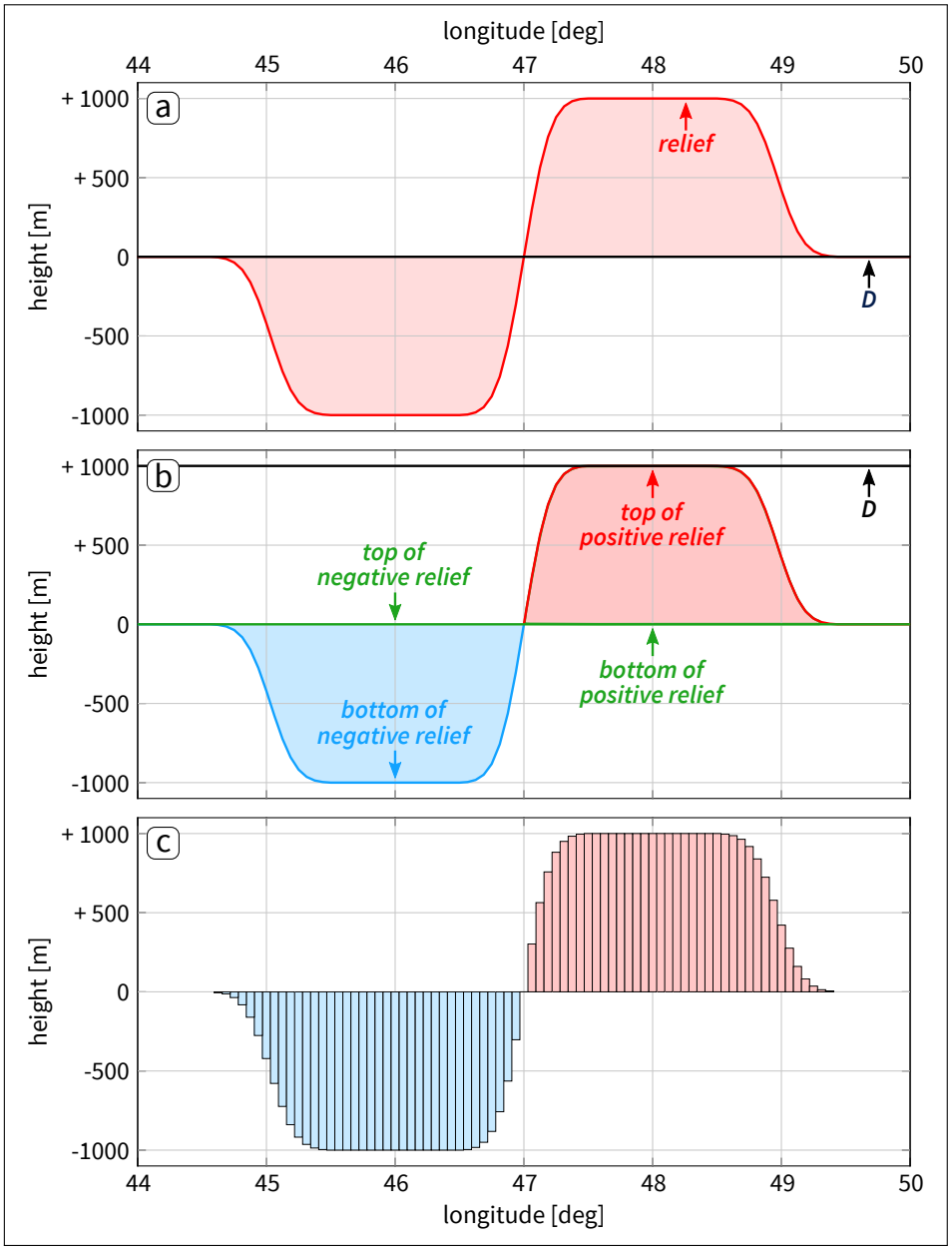

Figure 2.28.: Sections through the synthetic mass distribution (Fig. 2.27) in the three tested methods: **a)** one relief against a reference sphere of radius D, input for the unmodified spectral-domain method of Wieczorek (2007); **b)** the layer-wise spectral-domain strategy adopted in this chapter: two separate layers for the positive and negative density volumes, each defined by a top and bottom surface, and a common reference sphere; **c)** tesseroids discretisation (0.0625°×0.0625°), input for the spatial-domain method (Uieda et al., 2016). All heights are expressed in respect to a reference sphere with radius equal to 6378 km. The red-filled areas denote positive input densities (+1 g cm^{-3}) and the blue-filled ones denote negative input densities (−1 g cm^{-3}).

difference between the spectral and spatial output (spatial minus spectral g_z, lower left panel) lies inside a −0.92 to 0.92 mGal range. It is affected by the characteristic side lobes (*ringing*) which arise due to the boxcar truncation of the spherical harmonic expansion (Barthelmes, 2008). Applying a linearly decreasing weight (from 1 to 0) to all coefficients from degree 200 to 360 results in the differences plotted in the lower right panel. This *gentle cut* truncation was applied both to the coefficients resulting from the spectral method and to the results of Tesseroids modelling, by transforming the global grids in a spherical harmonics expansion, applying the truncation and synthesizing g_z. The filtered Δg_z is distributed between −0.0184 and 0.0181 mGal.

Four blocks test, power spectrum The same output can be expressed in the spectral domain, by comparing the power spectra of the modelled fields. The upper panel of Fig. 2.30 shows the degree variances (Eq. 2.17) of the potentials obtained with the spectral-domain method and with the spatial-domain one (after transforming the global grid in spherical harmonics). To better express the differences (spatial minus spectral), which are not evident in the degree variances plot, the spectrum of the standard deviation of Δg_z is shown in the bottom panel of the same figure. This spectrum was also obtained by prior spherical harmonics expansion of the synthesized g_z grids, unfiltered (no *gentle cut* applied). It is expressed cumulatively, reaching a maximum of 0.512 mGal at l_{max}.

Four blocks test, single relief against layer-wise method In addition to the spectral-domain (method **a)**) against spatial-domain (method **c)**) comparison, the consistency between two spectra-domain methods was tested: the unmodified relief-forward-modelling of Wieczorek (2007) (method **a)**) and its implementation as a layer-wise approach (method **b)**). The results, expressed in terms of power spectra (degree variances of the potential) and spectrum of g_z differences (cumulative degree standard deviation) are shown in Fig. 2.31. The two strategies converge to identical results, the only discrepancy likely arising from computational precision. Cumulative standard deviation of Δg_z at l_{max} is 1.23×10^{-12} mGal.

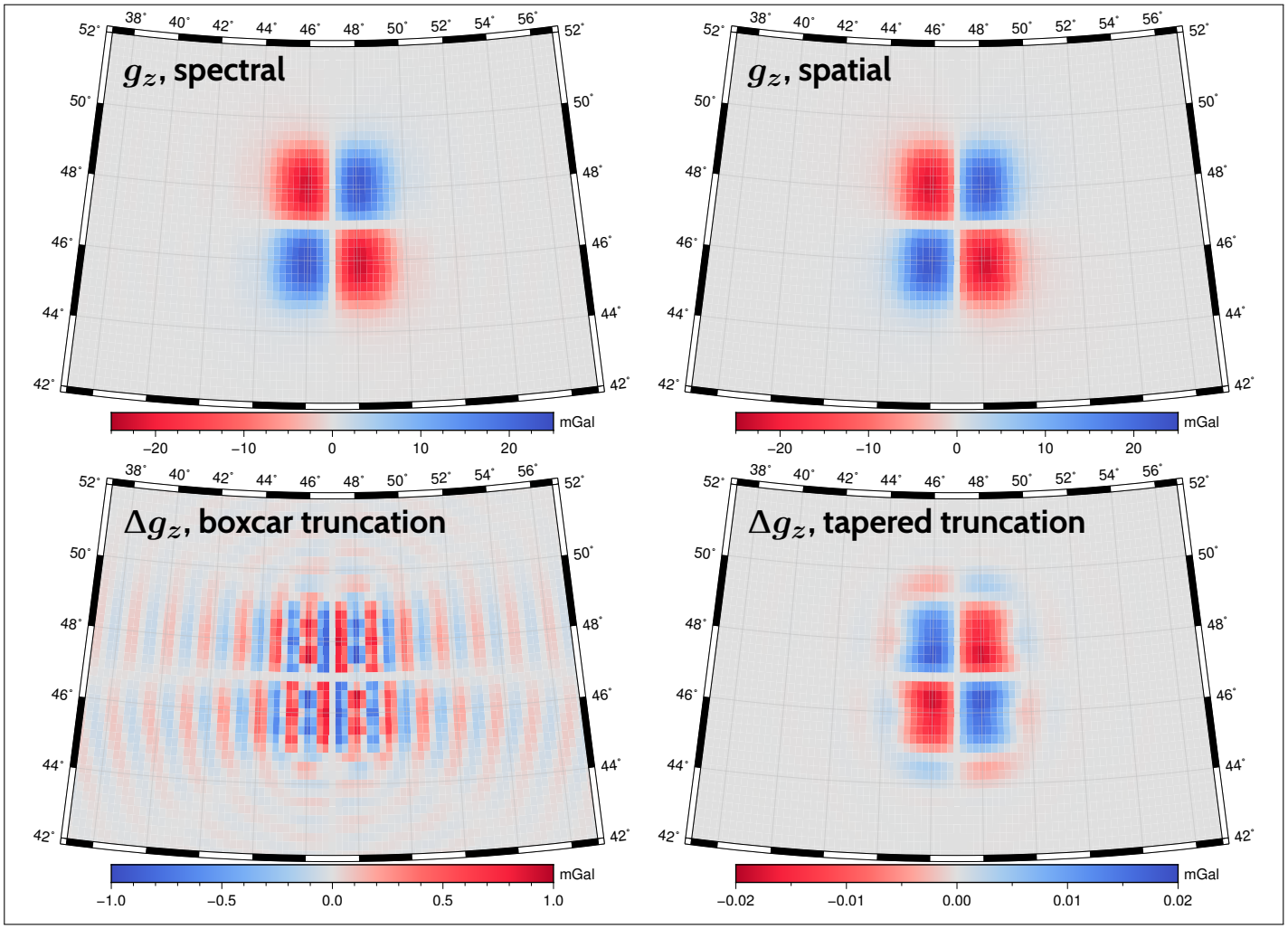

Figure 2.29.: Forward modelled output of the spectral–spatial comparison, "four blocks test". These four maps show the radial component g_z of the attraction of the modelled masses, expressed as positive upwards (i.e. a positive density contrast result in a negative g_z directly above it). The observation height is 40 km above the reference sphere. The two maps on bottom row show the spatial minus spectral g_z difference. In the lower left map, the spherical harmonics coefficients were synthesized up to degree and order l_{max} 360, with an abrupt truncation at l_{max}. In the lower right map, a linear taper was applied to the coefficients above degree 200, reaching zero weight at l_{max}.

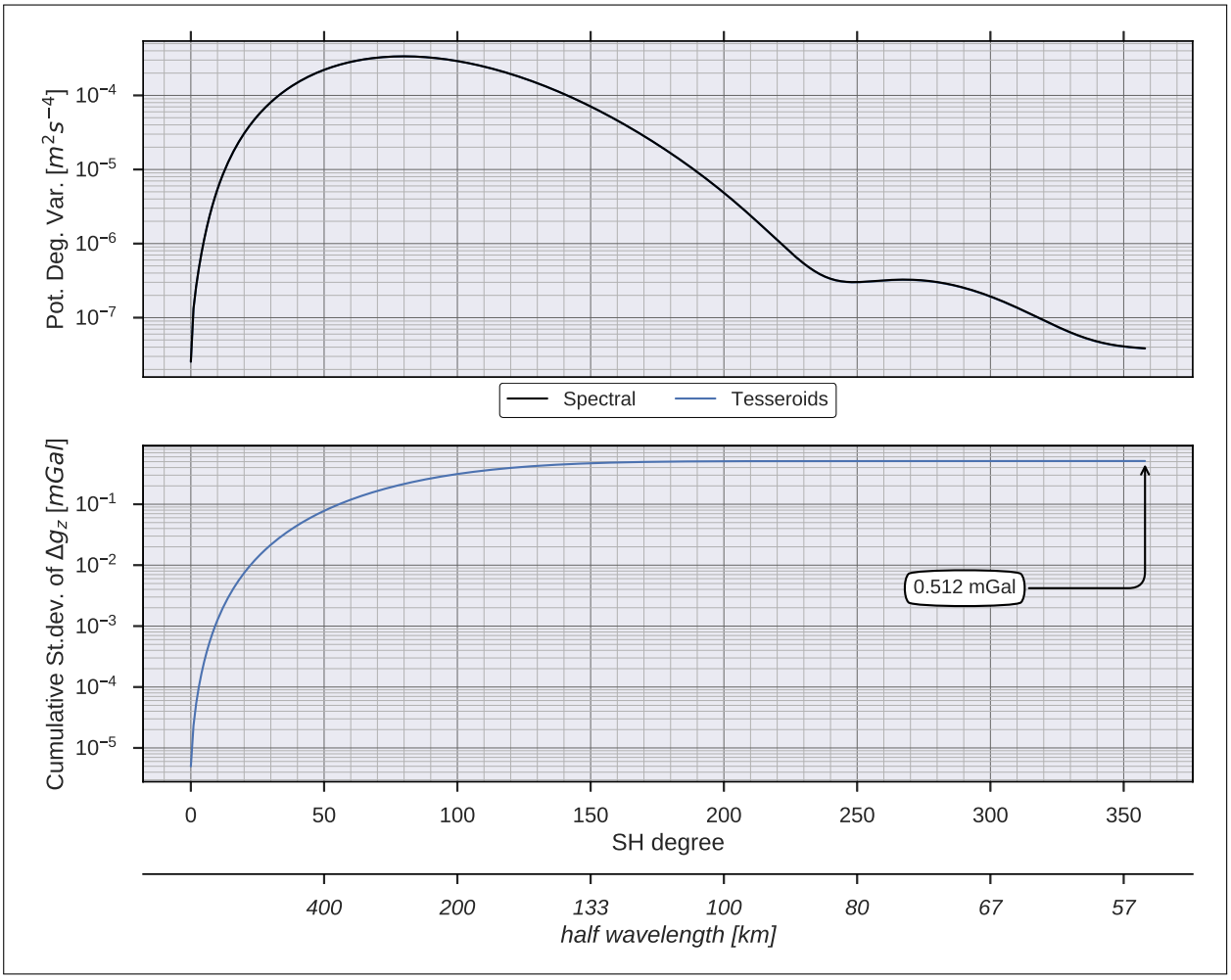

Figure 2.30.: Spectral domain (layer-wise) modelling against spatial domain (Tesseroids) modelling: potential degree variance (*Pot. Deg. Var.*) and difference spectra for the "four blocks test". The **upper panel** shows the degree variance power spectra of the forward-modelled potential of the two methods. Note that no difference can be graphically appreciated between the two plotted curves. The **lower panel** show the cumulative standard deviation spectra of the differences in radial component of gravity (g_z), computed as spatial-domain minus spectral-domain.

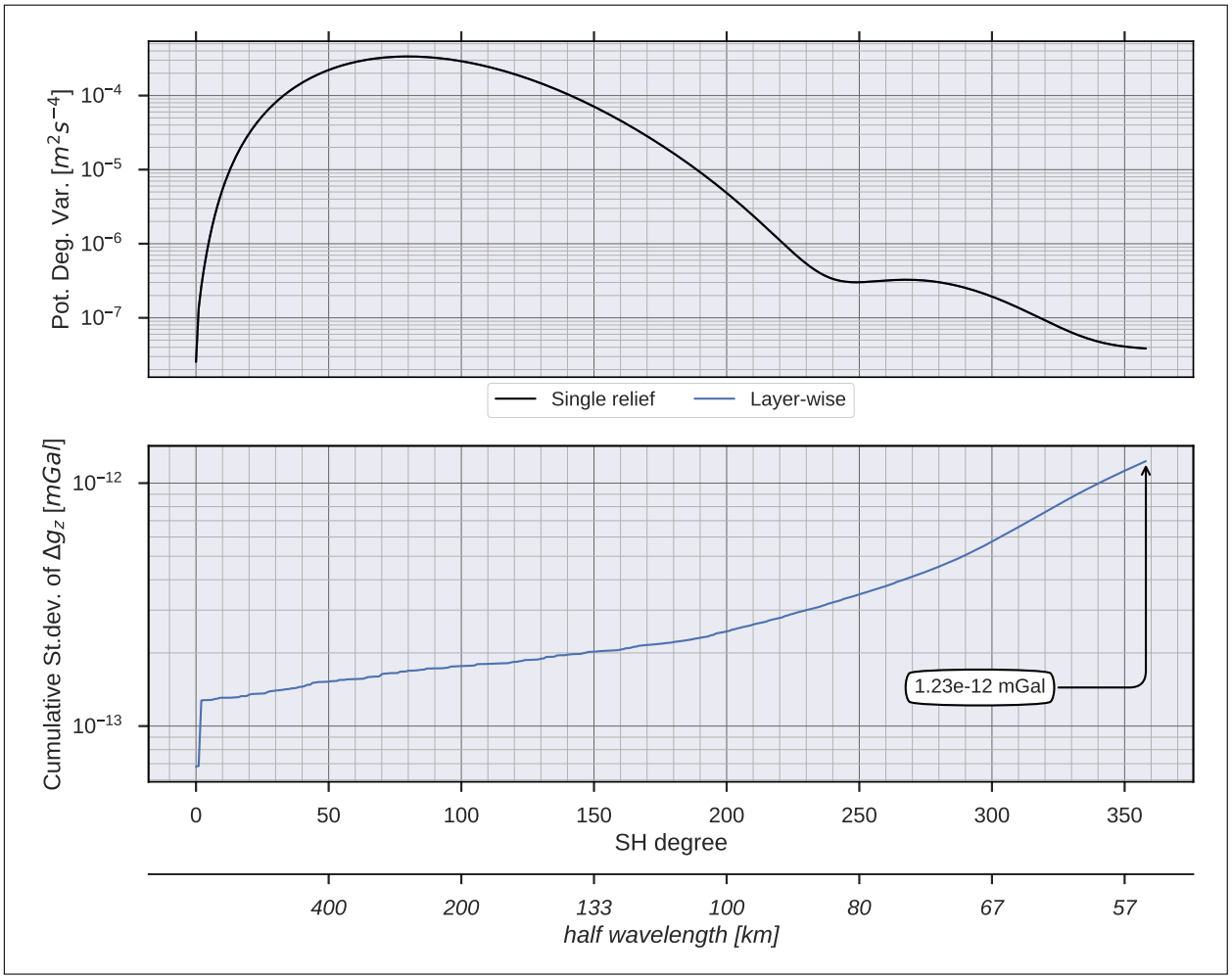

Figure 2.31.: "Single-relief" against layer-wise comparison: degree variance and difference spectra. The **upper panel** shows the degree variance power spectra of the potential resulting from the "four blocks test" in the single-relief setup (unmodified method of Wieczorek, 2007) and in the layer-wise strategy adopted in this chapter. The differences in input-masses representation between the two methods are shown in Fig. 2.28. Note that no difference can be graphically appreciated between the two plotted curves. The **lower panel** show the cumulative standard deviation spectra of the differences in radial component of gravity (g_z), computed as layer-wise minus single-relief.

2.A.2. Test using the SEDS1 layer

I am also including the output of another test: instead of the "synthetic relief" just shown in section 2.A.1, here the real layer boundaries of a layer from LITHO1.0 (Pasyanos et al., 2014) was used, representing a real step of the forward modelling carried out in this chapter. The SEDS1 layer is the most superficial among the layers modelled here (see the general model description in section 2.3.2). Representing the first of three sedimentary layers, it is derived from an updated version of the global sediment thickness map by Laske and Masters (1997). The only difference with the modelled reductions (section 2.5) is that the prescribed depths were referred to a sphere (instead of the WGS84 ellipsoid), the observation points were also spherical (40 km above the sphere) and density has been imposed constant at 2.17 g cm^{-3} (modelled as a −0.50 g cm^{-3} contrast against a 2.67 g cm^{-3} reference density). These three modifications simplified the generation of the corresponding tesseroids-discretised model and computation points grid, thus avoiding a potential source of discrepancy in the direct comparison.

The direct comparison on synthesized g_z maps is shown in Fig. 2.32. Differences, expressed as Tesseroids-modelled g_z minus spectral-domain layer-wise modelled g_z, are shown in the lower map. They are distributed between −0.099 and 0.129 mGal, with local maxima concentrating on margin areas – likely arising from issues in correctly modelling sharp edges with the limited bandwidth of the spectral method. The range of the difference expressed in relative terms (as percentage of the signal at the same point) is −0.448 % to 0.345 %. In regards to the maximum power (n_{max}) in the relief spherical harmonics expansion (Eq. 2.13), values ranging from 2 to 14 were tested, observing no significant change in spectral-to-spatial differences. Owing to the short time requirements for a single spectral forward modelling run, a mid-range n_{max} of 7 was chosen (the run times for n_{max} of 2, 7, 14 are 2.2 s, 4.2 s, 6.1 s respectively). The minimum and maximum difference are reported here for n_{max} equal to 2 and 14, respectively: −0.201 to 0.212 mGal and −0.099 to 0.129 mGal (the former are identical to the min/max range at $n_{max} = 7$).

Figure 2.33 shows the spectral- to spatial-domain comparison in terms of power spectra (upper panel) and cumulative standard deviation spectrum of the gravity (g_z) differences (lower panel). The same process adopted for the "four-block test" was adopted here: in order to perform a spectral domain comparison, the spatial domain output was transformed in a spherical harmonics expansion. Both plots show a satisfactory coherency. The two potential degree variance curves are non-distinguishable and the Δg_z spectrum plot, which amplifies the differences, shows a misfit level in the order of magnitude of tens of µGal. The cumulative standard deviation of Δg_z at l_{max} is 0.016 mGal.

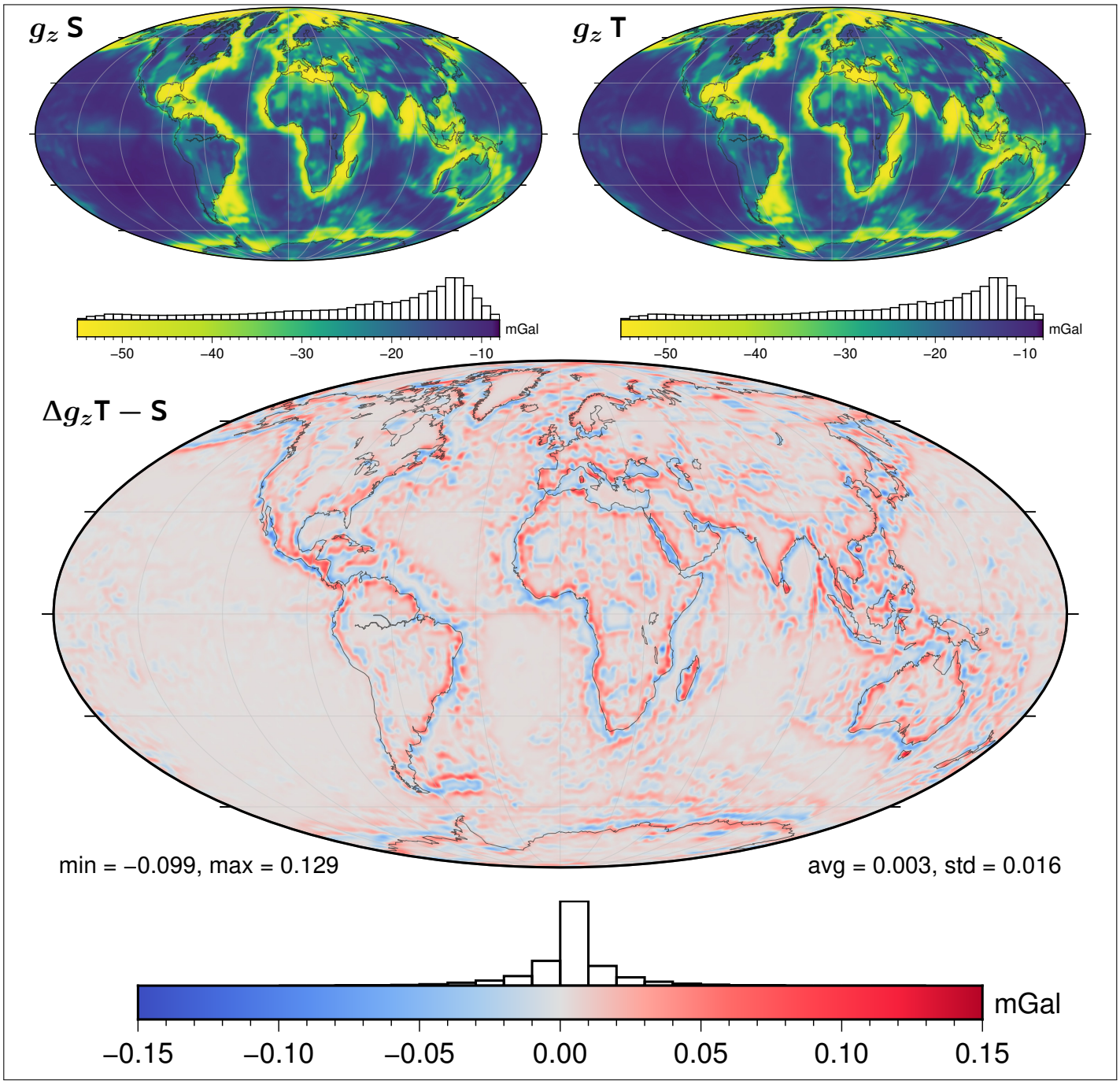

Figure 2.32.: Spectral domain (layer-wise) modelling against spatial domain (Tesseroids) modelling: direct comparison using the SEDS1 layer from LITHO1.0. All the maps show the vertical (radial) component of g. Upper left map: spectral domain g_z S, upper right map: spatial domain g_z T, lower map: difference, expressed as spatial minus spectral.

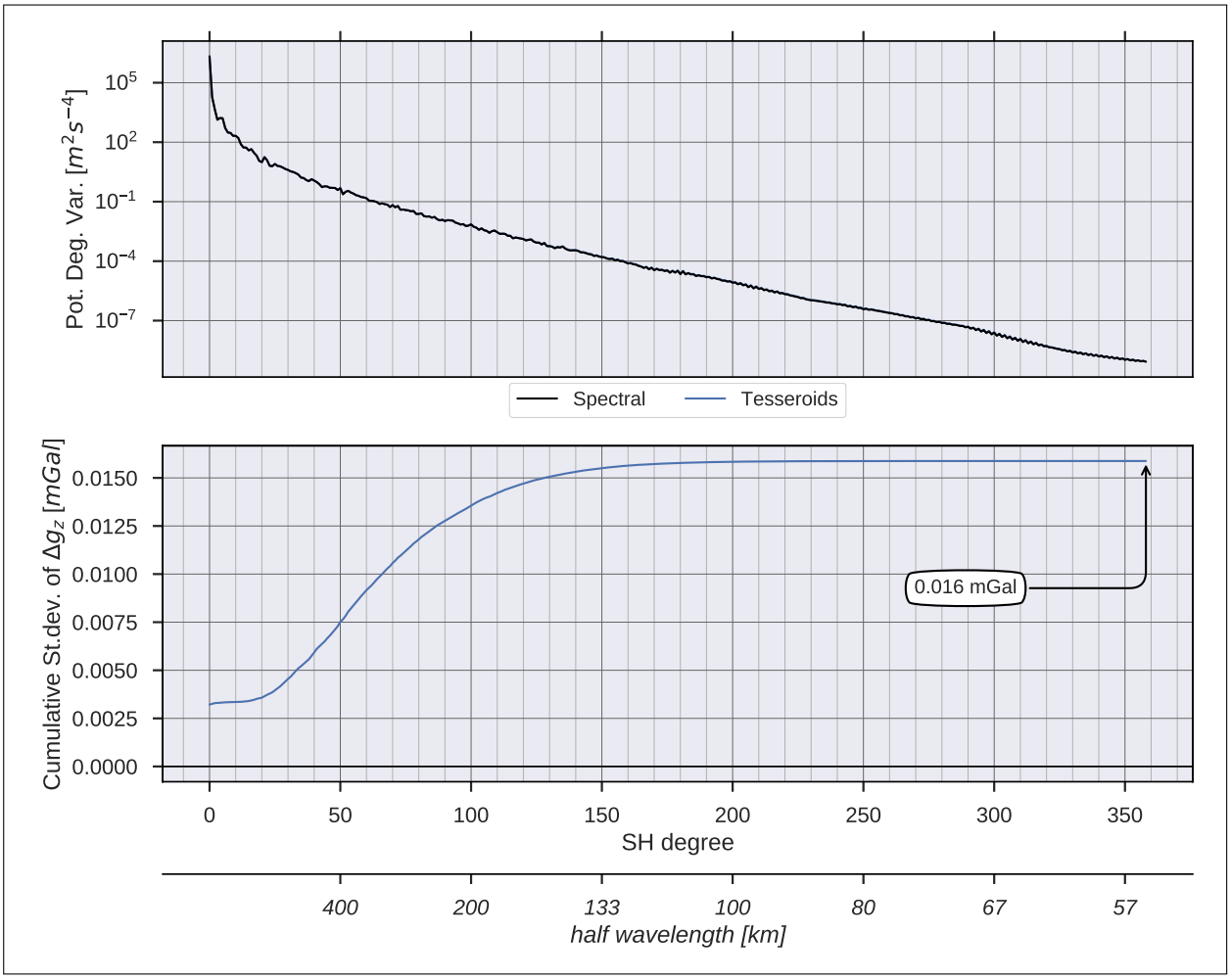

Figure 2.33.: Spectral domain (layer-wise) modelling against spatial domain (Tesseroids) modelling: degree variance and difference spectra for the SEDS1 test (Fig. 2.32). The **upper panel** shows the degree variance power spectra of the forward-modelled potential of the two methods. Note that no difference can be graphically appreciated between the two plotted curves. The **lower panel** shows the cumulative standard deviation spectra of the differences in radial component of gravity (g_z), computed as spatial-domain minus spectral-domain.

Overall, the two tests that were presented here show a satisfactory agreement between the spatial-domain method (adopted as a benchmark) and the layer-wise spectral-domain technique that was employed in computing the reductions and uncertainty-propagation of this chapter. Misfit levels, both in a synthetic 2×2 checker board test and with a realistic global layer, are small enough to exceed the application requirements: they lie below the uncertainties involved in the input mass distribution data. In addition, the layer-wise spectral-domain modelling technique, which relies on the superposition of the effects of the top and bottom surfaces of a layer, was shown to provide identical results to the single relief modelling provided in SHTOOLS (Wieczorek and Meschede, 2018).

The direct comparison of spatial- and spectral-domain methods also allowed to quantify and compare the computational time requirements, which has been the rationale for preferring the faster spectral-domain method for the Monte Carlo uncertainty propagation. For a single layer, provided on a global $n \times 2n$ grid with a 0.25° spacing, the spectral-domain method takes about 3 seconds, comprising two spherical harmonic transforms (for the top and bottom input reliefs), two calls to the forward-modelling routine, and a spectral harmonic synthesis to four output grids (the potential and the three components of its first derivative, g) In order to obtain a similar result in space domain, using Tesseroids (Uieda, 2017) on the same grid, a total number of 1 036 800 tesseroids × 1 036 800 computation points must be calculated. This requires a run time of about 240 hours, which becomes feasible only by resorting to parallelisation – the SEDS1 test was run on 100 parallel workers, requiring 2.26 hours.

However, it must be noted that this remarkable difference in computational requirements and this spatial- to spectral-domain equivalence is true only in this peculiar configuration, given the requirements of these reduction experiments: relatively low-resolution input data, with a large associated uncertainty, and a relatively low-degree band-limited output requirement (the satellite-only global gravity models at which the reductions are aimed).

3. Estimating the crustal heat production, surface heat flow and lithospheric temperature field in Central Europe

Chapter summary

In this chapter, the potential of a satellite-only global gravity model as a useful tools for estimating the thermal structure of the continental lithosphere is assessed, through a real-data test in Central-Eastern Europe, across the Trans-European Suture Zone. Heat flow, measured near the Earth surface, is the result of the superposition of a complex set of contributions, one of them being the heat production occurring in the crust. The crust is enriched in radioactive elements respect to the underlying mantle and crustal thickness is an essential parameter in isolating the thermal contribution of the crust. Obtaining reliable estimates of crustal thickness through inversion of GOCE-derived GGMs has already proven feasible, especially when weak constraints from other observables are introduced. A way to integrate this in a geothermal framework was tested, building a 3D, steady state, solid Earth conductive heat transport model, from the lithosphere-asthenosphere boundary to the surface. This thermal model is coupled with a crust-mantle boundary depth resulting from inverse modelling of gravity, after correcting the gravity model for the effects of topography, far-field isostatic roots and sediments. A mixed space- and spectral-domain based forward modelling strategy was employed to ensure full spectral coherency between the limited spectral content of the gravity model and the reductions. Deviations from a direct crustal thickness to crustal heat production relationship are accommodated using a subsequent substitution scheme, constrained by surface heat flow measurements, where available. The result is a 3D volume of the lithosphere characterised in temperature, radiogenic heat, and thermal conductivity. It provides added information respect to the lithospheric structure and sparse heat flow measurements alone, revealing a satisfactory coherence with the geologic features in the area and their controlling

effect on the conductive heat transport.

3.1. Introduction

The application presented in this chapter consists of a gravity data reduction and Moho inversion phase, which I describe in section 3.2, followed by a thermal modelling and parameter fitting phase, described in section 3.3. The thermal modelling procedure tested here uses crustal thickness, as inverted from gravity, and surface heat flow measurements. The former is available uniformly inside the study area, while the latter, as discussed afterwards, suffers from inhomogeneous sampling. The main research objective of the method presented here is overcoming the sampling problems of surface heat flow in areas devoid of measurements. This is achieved through iterative fitting of surface heat flow (where available) by subsequent substitution of crustal radioactive heat production estimates, as described in section 3.3.2. In each iteration of the 3D thermal forward model the misfit between modelled and observed surface heat flow is fitted for using a 1D column-wise approximation. Compared with simple interpolation of the surface heat flow, the fitted RHP values are interpolated, instead, and assigned to crustal columns of different thickness.

Satellite gravity data and direct surface heat flow data are integrated with a regional map of sediment thickness (topography to crystalline basement), as provided by Tesauro et al. (2008), by the global sediment thickness and Moho depth from the LITHO1.0 model (Pasyanos et al., 2014), and the depth of the lithosphere-asthenosphere boundary (LAB), as estimated from surface wave inversion, also from Pasyanos et al. (2014).

The study area (Fig. 3.1 and 3.2) is located in central-eastern Europe, encompassing different geological contexts and thermal regimes. It is bounded by a box limited by 45 to 55 °N, 15 to 35 °E, transitioning from Phanerozoic lithosphere (Polish-German basin, Carpathians, Pannonian Basin) interested by extension events and orogeny to the Russian platform, crossing the Trans-European Suture Zone (TESZ, Jones et al., 2010). In this area the available estimates of lithospheric thickness range from about 50 km to values in excess of 250 km across a steep transition zone, approximately 300 km wide. This lithospheric geometry is overlaid by a remarkable assortment of crustal features. These conditions result in a wide range of measured surface heat flow values (see section 3.3.3), ranging from 16 to 195 mW m^{-2} (mean: 57 mW m^{-2}). The measurements towards the extremes of this heat flow range and short-wavelength variations were attenuated with a spatial-domain filter, since it is expected that they are arising from non-conductive heat transport (e.g. hydrology, shallow melts). The regional grid of filtered surface heat flow measurements so obtained

(see section 3.5.1) constitutes the dependent variable of the fitting procedure presented here.

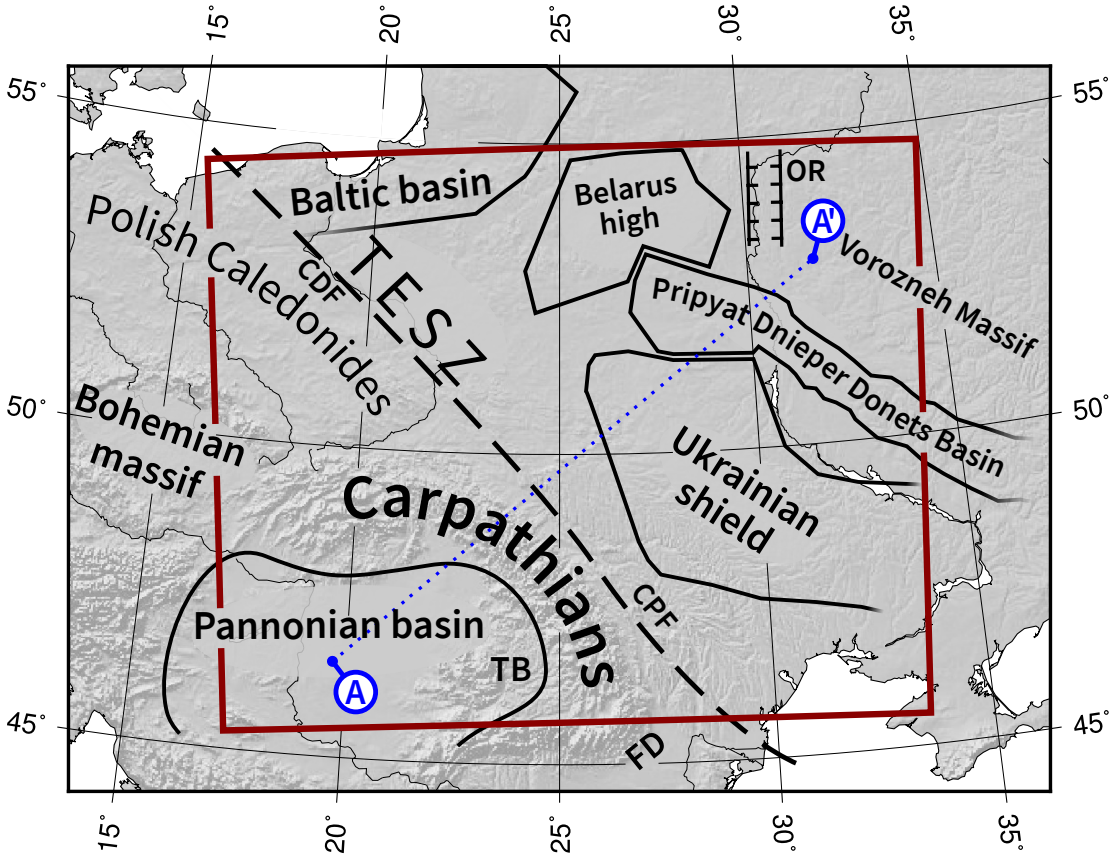

Figure 3.1.: Simplified map of the most significant geological units and boundaries inside the study area and in its proximity. The red rectangle encloses the extents of the Moho inversion result and of the thermal model. **TESZ** Trans-European Suture Zone, **CDF** Caledonides Foredeep, **CPF** Carpathians Foredeep, **TB** Transylvania Basin, **FD** Focşani Depression, **OR** Orsha Rift (Aulacogen). Data redrawn from Tărăpoancă et al. (2003), Tesauro et al. (2008), Artemieva and Thybo (2013), Mazur et al. (2016), and Starostenko et al. (2018). Profile *AA'* refers to the section shown in Fig. 3.17.

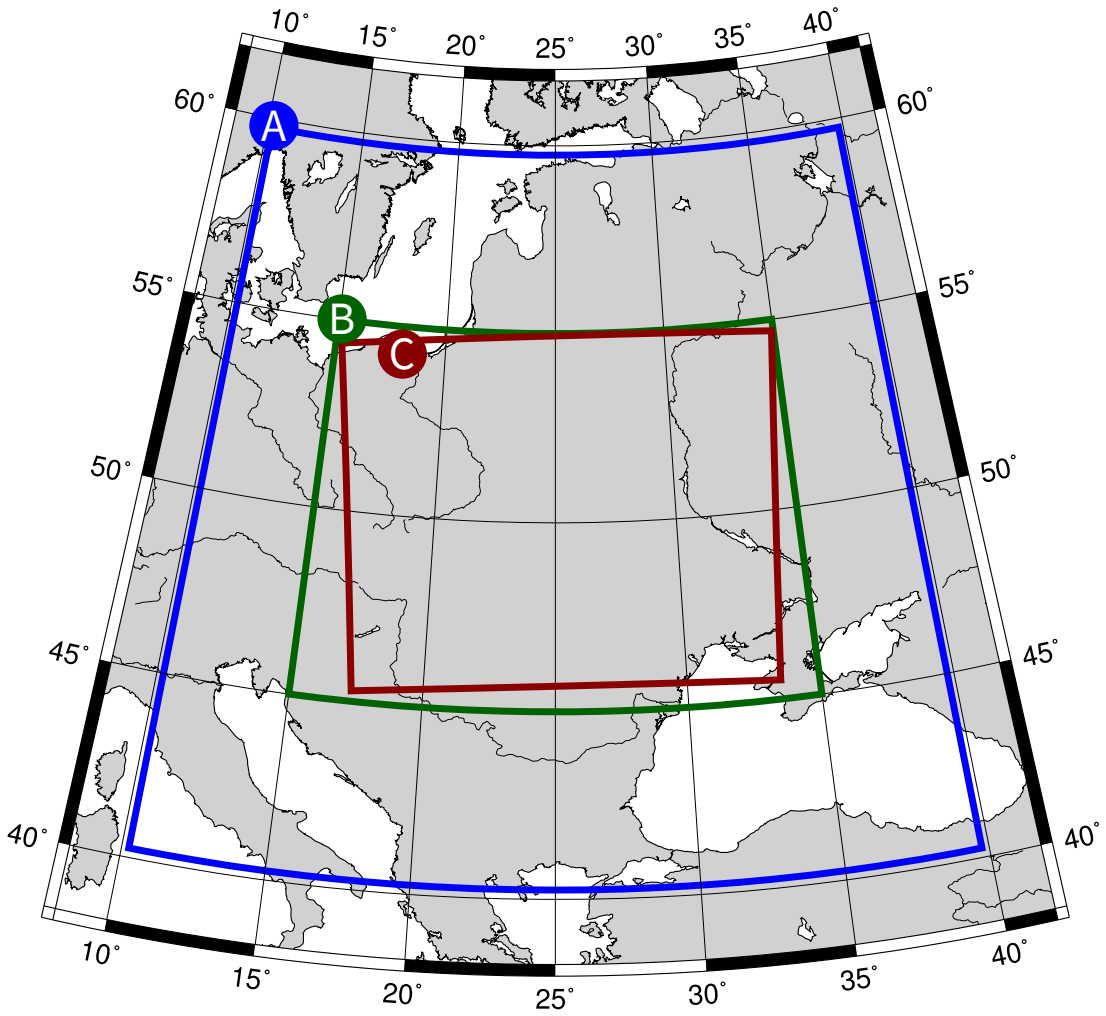

Figure 3.2.: Extents of the modelled areas. **A)** area outside of which the far-field gravity effect of crustal root (isostatic effect) was modelled. **B)** computation area for the gravity signal and reductions. **C)** extents of the inversion results and thermal model (UTM 35N grid).

3.2. Gravity model processing and inversion

The crustal thickness estimation employed here is based on the solution of a gravity to Moho undulation inverse problem. Its input signal is a reduced gravity disturbance from a global gravity model, which I pre-processed by computing and subtracting the contribution of topography, of far-field isostatic effects, and of the basement-to-topography sedimentary overburden. These reductions are aimed at obtaining an anomalous gravity quantity, then interpreted as the effect of the varying depth of a crust-to-mantle boundary, under the Vening Meinesz isostatic hypothesis (Vening Meinesz, 1931).

I have used the GO_CONS_GCF_2_TIM_r5 release (Brockmann et al., 2014; Pail et al., 2011; GOCE-ESA, 2014) of the global gravity model derived from the European Space Agency's *Gravity field and steady-state Ocean Circulation Explorer mission* (GOCE), providing a ppm-level accuracy for g with a half-wavelength resolution of about 70 km (Floberghagen et al., 2011). This release comprises both GNSS tracking data –which dominate the gravity field solution up to spherical harmonic degree 30– and observations of the on-board gradiometer, which cover the smaller spatial scales (higher degrees and orders). The harmonic coefficients are obtained from these measurements through a least square regression for full normal equations complete to degree/order 150 for the GNSS and to 280 for the gradiometry. A map of the gravity disturbance in the study area is shown in Fig. 3.5 A.

3.2.1. Reduction for the topographic and isostatic effects

I applied a global topography correction, computed as gravity disturbance, on a 15' by 15' regular grid at 8 km above the GRS80 ellipsoid. This was accomplished with the GrafLab software package (Bucha and Janák, 2013) and the spherical harmonics topography effect model dV_ELL_RET2014 by Rexer et al. (2016), based on the EARTH2014 global topography (Hirt and Rexer, 2015b). I then subtracted this from the GGM gravity disturbance computed on the same grid. Both the spherical harmonics expansions where evaluated up to degree and order 280. The reduction density for the topography correction was 2670 kg m^{-3} for above-sea-level relief and 1030 kg m^{-3} for oceans.

As shown by Szwillus et al. (2016), the 'global Bouguer anomaly' obtained with this procedure contains a significant long-wavelength bias due to the far-field effect of internal masses, including those involved in the isostatic compensation of topography (called *isostatic effect*). This is different from what would be obtained when processing local gravity data, using the 'classic topographic reduction' computed inside a 167 km radius (Hayford and Bowie, 1912).

I adopted one of the strategies suggested in Szwillus et al. (2016): accounting

for the isostatic effect from masses outside of the study area. I have chosen the LITHO1.0 model (Pasyanos et al., 2014) as a global reference crustal root model. By querying the 'access_litho' program point-wise on a global regular 0.125 by 0.125 degree grid, I extracted the crust-mantle boundary depth (bottom of the 'CRUST3' layer), its density, and V_P in the lithospheric mantle ('LID' layer).

This procedure provided outlier values on some nodes. I removed the values of crustal density and V_P in the lithospheric mantle outside the range defined by three standard deviations around the mean (i.e. $\overline{x} \pm 1.5\sigma$, with $\overline{x}$ mean value). This implied keeping only the values of crustal density between 2500 and 3300 kg m^{-3} and of lithospheric mantle V_P between 7500 and 8800 m s^{-1}. Crustal depths of less than zero or more than 80 km where also considered obvious interpolation artefacts, and removed.

I also compared each node value with a 1.5 by 1.5 degrees moving average (12 by 12 grid nodes). I have deleted the values with over 10 km, 200 kg m^{-3}, and 100 m s^{-1} of absolute difference with the local moving average of depth, density, and V_P respectively. These criteria removed the 2.5 ‰ of the points sampled from LITHO1.0: 10198 points on a 1441 by 2881 global grid. Linear interpolation was used to fill in the removed nodes.

This dataset was then low-pass filtered through convolution with a Gaussian kernel with a cut-off wavelength of 4 degrees, i.e. the wavelength at which the filter response value is $\exp(-0.5)$. This equals to a 0.5 filter response at 3.4 degrees. This was applied as an anti-aliasing filter, prior to downsampling the depth and density data to a 0.5 by 0.5 grid. With these three steps (over-sampling, outlier processing, and low-pass filtering) of the data extracted from LITHO1.0, I aimed at removing any artefacts that may arise due to re-gridding on a rectangular longitude-latitude grid. Since the target is computing and removing a low degree effect, I consider such a drastic smoothing of input data justified.

I then blanked out the grid over a 'study area' defined by 40 to 60 degrees latitude, 10 to 40 degrees longitude. This area and subsequent crops, which I applied due to edge effects or re-projections, is shown in Fig. 3.2.

This crustal root model was then discretised into 0.5 by 0.5 arc-degree wide spherical tesseroids (Uieda et al., 2016), centred on the same sampling grid. Each tesseroid density is equal to the contrast between the density of the lower crust and of the lithospheric mantle, against a reference Moho at -35 km. For each grid node, this equals to:

$$\Delta\rho = \begin{cases} \rho_C - \rho_M & \text{if } D < \overline{D} \\ \rho_M - \rho_C & \text{if } D > \overline{D} \end{cases} \tag{3.1}$$

with D Moho depth, positive upwards, $\overline{D}$ reference depth, and ρ_C crustal density as directly extracted from the model. ρ_M, the mantle density, is provided constant at 3300kg m^{-3} in LITHO1.0 (Pasyanos et al., 2014), although lateral variations in mantle velocity are provided. I therefore follow the approach used by Sebera et al. (2018), applying the linear density-V_P relation by Yegorova and Pavlenkova (2015), which is based on ACY400 (Montagner and Anderson, 1989):

$$\rho_M = 0.316 V_P + 769 \tag{3.2}$$

with V_P in m/s and ρ in kg m^{-3}.

This yields an average contrast of 380 kg m^{-3}, which I note is lower than the global estimates of 485 kg m^{-3} by Tenzer et al. (2012b) and of 448 ± 187 kg m^{-3} by Sjöberg and Bagherbandi (2011). A globally uniform linear velocity-to-density conversion is a simplified model, which disregards the concurring effects of temperature, pressure and composition. Nevertheless, I deemed it suitable to model a far-field, very long wavelength effect, which would be difficult to estimate otherwise (for a different approach, based on topography and the Airy-Heiskanen isostatic model, see Grombein et al., 2016). Small scale variations are expected to be significantly smoothed out, while still obtaining a more refined and observation-based estimate than the one that would result from a high-pass filter on the gravity model (e.g. by setting the low degree and order coefficients to zero, up to an arbitrary cut off degree).

The gravity effect was computed through space-domain integration, using the Tesseroids program, version 1.2.1 (Uieda et al., 2016; Uieda, 2017). I computed the gravity field on a spherical grid, on a radius equal to the semi-major axis of the GRS80 ellipsoid. This field was then filtered and synthesised on the working grid according to the procedure described in section 3.2.3. The result is shown in Fig. 3.3 B.

3.2.2. Reduction for the sediment layer effect

The low-density infill of sedimentary basins results in a negative bias of the Bouguer anomaly, since the topographic effect correction relies on the commonly used 2670 kg m^{-3} crustal reference density (Hinze, 2003). Since a negative density contrast is expected at the Moho, not accounting for this bias would result in an over-estimation of the crustal thickness. I thus applied a *sediment stripping correction* (Chen et al., 2014) to the gravity data, using the sediment thickness map provided in Tesauro et al. (2008) in the study area (Fig. 3.3 C) and the rest of the European platform. The rest of the Earth is covered by the sediment thickness data included in LITHO1.0 by Pasyanos et al. (2014). Using a global coverage enabled a realistic estimate of larger wavelengths.

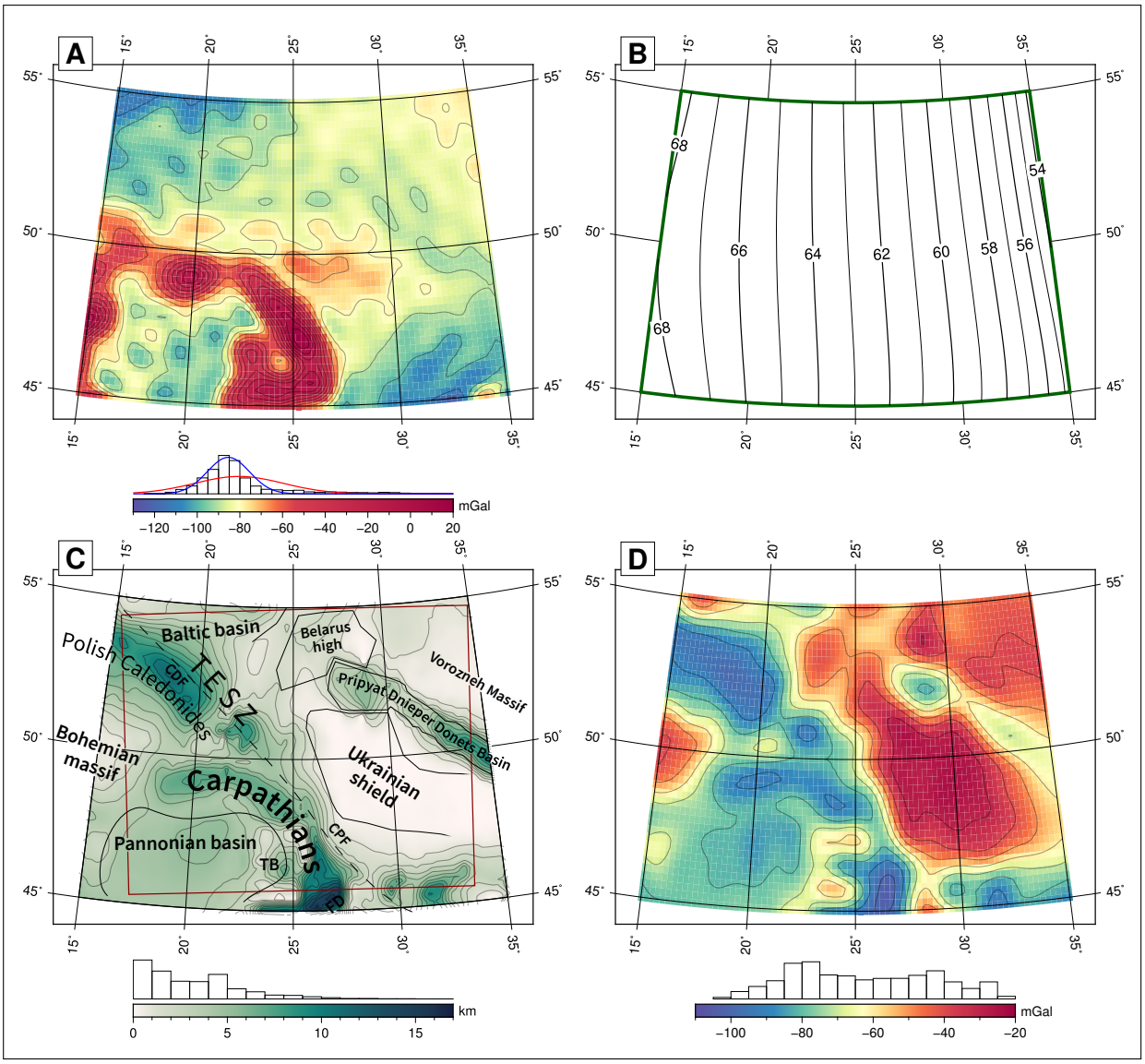

Figure 3.3.: Data reductions to the gravity model. **A)** Topographic effect (gravity disturbance) from the RET2014 model (Rexer et al., 2016). A median-centered normal fit is also plotted, in blue. **B)** Forward-modelled far field gravity signal (radial component) due to isostatic compensation outside the study area. **C)** Sediments thickness (km) in the study area, from Tesauro et al. (2008). Red rectangle: inversion results coverage. Geologic lineaments: see caption of Fig. 3.1. **D)** Sedimentary layer effect. Thicker sedimentary covers result in more negative values. Grid cells are shown on a 15' by 15' grid, without interpolation.

The decrease in porosity (i.e. the volumetric ratio between grains and voids) due to compaction is modelled with the exponential model of Woodside and Messmer (1961):

$$\phi(z) = \phi_0 \mathrm{e}^{-z/p} \tag{3.3}$$

Where z is depth (positive downwards), ϕ_0 the porosity at the surface, and p a characteristic skin-depth, such as $\phi(p) = \phi_0 \cdot \mathrm{e}^{-1}$. Density can thus be computed with a porosity-weighted sum:

$$\rho_{sed}(z) = [1 - \phi(z)]\rho_G + \phi(z)\rho_W \tag{3.4}$$

Where ρ_G and ρ_W represent the density of the grain matrix and of water filling the voids, respectively.

This reduction is critically dependent on two quantities: the estimates on the sedimentary cover thickness, and the spatial distribution of density in it. Geological heterogeneities (e.g. lithology, basin history, cementation) result in deviations from general depth-compaction laws (P. A. Allen and J. R. Allen, 2013), hindering the reliability of universal trends.

I computed a sediment effect estimate using the following values: $\rho_G = 2670\,\mathrm{kg\,m^{-3}}$, $\rho_W = 1030\,\mathrm{kg\,m^{-3}}$ (brine), $\phi_0 = 0.5$, $p = 4\,\mathrm{km}$ ($1/p = 0.25\,\mathrm{km^{-1}}$). This depth-density curve lies between the one provided for the Pannonian Basin by Kaban et al. (2010) ($\phi_0 = 0.4$, $p = 2.375\,\mathrm{km}$), and the compaction behaviour of shaly sandstones provided in (P. A. Allen and J. R. Allen, 2013) ($\phi_0 = 0.56$, $p = 2.5\,\mathrm{km}$).

This contribution was forward modelled with the same method used for the isostatic effect, through integration of discrete tesseroids. I modelled the depth-wise density variation by dividing each tesseroid radially, with a step coarsening with depth (from 50 m at the surface to 200 m at 8 km of depth and more). Each tesseroid density is equal to the contrast against a $2670\,\mathrm{kg\,m^{-3}}$ reference crustal density. The result is shown in Fig. 3.3 D.

3.2.3. Spectral-domain filtering of the computed reductions

Subtracting the aforementioned reductions from a band-limited global gravity model carries the risk of introducing spectrally inconsistent higher degree components. This is a consequence of adopting a space-domain forward modelling technique, which generates a band-unlimited gravity signal (Hirt and Kuhn, 2014). To remove any high-order component from the reductions, I carried out the following filtering procedure: (1) first, every reduction signal was computed out globally, in terms of gravity field, on a spherical global grid of radius equal

to GRS80 semi-major axis. This grid was an equally spaced grid ($N \times 2N$) compliant to Driscoll and Healy (1994) sampling theorem. (2) Then, I expanded it to a spherical harmonic expansion using SHTOOLS by Wieczorek and Meschede (2018). (3) Using the same software, I synthesised the radial component of gravity from the spherical harmonics coefficients of the field. The SH series was truncated at maximum degree and order 280, and the values were calculated on an ellipsoidal surface, 8 km above GRS80. This grid extends only over the study area.

3.2.4. Inverse modelling

I inverted for the crust-mantle interface (CMI) with the *iterative constrained inverse modelling* routine included in the Lithoflex software (Braitenberg et al., 2007), a method that has been extensively tested in similar schemes (Ebbing et al., 2001; Mariani et al., 2013). Its algorithm alternates direct forward modelling and downward continuation, and has some analogies with the strategy of Oldenburg (1974).

This procedure works in planar coordinates, therefore the obtained gravity signal was projected to a local coordinate reference system (WGS84 UTM zone 35N) on a 10 by 10 km grid. The horizontal spatial resolution for the maximum degree ($N = 280$) of the spherical harmonics expansion of the gravity model, defined as half of the minimum resolved wavelength, is about 71 km. This comes from the $\lambda_{min} \approx 40000$ km$/N$ rule (Hofmann-Wellenhof and Moritz, 2006). Therefore, the projected grid is oversampled with a factor of 7.1 with respect to the spatial resolution of the GGM.

The inversion parameters are D, the reference depth of the undulating interface, P_{min}, the minimum period of the raised cosine low-pass filter applied on the crustal root estimate, and $\Delta\rho$, the density contrast at the interface. The first two parameters are uniform over all the input grid, while $\Delta\rho$ can vary horizontally.

P_{min} is required for inversion stability and to attenuate any sharp Moho undulation that may result from inverting localised maxima and minima. A value of 160 km was chosen to filter out short-wavelength Moho geometries which would be spectrally inconsistent with the resolving power of the gravity model. D and $\Delta\rho$ are not estimated by the inversion itself and require integration with external constraints. I have extracted them from the global LITHO1.0 model (Pasyanos et al., 2014), adopting the average Moho depth in the study area (43.9 km) as D and a 4-degree low-pass filtered Moho contrast, as computed in section 3.2.1. The density contrast map is shown in the right map of Fig. 3.6. Density is a temperature dependent parameter, due to the effect of thermal expansion (P. A. Allen and J. R. Allen, 2013). Since the strategy presented here

includes the temperature distribution in the lithosphere among the outputs, I could update the density model accordingly (using a thermal expansion model) and re-compute the Moho depth estimate, iteratively. This has been tested for, resulting in local variations of up to 3.4 km, with a standard variation of 0.75 km after one iteration (see section 3.A.4). Owing to the much larger uncertainties in Moho estimates (± 5 to ± 15 percent, see Grad et al., 2009) and the additional parameter uncertainties involved, I opted to omit the thermal effect on density.

The use of a regional average Moho depth, different from the global reference depth of 35 km (that I adopted to compute the global isostatic effect), is justified by the fact that I then subtracted the average gravity value over the area, before inversion. Therefore, that average-free gravity anomaly is interpreted as deviations of the crust-mantle interface from the regional average depth.

3.3. Thermal modelling

The thermal modelling presented here is based on the assumption of steady state, three-dimensional heat conduction from the thermal-LAB to surface, on which the radioactive heat production is superimposed.

Both heat production and thermal conductivity are non uniform in the domain. This means solving the heat equation for a inhomogeneous media, in the following vector form:

$$\nabla \cdot (k(\mathbf{x})\nabla T(\mathbf{x})) = -A(\mathbf{x}) \tag{3.5}$$

With k thermal conductivity (isotropic), T temperature, A heat production per unit of volume, and $\vec{x}$ position vector. I solve eq. 3.5 with a finite difference scheme on a rectilinear 3D domain, implemented in Matlab. I adopt a planar approximation, which I deem suitable due to the small radial extent of the model (from the Earth surface to a depth of up to 205 km) in respect to its tangential extent (less than 10 by 20 arc-degrees, latitude by longitude). Node spacing along the depth axis is non-uniform, to allow for a coarser resolution at higher depths. A zero flux Neumann boundary condition (G. Smith, 1985) is imposed along the vertical sides of the domain.

Upper and bottom boundaries are Dirichlet conditions (G. Smith, 1985), which I set to 15 °C (surface temperature) and 1200 °C (LAB temperature, see section 3.3.3.2), respectively. To accommodate for a non-flat morphology of these two boundaries, the Jacobian matrix coefficients of all nodes above topography or below the LAB are set to identities (i.e. the temperature of those nodes is fixed). The solver input consists of the grid definition, the $\mathbf{k}$ and $\mathbf{A}$ arrays, and boundary conditions. The finite difference system of linear equations is solved with the Matlab built-in *UMFPACK* factorization for sparse arrays (Davis, 2006).

Table 3.1.: Summary of the adopted thermal parameters. For a detailed explanation of laws and symbols, refer to section 3.3.1. SCLM: Sub-Continental Lithospheric Mantle. Abbreviatiated sources: **V:** Vilà et al. (2010), **H:** Hasterok and Chapman (2011), **C:** Chapman (1986), **X:** Xu et al. (2004).

Layer	Heat production (A)	Thermal conductivity (k)
Sediments	exponential compaction $\phi_0 = 0.55$, $p = 2.5\,\mathrm{km}$, $A_{gr} = 0.93\,\mu\mathrm{W\,m^{-3}}$ [**V**], $A_{pf} = 0$	exponential compaction [Eq. 3.6] ϕ_0, p: same as A, $k_{gr} = 3.0\,\mathrm{W\,m^{-1}\,K^{-1}}$, $k_{pf} = 0.6\,\mathrm{W\,m^{-1}\,K^{-1}}$
Upper crust	initial guess $1.74\,\mu\mathrm{W\,m^{-3}}$ [**V**]	temperature and depth dependent [**C**, Eq. 3.7] $k_0 = 3.0\,\mathrm{W\,m^{-1}\,K^{-1}}$, $b = 1.5 \times 10^{-3}\,^{\circ}\mathrm{C}^{-1}$, $c = 1.5 \times 10^{-6}\,\mathrm{m}^{-1}$
Lower crust	initial guess $0.37\,\mu\mathrm{W\,m^{-3}}$ [**V**]	temperature and depth dependent [**C**, Eq. 3.7] $k_0 = 2.6\,\mathrm{W\,m^{-1}\,K^{-1}}$, $b = (1.0 \times 10^{-4}\,^{\circ}\mathrm{C}^{-1}$, $c = 1.5 \times 10^{-6}\,\mathrm{m}^{-1}$
SCLM	$0.02\,\mu\mathrm{W\,m^{-3}}$ [**H**]	temperature and pressure dependent, sum of: - lattice conduction term [**X**, Eq. 3.8] - radiative term [**H**, Eq. 3.9]

3.3.1. Thermal conductivity model

I adopt a reference thermal conductivity model of sediments, upper and lower crystalline crust and Sub-Continental Lithospheric Mantle (SCLM). It includes standard values, at surface conditions, and models of their dependency on temperature and pressure. Conductivity overall is strongly controlled by lithological properties such as mineralogy, porosity, free and bound water content (P. A. Allen and J. R. Allen, 2013; Schön, 2011). These properties in turn are highly variable parameters, due to the large crustal heterogeneity. This a-priori reference may not describe the exact distribution of parameters in each of the model column. It also should not be interpreted as a 'mean model' of thermal conductivity in the study area, since it samples a local geological setting that is realistically expected to be significantly skewed in respect to a global average. Nevertheless, it provides a reference, not unlike reference models used in seismic tomography – deviations from it can be expressed as anomalies and it provides a consistent benchmark to perform comparison with other strategies. The parameters and describing laws are summarised in Tab. 3.1. They are described in the next sections.

3.3.1.1. Sediments

The thermal conductivity in the sedimentary layer follows the same exponential compaction model adopted for the sediment reduction to the gravity signal (equation 3.3). Therefore, the bulk sediment conductivity can be modelled as a porosity-weighted sum of the conductivities of the rock matrix (grains, k_{gr}) and the pore-filling fluid (k_{pf}) (Woodside and Messmer, 1961; P. A. Allen and J. R. Allen, 2013):

$$k_{sed}(z) = [1 - \phi(z)]k_{gr} + \phi(z)k_{pf} \tag{3.6}$$

The porosity-depth compaction curve is the same used for the gravity modelling. I adopt a thermal conductivity of the solid matrix (k_{gr}) and of the pore fluid (k_{pf}, assumed brine) equal to 3.0 $\mathrm{W\,m^{-1}\,K^{-1}}$ and 0.6 $\mathrm{W\,m^{-1}\,K^{-1}}$, respectively (Revil, 2000).

3.3.1.2. Crystalline crust

I model the inverse dependence between temperature and thermal conductivity in the crystalline continental crust with the empirical relationships proposed by Chapman (1986):

$$k(T, z) = k_0(1 + cz)/(1 + bT) \tag{3.7}$$

where k_0 is the measured conductivity at surface standard conditions (273.15 K and 10^5 Pa), and c and b are two parameters expressing the dependency on depth and pressure, respectively.

3.3.1.3. Sub-continental lithospheric mantle

Owing to the higher temperatures reached in the SCLM, the effect of heat transfer by means of black body radiation cannot be overseen. Along with the scarceness of direct samples (i.e. mantle xenoliths), this makes the estimation of thermal conductivity in the SCLM a difficult task, requiring a refined modelling of the behaviour of the lattice of each mineral phase under mantle conditions (Hofmeister, 1999). While there is consensus on the reliability of the relationship between the tectonothermal age of the crust and the composition of the underlying lithospheric mantle (Afonso et al., 2008; Griffin et al., 2009), estimating the mineral assemblage given the pressure and temperature conditions requires an adequate thermodynamic modelling (e.g Guerri et al., 2015), which is outside the scope of this work.

I thus assume a reference SCLM, defined by its thermal conductivity at surface conditions and a model of its temperature and pressure dependency. Thermal

conductivity at depth is influenced by the superposition of a lattice effect – directly proportional to pressure and inversely proportional to temperature– and a radiative contribution –directly proportional to temperature, i.e. $k = k_{lat}(P,T) + k_{rad}(T)$. I adopt the lattice thermal conductivity (k_{lat}) model by Xu et al. (2004), using the values provided for Olivine in the 4 to 10 GPa range:

$$k_{lat} = k_{298}\left(\frac{298}{T}\right)^{n}(1 + aP) \tag{3.8}$$

where T is temperature in K, k_{298} the lattice conductivity at 298 K (4.13 W m^{-1} K^{-1}), n an empirical fitting factor (0.5), a the pressure dependency factor (0.032 GPa^{-1}), and P pressure in GPa. I computed P as a purely lithostatic pressure, by utilising the same sediment model used in the gravity reduction, a reference crust density of 2670 kg m^{-3}, and the same lithospheric mantle density that I calculated in Eq. 3.2.

I account for the radiative component (k_{rad}) by adopting the model of Hasterok and Chapman (2011):

$$k_{rad} = \frac{1}{2}k_{rad}^{max}\left[1 + \mathrm{erf}\left(\frac{T - T_R}{\omega}\right)\right] \tag{3.9}$$

Here the parameters are: k_{rad}^{max} maximum radiative conductivity (0.345 W m^{-1} K^{-1}), T_R reference temperature (i.e. the temperature at which $0.5 \cdot k_{rad}^{max}$ is reached, 762 K), and a scaling factor ω (256 K). The error function is denoted with erf.

3.3.1.4. Temperature dependency of thermal conductivity

The temperature dependency of k introduces a non-linearity and is thus accounted for iteratively, using subsequent substitution (or "Picard's method", e.g. Hauck et al., 1999). The starting condition is a linear geotherm from surface temperature to 1200 °C LAB (Fischer et al., 2010). After three iterations (i.e. when calculating the thermal conductivity using the temperature output of the second iteration) the procedure converges to less than 1 K variations in temperature and less than 0.4 mW m^{-2} variations in surface heat flow. See section 1 of the Supplementary Material for a test on the behaviour of this method.

3.3.2. Iterative fit of heat generation

Lacking direct measurements of radioactive heat production (RHP) throughout the whole crust thickness, estimates commonly rely on compilations of compositional data, e.g. Vilà et al. (2010), Artemieva et al. (2017), Hasterok and Webb (2017), and Hasterok et al. (2017).

The depth-wise distribution of radioactive elements is poorly modelled by simple functions (Jaupart and Mareschal, 2003) and is difficult to constrain from indirect observables. A decay with depth at large scale is commonly expected, owing to the progressive depletion of the lowermost crustal terms. Still, this model is challenged by evidence of heat-producing element rich bodies in the lower crust (Alessio et al., 2018), which suggests reconsidering the role attributed to crustal-scale differentiation. I therefore resort to using one bulk heat production for the whole crystalline crust, using an initial value that I derive from the lithotype medians reported in Vilà et al. (2010) and the reference crustal column of Wedepohl (1995).

This initial value of bulk heat production is then fitted to the measured surface heat flow, in cells where it is available, using the following scheme. The misfit between the forward-modelled surface heat flow and the measured one (ΔQ_0) is divided by the crustal thickness ($z_{Moho} - z_{Sed}$), thus converting the heat flow misfit in a heat production per unit of volume value. I use this to guess a new bulk crustal heat production (A). For the nth iteration, in the crustal column identified by u, v grid position, this can be expressed as:

$$A_n^{u,v} = A_{n-1}^{u,v} + \Delta Q_0^{u,v} / (z_{Moho} - z_{Sed})^{u,v} \tag{3.10}$$

The resulting $A_n^{u,v}$ is then partitioned according to the upper to lower crust thickness ratio of Wedepohl (1995) column (thickness ratio upper to lower crust = 0.485). This method constitutes an iterative subsequent substitution scheme. It is similar to the strategy adopted by Čermák and Bodri (1986), where the unknown was the the heat flow at the base of the model. That method was subsequently referred to as a 'pseudo-inverse' technique (Čermák, 1993).

The RHP in cells where no surface heat flow measurements are available is filled in by interpolating the fitted RHP values, using a natural neighbour interpolation (Sibson, 1981). Undulations in crustal thickness are not accounted for when performing this interpolation.

Note that in a model with only one-dimensional heat conduction (along the vertical axis) and no temperature-conductivity dependence, this would lead to an exact solution in only one iteration. Horizontal heat conduction results in thermal gradient deviations around an hotter (more radioactive) crust, and the decrease in thermal conductivity for a larger temperature enhances this effect (for a synthetic example, see section 2 of the Supplementary Material).

The radioactive heat production in the solid matrix of sediments is fixed at $0.93\,\mu W\,m^{-3}$, from Vilà et al. (2010), and follows the same exponential compaction law of thermal conductivity. I set A in the lithospheric mantle to $0.02\,\mu W\,m^{-3}$ (Hasterok and Chapman, 2011).

3.3.3. Thermal model input data

3.3.3.1. Surface heat flow

I based this work on the data available in the Global Heat Flow Database of the International Heat Flow Commission, as available in the version maintained by Gosnold (2011). The raw records included 2780 points inside the study area (Fig. 3.10, A). I edited them by discarding samples with heat flow above 300 mW m^{-2} (5 points in the 2.5° buffer around the study area, no points inside the study area) and below 15 mW m^{-2} (23 points in the buffer, 3 points inside the study area). Due to the whole-crust scale of this work compared with the typical measurement depth (less than a kilometre), no depth correction was applied to the records. I also did not apply any correction for the paleoclimatic effect, which in the area has been estimated ranging from 0 to20 mW m^{-2} by Majorowicz and Wybraniec (2011).

I corrected the records for the sampling bias toward high heat flow spots (Mareschal and Jaupart, 2013) and the short-wavelength components that may arise from near-surface phenomena. First, the study area is divided in a graticule of 40×40 km grid step, in local projected coordinates (UTM35N), and the median surface heat flow for each cell is calculated. Then the heat flow grid, which is treated as node-registered array, is convolved with a raised cosine kernel (the same kind used in the Moho inversion algorithm), resulting in a low-pass filtered heat flow grid. The filter kernel was sized for a cut-off wavelength of 320 km, twice the cut-off applied to the Moho undulations.

The processed surface heat flow grid (shown in Fig. 3.10, B) constitutes the input of the iterative accommodation of bulk crustal heat production, as described in section 3.3.2.

3.3.3.2. Lithosphere-Asthenosphere Boundary

I extracted the bottom boundary condition, a 1200 °C LAB-isotherm, from the lithospheric thickness estimates provided in LITHO1.0 by Pasyanos et al. (2014), which are obtained from the inversion surface wave dispersion data. The points were interpolated to a regular grid with a bilinear 2D spline interpolator (Wessel, 2009), finding an approximate fit explaining 99.9% of the input data variance. The data and the interpolated extents are shown in Fig. 3.4.

The chosen temperature is an approximation arising from the thermal definition of the lithosphere: a thermal boundary layer, where heat transport is purely conductive, overlying a convecting mantle (Eaton et al., 2009; Fischer et al., 2010). This boundary temperature is therefore tied to a rheological definition, separating the mantle from the rigid lithospheric domain, where convection is not sustainable and tectonic plates move coherently (Steinberger and T. W.

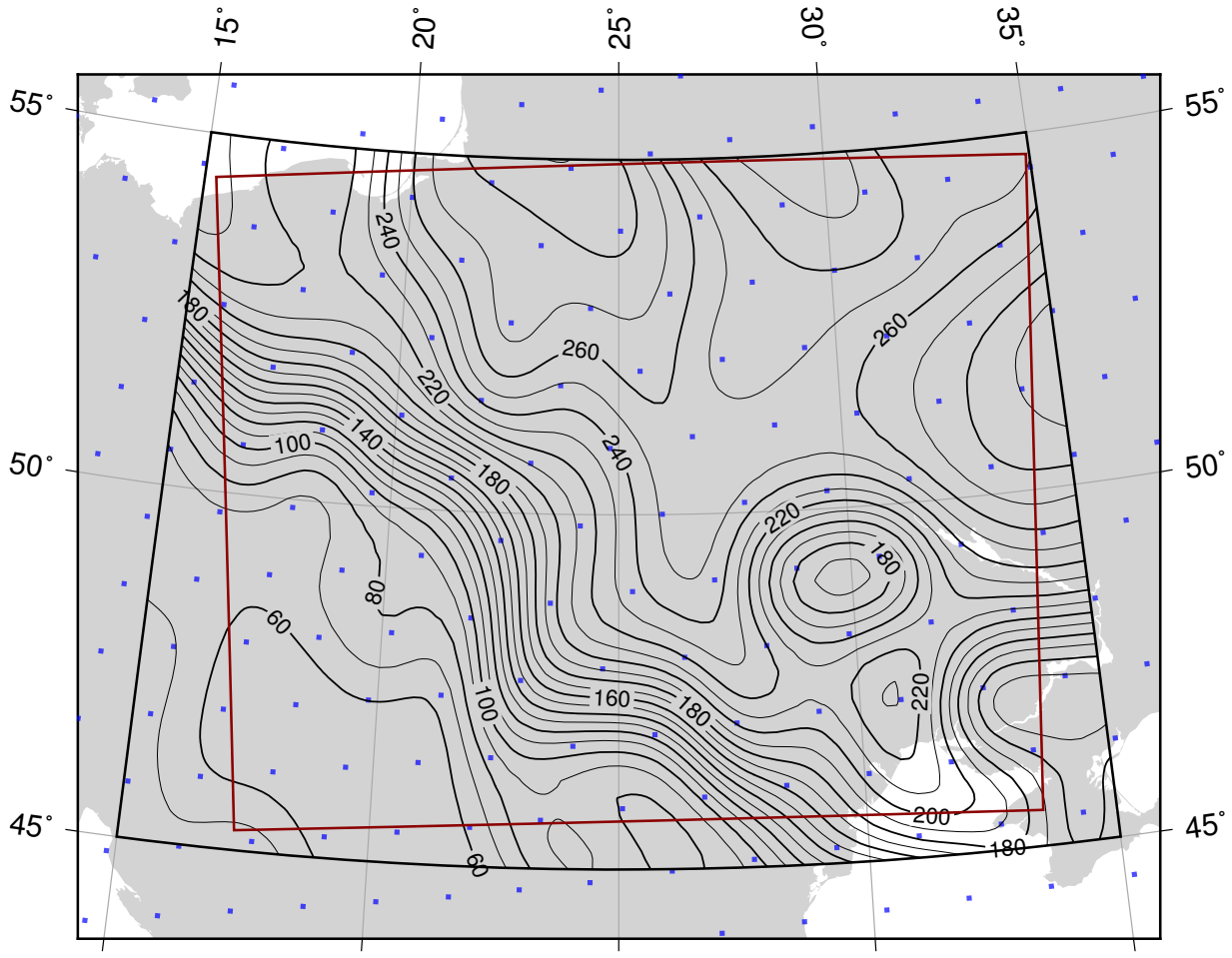

Figure 3.4.: Depth of lithosphere-asthenosphere boundary (LAB) in km, as provided in LITHO1.0 (Pasyanos et al., 2014). **Black polygon:** interpolation extents. **Red polygon:** extents of the thermal model. **Blue squares:** LITHO1.0 data nodes.

Becker, 2016). Common choices range from the mantle solidus temperature, which is pressure- and composition-dependent, to fractions of it, due to the evidence that even comparatively small melt percentages result in the seismic velocity drop associated with the LAB. The heat flow sensitivity to the chosen LAB temperature is small in respect to uncertainties in heat flow measurement or modelling – therefore, a thermal-LAB depth inverted from surface heat flow has an associated error in the order of tens of kilometres (Afonso et al., 2013a). When tested in the forward modelling setup, the difference in terms of Moho heat flow of a thermal-LAB temperature of 1300 °C versus 1200 °C is 1.44 mW m^{-2}, for the same 150 km deep LAB (Q_M of 17.05 and 15.61 mW m^{-2}, respectively).

Pasyanos et al. (2014) included prior information in their surface wave inversion, as a starting model which was then perturbated. This data includes "tectonic regions, crustal thickness from receiver functions and other information, upper mantle velocities from traveltime models, and thermotectonic information" (p. 2154, Pasyanos et al., 2014). I have preferred this model over other single-observable LAB models available in the area –e.g. receiver functions (Geissler et al., 2010), tomography inversion (Tesauro et al., 2009), seismic anisotropy (Plomerová and Babuška, 2010). A degree of dependence on prior data, including thermal models and Moho depth estimates, is unavoidable, since a common aspect of different techniques is requiring a correction for crustal effects (Jones et al., 2010). The adopted model provides a uniform coverage at an acceptable scale for the thermal footprint of LAB undulations, with a satisfactory resolving power of local features, such as the thin lithosphere underneath the Pannonian Basin (50 km).

3.4. Results of gravity reduction and inversion

3.4.1. Gravity reductions

Using the procedure described in section 3.2, I started from the gridded GOCE-GGM input signal shown in Fig. 3.5 A) and obtained a reduced signal, shown in Fig. 3.5 B), through subtraction of the effects of global topography (Fig. 3.3 A), far isostatic roots (Fig. 3.3 B), and sediments (Fig. 3.3 D). A histogram is plotted under each gravity signal map, its width coinciding with the colour-scale width. A continuous normal distribution, computed using the mean and standard deviation of the plotted data, is overlaid on each histogram. These two plots serve as a qualitative indicator of the signal distribution, while the quantitative statistics are shown in Tab. 3.2.

The cumulative effect of the reductions shifted the gravity signal towards

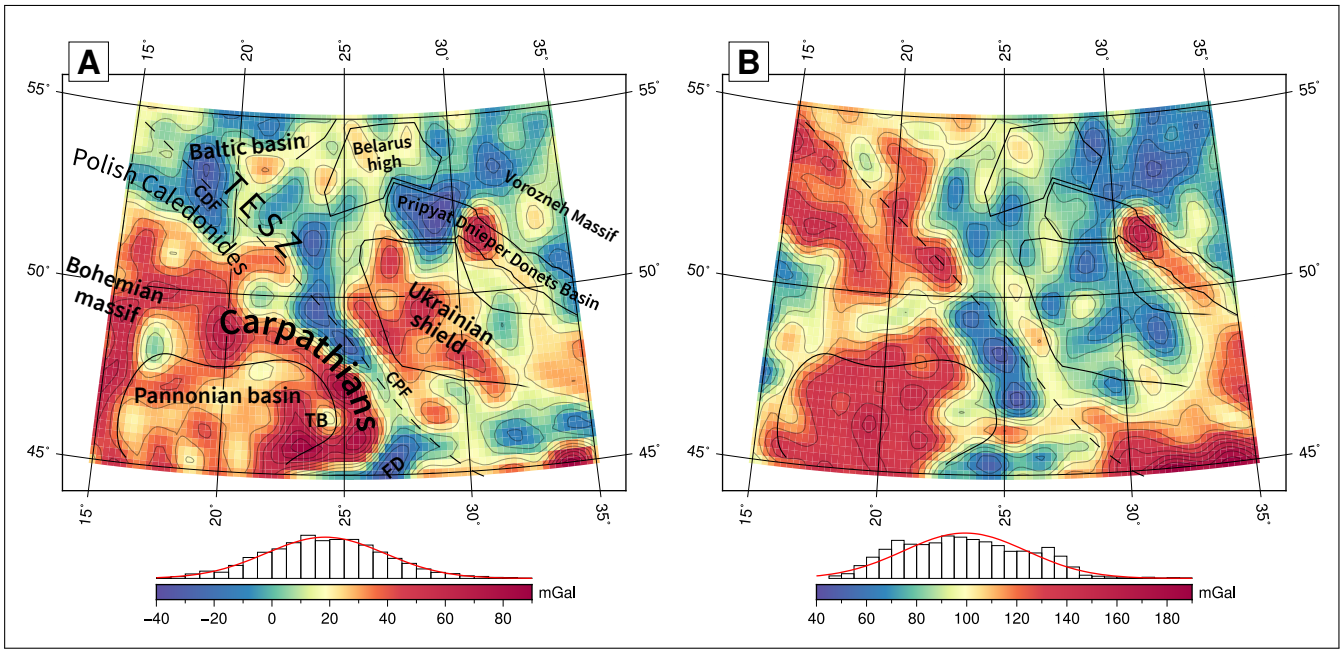

Figure 3.5.: Input and processed gravity data. **A)** Gravity disturbance, computed from the global gravity model GO_CONS_GCF_2_TIM_r5, at 8 km over GRS80. **B)** Sediment-reduced Bouguer anomaly, obtained by subtracting the topography, isostatic and sediment reductions from the GGM gravity disturbance. Grid cells are shown on a 15' by 15' grid, without interpolation. 1 mGal = 10^{-5} m s^{-2}.

Table 3.2.: Descriptive statistics of the input gravity signal, of its reductions, and of the inversion results (Moho depth and gravity residuals). GD: gravity disturbance, from the global gravity model. LPF: raised cosine low-pass filter, applied during the inversion algorithm.

		Min	Max	Mean	Median	St. Dev.
Input data						
GD, unprocessed	mGal	-38.0	87.6	18.5	18.1	20.6
Topographic effect	mGal	-121.5	19.6	-80.4	-85.4	20.7
Isostatic effect	mGal	53.6	69.0	62.4	62.8	—
Sediments thickness	km	0	16.3	3.1	2.6	2.6
Sediments effect	mGal	-104.5	-24.1	-62.8	-65.0	19.7
GD, reduced	mGal	46.77	186.6	99.3	98.8	24.6
GD, reduced, mean removed	mGal	-52.5	87.3	0	-1.2	24.6
Inversion results						
Inverted Moho depth (no LPF)	km	23.2	81.5	44.2	43.7	4.9
Inverted Moho depth (160 km LPF)	km	34.2	51.7	44.2	44.0	2.6
Residuals (no LPF)	mGal	-1.8	1.7	0.0	0.0	0.2
Residuals (160 km LPF)	mGal	-19.6	17.2	0.1	0.2	5.2

positive values, resulting in a 80.8 mGal increase of the average value. The global topography effect (Fig. 3.3 A) is negative over most of the study area, except the most central parts of large high topography areas: the Carpathians (centre-south of the study area), the Bohemian massif, and the easternmost portion of the Alps, at the western edge of the study area. The average topography in the area, from the EARTH2014 model at full resolution, is 220 m. It ranges from –113 m (small northern portion of the Black Sea, sampled on the southern edge) to 2109 m (Mt. Moldoveanu, SE Carpathians).

The crustal root effect outside of the study area ('isostatic effect', Fig. 3.3 B) is dominated by a east-west negative gradient, ranging from 68 to 54 mGal over a 20 degrees longitude range. The north-south gradient is negligible. A more complex velocity conversion method, based on thermodynamic modelling (Connolly, 2005), is presented and utilised in chapter 2. When adopted here, the results range from from 72 to 90 mGal (a 18 mGal range, compared to the 14 mGal range of the correction computed here).

The sediment thickness (Fig. 3.3 C) ranges from zero to 16.3 km, with an average of 3.1 km. The western half of the area is characterised by thick sedimentary covers: between the Caledonides Foredeep and the Baltic Basin (NW corner, 11 km maximum), and along the Carpathians Foredeep, up to the very deep, but localised, Focşani Depression (16.3 km maximum). The Pripyat-Dnieper-

Donets basin lies in the north-eastern part of the area. Basement depth reaches a maximum of 5 km there. The forward-modelled sediments effect, reaches a maximum of -102 mGal using the aforementioned compaction parameters. The depth-dependent exponential decay of compaction implies that the highest sensitivity of the gravity effect occurs in the first 6–8 km of thickness, where both the basement depth and the density modelling are critical, with the variance in the latter dominating the gravity signal (Kaban et al., 2010).

The gravity footprint of masses at distance is such that the minimum sediment effect value is −24.7 mGal, instead of zero, even over areas with little to no sedimentary cover.

I assumed a uniform sediment compaction model and a set of depth-dependence parameters which, albeit a realistic compromise, does not reflect the exact characteristics of any of the basins in the study area. This unmodelled variability is a source of uncertainty, which is usually addressed with integration with local well data, where available. The depth-density curve that Kaban et al. (2010) provide for the Pannonian Basin is defined by $\phi_0 = 0.4$ and $p = 2.375$ km, while the parameter used here are $\phi_0 = 0.5$ and $p = 4$ km. Their (Kaban et al., 2010) curve describes sediments which are less porous at the surface and that compacted faster with increasing depth. This means that for the same sediment thickness, a smaller gravity correction is obtained.

The sediment correction computed over the entire study area with those parameters is on average 22.8 mGal smaller, up to a maximum of 48.8 mGal, over the absolute maximum of sediment thickness, the aforementioned Focşani Depression. The standard deviation of the difference is 9.4 mGal. Over the Pannonian Basin (about 5.2 km of sediments), the correction using Kaban et al. (2010) parameters is 33 mGal smaller. Therefore, the inverted crustal thickness using Kaban et al. (2010) compaction model is consistently thicker, on average by 842 m. Resorting again to the Pannonian Basin as a benchmark, the estimate with those parameters is up to 2.4 km thicker. In absolute terms, this means that the adopted compaction model results in a 39.0 km Moho there, while their *basin-specific* one results in 41.2 km –even the less compacted model that I adopted is not enough to fully explain the Pannonian Basin thinning sensed by other crustal models, as it is discussed afterwards (section 3.4.3).

3.4.2. Moho estimate

The left map of Fig. 3.6 shows the input data for the inversion routine. The dataset was obtained by removing the mean value of the reduced gravity signal and projecting it on a local UTM grid. Removing the mean value complies with the fact that the reference depth is equal to the expected Moho average depth. This way I interpret the reduced input gravity signal as due to deviations of the

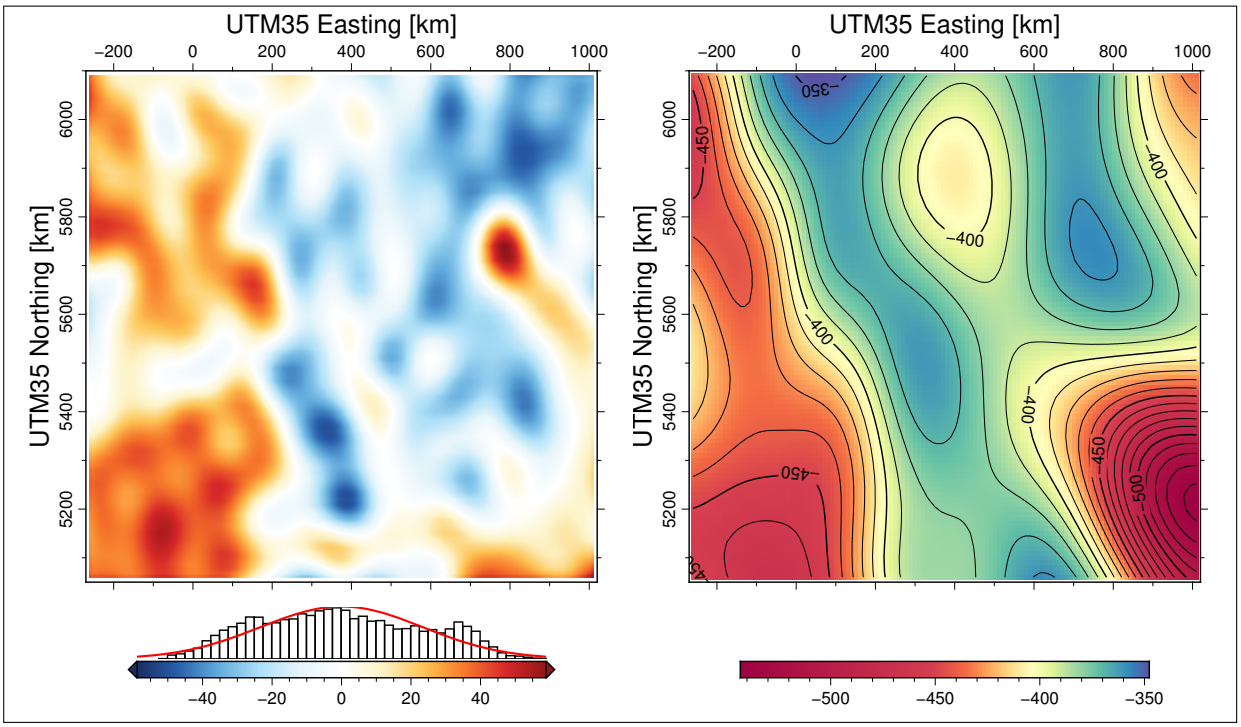

Figure 3.6.: Inversion input, projected to a 10 by 10 km UTM35N grid. **Left:** Inversion input gravity signal, in mGal. **Right:** Moho density contrast (kg m^{-3}) used in inversion, derived from LITHO1.0 (Pasyanos et al., 2014) and the linear V_P to SCLM density relationship by Yegorova and Pavlenkova (2015).

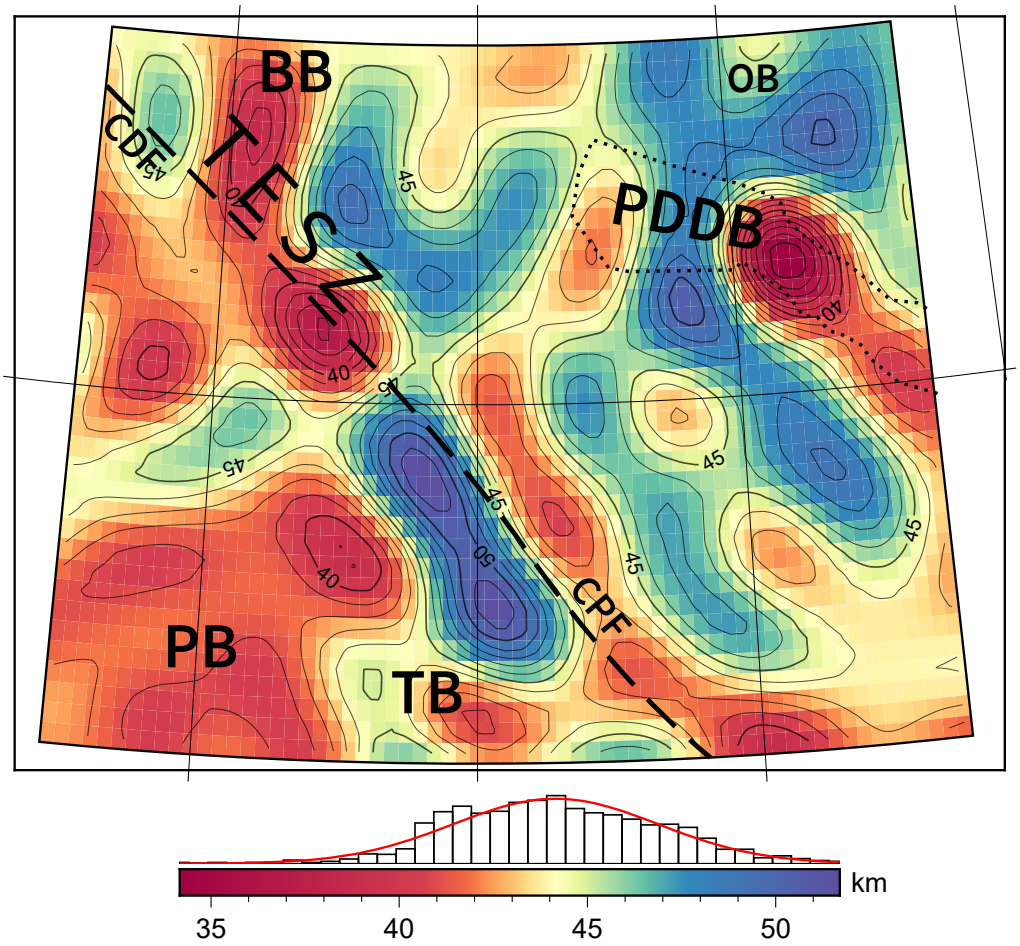

Figure 3.7.: Moho depth as obtained from the inversion, contour interval 1 km. Some of the geological features of Fig. 3.1 are shown: **TESZ** Trans-European Suture Zone, **CDF** Caledonides Foredeep, **CPF** Carpathians Foredeep, **TB** Transylvania Basin, **PB** Pannonian Basin, **PDDB** Pripyat-Dnieper-Donets basin, **BB** Baltic Basin.

crust-mantle interface from its average value in the study area. The inversion result, re-projected to WGS84 coordinates, is shown in Fig. 3.7. Loss of edges occurs due to convergence of meridians, since the projection to the UTM grid is cropped to a rectangular domain (the extents are compared in Fig. 3.2, area B and C). The 160 km low-pass filter results in residuals (i.e. the difference between the input gravity signal and the forward-modelled signal of the Moho estimate) ranging from -19.6 to 17.2 mGal, shown in Fig. 3.8. As shown in the statistics of Tab. 3.2, the residuals are negligible when no Moho low-pass filter is applied. This comes at a cost for the Moho estimate morphology, which exhibits local spikes of up to 23.2 km (minimum depth) and 81.5 km (maximum depth) before filtering. The final RMS misfit at the 10^{th} iteration of the inversion algorithm is of 4.96 and 0.24 mGal with and without low-pass filtering, respectively.

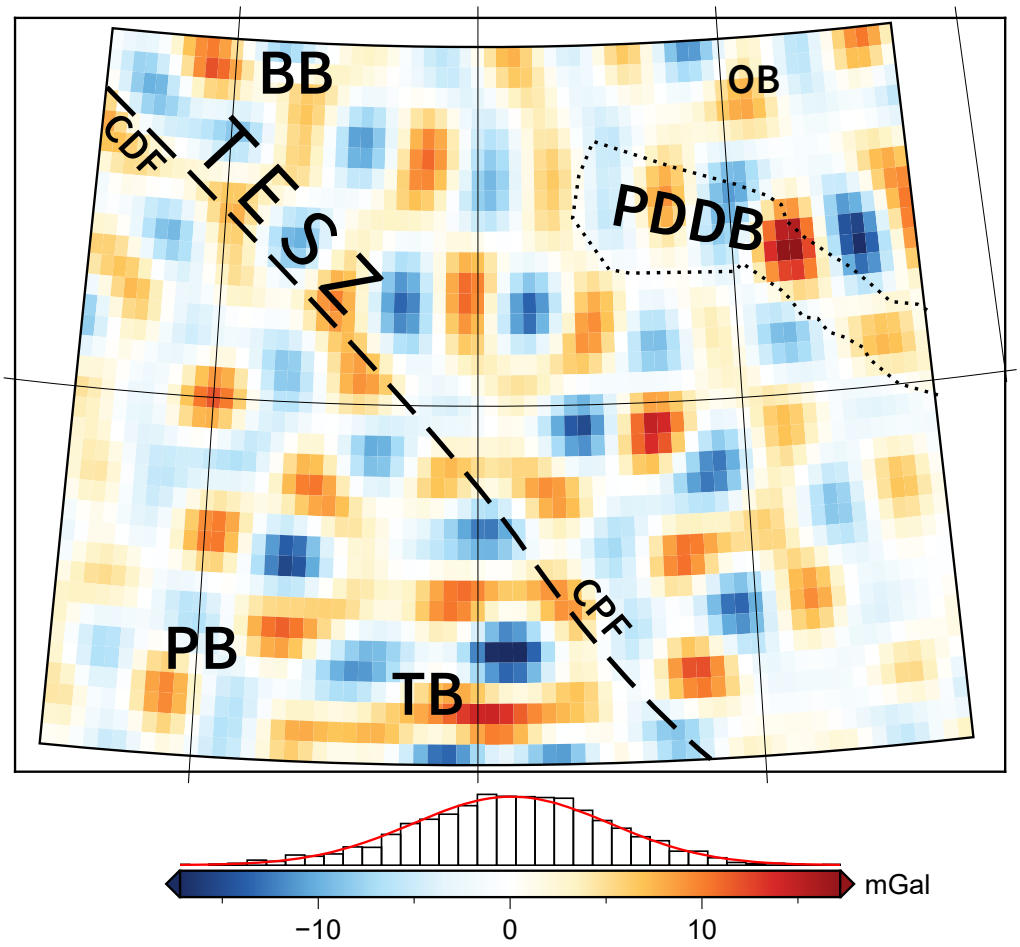

Figure 3.8.: Inversion residuals: input gravity signal minus forward-modelled Moho undulation effect. Labelled features: see Fig. 3.7.

The Moho estimate that I obtained from inversion exhibits a thickening under the East Carpathians up to 51.7 km and up to 46.4 km under their north-west portion. The two sectors are interrupted by a relatively shallow saddle (44.2 km) at 49 °N 22 °E.

A dominant north-west to south-east lineament is observed in the whole area, parallel to the TESZ. This could be discerned already in the input data, even before integration with the LITHO1.0 density contrast, which too shows a sharp NW-SE gradient across the suture zone.

Crustal thinning in the Caledonides Foredeep (CDF) and the Baltic Basin (BB), in the north-west sector of the area, reaches 38.0 km. Underneath the longitudinally central part of the Pripyat-Dnieper-Donets Basin (PDDB), the Moho rises up to 34.2 km locally. This thinning coincides with the Chernigov High, attributed to lower crustal mafic intrusions (Starostenko et al., 2018). Relatively thin crust (not exceeding 41.1 km) persists eastwards of this local minimum, following the basin shape. It is interrupted westwards, instead, by a 48 km thick lineament orthogonal to the basin longitudinal axis.

I observe a thin crust under the Pannonian Basin (PB, south-west corner of the study area), never exceeding 41.8 km and reaching a local minimum of 38.9 km at 48 °N 22.75 °E.

3.4.3. Comparisons and critical aspects

I adopt three different crustal models as benchmarks for the inverted Moho depth estimate: the European Moho depth by Grad et al. (2009), the global GOCE-based model GEMMA by Reguzzoni and Sampietro (2015), and the global lithospheric model LITHO1.0 by Pasyanos et al. (2014), which is based on surface wave dispersion. While the existence of completely independent models is unlikely, I expect a satisfyingly low degree of inter-dependence between these three, since they are based on different observables and strategies. These models and the differences from this chapter estimate are shown in the maps of Fig. 3.9. The difference is expressed as the depth estimate of this work minus the compared Moho.

The Moho depth by Grad et al. (2009) is the result of a large compilation of data from different methods (seismic reflection and refraction, receiver functions, tomography, joint seismic–gravity inversion), which where harmonised using relative weights. The model is accompanied by an uncertainty map, obtained from error estimates provided with data or from method-dependent assumptions, when the former were not available. It is the highest resolution model among these three.

The model by Reguzzoni and Sampietro (2015), a global estimate of crustal thickness (and associated uncertainty), is based on data from GOCE, albeit with a

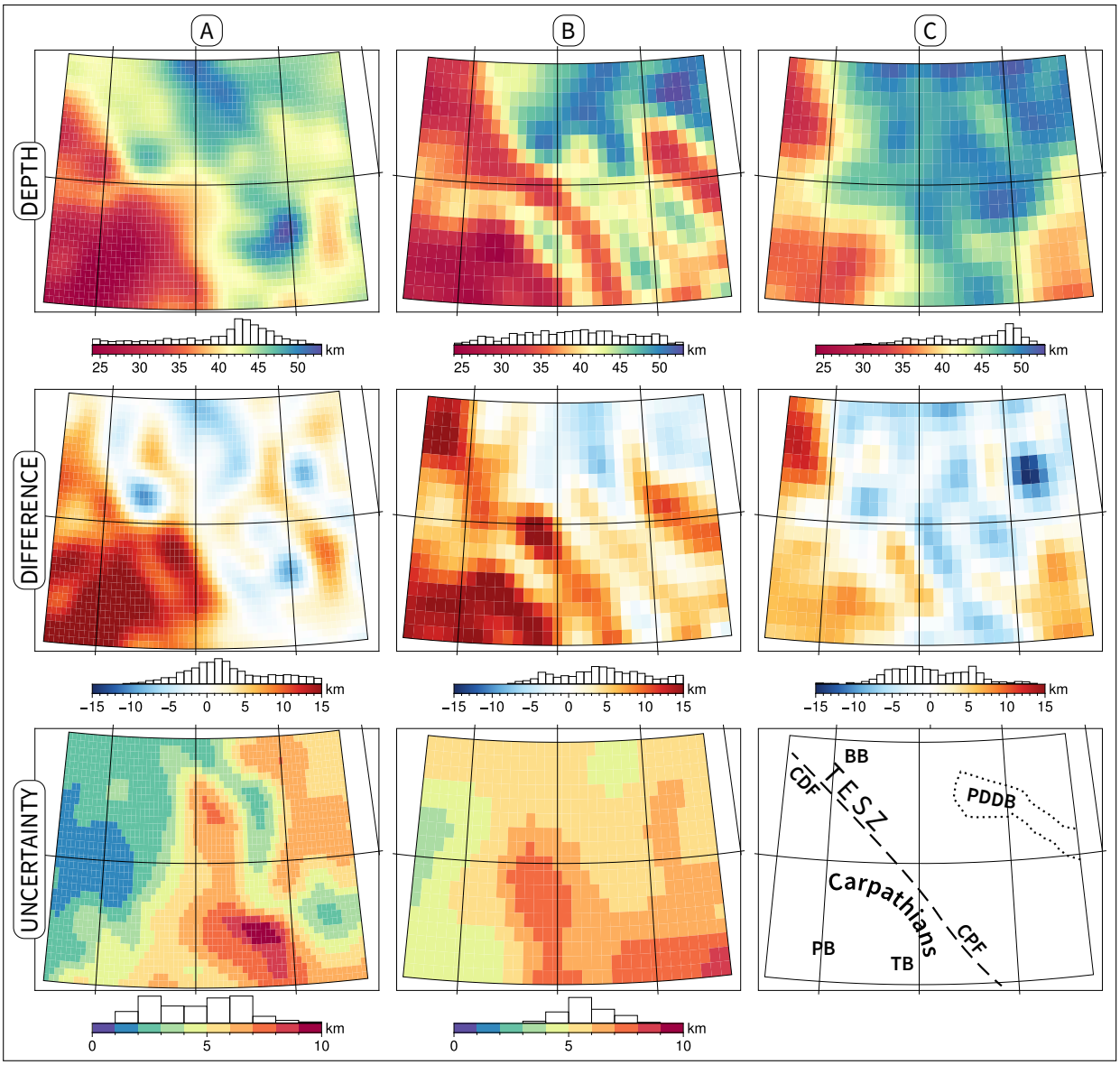

Figure 3.9.: Comparisons with three selected crustal models: **A)** European Moho depth by Grad et al. (2009), **B)** GEMMA GOCE-based global Moho by Reguzzoni and Sampietro (2015), **C)** LITHO1.0 global surface-wave-dispersion model by Pasyanos et al. (2014). First row: Moho depths. Second row: differences, expressed as the inverted depth estimate minus the compared Moho. Third row: uncertainty estimates (not available for LITHO1.0 depths). Lower-right corner: geological features, see Fig. 3.7.

Table 3.3.: Statistics of differences between the inverted Moho depth estimate and the three benchmarks. This chapter estimate minus the compared Moho depth, expressed in km.

Crustal model	Min	Max	Mean	Median	St. Dev.
A) Grad et al. (2009)	-10.1	18.3	3.7	2.4	6.2
B) Reguzzoni and Sampietro (2015)	-7.7	17.4	5.0	4.7	5.7
C) Pasyanos et al. (2014)	-14.6	13.1	0.1	0.6	4.9

different strategy from the one used here, including a novel inversion algorithm. It is by design highly independent from seismic data ('weakly constrained'), requiring only at least $M + 1$ a-priori Moho depths for an Earth divided in M geological provinces.

I have already mentioned and utilised the LITHO1.0 (Pasyanos et al., 2014) model in this chapter procedure: in the gravity reduction phase to compute a global crustal root effect ('isostatic effect') and in the inversion, where it provided the reference depth (average Moho depth in the study area) and the starting $\Delta\rho$ map. For these reasons, care must be taken in interpreting the comparison: e.g. the average difference is almost zero due to the chosen average reference depth.

I performed each comparison by downsampling the higher resolution grid to the lower resolution one, between the model obtained in this work and the compared one. Therefore, the Moho by Grad et al. (2009), which is provided on a 0.1° grid, was downsampled to my 0.25° grid; the Moho by Reguzzoni and Sampietro (2015), provided on a 0.5° grid was left as is and I downsampled my Moho to 0.5°. The comparison with LITHO1.0 was also performed on a 0.5° grid, due to the non-rectangular tessellation of its original 1 arc-degree spaced global grid.

I summarise the difference range, mean, median, and standard deviation in Tab. 3.3. The mean difference is directly controlled by the inversion reference depth parameter. It is positive (i.e. my inverted Moho is deeper) for both Grad et al. (2009) and Reguzzoni and Sampietro (2015) models, by 3.7 and 5.0 km respectively. This partly explains the consistently positive difference over the areas of thin crust. The distribution of differences against the three models is never symmetric: the difference between mean and median indicates a positive skew for Grad et al. (2009) and Reguzzoni and Sampietro (2015) and a negative skew against the Moho of Pasyanos et al. (2014).

In terms of geological structures, the Moho depth I obtained uniformly underestimates the crustal thinning under the Pannonian basin: in the three compared models it reaches a minimum thickness ranging from 25 to 35 km, while mine

stops at 39 km. Such a discrepancy may be explained by an insufficient correction for the sedimentary infill (which would require an even less compacted depth-density model, as discussed before) or by the complex Moho structure in extensional settings (e.g. due to underplating, see O'Reilly and Griffin, 2013), which is resolved differently by seismic methods.

The thickened root of the Carpathians is not resolved in the Moho by Grad et al. (2009), while it is present in my model and in the ones by Reguzzoni and Sampietro (2015) and Pasyanos et al. (2014). Its absence in the seismic model could be an artefact of locally poor coverage, a strong point for adopting gravity-derived models even in relatively well-surveyed areas.

I observe a thin NW-SE lineament, from the centre of the study area towards the lower half, in the GEMMA model (**B**), which is not resolved by the other models. It is also resolved by my model, and corresponds to a similar lineament in the GOCE data, then enhanced by the sediment correction. There is a 5 to 10 km positive misfit between GEMMA and my model, along this lineament. I speculate it may be originated by the different sediment reduction models, which the authors also applied before inversion. A thinner crust may result from a larger estimate (in thickness and/or in density) of the effect of the infill of the Carpathians Foredeep.

The misfits are uniformly less over the NE portion of the study area, roughly corresponding to the Russian Platform. The sensibly thinner crust of the Pripyat-Dnieper-Donets rift is resolved only by the GEMMA model, while it is fainter in the Moho by Grad et al. (2009). The thermal model also resolves that, albeit with the aforementioned underestimation of thinning. The discrepancy with GEMMA can be attributed to their use of geological provinces, through a variable density scale factor for each one. Such a strategy allows to accommodate the sharp differences in Moho contrast of different tectonic regimes, albeit with the added issues of depending on surface data.

Some small-scale Moho undulations in the Russian Platform are resolved by the Moho obtained here and the first two compared models, albeit with different magnitude. They are not present in the LITHO1.0 Moho and are the source of the large localised negative misfits (up to -15 km). The absence of such small features (about 1 arc-degree across) can be attributed to the lower resolution of LITHO1.0.

The misfit with the other models arises due to the unaccounted density variations throughout the crust, which bias the inversion results, and from density variations in the mantle that I am not separating from the crustal contribution. The former, the intra-crustal masses, can be partly addressed with data integration, where available: it is the case of the sediment stripping reduction I computed and applied. This can prevent some of the larger systematic errors, such as estimating a thick crust to fit the negative anomaly caused by the low-

density infill of a basin. Still, the choice of a-priori parameters, such as a general compaction model, does not take into account the large variance of geological heterogeneity. This can range from different compaction curves due to different basin histories P. A. Allen and J. R. Allen (2013), to salt structures (which do not follow ordinary depth-dependence curves), to circumstances which would require more detailed models (e.g uplifted and eroded sedimentary formations, resulting in outcropping rocks with negligible porosity).

The latter, the 'mantle effect', cannot be reliably separated by spectral means (e.g. by truncating the lowest spherical harmonic degrees of the GGM), since large near-surface structures and mantle contributions often overlap (Kaban et al., 2004). A viable option is computing a density distribution from a mantle model of velocity anomalies (e.g. Kuhn and Featherstone, 2005), which is the strategy adopted by Reguzzoni and Sampietro (2015), who used the GyPSuM model (Simmons et al., 2010). I have chosen to not perform such kind of reduction, owing to the additional uncertainties involved and on its temperature dependency. I have taken into account only the lateral variation of the lithospheric mantle density, which I included in the 'isostatic correction' to calculate a global Moho contrast (see Eq. 3.1 and 3.2).

3.5. Thermal modelling results

3.5.1. Heat flow data

The filtered and gridded surface heat flow measurements (shown in Fig. 3.10, B) highlight two distinct thermal regimes, which after filtering are distributed in a 80 mW m^{-2} wide range. There is a south-west to north-east gradient across the TESZ lineament, albeit complicated by small wavelength variations. The cells with highest values are clustered in the Pannonian Basin, where considerable variance is observed (70 to 105 mW m^{-2}). The lower-than-average heat flow cells in the Russian Platform include a superimposed local maximum (54.9 mW m^{-2}) coinciding with part of the Pripyat-Dnieper-Donets rift. Note that this also coincides with a spot of thin crust (up to 35 km).

Block-median gridding and low pass filtering decreased the standard deviation from 23.6 to 17.81 mW m^{-2}. The average of the raw samples is 57.1 mW m^{-2}, it becomes 54.8 mW m^{-2} after processing. Processed surface heat flow in the grid cells range from 26.2 to 98.0 mW m^{-2}. For comparison, the global average continental surface heat flow is estimated at 64 mW m^{-2}, as concordantly found with different strategies by J. H. Davies and D. R. Davies (2010) and Pollack et al. (1993). No-data cells cover 58% of the study area.

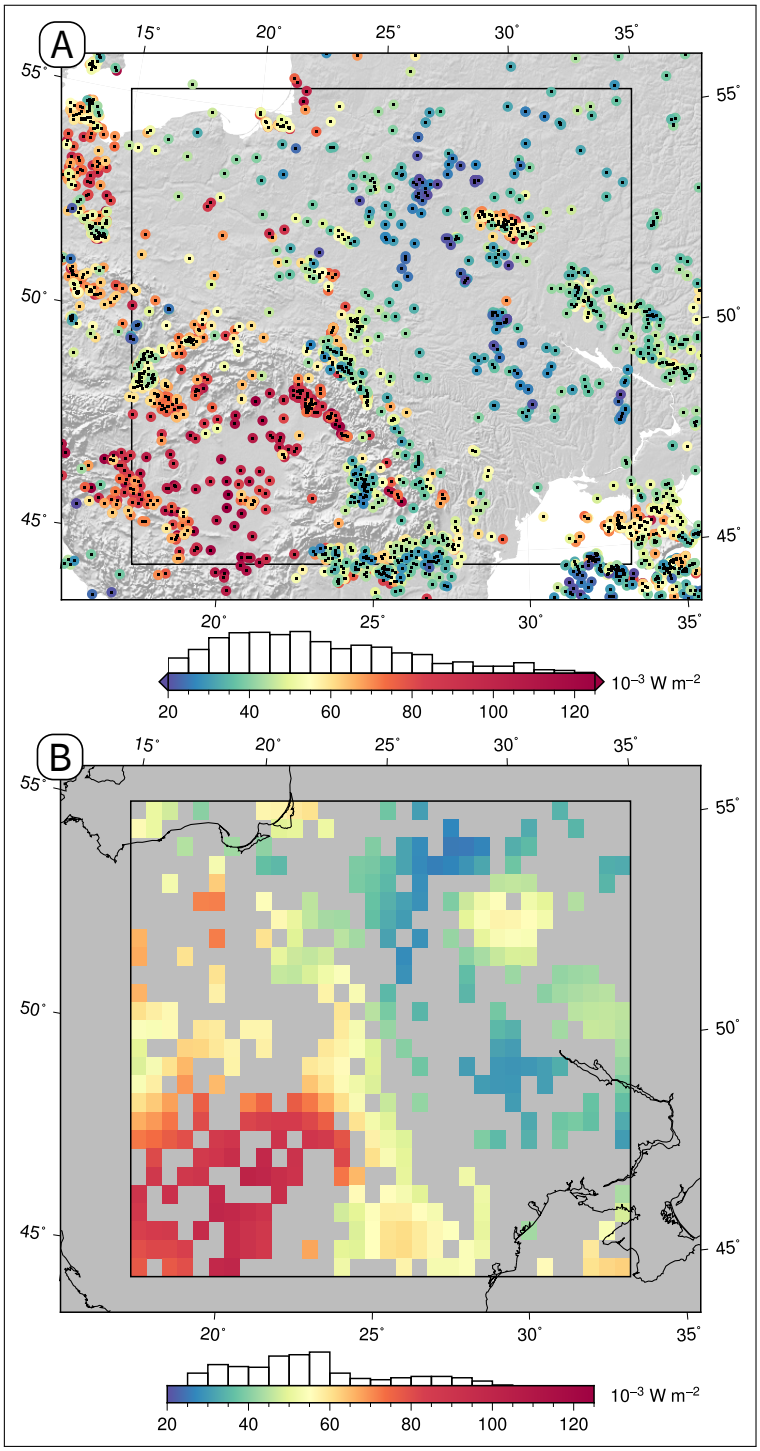

Figure 3.10.: A): surface heat flow sample points, from Gosnold (2011). The histogram counts only the points inside the study area (inner rectangle). Note that there is considerable overlap in the most sampled spots, this is partly conveyed by the overlayed black dots. **B)**: the processed surface heat flow grid, after block-median and raised cosine low-pass filtering of the sample points.

3.5.2. Iterative forward modelling output

The top row of Fig. 3.11 shows the output after the first iteration of the thermal model ('first guess', as described in section 3.3.2). The surface heat flow misfit between the forward model (left map, $Q_{0,\text{first}}$) and the measurements is shown in the central map ($\Delta Q_{0,\text{first}}$). The average misfit is -7.5 mW m^{-2}, with a standard deviation of 13.7 mW m^{-2}. Those results indicate how the crust thickness alone can explain only a limited part of the variance in the observed heat flow, confirming a common finding (e.g. Jaupart et al., 2016). The first-guess was run with a laterally uniform crustal heat production per unit of volume of 1.04 µW m^{-3}, partitioned between the upper crust (1.74 µW m^{-3}) and the lower crust (0.37 µW m^{-3}). The right map ($Q_{0,\text{first}}$) shows the crustal heat flow contribution, expressed as the difference between the heat flow at the base of the sediments layer and the heat flow at the crust-mantle boundary. At this stage, it is directly proportional to crustal thickness.

The bottom row of Fig. 3.11 shows the same variables of the first row, at the sixth crustal RHP fitting iteration. The same colour scale is adopted. Here practically all the signal in the surface heat flow is modelled, leaving a mean misfit of 0.005 mW m^{-2} (standard deviation 0.038 mW m^{-2}). The converging behaviour of RMS misfit over the six iterations is shown in the top plot of Fig. 3.12: it decreased from 13.0 mW m^{-2} to 0.03 mW m^{-2}. The trend of the distribution of fitting heat production is shown in the bottom plot of the same figure. While the median value of heat production is reduced by of 0.26 µW m^{-3} from start to end, the fitted values are distributed between 0.18 to 2.18 µW m^{-3} (minimum to maximum) after the last iteration. The width of their distribution appears directly connected to the decreasing misfit shown in the top plot. The map on the right in Fig. 3.13 shows the fitted heat production values, for each crustal column. Their distribution is skewed toward low values, resembling the empirically observed asymmetrical distribution of rock heat production values (Vilà et al., 2010; Artemieva et al., 2017; Hasterok and Webb, 2017), which has been modelled with a log-normal distribution sometimes (e.g. Jokinen and Kukkonen, 1999; Huang et al., 2013).

The spatial distribution of crustal heat production shows a first-order correlation with surface heat flow. This is a direct consequence of fitting all the variance not arising from the thickness of the crust and lithosphere with heat production, as I have shown before. Still, deviations from a pure correlation between heat flow and heat production arise from the contribution of crustal thickness, as can be seen by comparing the crustal heat flow contribution, in the right map of Fig. 3.11, against the thickness of the crystalline crust (left map of Fig. 3.13). I resort to the cross-plots of Fig. 3.14 to better show this.

The line overlain to scatter plots **A** to **C** represents the results of the first

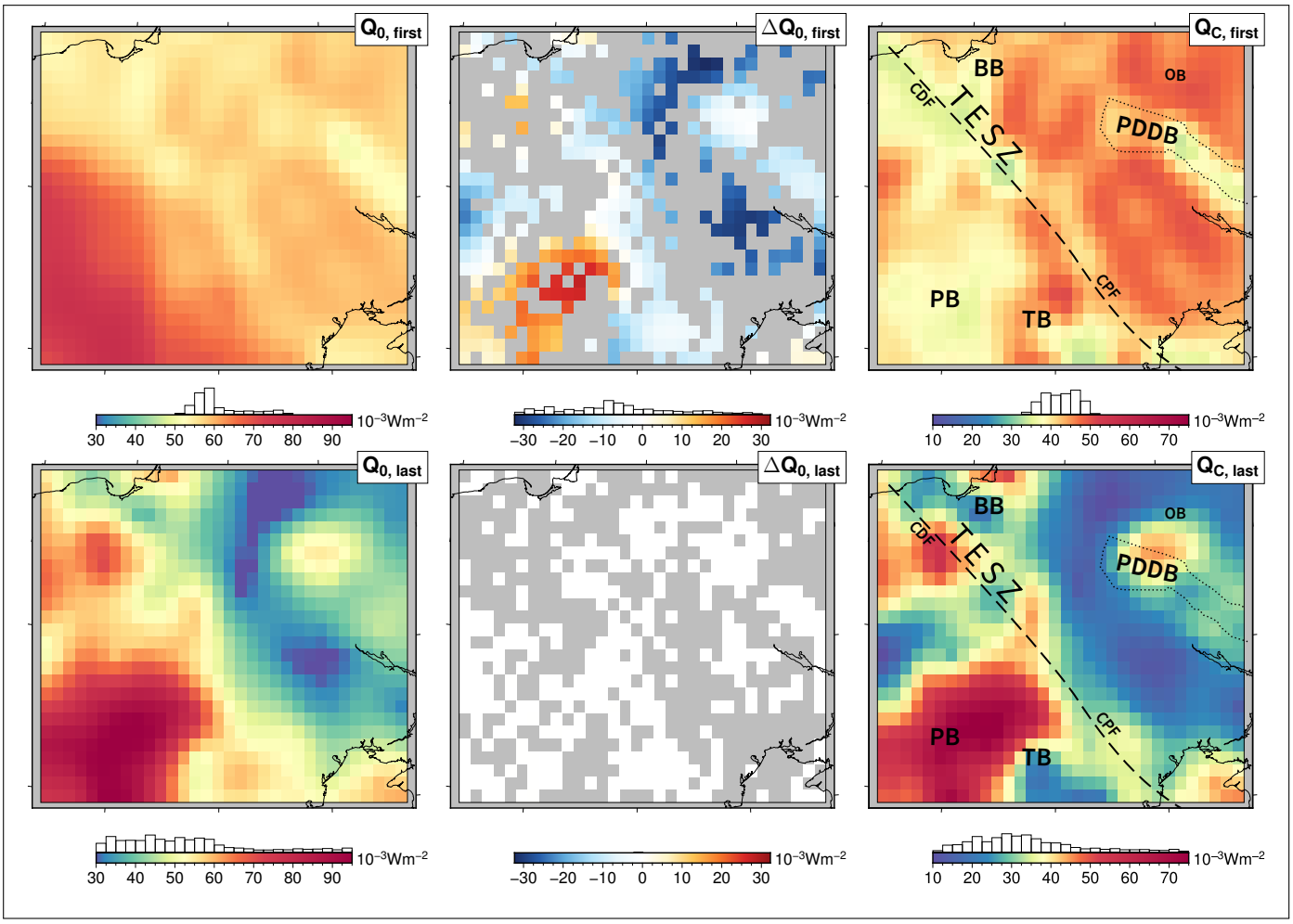

Figure 3.11.: Results of the iterative fit on the thermal model, in terms of surface heat flow. **Top row:** first iteration, only a-priori crustal heat production. **Bottom row:** last iteration. **Left column:** surface heat flow; **middle column:** misfit between heat flow measurements and forward-modelled heat flow; **right column:** crustal (radiogenic) component of surface heat flow.

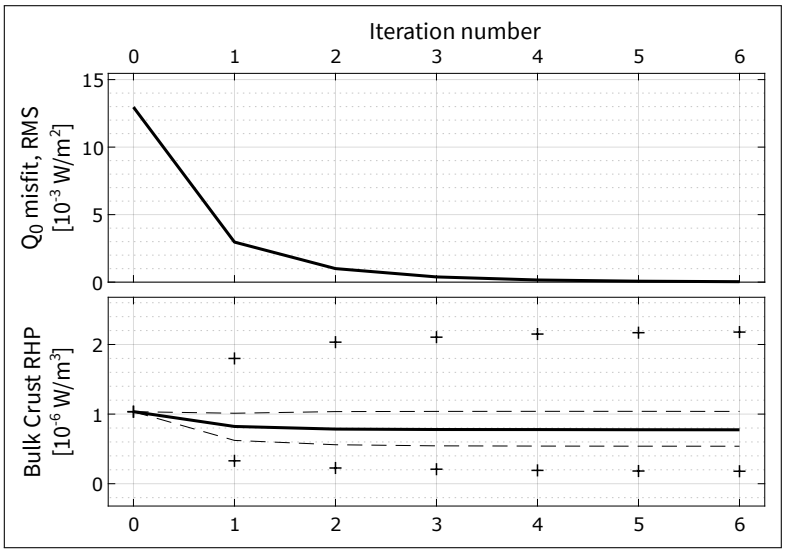

Figure 3.12.: Behaviour of the subsequent substitution fitting procedure in 6 iterations, plus the first guess. RMS surface heat flow misfit (**top**) and radiogenic heat production in the upper crust (per unit of volume, **bottom**). The tick line denotes the median, the two dashed lines the first and third quartiles, respectively, the crosses minimum and maximum values.

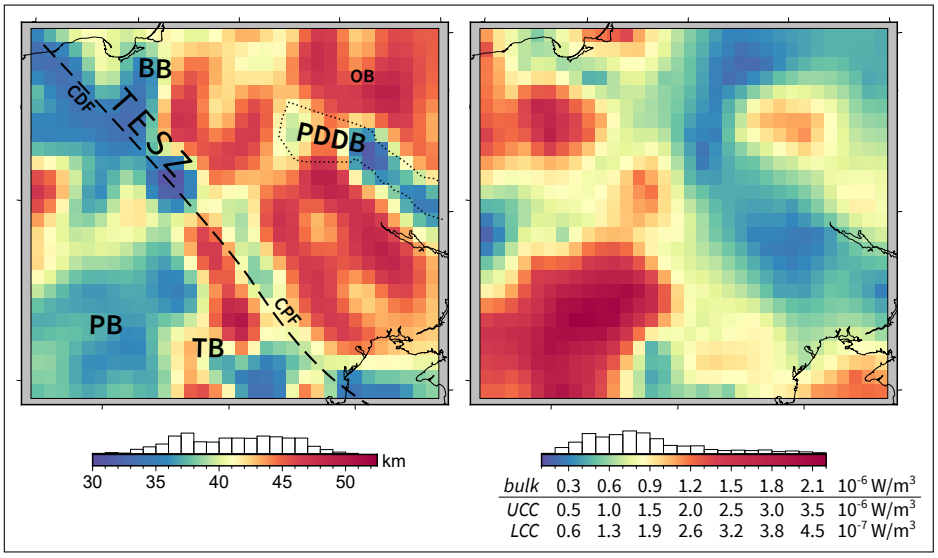

Figure 3.13.: Fitted radiogenic heat production (RHP) in the crystalline crust, per unit of volume. **Left:** thickness of crystalline crust: Moho depth minus sediment basement depth; **right:** RHP: bulk and partitioned to upper and lower crystalline crust (note that the lower crust RHP unit is one order of magnitude smaller). Geographical labels: see Fig. 3.7.

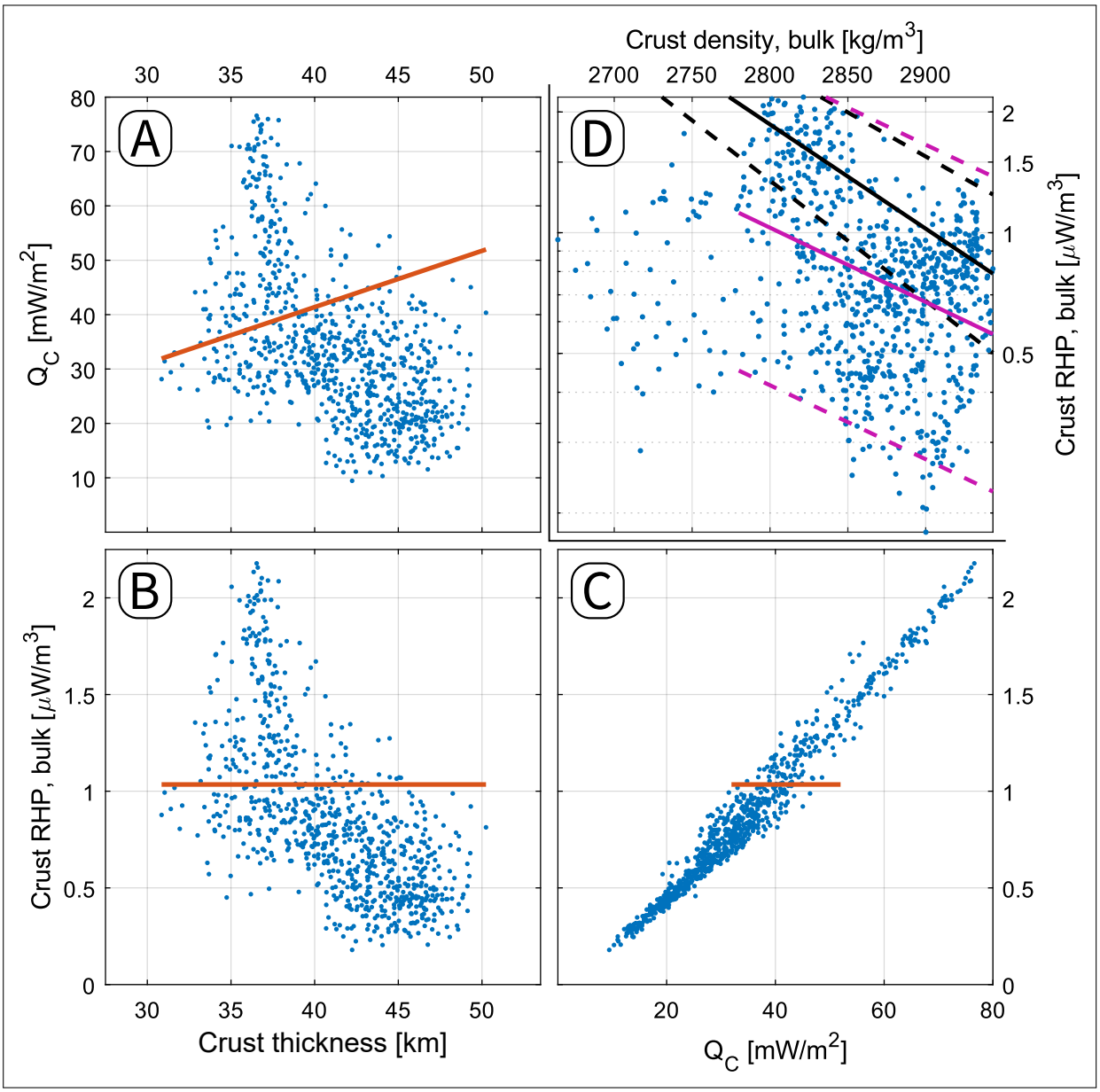

Figure 3.14.: Cross plots between thickness of the crystalline crust (Moho depth minus basement depth), radioactive heat production (RHP) of the bulk crystalline crust, crustal component of heat flow (Q_C), and crust density. The line overlaid on scatter plots **A)** to **C)** represents the first guess, using the a-priori constant RHP. Plot **D)**: bulk density of the crystalline crust plotted against the radioactive heat production (RHP). The density-heat production relationship by Hasterok and Webb (2017) is plotted in black. The fit with this chapter data is plotted in purple. Dashed lines depict upper and lower confidence bounds.

guess, in a perfect crustal thickness to crustal heat flow relationship, with no lateral variations in RHP. Two distinct behaviours of departure from the first guess line can be observed: the first, a cluster which has most of its points confined between 35 and 40 km of thickness, increased its RHP value with respect to the first guess. It corresponds to those heat flow values found in the extensional basins, as shown in the maps of Fig. 3.11. The other, which involves the remainder of points, is considerably scattered along a trend of inverse proportionality between crustal thickness and RHP, opposite to the first guess. This weak negative relationship is a common finding of studies on relationships between heat flow and crustal thickness (Čermák, 1993; Mareschal and Jaupart, 2013).

As described before, the RHP fill-in method presented here relies on the interpolation of fitted RHP, which is available in cells where surface heat flow measurements are available, over cells where there are none. I assumed that A, the RHP per unit of volume, is uncorrelated to crustal thickness. Therefore, the interpolation does not take into account Moho undulations. As shown in plot **B)** of the crossplots figure (Fig. 3.14), I observe a negative proportionality between Moho depth and fitted RHP. This a-posteriori observation suggest that a correlation between the two exist and could be exploited to further constraint the RHP fill-in. Nevertheless, it should be interpreted with caution. There is an issue with the attribution of heat flow misfit to crustal or mantle sources, which I address in the next section.

In Fig. 3.14 **D** I plotted the fitted RHP of this work against the bulk density of LITHO1.0 (Pasyanos et al., 2014) crystalline crust, computed by thickness-weighted averaging of the three crustal layers. I did so in order to compare my result to the density to heat production relationship provided by Hasterok and Webb (2017): $\log_{10} A = -0.0027(\rho - 2700) + 0.53$ (plotted in black). In contrast to my indirect estimates, their results are based on geochemical data of more than 100,000 samples. I perfomed a log-linear fit to the fitted RHP data, obtaining the following relationship, plotted in purple:

$$\log_{10} A = -0.0019(\rho - 2700) + 0.20 \tag{3.11}$$

The 2σ confidence interval of this fit is -0.0022 to -0.0015 $(\log_{10} \mu W/m^3)(kg/m^3)^{-1}$ for the slope and 0.14 to 0.26 $\mu W\,m^{-3}$ for the intercept. R^2 is 0.1274. I excluded the nodes with a bulk density lower than 2780 $kg\,m^{-3}$, since they are underrepresented in the study area (less than 7% of total nodes, clustered in the southeast corner). A negative relationship between density and RHP can be observed –it can be attributed to the increased content in heat producing elements in less dense, more felsic rocks (Hasterok and Webb, 2017). The two fits, albeit different, overlap in their uncertainty interval. A

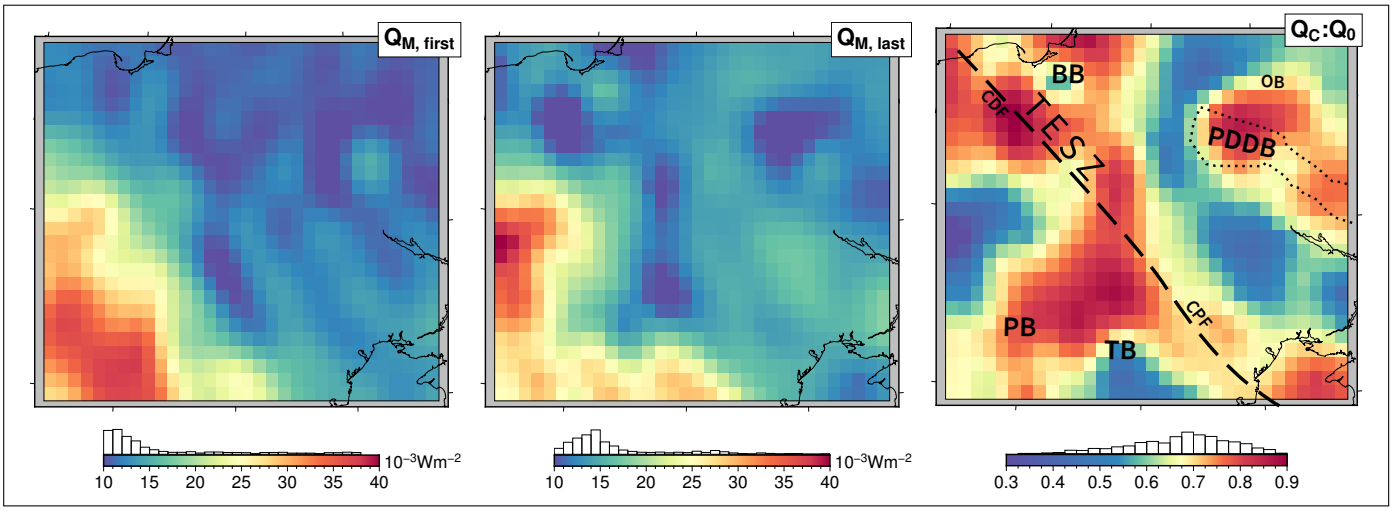

Figure 3.15.: Basal heat flow (Q_M), at the crust-mantle boundary. **Left:** Q_M at the first iteration (a-priori parameters); **middle:** Q_M at the last iteration; **right:** partition coefficient, expressed as the ratio between crustal component of heat flow (Q_C) and the total surface heat flow (Q_0), at the last iteration.

version of the scatter plots of Fig. 3.14 in which a colour scale is used to depict each node density, and a map of the bulk density of the crystalline crust in the study area are provided in the appendix (section 3.B, Fig. 3.34).

I also compared this fitted-RHP estimate with the V_P to heat production conversion provided in Hasterok and Webb (2017), using their log-linear relationship for the continental crust ($\log_{10} A = -0.70(V_P - 6) + 0.48$). Due to the relationship between density and V_P, the pattern is similar to what I just discussed concerning density. A similar trend of negative correlation is observed, with the the results presented here shifted toward lower values: $\log_{10} A = -0.56(V_P - 6) + 0.19$. The geochemistry-based linear fit and the one that I obtained by linear regression on the inverted data again overlap in their 2σ uncertainty interval. The V_P-converted RHP is consistently higher than my estimate over the whole area (mean $+0.42\,\mu W\,m^{-3}$, with a local maximum of $+1.84\,\mu W\,m^{-3}$ in the southeastern corner of the area (local cluster with V_P less than $6.2\,km\,s^{-1}$. The inverted RHP estimate (i.e. constrained by crustal thickness, surface heat flow and thermal modelling) is higher than the V_P-converted one only in the Pannonian Basin (difference of up to $-0.59\,\mu W\,m^{-3}$). A figure with a scatter plot of V_P and RHP, accompanying maps and further details on the log-linear fit to my data are provided in the appendix material (section 3.B).

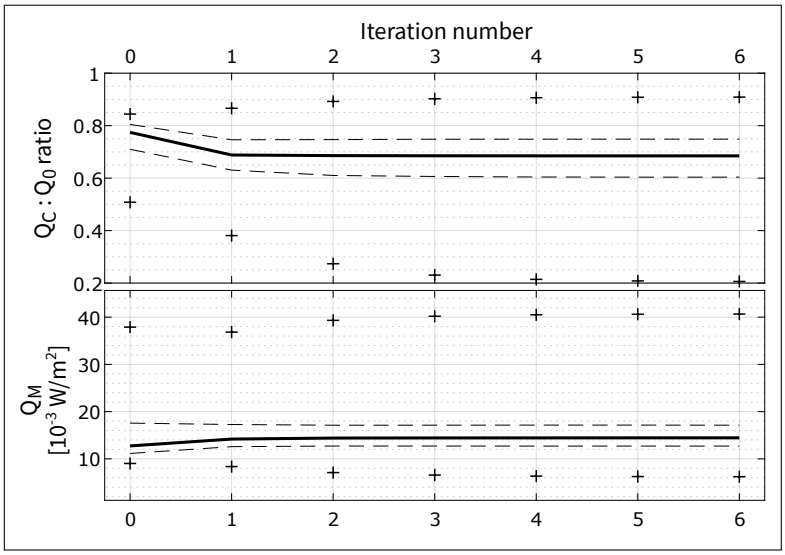

Figure 3.16.: Top: ratio of the crustal heat flow component (Q_C) against the surface heat flow (Q_0), as shown in the right map of Fig 3.15. **Bottom:** heat flow at the crust-mantle boundary (Q_M). The distribution statistics at each iteration are plotted with different symbols. For a legend, refer to the caption of Fig. 3.12.

3.5.3. Partitioning of heat flow between crust and mantle sources

Since the strategy presented here is based on the assumption that all the surface heat flow misfit can be attributed to omitted crustal heat production, I analyse what this implies for the partition between the crustal contribution (Q_C) and the basal, mantle-borne, heat flow component (Q_M, Fig. 3.15). This has also been referred to as 'partition coefficient'. Hasterok and Gard (2016) expressed it as the basal to surface heat flow ratio. Here I have adopted the crustal to surface heat flow ratio ($Q_C : Q_0$) as a partition metric. I also define the basal heat flow as the heat flow through the crust-mantle boundary, since I am including lateral variations of heat production in the lower crust. A larger ratio indicates a thermal regime dominated by crustal heat production.

The top plot of Fig. 3.16 shows how this partition varies through the iterations: the largest variation occurs between the first guess (iteration zero) and iteration one, where the median $Q_C : Q_0$ drops by 8.6 points percent. No significant variation in the median occurs between iteration 1 and 6. The range between the extreme values (denoted with 'plus' signs) and the inter-quartile range (between the first and thirt quartile, plotted with dashed lines) widen, with a trend that flattens after iteration 4.

The bottom plot of Fig. 3.16 represents the trend of Q_M, which appears anticorrelated with the $Q_C : Q_0$ ratio. This behaviour stems from the suppression of basal heat flow that is observed for an increase in crustal heat production.

Basal heat flow, for a fixed radiogenic Q_C, would be only controlled by the depth of the LAB-isotherm and the series thermal resistance of the LAB-to-surface path. A steeper geotherm (i.e. a warmer crust) decreases the thermal conductivity of the crust (see Eq. 3.7 here and Chapman, 1986), resulting in a lower Q_M for the same LAB depth. In addition, thermal refraction is observed around an hotter crustal body, since the steepest temperature path is not along vertical any more (for synthetic examples, see sections 2 and 3 provided in the Supplementary Material).

This implies that whenever a positive misfit in Q_0 (i.e. not enough crustal heat production) is fitted for, Q_M in the same model column will decrease in the subsequent forward modelling iteration. This will result in a positive misfit again, albeit smaller. The opposite happens for a negative misfit, whenever the forward modelled surface heat flow is higher than the observed.

Plotting the evolution of Q_M on a map (Fig. 3.15) provides further information on the spatial distribution of this variation, and its relationship with geology. The left map (iteration zero, labelled $Q_{M,first}$) shows a thermal regime which is strongly controlled by the LAB morphology (Fig. 3.4): the warmer and thinner south-west European Phanerozoic lithosphere and the colder, thicker, platform across the suture zone. The local effect of overlying crustal structures can be already seen, superimposed. The middle map (sixth iteration, labelled $Q_{M,last}$) highlights where the starting situation was conserved and where it was reversed. By comparing it with the iteration zero misfit map of Fig. 3.11 (middle top row), it can be seen how the strongest transitions from high to low Q_M and vice versa are clustered on the areas of largest misfit. This reversal can be thus attributed to the inverse dependence mechanism described before.

Overall, the local extremes in Q_C, and their accompanying minimums in Q_M should be interpreted with caution: comparison with the geological settings suggests that they may be a symptom of over-estimation of the $Q_C : Q_0$ ratio, when the source of increased heat flow should be attributed to others factors, instead. This is most evident in the Pannonian Basin and, to a lesser extent, in the Pripyat-Dnieper-Donets basin and in the Caledonides Foredeep. This can be attributed to the persistence of non-stationary heat transport. The Pannonian Basin is expected to have significant departures from thermal equilibrium. I obtain a rough order of magnitude estimate with the end of its rifting phase, around 14 Ma (Horváth et al., 2015) and the characteristic time scale for reaching quasi-steady state conditions, as defined in (Stüwe, 2007). The $l^2/2\kappa$ rule, as provided in Stüwe (2007), with l length scale and κ thermal diffusivity, results in a time scale for reaching equilibrium on the order of 10^2 My for a 10^8 m length scale (lithospheric thickness).

Note how spots of localised thinning of the crystalline crust (see Fig. 3.13, left) result in enhanced Q_m, persisting through the iterations: this is the result of

higher effective thermal conductivity of the LAB-to-surface path, since thermal conductivity is lower in the crust than in the lithospheric mantle. It is a phenomenon similar to the blanketing and chimney effects observed by Przybycin et al. (2015) for variations in sediment thickness.

3.5.4. AA' section

In Fig. 3.17 a 2D slice under the AA' profile is plotted (shown in the geological setting map, Fig. 3.1). It encompasses the different thermal regimes encountered across the study area, which are dominated by the aforementioned southwest-to-northeast transition to older and colder lithosphere.

The effect of the crust, including sediments, is superimposed on the signal from lithospheric thickness. The thermal conductivity section shows the effect of thermal dependence of k and its role in controlling Q_M. The portions of hotter crust and lithosphere (e.g. the SW portion of the section) are accompanied by a strong reduction in k in the upper crust and in the lithospheric mantle. The lower crust sees the concurrent effect of the temperature-driven decrease of k —a dependence which is an order of magnitude weaker than in the upper crust, in the adopted Chapman (1986) model— and increase of k due to rising pressure. The total effect is a slight increase in conductivity with depth, in concordance with the data shown in Chapman (1986). This depth-wise trend is clearly represented for 4 sample columns in the middle plot of Fig. 3.18. I must emphasize how this outcome is strongly dependent on the reliability of the assumed temperature-conductivity relationships, therefore it should be interpreted only in conjunction with other temperature proxies (e.g. xenoliths, Curie depth, effective elastic thickness).

Thick sedimentary covers (Pannonian basin, Carpathians foredeep: columns *i* and *ii*, plotted in blue and orange respectively) further contribute in the reduction of the total thermal conductivity of the lithosphere, attenuating the effect of LAB undulations. Q_M exhibits a relative maximum across the Ukrainian shield (column *iii*, plotted in green), albeit being over a very thick lithosphere. There, a combination of thin sedimentary cover, a cold crystalline crust, and a relatively cold lithospheric mantle (note the depression in isotherms in plot **d**) result in a more conductive lithosphere overall.

3.5.5. Sensitivity of the result to crustal thickness

In Fig. 3.19 I present the comparison of the results obtained with a flat Moho (44 km, i.e. the average of the inverted Moho depth estimate) and a synthetic 'checkerboard Moho'. The latter alternates between 40 and 48 km of thickness, on 120 by 120 km tiles. I plotted the difference between fitted RHP, basal heat

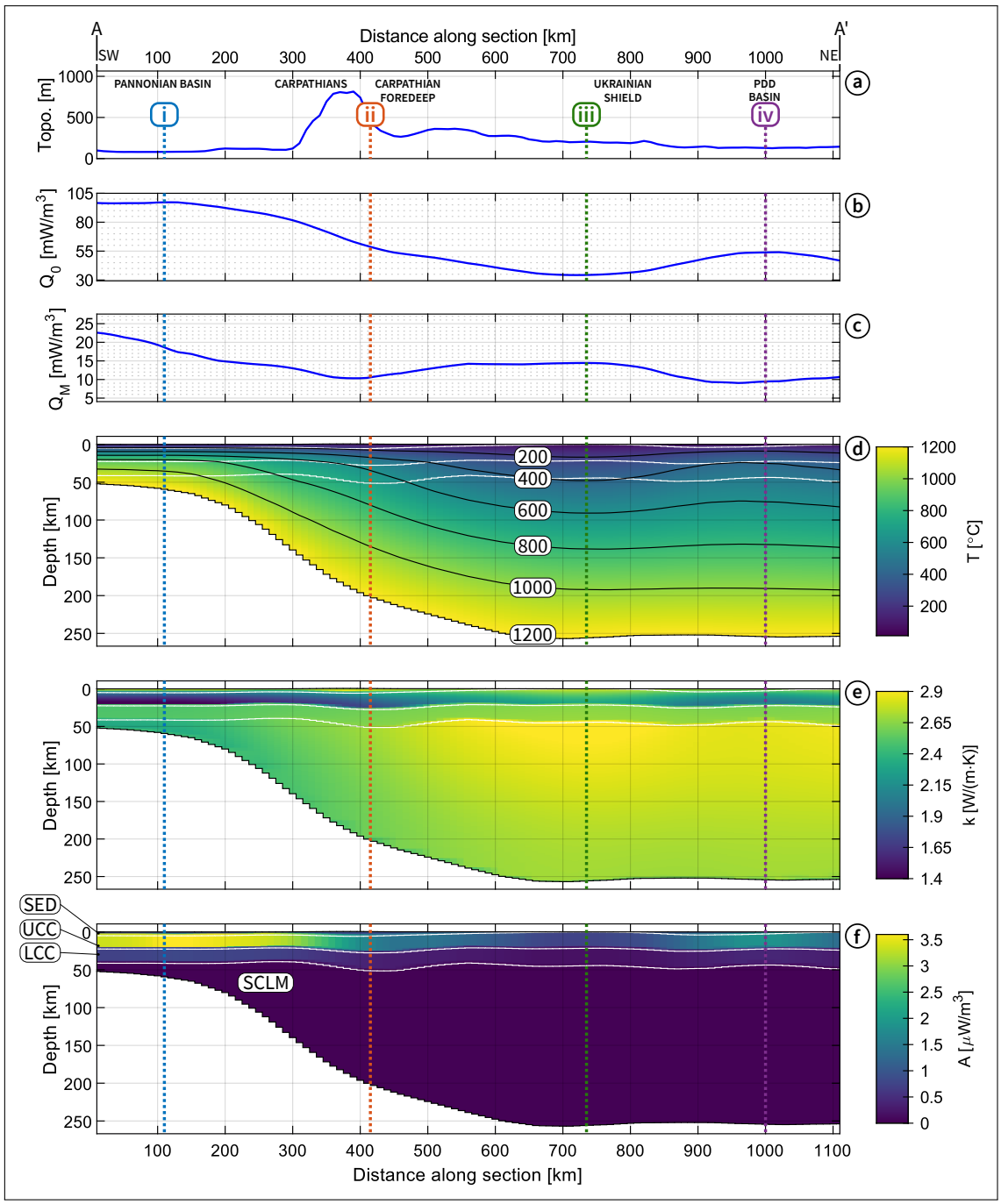

Figure 3.17.: Thermal model section *AA'* (extents are shown in Fig. 3.1). **a)** topographic profile. **b)** Q_0, surface heat flow profile **c)** Q_M, Moho heat flow profile. **d)** temperature slice. **e)** thermal conductivity slice. **f)** radiogenic heat production slice. Layer boundaries are shown in white and labelled on the left side of the bottom slice. Abbrevations: **PDD** Pripyat-Dnieper-Donets basin, **SED** sediments, **UCC** upper crystalline crust, **LCC** lower crystalline crust, **SCLM** sub-continental lithospheric mantle.

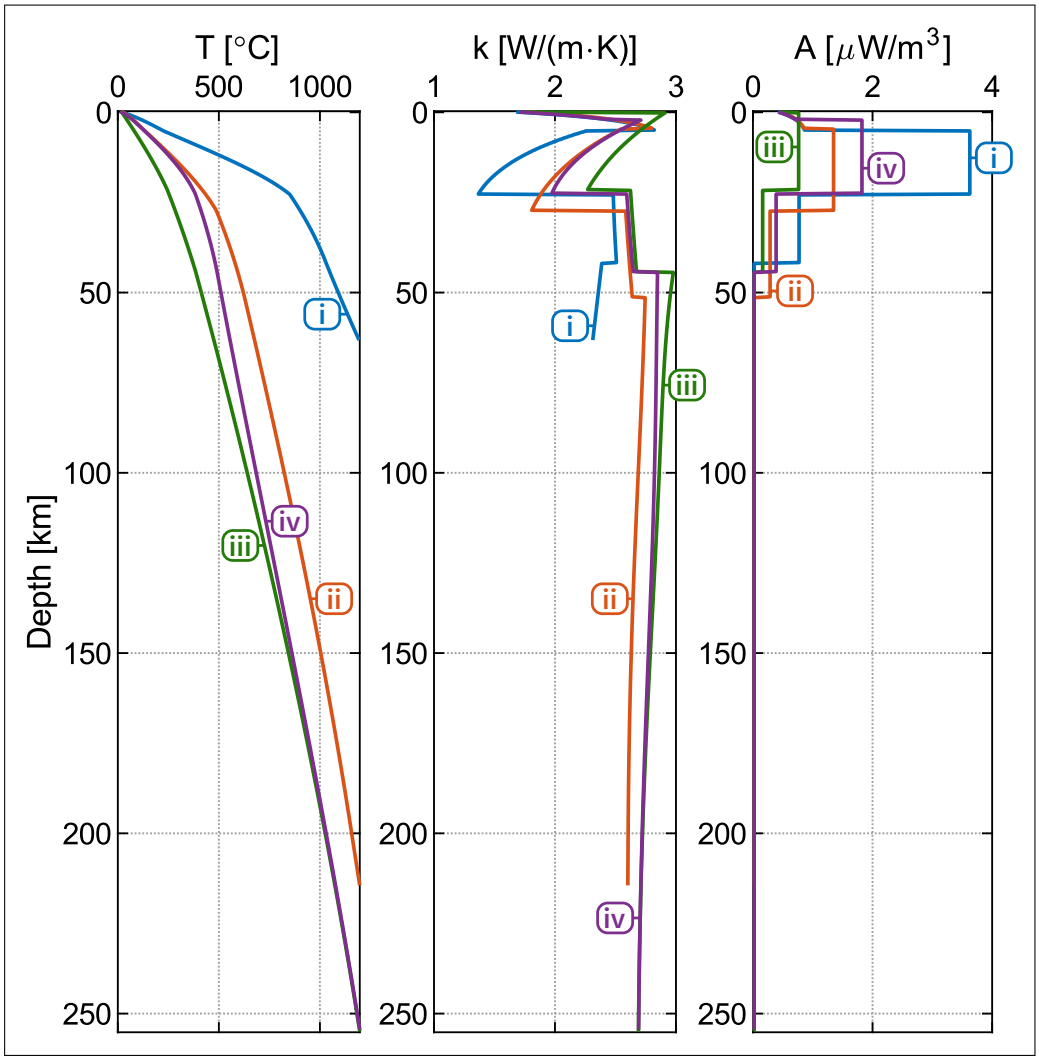

Figure 3.18.: Plots of temperature, thermal conductivity and heat production in four columns of section AA' (Fig. 3.17). Colours and roman numerals refer to the corresponding labels in the section figure. **i)** Pannonian Basin, **ii)** Carpathians, **iii)** Ukrainian Shield, **iv)** Pripyat-Dnieper-Donets Basin.

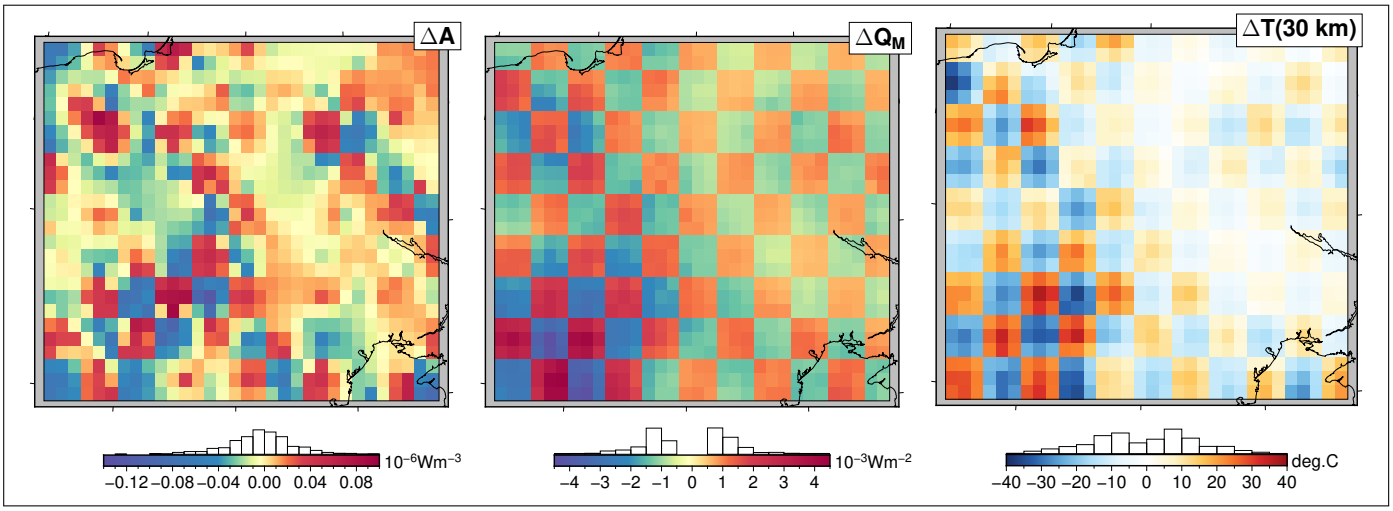

Figure 3.19.: Checkerboard Moho test. Differences in bulk crustal RHP (ΔA), basal heat flow (ΔQ_M), and temperature at 30 km depth ($\Delta T(30\,\text{km})$) are expressed as flat Moho (44 km) minus checkerboard Moho (40 to 48 km, 120 km square tiles). The south-west checkerboard tile is a thin tile (40 km).

flow, and temperature at 30 km. The difference is expressed as the value obtained with the flat-Moho model minus the value obtained with the checkerboard-Moho one, i.e. positive values indicate larger results in the latter. As a reference for the alternating pattern, the south-west corner is a thin tile (40 km thick crust).

The differences in fitted RHP (ΔA, left map of Fig. 3.19) are at most one order of magnitude smaller than the range of variation in RHP observed in the model (Fig. 3.13). In the majority of cases, a difference of $\pm 0.04\,\mu\text{W m}^{-3}$ in RHP per unit of volume is enough to compensate a ±4 km variation in crustal thickness. The RHP increases (negative difference) for a thinner crust. The sensitivity of RHP fitting with respect to the Moho model seems low –this is an expected consequence of all the non crust-correlated RHP variance that I had fitted for. Larger values (in absolute terms) are observed in cells where the $Q_C : Q_0$ indicates a thermal regime dominated by the crustal contribution (larger values in the right map of Fig. 3.15).

Differences in basal heat flow (ΔQ_M, central map of Fig. 3.19) are of comparable magnitude to those observed in the thermal model (Fig. 3.15). A thinner crust results in an increased Q_M, and vice versa. There is a subtle variation superimposed on the checkerboard pattern, which becomes more evident in the temperature differences ($\Delta T(30\,\text{km}$, right map of Fig. 3.19). These are distributed in a zero-average ±37 °C range. A thinner crust tile results in increased temperature, and vice versa, following the same pattern observed with Q_M. The differences attenuate from a full-range alternating pattern in the south-west

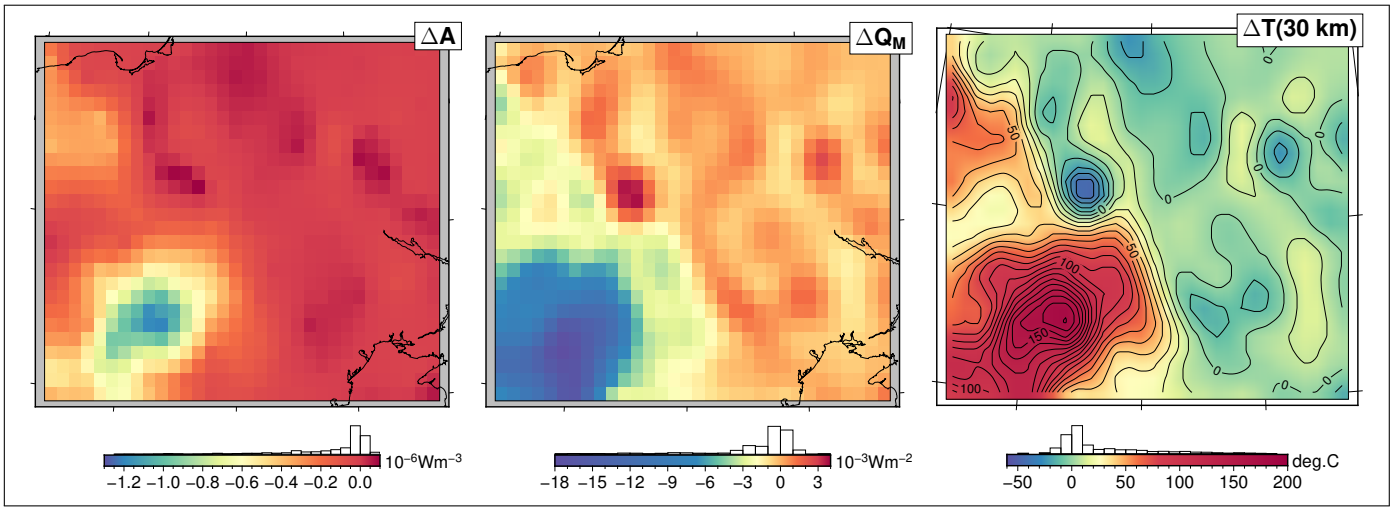

Figure 3.20.: Thermal results comparison between my Moho model and the one by Grad et al. (2009). Differences in bulk crustal RHP (ΔA), basal heat flow (ΔQ_M), and temperature at 30 km depth ($\Delta T(30\,\text{km})$) are expressed as results using my Moho minus results using the compared one.

portion of the area to almost zero in the north-east part. In contrast to what I observed with ΔA, there is no evident relationship with $Q_C : Q_0$, while the controlling factors appear to be the lithospheric thickness and surface heat flow (which are correlated).

I also tested the effect of using a different crustal model: the seismic Moho by Grad et al. (2009), that I had already compared with the satellite-only estimate presented in this chapter, in Fig. 3.9 and discussed in section 3.4.2. In Fig. 3.20 I have plotted the differences of three modelling outputs, using the same scheme of the 'checkerboard Moho' figure. Those differences are expressed as: results using my Moho estimate minus results using Grad et al. (2009), i.e. a negative difference where the latter results in a larger value.

In the ΔA map of Fig. 3.20, I observe a local minimum of $1.2\,\mu\text{W m}^{-3}$ in the Pannonian Basin. The shallower Moho by Grad et al. (2009) (24.4 km minimum, compared to 39.9 km in my Moho model) has been compensated with an higher RHP, to obtain the same Q_C with a smaller crustal volume. There are localised spots of positive ΔA, corresponding to structures where the inverted Moho model is thinner (see A) column plots in Fig. 3.9). The Q_M and $\Delta T(30\,\text{km})$ maps show a similar pattern: the thinner crust of Grad et al. (2009) results in more basal heat flow under the Pannonian Basin and higher temperatures, up to +180 °C. Crustal geometry therefore exerts significant effect on heat transport and temperature distribution, and, to a lesser extent, on the results of RHP fitting. Therefore, a reliable crust estimate appears of utmost importance in their modelling and in their applications, such as thermo-rheological forward

modelling (e.g. Burov and Diament, 1995).

3.6. Conclusions

I have presented the outcome of a comprehensive gravity-thermal strategy: from the geophysical data reduction of a global gravity model relying on GOCE observations to a regional-scale estimate of crustal thickness, which I then included in a steady-state thermal forward model and a subsequent substitution radioactive heat production fitting technique. The inverted crustal thickness estimate and the available surface heat flow measurements acted as main constraints.

The gravity reductions that I computed and applied involve global modelling, through a combination of space-domain forward modelling and spectral-domain filtering to ensure full spectral consistency with the band-limited global gravity model. The Moho undulations that I obtained by inversion of the anomaly that I isolated resulted in a crustal thickness model which resolves most of the features found in the three benchmarks (Grad et al., 2009; Reguzzoni and Sampietro, 2015; Pasyanos et al., 2014), albeit with discrepancies arising from differences in methods and data.

The results show consistency with the thermal regime of the study region, a test box across the Trans-European Suture Zone, at a similar spatial scale as sensed by the gravity model. Control of the Moho undulations on the temperature distribution is evident, both in terms of heat production and in shaping the mantle-to-surface heat transport, including the effect thermal refraction around hotter and less conductive crustal bodies.

Overall, the suitability of a satellite gravity data to thermal model work flow was assessed. It is providing useful quantitative insights even when integration with other data is kept to a minimum. The unparalleled spatial homogeneity in sampling and data quality that satellite-only global gravity models provide is already used to estimate crustal thickness in areas devoid of surface data. This test has shown how the same approach can be extended to thermal modelling, improving the models of poorly covered areas.

A pitfall of crustal thickness inversion from gravity models is the omission of structures that are instead resolved by seismic methods, due to unmodelled parameters (e.g. density variations) and uncertainties in data reductions. In the test presented in this chapter I deliberately avoided hard constraints from the seismic Moho models available in the area. The effects of the discrepancies between this gravity-inverted Moho estimate and the model by Grad et al. (2009) was assessed in terms of thermal modelling results. The outcome indicated how the Moho depth is more critical the higher the reduced heat flow (Q_M) is, resulting in significant differences under part of the study area. While the

magnitude of this difference is not detrimental to the thermal model reliability, it suggests that an accompanying uncertainty estimate would be beneficial.

Overall, the thermal modelling strategy designed and presented here as a proof of concept has proven fit for its purpose. The non-uniqueness in heat flow isolation (separating the crustal radiogenic contribution from other concurring thermal factors, such as basal heat flow, long wavelength near surface effects, and tectonic transients) calls for a multivariate inversion problem. This could be addressed by using an adequate scheme, such as Bayesian inversion (Mosegaard and Tarantola, 1995) –which is already commonly adopted in multi-observable lithospheric modelling (e.g Mather et al., 2018)– or data assimilation schemes (e.g. the ES-MDA method: Emerick and Reynolds, 2013; Limberger et al., 2018), and by including other temperature-dependent constraints, such as the effective elastic thickness (Burov and Diament, 1995) and its effects on flexural isostasy (Wienecke et al., 2007; Watts and Moore, 2017) – which can be independently sensed by gravity (e.g Kirby, 2014; Eshagh and Pitoňák, 2019).

3.A. Behaviour of the thermal fitting method

3.A.1. Stability of iterations to account for the temperature dependence of thermal conductivity

Temperature dependence of thermal conductivity ($k(T)$) is accounted for using a *subsequent substitution* procedure ("Picard's method", see e.g. Hauck et al., 1999), as described in section 3.3.1.4. Every forward call to the thermal model has been run by stopping at the third $k(T)$ substitution iteration. This means that a first-guess run ('iteration zero') was performed using thermal conductivity (k) computed from a linear geotherm (surface temperature to 1200 °C LAB). Then, the temperature resulting from the solution of 'iteration zero' was used to calculate k of the first iteration, and so on. Here I have tested the behaviour of k and T through iterations, using a synthetic 1D column of lithosphere. Figure 3.21 shows the results with a linear first-guess geotherm, while a different first-guess was used in Figure 3.22. The latter is defined by two segments: first from the surface to a mid-crustal boundary (22 km) set at 550 °C, then from there to the 1200 °C LAB. The iteration-counting convention adopted here is such as at the n-th iteration I am using the k_n calculated using the temperature at iteration $n-1$. In the figures I show how: (a) Variations in $k(T)$ and T are strongly attenuated after iteration one. Their values at that point are already smaller than parameter uncertainty. (b) Two different first-guess linear geotherms converge to the same results, regardless of under- or over-shooting the final geotherm (Fig. 3.21 and 3.22, respectively). The temperature differences at the 6th iteration is shown in figure 3.23: they are on the order of 10^{-5} K.

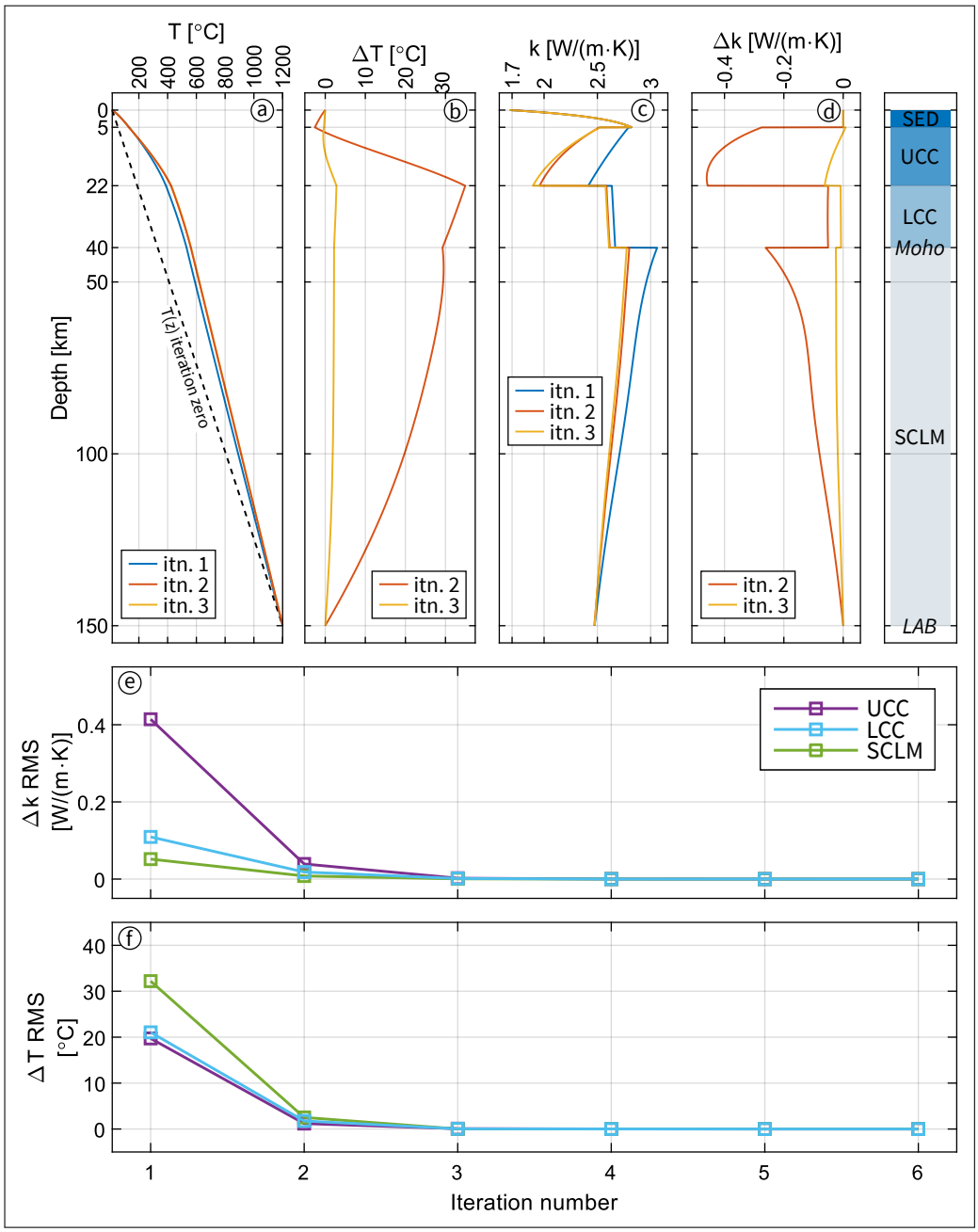

Figure 3.21.: Iterative modelling of temperature-dependent thermal conductivity. Case 1: first guess with a linear geotherm. **a)** geotherm curve, **b)** temperature difference in respect to previous iteration, **c)** thermal conductivity, **d)** thermal conductivity difference in respect to previous iteration, **e)** root mean square of difference in k with previous iteration, separated for the 3 layers with temperature-dependent thermal conductivity, **f)** same as e), for temperature. SED: sediments, UCC: upper crystalline crust, LCC: lower crystalline crust, SCLM: sub-continental lithospheric mantle. Plots a) through d) stop at the third iteration, the subsequent variations are too small to be visualised. The difference between T of iteration 1 and the first guess is not shown.

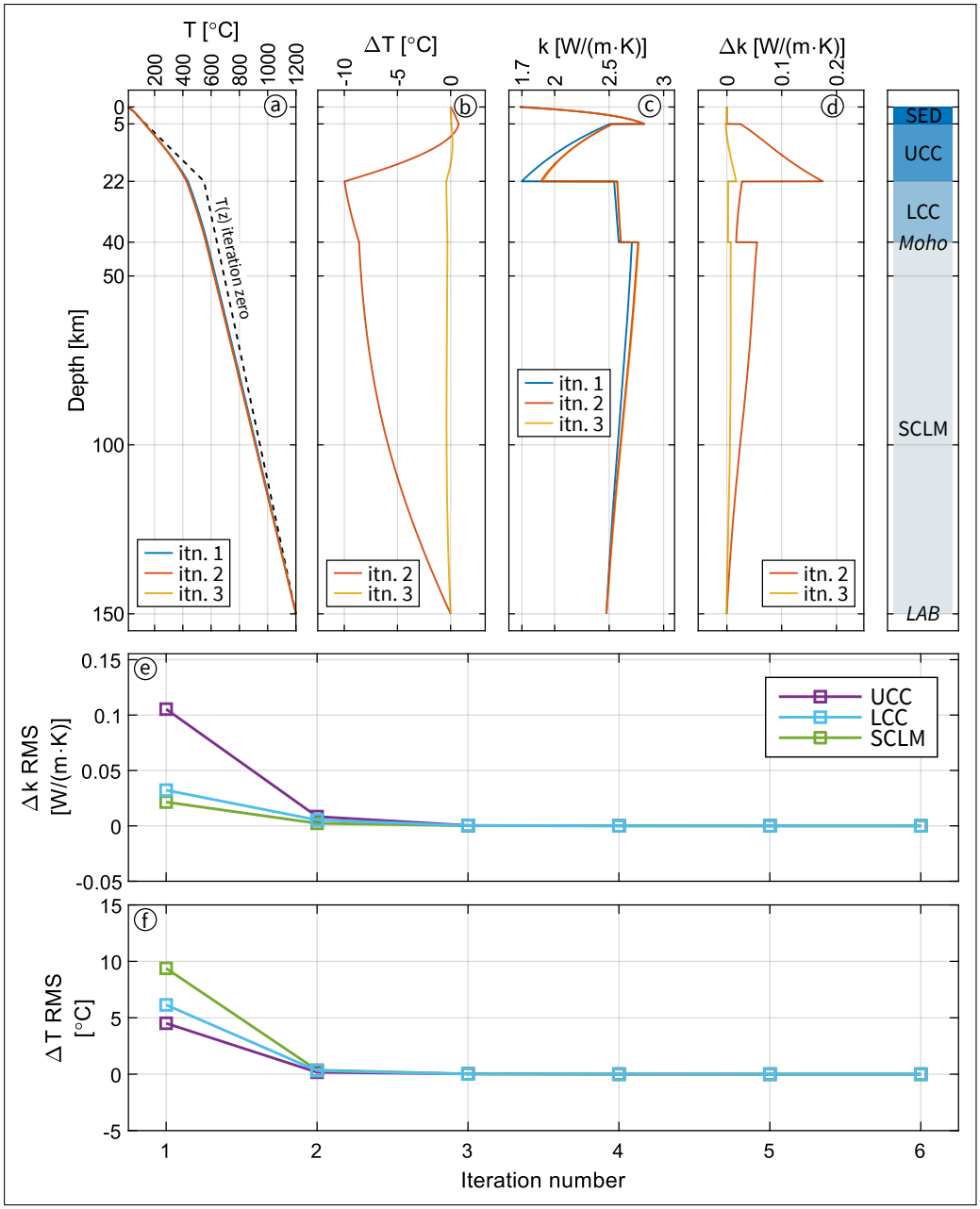

Figure 3.22.: Iterative modelling of temperature-dependent thermal conductivity. Case 2: first guess with a segmented geotherm. Description: see caption of Fig. 3.21.

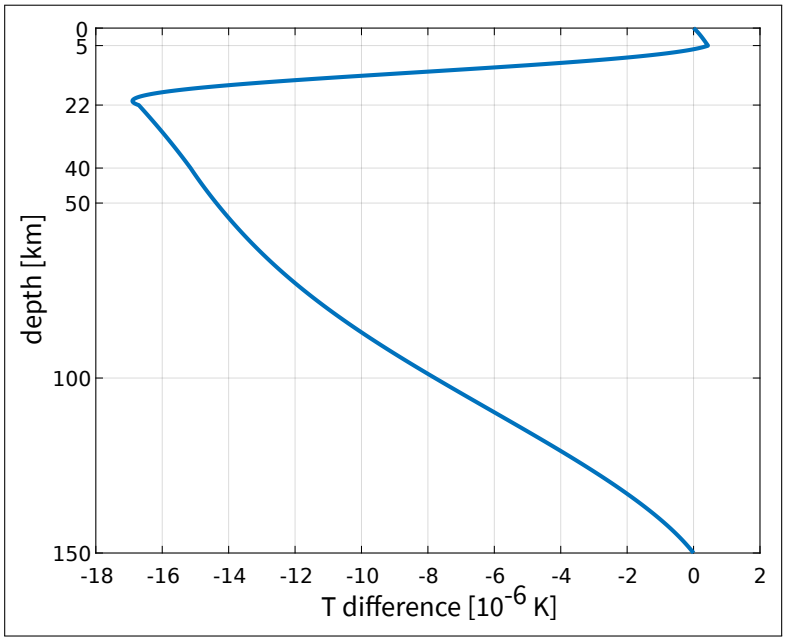

Figure 3.23.: Iterative modelling of temperature-dependent thermal conductivity: difference between geotherms obtained with the first guess of case 1 (Fig. 3.21) and case 2 (Fig. 3.22). Note the less than significant order of magnitude.

3.A.2. Iterative fitting of radioactive heat production

In figures 3.24 trough 3.28 I am showing the output of the fitting procedure (section 3.3.2), iteration by iteration. "Iteration zero" refers to the first-guess radioactive heat production (RHP) value, which is used to run the first forward model. It is constant throughout the area ($\mathbf{A_C}$ **0** map, Fig. 3.24).

In these maps the crustal heat production is expressed as one *bulk value*. Throughout the adopted strategy, this value is partitioned between the upper and lower crystalline crust using a reference ratio. The increasing trend in the range of RHP values is described and discussed in section 3.5.2, where it is summarised with a plot (Fig. 3.12) of the RMS value for each iteration and maps at iteration zero and six only. Here it si plotted for all the iterations.

The "Q_M suppression" is shown in Fig. 3.26. By comparing those maps with those of the crustal component of heat flow (Q_C, Fig. 3.25, computed as heat flow at the sediment-crystalline crust interface minus heat flow at the crust-mantle interface), I can identify a progressive reduction in Q_M in areas of increasing crustal heat production.

As described before (section 3.3.2), I have chosen this iterative fitting strategy due to the concurring behaviour of the temperature dependence of thermal conductivity and the non-horizontal heat conduction phenomena arising in a truly 3D thermal model. I recall that in a 1D model (i.e. only vertical conduction,

column-wise), I could compute the RHP per unit of volume in the crust dividing the crustal component of surface heat flow (stripped from other contributions) by the crustal thickness. In Fig. 3.27 I show the value of crustal RHP that results from doing so. I computed it a-posteriori, after each thermal forward model run. In Fig. 3.28 I show the difference between the actual values used in the model, iteration by iteration, and the ones obtained using the aforementioned '1D approximation'. Differences correlate with the actual (i.e. modelled) RHP values, but sharp variations are observed where lateral variations in RHP or in Moho depth occur, resulting in departure from vertical conduction.

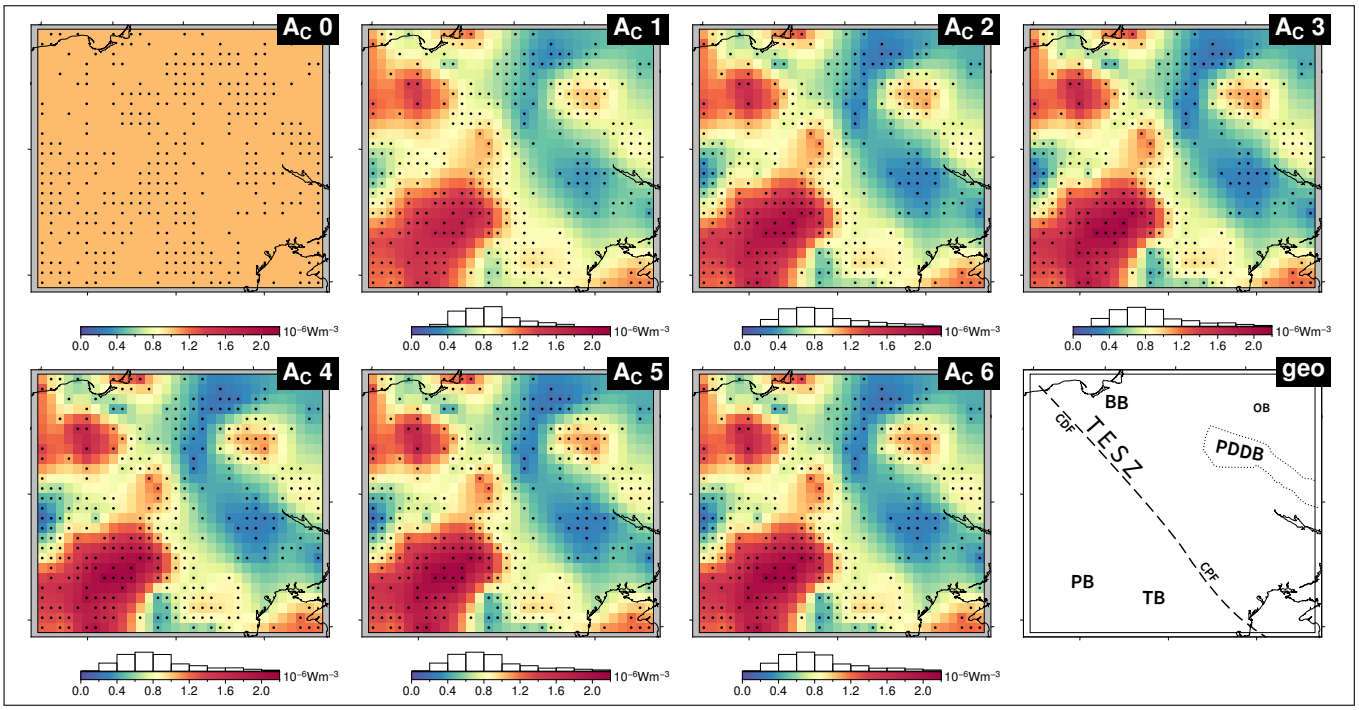

Figure 3.24.: Value of bulk heat production of the crystalline crust, trough the fitting iterations.

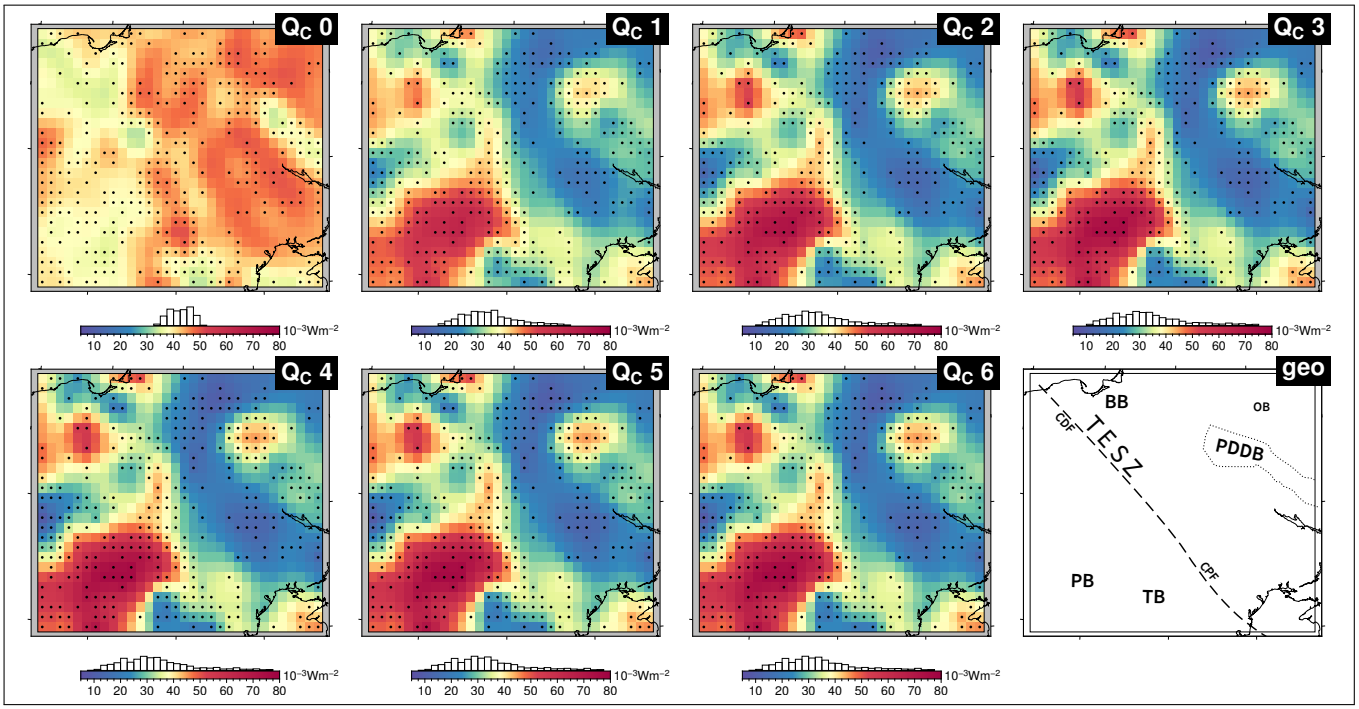

Figure 3.25.: Crustal contribution to the surface heat flow, computed as heat flow at the sediment-crystalline crust interface minus heat flow at the crust-mantle interface, trough the fitting iterations.

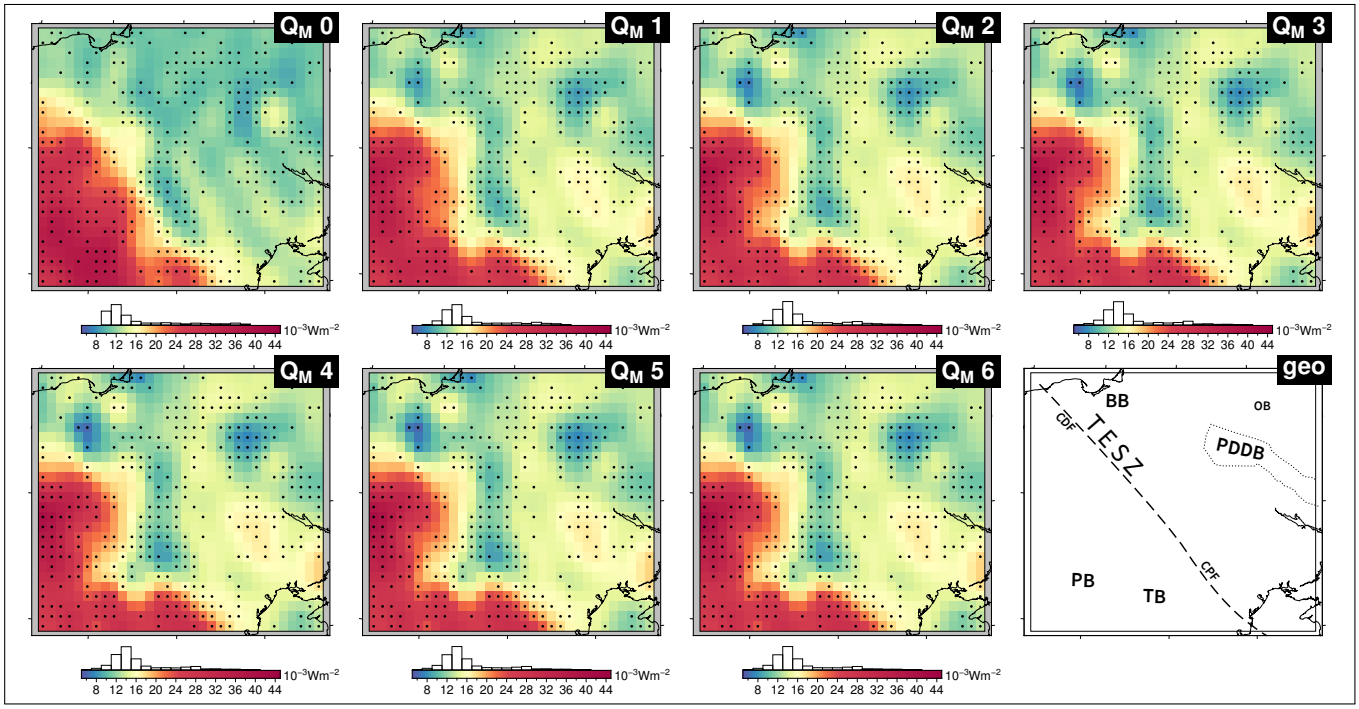

Figure 3.26.: Heat flow at the crust-mantle interface (basal heat flow), trough the fitting iterations.

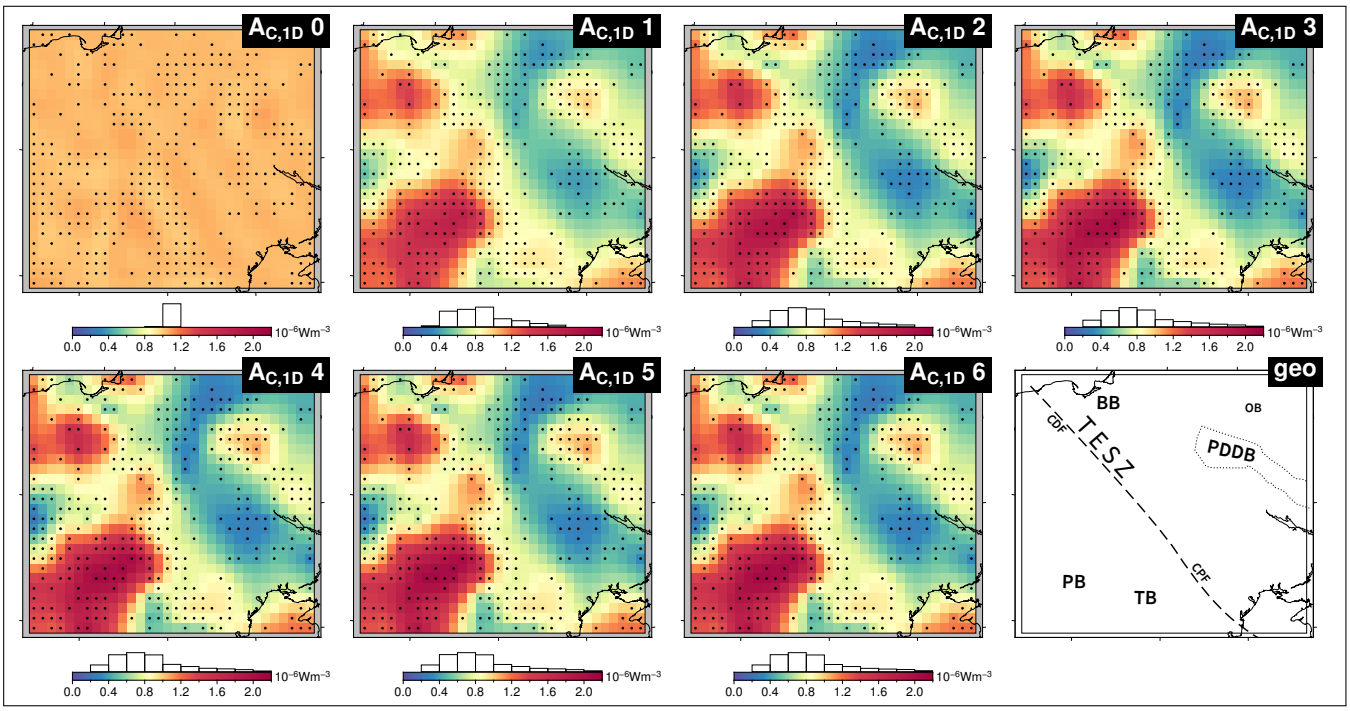

Figure 3.27.: Crustal heat production computed a-posteriori using a 1D approximation, i.e. crustal heat flow divided by crustal thickness.

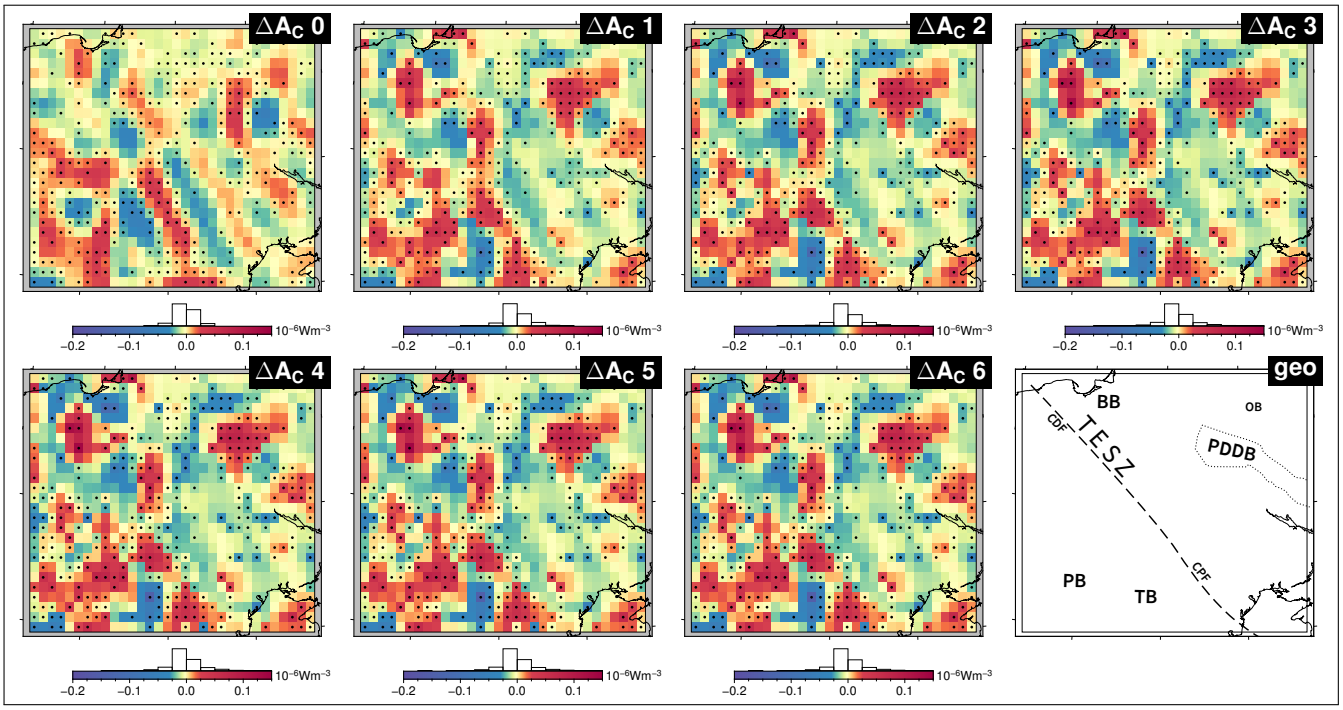

Figure 3.28.: Difference between the crustal heat production as used in the 3D model (Fig. 3.24), and the a-posteriori 1D-computed heat production (Fig. 3.27).

3.A.3. Effects of horizontal heat conduction

I include the result of a synthetic experiment showing the significance of non-vertical heat conduction. The forward model is parametrised with the same reference conductivity and heat production (first-guess) values previously presented in section 3.3 and Tab. 3.1. It consists of a 600 km 2D x-z section. It is one-element thick along the y axis (normal to the section) and a zero-flux conditions is imposed on the front and back sides (y-wise). Therefore, it represent a model of infinite extent along the y-axis. The grid step is 1 km and 50 m along x and z, respectively. No grid step coarsening has been applied along z, owing to the small model size in terms of computational budget. The results are shown in Fig. 3.29.

The model geometry includes a step in the crustal thickness: the undisturbed Moho is 40 km deep, while the it reaches 48 km in the thickened part, in the section center. The upper-lower crust boundary is set proportionally. In the left side of the section the step is a sharp transition, taking place from one model node to the next. In the right side it was smoothed with a Gaussian filter (100 km cutoff wavelength). The sediment basement and the LAB are flat, at 4 km and 100 km respectively. The topography is also flat. Three $k(T)$ iterations were used.

Plot **a)** of Fig. 3.29 represents the surface heat flow, computed from the temperature section using the following:

$$Q_0 = \frac{T(z_1) - T(z_0)}{z_1 - z_0} \cdot \frac{k(z_1) + k(z_0)}{2} \tag{3.12}$$

Where z_0 and z_1 are the z-coordinate of the surface and first sub-surface node, respectively. z is defined positive downwards. The second term of the product is an arithmetic mean of the thermal conductivities of the two nodes. This numerical vertical heat flow resembles a near-surface heat flow measurement in a well, under ideal conditions. In plot **b)** of Fig. 3.29, I am comparing Q_C obtained by two methods:

2D, blue curve: the crustal component of surface heat flow derived from the model, computed as a difference between the heat flow at the sediment basement (boundary between 'SEDS' and 'UCC' layers) and the basal heat flow (boundary between 'LCC' and 'SCLM' layers). This follows the same convention outlined in eq. 3.12;

1D, orange curve: the crustal component computed as the integral of crustal heat production per unit of volume along the crustal thickness. This resembles a 1D, column-wise, model. Notice the different response to the sharp step (left side).

In plot **c)** of Fig. 3.29, I am comparing Q_M obtained by two methods:

2D, blue curve: the basal heat flow as numerical heat flow at the Moho (boundary between 'LCC' and 'SCLM' layers);

1D, orange curve: basal heat flow interpreted as 'reduced heat flow' in a 1D approach: I subtracted the column-wise 1D Q_C to Q_0. Notice how the misfit becomes larger near the edges of the thickened crust (both step and smooth transitions), while it is almost zero at its center.

Plot **d)** of Fig. 3.29 shows the temperature field as contours, in degrees Celsius. The layer structure is plotted in the background. In plot **e)** of Fig. 3.29 I am showing the deviation from a purely vertical temperature gradient (angle α). It was calculated with the following:

$$\alpha_i = \arctan \frac{\text{abs}\,(\nabla_x T_i)}{\nabla_z T_i} \tag{3.13}$$

where ∇ indicates the numerical gradient calculated between nodes of the temperature field. A sketch is included in the bottom of Fig. 3.29. To improve the plot clarity, the sign of the horizontal gradient was discarded: its direction is towards negative-x in the left side of the plot, towards positive-x in the right side – i.e. heat flow is deviated around the thickened, hotter portion of crust.

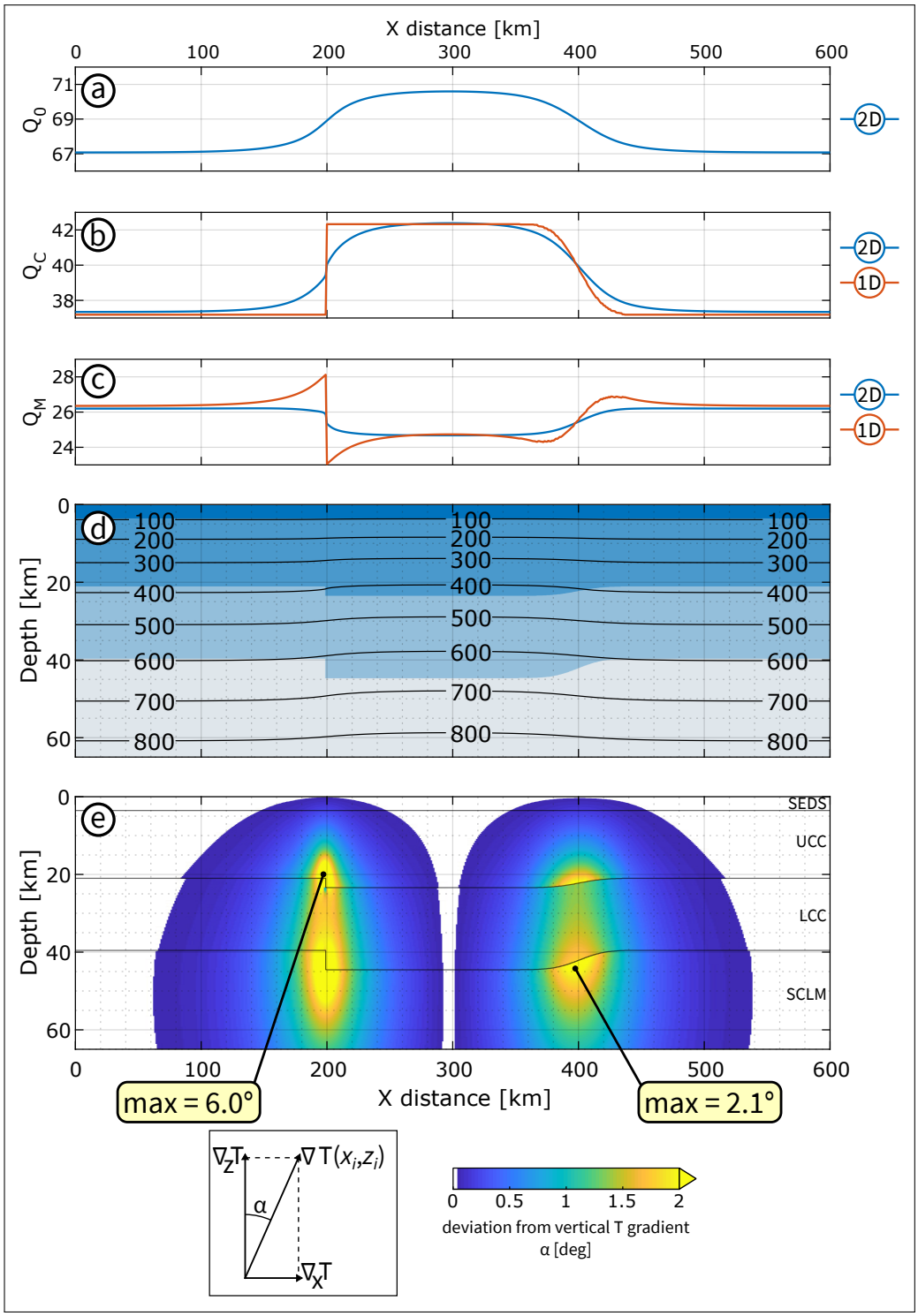

Figure 3.29.: Synthetic experiment showing the effect of horizontal heat conduction.

3.A.4. Effect of a temperature-dependent Moho density contrast

To assess the effect of temperature on the densities used in the inverted Moho depth estimates, I have tested the effect of re-computing the Moho density contrast using the thermal modelling results. The densities were updated according to the following, from P. A. Allen and J. R. Allen (2013):

$$\rho(T, P) = \rho_0(1 - \alpha_V \Delta T + \beta P)$$

where ρ_0 is the initial density, α_V the volumetric coefficient of thermal expansion (in K^{-1}), ΔT the change in temperature, β compressibility (in Pa^{-1}), and P pressure (in Pa). I used a β of 3×10^{-11} and 1×10^{-11} K^{-1} for the crust and lithospheric mantle (assumed peridotite), respectively, and a α_V of 2.4×10^{-5} Pa^{-1} for both the crust and the lithospheric mantle.

The new inverted Moho, in Fig. 3.33, shows a variation (after minus before) ranging from −2.3 km to +3.4 km, with an average of −0.13 km and a standard deviation of 0.75 km. This equals to a −12.2 % to +14.8 % variation against the original value (average: +4.2 %). The range and variance of these discrepancies are inside or less than the typical uncertainties of crustal thickness estimation (±5 to ±15 percent, i.e. ±2 to ±6 km for a 40 km thick crust, see Grad et al., 2009 and references therein).

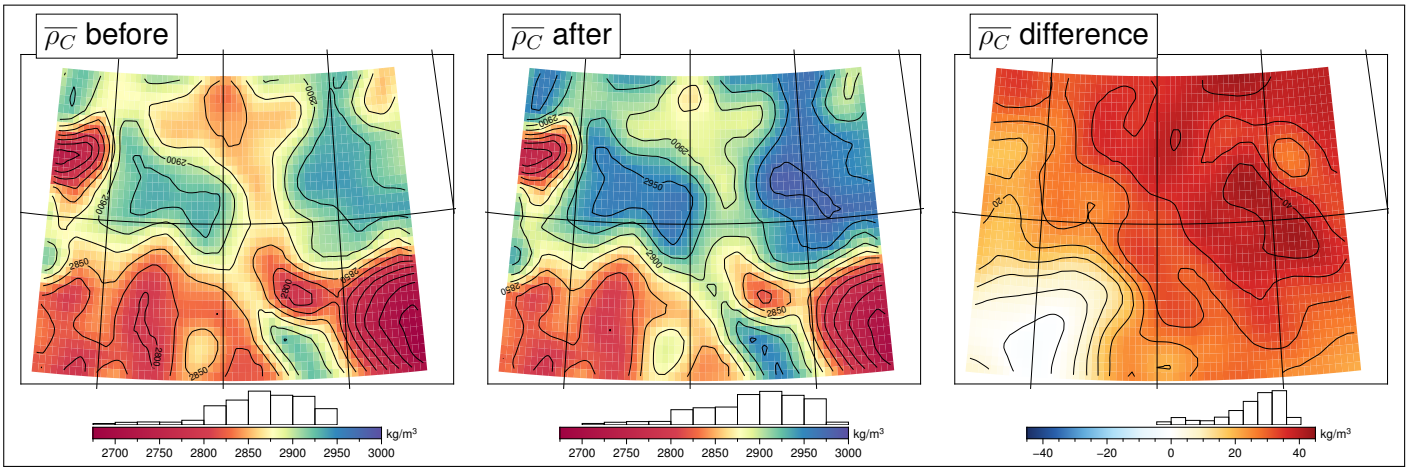

Figure 3.30.: Bulk density of the crystalline crust. Left: from LITHO1.0. Center: updated with (T, P) effect, with the output of the thermal modelling. Right: (T, P) effect contribution, updated density minus original density.

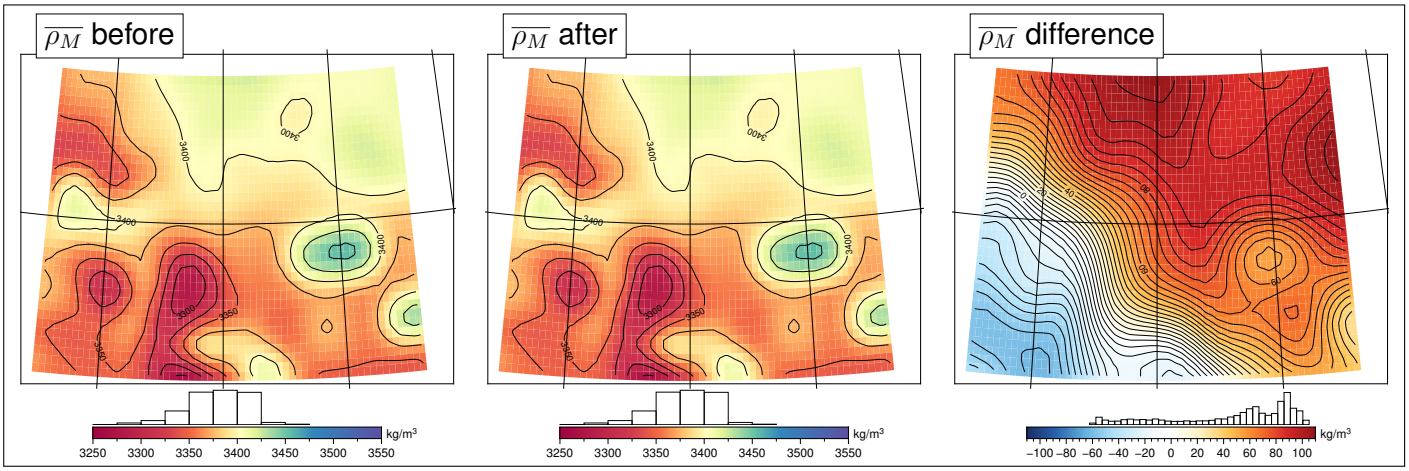

Figure 3.31.: Bulk density of the lithospheric mantle. Left: from LITHO1.0. Center: updated with (T, P) effect, with the output of the thermal modelling. Right: (T, P) effect contribution, updated density minus original density.

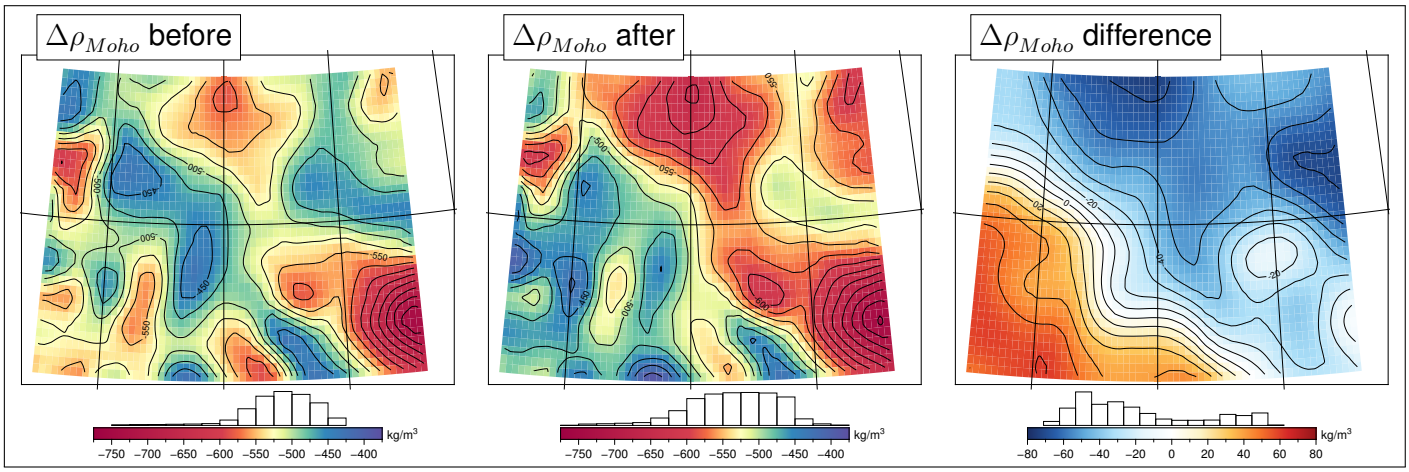

Figure 3.32.: Moho contrast, expressed as bulk crust density (Fig. 3.30) minus lithospheric mantle bulk density (Fig. 3.31). Left: from LITHO1.0. Center: updated with (T, P) effect, with the output of the thermal modelling. Right: (T, P) effect contribution, updated density minus original density.

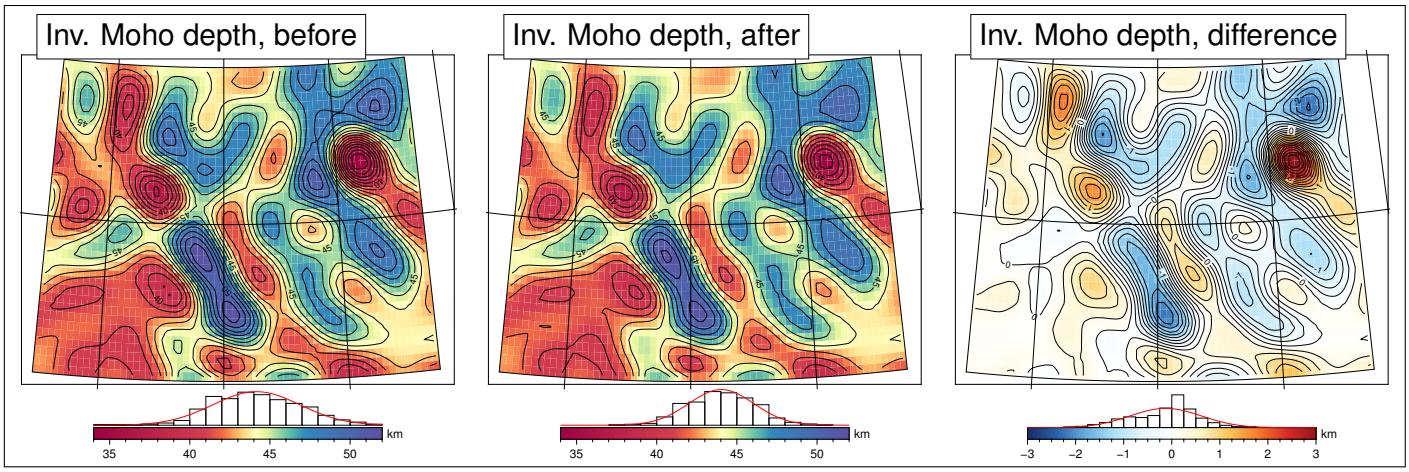

Figure 3.33.: Inverted Moho depth. Left: using the density contrast from LITHO1.0, unmodified. Center: using the density contrast updated with (T, P) effect, with the output of the thermal modelling. Right: (T, P) effect contribution, updated Moho minus initial Moho estimate.

3.B. A-posteriori test of RHP relationships with other physical properties

3.B.1. Relationship of RHP with density

Fig. 3.34 provides an alternate representation of Fig. 3.14. Instead of the RHP versus density scatter plot (upper right axes), here I am including a map of the spatial distribution of the bulk crustal density. The density of the samples in all the scatter plots (each sample a model column) is plotted with the same colour scale used in the density map.

3.B.2. Relationship of RHP with V_P

Fig. 3.35 shows the comparison between the inverted RHP estimate and the output of (Hasterok and Webb, 2017) V_P-RHP relationship (using data for the continental crust), as discussed at the end of section 3.5.2. Log-linear fits are in the following form (Eq. 4 in Hasterok and Webb, 2017):

$$\log_{10} A = m(V_P - 6) + b$$

With m in $(\log_{10}(\mu W\ m^{-3}))\ (km\ s^{-1})^{-1}$, b in $\log_{10}(\mu W\ m^{-3})$, V_P in $km\ s^{-1}$. Hasterok and Webb (2017) fit parameters ('continental') are: $m = -0.70 \pm 0.10$, $b = 0.48 \pm 0.08$. The fit I have obtained on data of this chapter (by regression) is: $m = -0.56 \pm 0.18$, $b = 0.19 \pm 0.11$. Confidence interval provided for $\pm 2\sigma$.

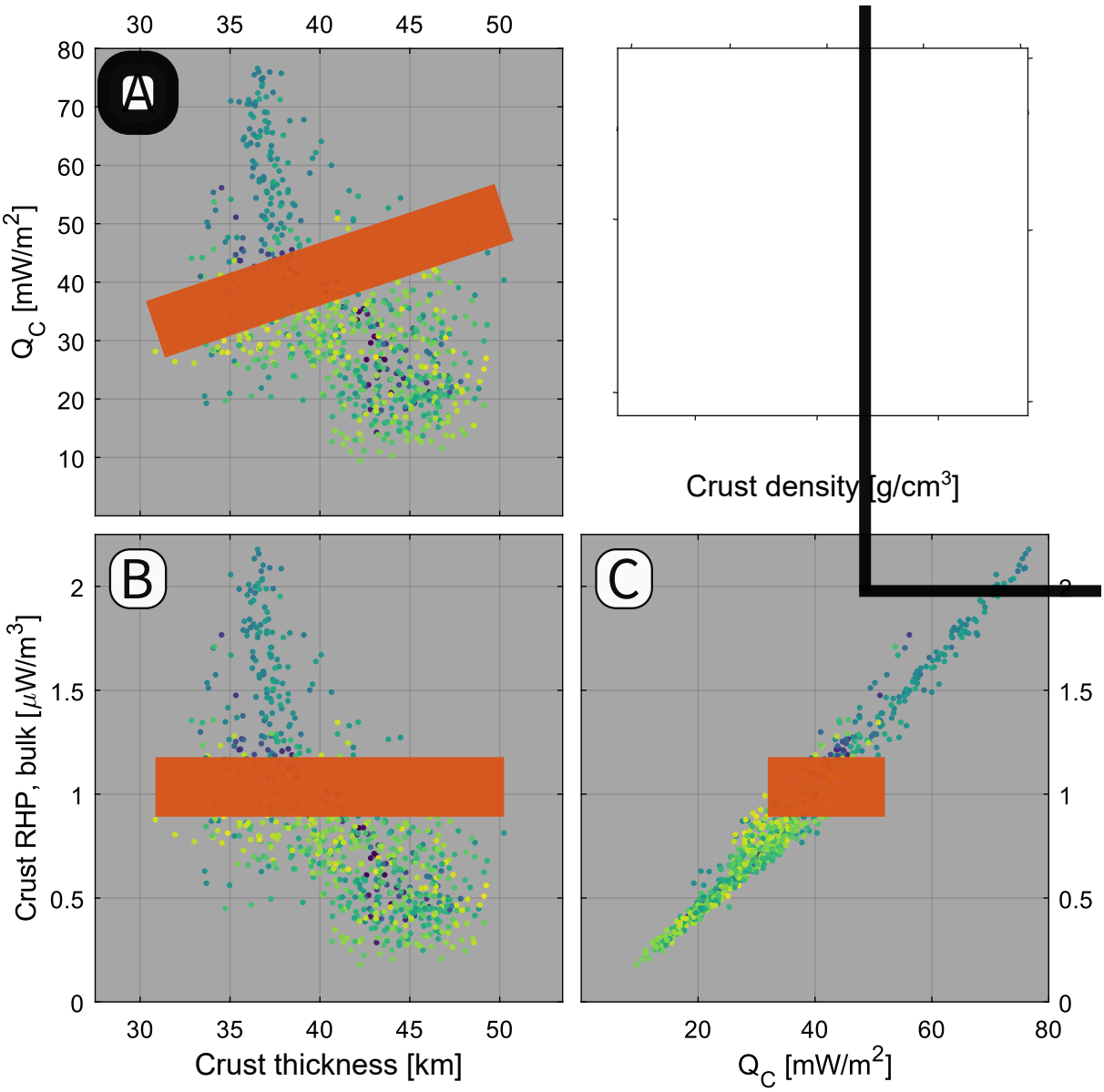
A
B
C
Q_C [mW/m^2]
Crust RHP, bulk [μW/m^3]
Crust thickness [km]
Q_C [mW/m^2]
Crust density [g/cm^3]

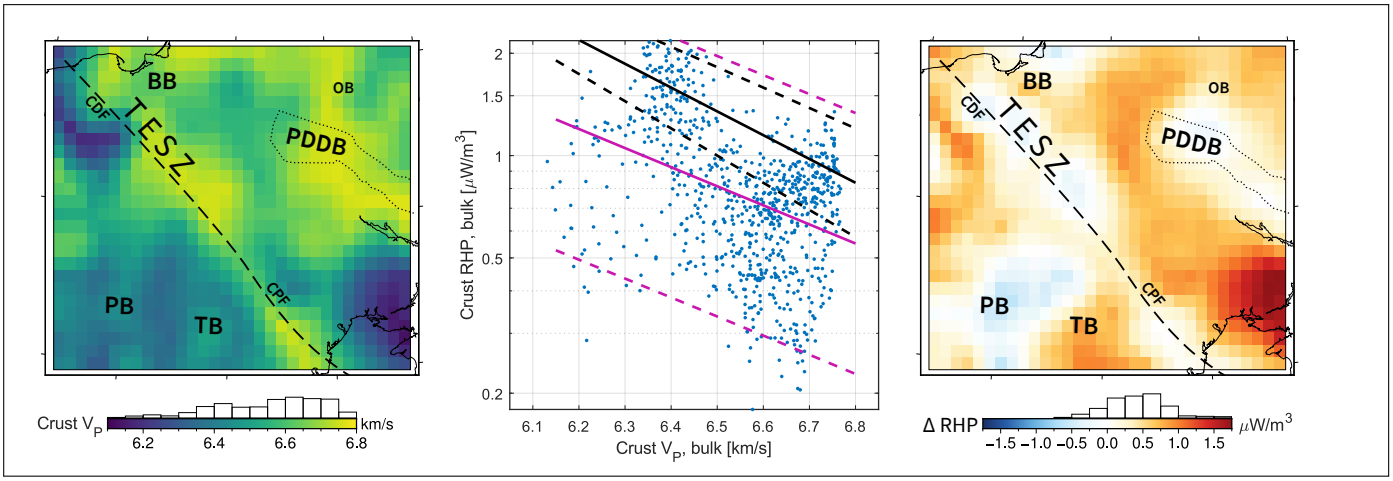

Figure 3.35.: Left: V_P of the crystalline crust (thickness-weighted average of Pasyanos et al., 2014 data), computed along the nodes of each model column. **Center:** scatter plot of crustal V_P against the inverted crustal RHP estimate. The V_P-RHP relationship by Hasterok and Webb, 2017 is plotted in black. A log-linear fit to the inverted data is plotted in purple. Dashed lines depict upper and lower confidence bounds (±2 standard deviations). **Right:** V_P-RHP estimate minus the inverted estimate.

4. Conclusions and outlook

The research presented in this dissertation dealt with the application of satellite-only gravity models to modelling of the temperature distribution in the continental lithosphere and surface heat flow. In the wider context of using gravity to perform inference on the structure of the planet interior, I have provided contributions in the following topics:

- forward modelling of prior models of sub-surface density, pursuing signal isolation in gravity data;
- crustal-thickness-constrained geothermal modelling, aimed at using a result of gravity inversion to turn the sparse measurements of surface heat flow in a complete thermal volume, adding information at surface and in depth.

Interest in addressing such a problem stems from the difference between regional scale gravity (e.g. about 100 km) and surface heat flow measurements. The former is an observable that can benefit from unparalleled global homogeneity in sampling and quality, thanks to satellite gravity missions. The latter suffers from the well-known spatial sampling issues that affect all terrestrial measurements.

Consequently, when starting to enquiry if *"gravity may fill-in the heat flow blanks"*, the main research question was formulated: *"can we use gravity and thermal modelling to provide a physics-based interpolation of surface heat flow?"*.

The methodology developed here aimed at assessing this, starting from an a-priori experimental constrain: reliance on external data, other than satellite-gravity models and surface heat flow, should be kept at a reasonable minimum. Therefore, as discussed in depth in chapter 3, the results are unavoidably affected by the well-known issues of non-uniqueness that are commonly addressed with multi-observable modelling (Afonso et al., 2013a), such as partition between basal heat flow and crustal heat production.

However, even under the limiting conditions imposed, the results have provided a satisfactory consistency with current knowledge of the modelled study area, across the Trans-European Suture Zone – a relatively well surveyed zone, compared to most of the Earth surface. The proposed method could thus be

scaled to surface heat flow fill-in in areas devoid of measurements, fully exploiting the potential of gravity models.

The methodology described in chapter 2 and the associated data-reduction experiments provide an efficient framework for turning global mass distribution models in global gravity reductions, a fundamental step in the gravity inverse problems involved in solid-Earth geophysics. The relief forward modelling method by Wieczorek (2007) was employed in a 'layer-wise' configuration, based on the difference between the gravity field of the bottom and top boundaries defining a layer. The proposed method competes with spatial-domain forward modelling, especially in at the comparatively low resolutions imposed by the current state-of-the-art both in satellite only gravity models and global compilations of subsurface data.

In the forward-modelling test I carried out, the input densities were modelled as contrasts against a reference density model. Common solutions for this aspect involve the computation of average densities from the layers of the input model, e.g. of the whole crust (Tenzer et al., 2015; Tenzer and Chen, 2019). Here, a novel solution was designed and implemented: the reference density model is defined in concentric shells of constant thickness. Since each shell may intersect different layers, with large differences in layer-wise average densities, this strategy enabled the concurrent modelling of different layers referred to the same reference. When average densities are compiled using complete shells, if necessary filling in the portion not included in the input model (e.g. the sublithospheric mantle) with a reference value, zero-average shell-wise corrections can be computed.

The obtained result is a whole-lithosphere reduction field, in spherical harmonics and synthesised global maps of gravity corrections. It was applied to the combined satellite-only GOCO06s (Kvas et al., 2019a), for which the residual gravity disturbances are presented, after reduction. Spectral domain comparisons were performed between the modelled masses and the input gravity model. Among their results, the effective bandwidth of the input density model was assessed: there is a sudden decay in degree cross-correlations between SH degree 60 and 110 (half-wavelengths of 3 to 1.6 arc degree).

Pursuing the objective of estimating what is the error introduced by data reductions, a Monte Carlo uncertainty propagation scheme was set up and tested with a simplified error model for the input data. It may be scaled to more complex error models.

The thermal application of chapter 3 made extensive use of the method and findings of the data reduction strategy, chiefly in two steps of the Moho signal isolation procedure: (1) in modelling the far-field 'isostatic effect', to remove the long-wavelength component that affects gravity data from GGM after correcting them with global terrain effect models; (2) in harmonising the

more detailed regional sediment thickness model that was utilised inside the study area (EuCRUST, Tesauro et al., 2008) with a global low-resolution model (LITHO1.0, Pasyanos et al., 2014), in order to perform spectral-domain filtering on a global spherical harmonics model of sediments correction.

After the gravity data reduction step, the thermal strategy relies on inversion of the isolated Moho signal. Thickness of the consolidated crust is the quantity that enables the fill-in of the areas devoid of surface heat flow measurements, after fitting the radioactive heat production in cells with measurements. The obtained Moho images a crustal morphology which is comparable with other models in the regions, adopted as benchmarks. Gravity based methods have a well proven record in retrieval of crustal thickness, showing their most promising results in integrated inverse modelling strategies (e.g. Eshagh et al., 2011; Reguzzoni and Sampietro, 2015), combining data from different geophysical observables. Here, by design, the performance of a satellite-only approach was assessed, relying as less as reasonably possible on other sources.

A 3D finite-difference thermal forward operator for solving the steady state heat equation has been developed for the purposes of this research (appendix A). It allows a radioactive heat production inversion technique, which progresses iteratively through a succession of 1D approximations and subsequent substitution of the parameter sought for. It enabled the production of a complete volume of temperature and thermal parameters in the study area, resulting in a gravity-controlled, physics-based, fill-in of the no-data cells – both at surface and in depth.

In summary, with the findings of the experiments and applications carried out in this dissertation, I have shown that:

1. **Thermal modelling strategy:** a radioactive heat production fitting strategy, constrained by uniformly-sampled crustal thickness and sparsely-sampled surface heat flow, can provide added thermal information on areas lacking direct measurements, either because they are not yet available (surface heat flow) or are logistically not feasible (temperature at depth). Estimates are comparable with the results of petrophysical relationships. In terms of open issues, the tests demonstrated how uncertainty in crustal thickness is more critical the higher the estimated basal heat flow (Q_M). In addition, the ambiguity in Q_M separation is affected by the potentially unstable behaviour of temperature-dependent thermal conductivity.

   Further development Multivariate and probabilistic inversion seems justified even for an inverse problem constrained only by two observables (gravity and heat flow). Topography, another observable not suffering from sampling issues (at this scale) could provide added

informations in assessing the basal heat flow: the effective elastic thickness. In addition, the predictive performance of the physics-based fill-in strategy could be quantitatively assessed against the simple interpolation of surface heat flow values, resorting to cross-validation methods (e.g. Bishop, 2006, chapter 1)

2. **Moho inversion for regional thermal modelling:** A well-tested procedure was employed to invert a Moho depth from the isolated gravity signal, in local cartesian coordinates. The performance of this crustal thickness estimate are comparable with those obtained by using an integrated seismic based Moho: it is successful in resolving the deep structures controlling the shallow thermal regime and in providing a uniformly-sampled quantity for the RHP-fitting strategy. Results are significantly better than those provided by a checker board Moho test, with higher sensitivity in cells of higher heat flow. The effect of crustal thickness in controlling the observed pattern of surface heat flow –as observed in thermal modelling works of similar focus (Scheck-Wenderoth et al., 2014; Przybycin et al., 2015; Limberger et al., 2018, to name a few)– was also reproduced.

   Further development The effect of temperature on density, and then on Moho inversion, was assessed using the output of the forward thermal model: it results in variations of −12.2 % to +14.8 % respect to the Moho inversion that disregarded the thermal effect. While this is deemed an acceptable uncertainty, it would make sense to not discard the temperature information that this modelling method provides. This is also suggested by the existing research on thermal effects on crustal gravity modelling have already provided results (e.g. Bagherbandi et al., 2017).

3. **Satellite-only gravity for thermal modelling:**

   - The suitability of gravity as an independent constraint in thermal modelling was demonstrated in this thesis with a proof-of-concept regional application. The continental lithosphere poses lots of issues due to local heterogeneities that superimpose over the necessary simplification of general models. Reality deviates from a simple two-layer crust-mantle model, and thermal parameters are no exception in this – the vertical distribution of radioactive elements being only a first-order approximation (Jaupart and Mareschal, 2003; Alessio et al., 2018) and active tectonics hindering the applicability of steady-state modelling. The thermal strategy mentioned above was designed to overcome these issues, at least in part. A compromise between

uniform coverage and resolution is required – a direct consequence of the band-limited input data provided by the input gravity data. In addition, uncertainties in the a-priori data reductions are one to two orders of magnitude larger than the mGal-level cumulative formal errors of the GGMs. Nevertheless, data from a state-of-the-art satellite-only GGM have been shown suitable for this purpose.

- The thermal application included a bare-minimum integration with external data sources: a sedimentary reduction using a basement depth model (local and global), a low-resolution Moho density contrast model, removal of the distant isostatic effect using a global crustal model, and a thermal lithospheric thickness provided by a surface wave inversion model. Most of these data sets are available at least at low resolution globally, albeit assessing their data quality can be non trivial. The data-reduction forward modelling presented in this thesis, in addition to the computation of global corrections and uncertainty propagation, proposes spectral comparison as a tool to assess coherency in effective bandwidth between input gravity models and reductions.

Further development Scaling the thermal modelling framework to larger extents, e.g. on all the continental crust using a moving-window approach, is its natural further step. While unavailability of terrestrial data is not easily overcome, uncertainty-aware modelling can at least provide "error bars" on the output of a modelling strategy. Propagation of uncertainties in the reductions to the final thermal estimate is surely an aspect that warrants further investigation. The lean modelling tools that the modelling work flow presented here is composed of throughout (from gravity reduction to thermal modelling) could easily allow such a development.

A. Supplementary: thermal forward modelling operator

The thermal parameter fitting strategy and the obtained thermal model (chapter 3) rely on a finite-difference solver for the steady-state heat equation. Its fundamental relationship can be expressed in the following vector form:

$$\boldsymbol{\nabla} \cdot (k(\boldsymbol{x})\boldsymbol{\nabla}T(\boldsymbol{x})) = -A(\boldsymbol{x}) \tag{A.1}$$

with k thermal conductivity (considered isotropic), T temperature, A heat production per unit of volume, and $\boldsymbol{x}$ position vector. This form results from simplification of the well known heat equation in its full form (Carslaw and Jaeger, 1959; Fourier, 1822), a heat source term included:

$$\frac{\partial T}{\partial t} = \alpha \boldsymbol{\nabla}^2 T + \frac{A}{\rho c_p} \tag{A.2}$$

where t denotes time and α 'thermal diffusivity', i.e. the product of thermal conductivity (k), density (ρ), and specific heat (c_p). The steady-state assumption imposes:

$$\frac{\partial T}{\partial t} = 0 \tag{A.3}$$

This allows simplification of Eq. A.2 to:

$$0 = \rho c_p \left(k \boldsymbol{\nabla}^2 T + A\right) \tag{A.4}$$

therefore:

$$k \boldsymbol{\nabla}^2 T = -A \tag{A.5}$$

which is equivalent to Eq. A.1, as expressed above (e.g. Stüwe, 2007, chapter 3).

Analytical solutions to this partial differential equation exist: plenty are available for specific cases in the Earth sciences (see e.g. Turcotte and Schubert, 2014, chapter 4.6; Stüwe, 2007, chapter 3.4). As pointed out by Gerya (2010) a pitfall of analytical methods for PDE solution is that they are "restricted to relatively simple problems" (Gerya, 2010, chapter 3.1). To analytically express the distribution of parameters' fields (e.g. A, k) is often cumbersome, sometimes impossible. For the purposes of this thesis, a solver to the steady-state heat

equation based on the finite-difference method (Patankar, 1980, chapter 4.2; Gerya, 2010, chapter 10) was developed. Resorting to finite differences implies discretising the infinite model continuum on a mesh of points, which describe the geometrical distribution of physical properties in the model, and then substituting the partial differential equations (i.e. the heat equation as in Eq. A.5 and the equations describing the boundary conditions) at the grid points with linear equations which locally approximate derivatives. This procedure results in a system of linear equations, which is solved to obtain the value of the unknowns at each of the grid points.

Leaving the thorough description of the mathematical basis of finite differences (FD) and of the fundamentals of their implementation to the works cited above, this supplementary chapter provides a description on the modelling solution devised for the aim of this thesis.

A.1. Finite-difference approximation of the steady-state heat equation

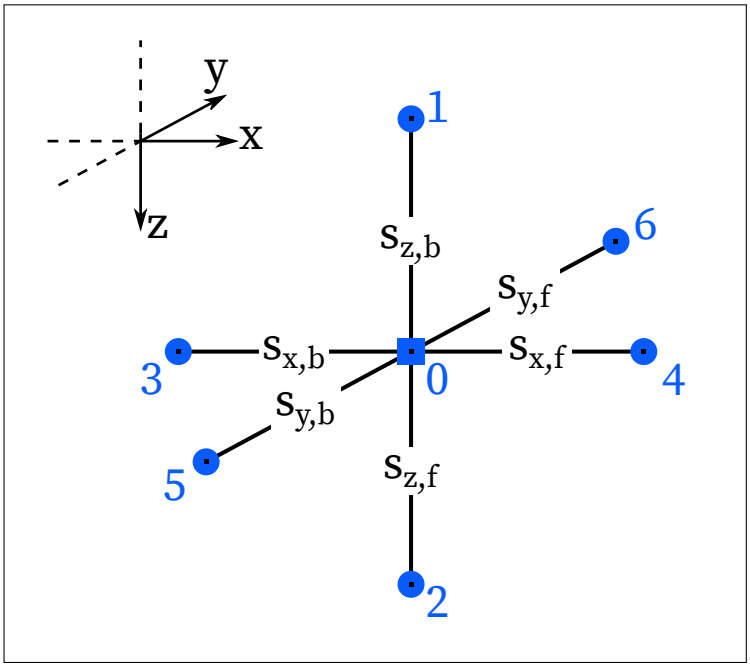

Figure A.1.: The 7-point stencil used to formulate the central finite differences for the heat equation around node 0 (neighbours nodes 1 to 6). Each i-th node corresponds to a value of T_i, k_i, A_i. The axis convention is shown in the upper left corner. $s_{m,n}$ denotes the grid spacing between nodes, along the m-axis and n-direction along axis (b backwards, f forwards).

The heat equation under the assumed conditions (Eq. A.5) can be formulated using *central finite differences* for a node and its six neighbours in a 3-D rectangular grid. The 7-node *stencil* of this nodal configuration (i.e. its graphical representation) is shown in Fig. A.1.

Remembering Fourier's law of heat conduction, which defines heat flux Q:

$$\boldsymbol{Q} = -k\boldsymbol{\nabla}T \tag{A.6}$$

we express it in the Leibniz's notation for Cartesian coordinates, which will come useful further in this description:

$$\boldsymbol{Q} = -k\left(\frac{\partial T}{\partial x}\hat{\boldsymbol{i}} + \frac{\partial T}{\partial y}\hat{\boldsymbol{j}} + \frac{\partial T}{\partial z}\hat{\boldsymbol{k}}\right) \tag{A.7}$$

with $\hat{\boldsymbol{i}}, \hat{\boldsymbol{j}}, \hat{\boldsymbol{k}}$ unit vectors of x, y, z coordinates. For the sake of clarity, we indicate each of these heat flux components as Q_x, Q_y, Q_z:

$$\boldsymbol{Q} = \left(-k\frac{\partial T}{\partial x}\hat{\boldsymbol{i}}\right) + \left(-k\frac{\partial T}{\partial y}\hat{\boldsymbol{j}}\right) + \left(-k\frac{\partial T}{\partial z}\hat{\boldsymbol{k}}\right) = Q_x\hat{\boldsymbol{i}} + Q_y\hat{\boldsymbol{j}} + Q_z\hat{\boldsymbol{k}} \tag{A.8}$$

By substituting this into the $k\boldsymbol{\nabla}^2T$ term of Eq. A.5 we get:

$$\begin{aligned} -1\cdot(k\boldsymbol{\nabla}^2T) &= -1\cdot(-A) \\ -k\boldsymbol{\nabla}^2T &= A \\ \boldsymbol{\nabla}(-k\boldsymbol{\nabla}T) &= A \\ \frac{\partial}{\partial x}Q_x + \frac{\partial}{\partial x}Q_y + \frac{\partial}{\partial x}Q_z &= A \end{aligned} \tag{A.9}$$

Turning to finite differences, Eq. A.9 can be expressed for each internal node and its 6 neighbours in the model mesh, as illustrated in Fig. A.1. Each i-th node is characterised with its associated parameters: T_i, k_i, A_i. On each segment of the graph connecting 'node 0' and its neighbours we add a *staggered node* representing the heat flux between the neighbour and the central node, therefore we have split each component of heat flux $\boldsymbol{Q}$ in its backwards and forwards parts, respect to the central node, along the direction defined by each of the unit vectors. To prevent further cluttering Fig. A.1, these $Q_{m,n}$ heat flux nodes are represented on a separate stencil, in Fig. A.2.

Using one of the terms of Eq. A.9 as an example, this implies that:

$$\frac{\partial}{\partial x}Q_x \approx \frac{\Delta Q_x}{\Delta x} = \frac{Q_{x,f} - Q_{x,b}}{(s_{x,b} + s_{x,f})/2} = 2\frac{Q_{x,f} - Q_{x,b}}{s_{x,b} + s_{x,f}} \tag{A.10}$$

The sketch provided in Fig. A.3 helps in representing the finite difference approximation just shown in Eq. A.10. In that figure the grid spacings $s_{x,b}$ and $s_{x,f}$

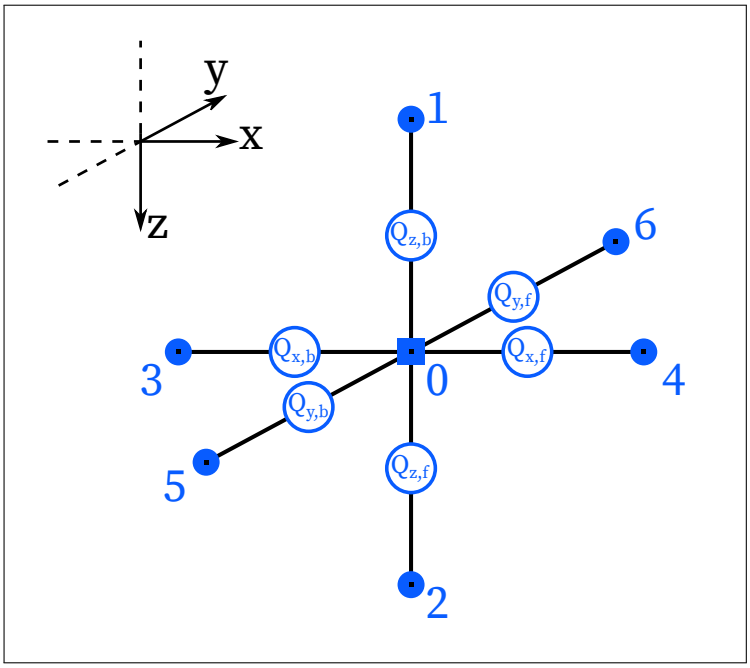

Figure A.2.: The 6 additional *fully staggered points* used in the central finite difference formulation, where heat fluxes ($Q_{m,n}$) between node 0 and its neighbours are expressed. The m subscript denotes the axis, the n subscript the along-axis direction (b backwards, f forwards).

are plotted as sensibly different on purpose, to highlight the fact that they may be not equal, in the general case.

We can now write the FD approximation for the fluxes in Eq. A.9:

$$2\frac{Q_{x,f} - Q_{x,b}}{s_{x,b} + s_{x,f}} + 2\frac{Q_{y,f} - Q_{y,b}}{s_{y,b} + s_{y,f}} + 2\frac{Q_{z,f} - Q_{z,b}}{s_{z,b} + s_{z,f}} = A_0 \tag{A.11}$$

It is now the turn of FD approximation of the $Q_{m,n}$ fluxes at the staggered nodes. Using node $Q_{x,b}$ as an example (see Fig. A.4 for a sketch):

$$Q_{x,b} = -k_{x,b}\frac{\partial T}{\partial x} \approx -k_{x,b}\frac{\Delta T}{\Delta x} = -k_{x,b}\frac{T_0 - T_3}{s_{x,b}} \tag{A.12}$$

A value of thermal conductivity at the staggered node has been added ($k_{x,b}$). It is computed as the arithmetic average between the conductivities of the central node (node 0) and its neighbour (node 3 in this example):

$$k_{x,b} = \frac{k_0 + k_3}{2} \tag{A.13}$$

By doing so for all the remaining $Q_{m,n}$ fluxes at staggered nodes around

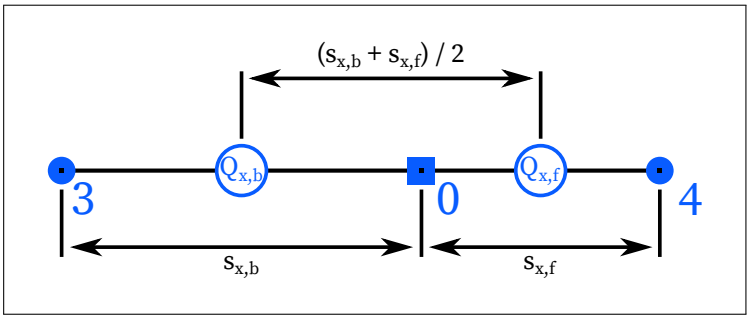

Figure A.3.: One dimensional sketch showing the nodes (basic and staggered) and the spacing distances involved in the FD example of Eq. A.10.

node 0, Eq. A.11 becomes:

$$
\begin{aligned}
&2\frac{\left(-k_{x,f}\dfrac{T_4-T_0}{s_{x,f}}\right)-\left(-k_{x,b}\dfrac{T_0-T_3}{s_{x,b}}\right)}{s_{x,b}+s_{x,f}}+\\
&2\frac{\left(-k_{y,f}\dfrac{T_6-T_0}{s_{y,f}}\right)-\left(-k_{y,b}\dfrac{T_0-T_5}{s_{y,b}}\right)}{s_{y,b}+s_{y,f}}+\\
&2\frac{\left(-k_{z,f}\dfrac{T_2-T_0}{s_{z,f}}\right)-\left(-k_{z,b}\dfrac{T_0-T_1}{s_{z,b}}\right)}{s_{z,b}+s_{z,f}}=A_0
\end{aligned}
\tag{A.14}
$$

Further expressing the averaged conductivities at staggered nodes $k_{m,n}$, we

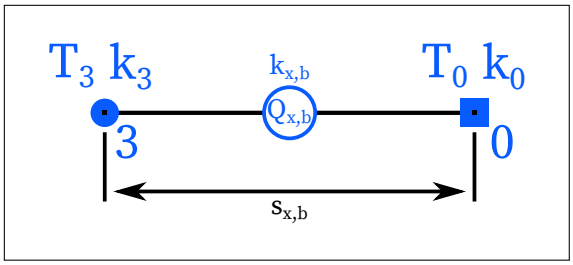

Figure A.4.: One dimensional sketch showing the nodes, parameters, and spacing involved in the example of Eq. A.12, the FD approximation of heat flux at a staggered node $Q_{x,b}$.

obtain:

$$
\begin{aligned}
&2\frac{\left(\frac{k_0+k_4}{2}\frac{T_0-T_4}{s_{x,f}}\right)-\left(\frac{k_0+k_3}{2}\frac{T_3-T_0}{s_{x,b}}\right)}{s_{x,b}+s_{x,f}}+\\
&2\frac{\left(\frac{k_0+k_6}{2}\frac{T_0-T_6}{s_{y,f}}\right)-\left(\frac{k_0+k_5}{2}\frac{T_5-T_0}{s_{y,b}}\right)}{s_{y,b}+s_{y,f}}+\\
&2\frac{\left(\frac{k_0+k_2}{2}\frac{T_0-T_2}{s_{z,f}}\right)-\left(\frac{k_0+k_1}{2}\frac{T_1-T_0}{s_{z,b}}\right)}{s_{z,b}+s_{z,f}}=A_0
\end{aligned}
\tag{A.15}
$$

note that the order of ΔT differences was swapped, to take into account the negative sign of k in Eq. A.14.

We started with the FD discretisation of fluxes at the central node (Eq. A.11), then formulated the FD discretisation of fluxes at staggered nodes (Eq. A.12). This is called a 'conservative finite-difference discretisation', which allows for variable thermal conductivity. Gerya (2010) provides a thorough explanation on its rationale, using the Stokes equation with variable viscosity and the Lagrangian heat conservation equation (non-steady state) as examples.

A.2. Definition of the system of linear equations

With the derivation described in the previous section, a finite-difference approximation for the steady-state heat equation was obtained for one node, surrounded by a neighbour in each Cartesian direction. In order to turn that into a thermal model, we need to transform the FD formulations of each node into a system of linear equations. In addition, the boundary conditions must be defined and specified in the appropriate form. The system is in the following form:

$$\boldsymbol{L}\boldsymbol{T} = \boldsymbol{R} \tag{A.16}$$

For a system of n equations (i.e. n nodes, including those used to impose boundary conditions), $\boldsymbol{T}$ is n by 1 vector of unknowns (the sought temperature at each node), $\boldsymbol{R}$ is a 1 by n vector of the right-hand-sides of the equations, and $\boldsymbol{L}$ is a n by n matrix of coefficients which multiply the elements of T. In the FD modelling case of this thesis, $\boldsymbol{L}$ is a sparse matrix, i.e. most of its elements are zero. This is a direct consequence of the 7-nodes stencil that define the parameters of the heat equation in each node: each linear equation, thus each line in matrix $\boldsymbol{L}$, has 7 non-zero parameters for inner nodes. As described afterwards,

boundary nodes have one to two non-zero elements in $\boldsymbol{L}$, depending on their type.

By expressing an FD model as a system of linear equations (Eq. A.16) we can solve for the unknown $\boldsymbol{T}$, provided that $\boldsymbol{L}$ is nonsingular:

$$\boldsymbol{T} = \boldsymbol{L}^{-1}\boldsymbol{R} \tag{A.17}$$

As mentioned when describing the thermal application (chapter 3), for the aim of this thesis $\boldsymbol{L}$ was inverted using the *UMFPACK* factorization for sparse matrices (Davis, 2006). It is a direct solver therefore, for an increasing number of dimensions and model nodes, it may result in an unmanageable amount of memory. The call to a fall-back alternative, an iterative solver (the generalized minimal residual method, *gmres*, see Saad and Schultz, 1986), has been included in the code, but it never occurred to require resorting to it, in the experiments described here.

Indexing in the coefficient matrix The form of the system (Eq. A.16) requires that each T_i that appears in the equation of each node is expressed in a separate term, multiplied by a coefficient L_i. This results in an equation in the general form $\sum(L_i T_i) = R_r$, an equation for each r-row of $\boldsymbol{L}$. The coefficients of each equation are then placed in the proper column of $\boldsymbol{L}$, i.e. the column corresponding to the element of vector $\boldsymbol{T}$ that they multiply.

Using the r-th row of the coefficient matrix $\boldsymbol{L}$ as an example, expressing the coefficients in the left-hand-side of the equation of the r-th node of the model, we can formulate the following. The coefficient that multiplies the temperature in the r-th node is in $L_{r(0),r(0)}$. This is T_0 in the heat equation for an inner node (Eq. A.15). Leaving the issue of indexing aside for a moment – for the sake of clarity – we call $r(i)$ the index related to the i-th neighbour in the notation of Eq. A.15. The structure of this r-th row of $\boldsymbol{L}$ will be:

$$\cdots \quad L_{r(0),r(5)} \quad \cdots \quad L_{r(0),r(3)} \quad \cdots \quad L_{r(0),r(1)} \quad L_{r(0),r(0)} \quad L_{r(0),r(2)} \quad \cdots \quad L_{r(0),r(4)} \quad \cdots \quad L_{(0),r(6)} \quad \cdots$$

The ellipses ($\cdots$) indicate zero elements in the sparse matrix.

In order to fill the coefficient matrix, the geometric coordinates of each node in the 3-D mesh must be transformed to a *global index* r that expresses its position in $\boldsymbol{T}_r$, $\boldsymbol{L}_{r,r}$, $\boldsymbol{R}_r$. This is trivial for a rectilinear mesh, by knowing the number of nodes along each axis (x_n, y_n, z_n) and the defined axis ordering (z, then x, then y, in this case). The vectors of grid steps along each axis, which are not necessarily constant, are known and provide a linear map between axis coordinates (z, x, y) and element along the axis (u, v, w). The *global index* for a node in u, v, w is therefore:

$$r(u, v, w) = (w - 1)x_n z_n + (v - 1)z_n + u \tag{A.18}$$

when u, v, w are counted starting from 1. Therefore, moving to the next node:

- along z implies changing r by one;
- along x implies changing r by z_n;
- along y implies changing r by x_n times z_n.

An example for a 3×3 model is shown in Fig. A.5.

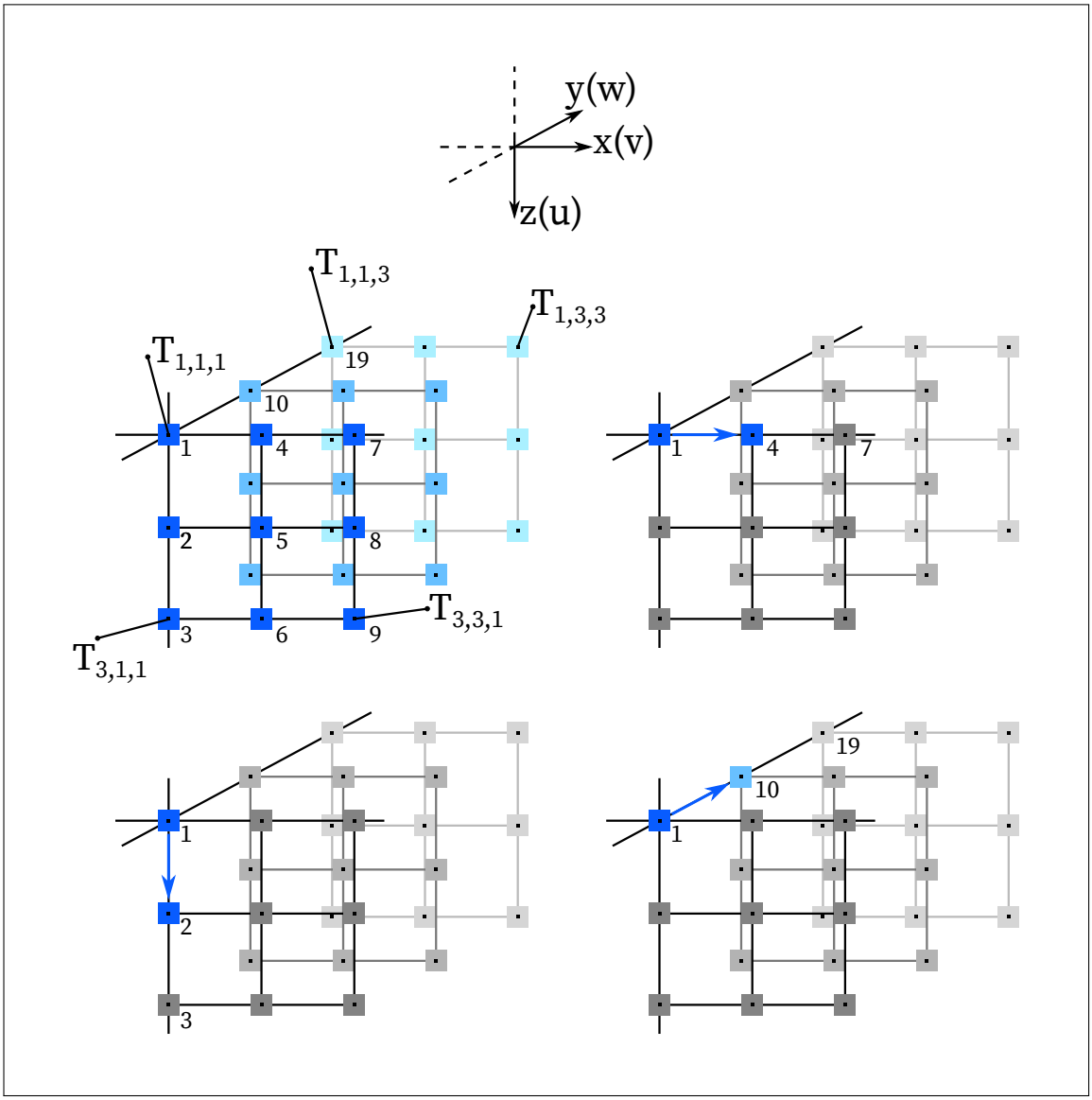

Figure A.5.: Cartesian coordinates and global indexing, illustrated for a 3×3 mesh. The value of $r(u, v, w)$ (Eq. A.18) is shown beside each node square. Three examples of node-by-node movement are shown.

A.3. Boundary conditions

Two types of boundary conditions are specified for the nodes at the boundary of the model mesh:

- at the top and bottom boundaries, temperature is set: a first-type (Dirichlet) boundary condition in the form $T(\text{boundary}) = T$;
- at the vertical boundaries (the sides normal to the x and y axes), zero-flux is set: a second-type (Neumann) boundary condition in the form $\partial T / \partial x = 0$ (where x is the cartesian axis the boundary is normal to).

First type: boundary temperature In the matrix form of the system of linear equations, the first-type boundary condition for the r-th node results in the following equation:

$$1 \cdot T(r) = T_b \tag{A.19}$$

where T_b is the temperature at the boundary (in this work, either the surface temperature or the lithosphere-asthenosphere boundary temperature). This results in only one coefficient for the r-th row in the coefficient matrix $\boldsymbol{L}$: $\boldsymbol{L}_{r,r} = 1$. In the general case, the topography and the base of the lithosphere are not flat. This is achieved by imposing the same condition, using coefficients, to all the inner mesh nodes at and above the topography and at and below the lithosphere-asthenosphere boundary. An alternative formulation for the bottom boundary is to provide it flat with a varying temperature – this use case, which was implemented but not employed in this work, allows to use the type of depth-slice data which can be inferred from e.g. seismic tomography. As a side note, the physical meaning of this type of boundary, in steady state, is that the heat transfer and heat production from the base of the lithosphere to the topography is not increasing the temperature of the atmosphere (or ocean) above the latter, nor decreasing the temperature of the asthenosphere beneath the former – this is a fundamental assumption of steady state thermal modelling.

Second type: no heat flux boundary Imposing a zero heat flux means that no temperature gradient should be present across the boundary: i.e. given a temperature T_0 at the boundary node (global index r_0) and a temperature T_1 at an additional node outside the boundary (global index r_1), then $T_0 - T_1 = 0$. In the matrix form of the system of linear equations, this results in:

$$1 \cdot T(r_0) - 1 \cdot T(r_1) = 0 \tag{A.20}$$

Thus we now have two coefficients for the r_0-th row in the coefficient matrix $\boldsymbol{L}$: $\boldsymbol{L}_{r_0,r_0} = 1$ and $\boldsymbol{L}_{r_0,r_1} = -1$. Note that zero horizontal flux would be observed for a

model which is infinitely uniform along the zero-flux axis. This implies that 2-D 'sections' or 1-D 'columns' can be also modelled with this 3-D implementation, provided that the mesh is built accordingly.

A.4. Building the coefficient matrix

As mentioned in section A.2, the temperature at neighbour nodes that appear in the FD formulation of the heat equation (Eq. A.15) must be expressed in separate terms, i.e. the equation must be rearranged in the 'explicit form' for T. Starting again with the first term only (the one dealing with the two neighbours along x), as an example:

$$
\begin{aligned}
&2\frac{\left(\frac{k_0+k_4}{2}\frac{T_0-T_4}{s_{x,f}}\right)-\left(\frac{k_0+k_3}{2}\frac{T_3-T_0}{s_{x,b}}\right)}{s_{x,b}+s_{x,f}}= \\
&=\frac{\frac{(k_0+k_4)(T_0-T_4)}{s_{x,f}}-\frac{(k_0+k_3)(T_3-T_0)}{s_{x,b}}}{s_{x,b}+s_{x,f}}= \\
&=\frac{(k_0+k_4)(T_0-T_4)}{s_{x,f}(s_{x,b}+s_{x,f})}-\frac{(k_0+k_3)(T_3-T_0)}{s_{x,b}(s_{x,b}+s_{x,f})}= \\
&=\frac{T_0(k_0+k_4)}{s_{x,f}(s_{x,b}+s_{x,f})}-\frac{T_4(k_0+k_4)}{s_{x,f}(s_{x,b}+s_{x,f})}+ \\
&\quad-\frac{T_3(k_0+k_3)}{s_{x,b}(s_{x,b}+s_{x,f})}+\frac{T_0(k_0+k_3)}{s_{x,b}(s_{x,b}+s_{x,f})}= \\
&=T_0\left(\frac{k_0+k_4}{s_{x,f}(s_{x,b}+s_{x,f})}+\frac{k_0+k_3}{s_{x,b}(s_{x,b}+s_{x,f})}\right)+ \\
&\quad-T_4\frac{k_0+k_4}{s_{x,f}(s_{x,b}+s_{x,f})}-T_3\frac{k_0+k_3}{s_{x,b}(s_{x,b}+s_{x,f})}=
\end{aligned}
\tag{A.21}
$$

Therefore, the coefficients in $\boldsymbol{L}$ are:

$$
3: \qquad \boldsymbol{L}_{r(u,v,w),r(u,v-1,w)} = -\frac{k_0+k_3}{s_{x,b}(s_{x,b}+s_{x,f})} \tag{A.22}
$$

$$
4: \qquad \boldsymbol{L}_{r(u,v,w),r(u,v+1,w)} = -\frac{k_0+k_4}{s_{x,f}(s_{x,b}+s_{x,f})} \tag{A.23}
$$

keeping in mind that the global indexes r for neighbour-3 and neighbour-4 (one grid step along x) are given by Eq. A.18.

The coefficients for the terms regarding the neighbours along y and along z follow from similar derivations, which are omitted for brevity. The result is:

$$5: \quad \boldsymbol{L}_{r(u,v,w),r(u,v,w-1)} = -\frac{k_0 + k_5}{s_{y,b}(s_{y,b} + s_{y,f})} \tag{A.24}$$

$$6: \quad \boldsymbol{L}_{r(u,v,w),r(u,v,w+1)} = -\frac{k_0 + k_6}{s_{y,f}(s_{y,b} + s_{y,f})} \tag{A.25}$$

$$1: \quad \boldsymbol{L}_{r(u,v,w),r(u-1,v,w)} = -\frac{k_0 + k_1}{s_{z,b}(s_{z,b} + s_{z,f})} \tag{A.26}$$

$$2: \quad \boldsymbol{L}_{r(u,v,w),r(u+2,v,w)} = -\frac{k_0 + k_2}{s_{z,f}(s_{z,b} + s_{z,f})} \tag{A.27}$$

By grouping the T_0 terms obtained in Eq. A.21 for x-neighbours and their analogues for y- and z-neighbours (omitted), we obtain the coefficient on the diagonal:

$$\begin{aligned} 0: \quad \boldsymbol{L}_{r(u,v,w),r(u,v,w)} = &\left(\frac{k_0 + k_3}{s_{x,b}(s_{x,b} + s_{x,f})} + \frac{k_0 + k_4}{s_{x,f}(s_{x,b} + s_{x,f})}\right) + \\ &+ \left(\frac{k_0 + k_5}{s_{y,b}(s_{y,b} + s_{y,f})} + \frac{k_0 + k_6}{s_{y,f}(s_{y,b} + s_{y,f})}\right) + \\ &+ \left(\frac{k_0 + k_1}{s_{z,b}(s_{z,b} + s_{z,f})} + \frac{k_0 + k_2}{s_{z,f}(s_{z,b} + s_{z,f})}\right) \end{aligned} \tag{A.28}$$

Contents of the coefficient matrix The structure of the sparse matrix $\boldsymbol{L}$ may be better understood by showing the position of its non-zero elements. Fig. A.6 shows the non-zero elements of the coefficient matrix for a $79 \times 75 \times 104$ node model ($x \times y \times z$). The size of $\boldsymbol{L}$ in this case is $616\,200 \times 616\,200$, with 3 588 570 non-zero elements over a total of about 3.8×10^{11} elements (its sparsity ratio is about of 9×10^{-6}). The coefficient structure of each equation is not discernible at this scale. Fig. A.7 shows a zoom in towards the first ten thousands of elements of a relatively smaller model with part of its structure labelled. Note that the adjacent elements of the matrix are still too close to be plotted, therefore the inner node equations appear to have 5 terms instead of 7.

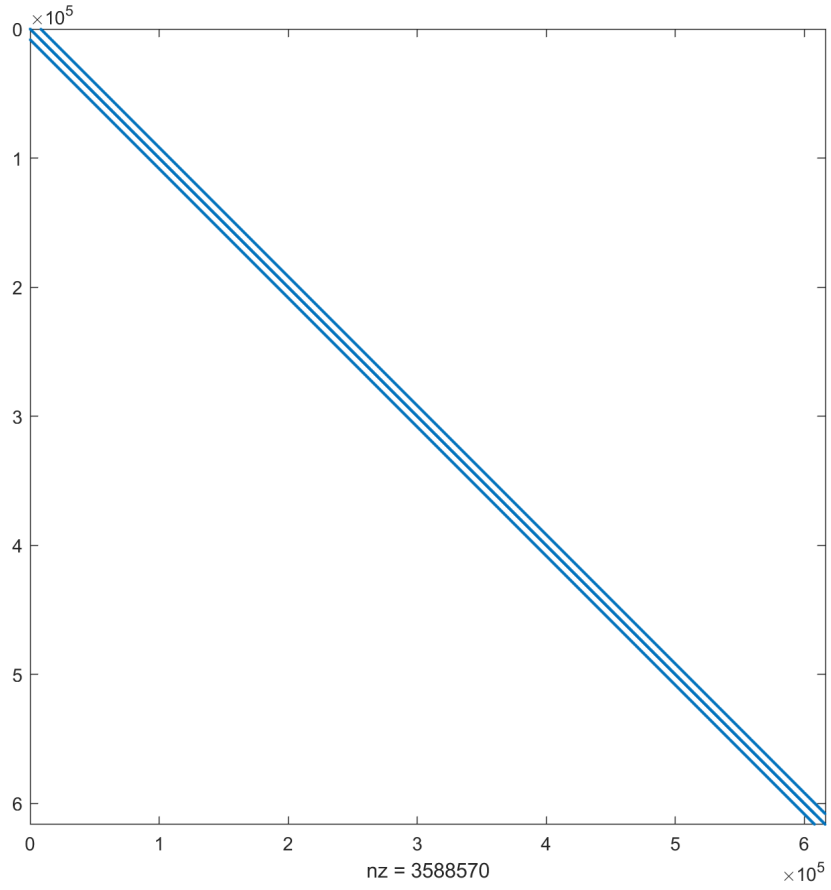

Figure A.6.: Example showing the non-zero elements of the coefficient matrix $\boldsymbol{L}$ for a 616 200-node model. Note that at this scale it appears as a symmetrical banded matrix: this is not the case, due to the boundary conditions.

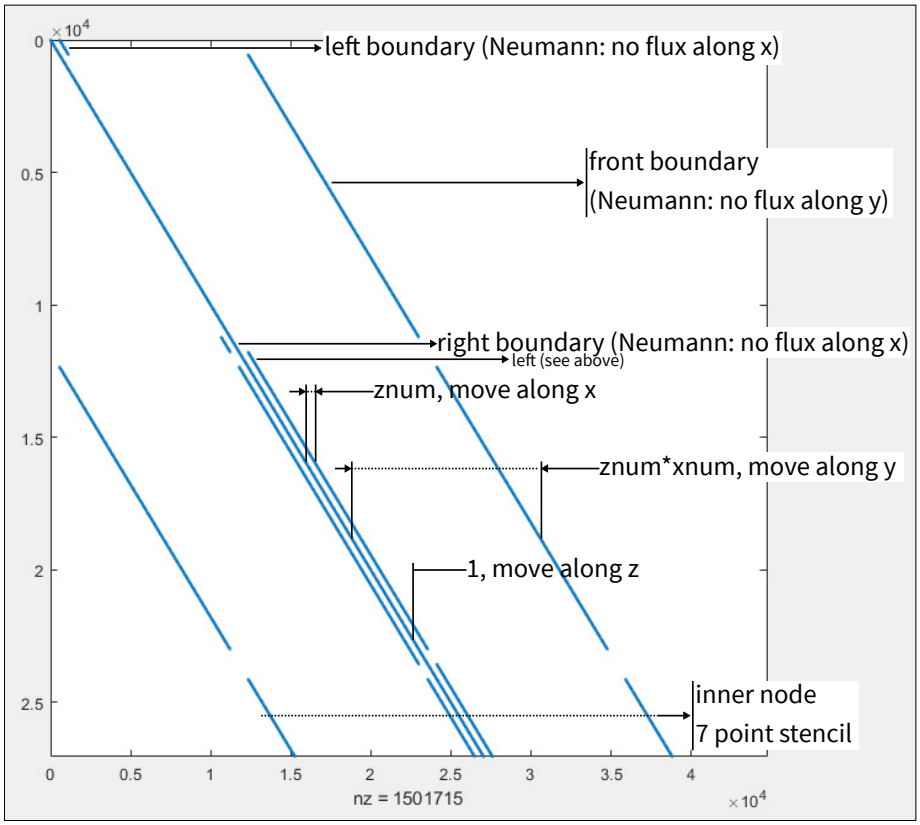

Figure A.7.: Zoomed-in portion of an example of coefficient matrix $\boldsymbol{L}$, with the non-zero elements plotted as dots. The different arrangements of coefficients for the equations of inner nodes and boundaries are labelled. Note that the zoom level here is still not sufficient to resolve the elements adjacent to the diagonal, i.e. the coefficients for neighbour nodes along z.

Bibliography

Afonso, J. C., Fernàndez, M., Ranalli, G., Griffin, W. L., and Connolly, J. A. D. (2008). "Integrated geophysical-petrological modeling of the lithosphere and sublithospheric upper mantle: Methodology and applications". *Geochemistry, Geophysics, Geosystems* 9.5, pp. 1–36. ISSN: 1525-2027. DOI: 10.1029/2007GC001834.

Afonso, J. C., Fullea, J., Griffin, W. L., Yang, Y., Jones, A. G., Yang, Y., Connolly, J. A. D., and Reilly, S. Y. O. (2013a). "3-D multiobservable probabilistic inversion for the compositional andthermal structure of the lithosphere and upper mantle. I: A priori petrological information and geophysical observables". *Journal of Geophysical Research: Solid Earth* 118.5, pp. 2586–2617. DOI: 10.1002/jgrb.50124,2013.

Afonso, J. C., Fullea, J., Yang, Y., Connolly, J., and Jones, A. (2013b). "3-D multi-observable probabilistic inversion for the compositional and thermal structure of the lithosphere and upper mantle. II: General methodology and resolution analysis". *Journal of Geophysical Research: Solid Earth* 118.4, pp. 1650–1676. DOI: 10.1002/jgrb.50123. URL: http://doi.wiley.com/10.1002/jgrb.50123.

Afonso, J. C., Salajegheh, F., Szwillus, W., Ebbing, J., and Gaina, C. (2019). "A global reference model of the lithosphere and upper mantle from joint inversion and analysis of multiple data sets". *Geophysical Journal International* 217.3, pp. 1602–1628. DOI: 10.1093/gji/ggz094.

Aitken, A., Altinay, C., and Gross, L. (2015). "Australia's lithospheric density field, and its isostatic equilibration". *Geophysical Journal International* 203.3, pp. 1961–1976. DOI: 10.1093/gji/ggv396.

Akima, H. (1974). "A Method of Bivariate Interpolation and Smooth Surface Fitting Based on Local Procedures". *Communications of the ACM* 17.1, pp. 18–20. DOI: 10.1145/360767.360779.

Alessio, K. L., Hand, M., Kelsey, D. E., Williams, M. A., Morrissey, L. J., and Barovich, K. (2018). "Conservation of deep crustal heat production". *Geology* 46.4, pp. 2–5. DOI: 10.1130/G39970.1.

Allen, P. A. and Allen, J. R. (2013). *Basin analysis: Principles and application to petroleum play assessment*. John Wiley & Sons. ISBN: 9780470673775.

Artemieva, I. M. (2006). "Global 1°×1° thermal model TC1 for the continental lithosphere: Implications for lithosphere secular evolution". *Tectonophysics*

416.1. part of special issue: The Heterogeneous Mantle, pp. 245–277. DOI: 10.1016/j.tecto.2005.11.022.

Artemieva, I. M. and Thybo, H. (2013). "EUNAseis: A seismic model for Moho and crustal structure in Europe, Greenland, and the North Atlantic region". *Tectonophysics* 609, pp. 97–153. DOI: 10.1016/j.tecto.2013.08.004.

Artemieva, I. M., Thybo, H., Jakobsen, K., Sørensen, N. K., and Nielsen, L. S. (2017). "Heat production in granitic rocks: Global analysis based on a new data compilation GRANITE2017". *Earth-Science Reviews* 172.July, pp. 1–26. DOI: 10.1016/j.earscirev.2017.07.003.

Aster, R. C., Borchers, B., and Thurber, C. H. (2013). *Parameter Estimation and Inverse Problems*. 2nd ed. Elsevier Science. 376 pp. ISBN: 978-0-12-385048-5. DOI: 10.1016/C2009-0-61134-X.

Bagherbandi, M., Bai, Y., Sjöberg, L. E., Tenzer, R., Abrehdary, M., Miranda, S., and Alcacer Sanchez, J. M. (2017). "Effect of the lithospheric thermal state on the Moho interface: A case study in South America". *Journal of South American Earth Sciences* 76, pp. 198–207. DOI: 10.1016/j.jsames.2017.02.010.

Bagherbandi, M. and Sjöberg, L. E. (2012). "Non-isostatic effects on crustal thickness: A study using CRUST2.0 in Fennoscandia". *Physics of the Earth and Planetary Interiors* 200-201, pp. 37–44. DOI: 10.1016/j.pepi.2012.04.001.

Balmino, G., Vales, N., Bonvalot, S., and Briais, A. (2012). "Spherical harmonic modelling to ultra-high degree of Bouguer and isostatic anomalies". *Journal of Geodesy* 86.7, pp. 499–520. DOI: 10.1007/s00190-011-0533-4.

Bamber, J. L., Griggs, J., Hurkmans, R., Dowdeswell, J., Gogineni, S., Howat, I., Mouginot, J., Paden, J., Palmer, S., Rignot, E., et al. (2013). "A new bed elevation dataset for Greenland". *The Cryosphere* 7.2, pp. 499–510. DOI: 10.5194/tc-7-499-2013.

Barthelmes, F. (2008). *Low Pass Filtering of Gravity Field Models by Gently Cutting the Spherical Harmonic Coefficients of Higher Degrees*. URL: http://icgem.gfz-potsdam.de/gentlecut_engl.pdf.

Barthelmes, F. (2013). *Definition of Functionals of the Geopotential and Their Calculation from Spherical Harmonic Models, Scientific Technical Report STR09/02, Revised Edition*. Tech. rep. Potsdam: GFZ. DOI: 10.2312/GFZ.b103-0902-26. URL: http://icgem.gfz-potsdam.de/str-0902-revised.pdf.

Bassin, C., Laske, G., and Masters, G. (2000). "The current limits of resolution for surface wave tomography in North America". In: EOS Trans. AGU. 81: Fall Meet. Suppl., Abstract.

Becker, J. J., Sandwell, D. T., Smith, W. H. F., Braud, J., Binder, B., Depner, J., Fabre, D., Factor, J., Ingalls, S., Kim, S.-H., Ladner, R., Marks, K., Nelson, S., Pharaoh, A., Trimmer, R., Rosenberg, J. V., Wallace, G., and Weatherall, P. (2009). "Global Bathymetry and Elevation Data at 30 Arc Seconds Resolution: SRTM30_PLUS". *Marine Geodesy* 32.4, pp. 355–371. DOI: 10.1080/01490410903297766.

Benedek, J. (2009). “The synthetic modeling of the gravitational field”. PhD thesis. The University of West Hungary.

Benedek, J. (2016). “The effect of the point density of gravity data on the accuracy of geoid undulations computed by Stokes FFT method”. *Publications in Geomatics* 19.

Bishop, C. M. (2006). *Pattern Recognition and Machine Learning (Information Science and Statistics)*. Berlin, Heidelberg: Springer-Verlag. ISBN: 0387310738.

Blakely, R. (1996). *Potential Theory in Gravity and Magnetic Applications*. Stanford-Cambridge Program. Cambridge University Press. ISBN: 9780521575478.

Block, A. E., Bell, R. E., and Studinger, M. (2009). “Antarctic crustal thickness from satellite gravity: Implications for the Transantarctic and Gamburtsev Subglacial Mountains”. *Earth and Planetary Science Letters* 288.1, pp. 194–203. DOI: 10.1016/j.epsl.2009.09.022.

Bormann, P. (2002). “Global 1-D Earth models”. In: *New Manual of Seismological Observatory Practice (NMSOP-2)*. Ed. by P. Bormann. GFZ German Research Centre for Geosciences, Potsdam, pp. 1–12. DOI: 10.2312/GFZ.NMSOP-2_DS_2.1. URL: http://bib.telegrafenberg.de/publizieren/vertrieb/nmsop/.

Bouman, J., Ebbing, J., Meekes, S., Fattah, R. A., Fuchs, M., Gradmann, S., Haagmans, R., Lieb, V., Schmidt, M., Dettmering, D., and Bosch, W. (2015). “GOCE gravity gradient data for lithospheric modeling”. *International Journal of Applied Earth Observation and Geoinformation* 35, Part A. ESA GOCE solid earth workshop, 16-17 October 2012, pp. 16–30. DOI: 10.1016/j.jag.2013.11.001.

Bowin, C. (1983). “Depth of principal mass anomalies contributing to the earth’s geoidal undulations and gravity anomalies”. *Marine Geodesy* 7.1-4, pp. 61–100. DOI: 10.1080/15210608309379476.

Braitenberg, C., Mariani, P., and Pivetta, T. (2011). “GOCE observations in exploration geophysics”. In: *Proceedings of the 4th International GOCE User Workshop*. Vol. ESA SP-696. Technische Universität München (TUM), Munich, Germany.

Braitenberg, C., Wienecke, S., Ebbing, J., Born, W., and Redfield, T. (2007). “Joint gravity and isostatic analysis for basement studies–a novel tool”. In: *EGM 2007 International Workshop*. URL: http://www.lithoflex.org/bib/egm_07_1.pdf.

Brockmann, J. M., Zehentner, N., Höck, E., Pail, R., Loth, I., Mayer-Gürr, T., and Schuh, W.-D. (2014). “EGM_TIM_RL05: An independent geoid with centimeter accuracy purely based on the GOCE mission”. *Geophysical Research Letters* 41.22, pp. 8089–8099. DOI: 10.1002/2014GL061904.

Bucha, B. and Janák, J. (2013). "A MATLAB-based graphical user interface program for computing functionals of the geopotential up to ultra-high degrees and orders". *Computers & Geosciences* 56, pp. 186–196. ISSN: 0098-3004. DOI: 10.1016/j.cageo.2013.03.012.

Burov, E. B. and Diament, M. (1995). "The effective elastic thickness (Te) of continental lithosphere: What does it really mean?" *Journal of Geophysical Research: Solid Earth* 100.B3, pp. 3905–3927. DOI: 10.1029/94JB02770.

Cammarano, F., Tackley, P., and Boschi, L. (2011). "Seismic, petrological and geodynamical constraints on thermal and compositional structure of the upper mantle: Global thermochemical models". *Geophysical Journal International* 187.3, pp. 1301–1318. DOI: 10.1111/j.1365-246X.2011.05223.x.

Carslaw, H. S. and Jaeger, J. C. (1959). *Conduction of Heat in Solids*. 2nd ed. Clarendon Press Oxford. ISBN: 9780198533030.

Čermák, V. (1993). "Lithospheric thermal regimes in Europe". *Physics of the Earth and Planetary Interiors* 79.1-2, pp. 179–193. DOI: 10.1016/0031-9201(93)90147-2.

Čermák, V. and Bodri, L. (1986). "Two-dimensional temperature modelling along five East-European geotraverses". *Journal of Geodynamics* 5.2, pp. 133–163. DOI: 10.1016/0264-3707(86)90003-7.

Chan, T. F., Golub, G. H., and LeVeque, R. J. (1982). "Updating Formulae and a Pairwise Algorithm for Computing Sample Variances". In: *COMPSTAT 1982 5th Symposium held at Toulouse 1982*. Ed. by H. Caussinus, P. Ettinger, and R. Tomassone, pp. 30–41. DOI: 10.1007/978-3-642-51461-6_3.

Chapman, D. S. (1986). "Thermal gradients in the continental crust". *Geological Society, London, Special Publications* 24.1, pp. 63–70. DOI: 10.1144/GSL.SP.1986.024.01.07.

Chen, W., Tenzer, R., and Gu, X. (2014). "Sediment Stripping Correction to Marine Gravity Data". *Marine Geodesy* 37.4, pp. 419–439. DOI: 10.1080/01490419.2014.932870.

Connolly, J. A. (2009). "The geodynamic equation of state: What and how". *Geochemistry, Geophysics, Geosystems* 10.10. DOI: 10.1029/2009GC002540.

Connolly, J. A. (2005). "Computation of phase equilibria by linear programming: A tool for geodynamic modeling and its application to subduction zone decarbonation". *Earth and Planetary Science Letters* 236.1-2, pp. 524–541. DOI: 10.1016/j.epsl.2005.04.033.

Cooper, C. M., Miller, M. S., and Moresi, L. (2017). "The structural evolution of the deep continental lithosphere". *Tectonophysics* 695, pp. 100–121. DOI: 10.1016/j.tecto.2016.12.004.

Davies, J. H. (2013). "Global map of solid Earth surface heat flow". *Geochemistry, Geophysics, Geosystems* 14.10, pp. 4608–4622. ISSN: 1525-2027. DOI: 10.1002/ggge.20271.

Davies, J. H. and Davies, D. R. (2010). "Earth's surface heat flux". *Solid Earth* 1.1, pp. 5–24. ISSN: 1869-9529. DOI: 10.5194/se-1-5-2010.

Davis, T. (2006). *Direct Methods for Sparse Linear Systems*. Society for Industrial and Applied Mathematics. Chap. 4, pp. 37–68. ISBN: 978-0-89871-613-9. DOI: 10.1137/1.9780898718881.

Deschamps, F., Snieder, R., and Trampert, J. (2001). "The relative density-to-shear velocity scaling in the uppermost mantle". *Physics of the Earth and Planetary Interiors* 124.3-4, pp. 193–212. DOI: 10.1016/S0031-9201(01)00199-6.

Driscoll, J. R. and Healy, D. M. (1994). "Computing fourier transforms and convolutions on the 2-sphere". 15.2, pp. 202–250. DOI: 10.1006/aama.1994.1008.

Dziewonski, A. M. and Anderson, D. L. (1981). "Preliminary reference Earth model". *Physics of the Earth and Planetary Interiors* 25.4, pp. 297–356. DOI: 10.1016/0031-9201(81)90046-7.

Eaton, D. W., Darbyshire, F., Evans, R. L., Grütter, H., Jones, A. G., and Yuan, X. (2009). "The elusive lithosphere-asthenosphere boundary (LAB) beneath cratons". *Lithos* 109.1-2, pp. 1–22. DOI: 10.1016/j.lithos.2008.05.009.

Ebbing, J., Braitenberg, C., and Götze, H. (2001). "Forward and inverse modelling of gravity revealing insight into crustal structures of the Eastern Alps". *Tectonophysics* 337.3-4, pp. 191–208. DOI: 10.1016/S0040-1951(01)00119-6.

Ebbing, J., Braitenberg, C., and Götze, H.-J. (2006). "The lithospheric density structure of the Eastern Alps". *Tectonophysics* 414.1–4. TRANSALP Transect Through a Young Collisional Orogen Conference, pp. 145–155. ISSN: 0040-1951. DOI: 10.1016/j.tecto.2005.10.015.

Emerick, A. A. and Reynolds, A. C. (2013). "Ensemble smoother with multiple data assimilation". *Computers & Geosciences* 55, pp. 3–15. DOI: 10.1016/j.cageo.2012.03.011.

Eshagh, M., Bagherbandi, M., and Sjöberg, L. E. (2011). "A combined global Moho model based on seismic and gravimetric data". *Acta Geodaetica et Geophysica Hungarica* 46.1, pp. 25–38. DOI: 10.1556/AGeod.46.2011.1.3.

Eshagh, M., Ebadi, S., and Tenzer, R. (2017). "Isostatic GOCE Moho model for Iran". *Journal of Asian Earth Sciences* 138, pp. 12–24. DOI: 10.1016/j.jseaes.2017.01.033.

Eshagh, M., Hussain, M., Tenzer, R., and Romeshkani, M. (2016). "Moho density contrast in central Eurasia from GOCE gravity gradients". *Remote Sensing* 8.5, pp. 1–18. DOI: 10.3390/rs8050418.

Eshagh, M. and Pitoňák, M. (2019). "Elastic Thickness Determination from on-orbit GOCE Data and CRUST1.0". *Pure and Applied Geophysics* 176.2, pp. 685–696. DOI: 10.1007/s00024-018-2018-3.

Fischer, K. M., Ford, H. A., Abt, D. L., and Rychert, C. A. (2010). "The Lithosphere-Asthenosphere Boundary". *Annual Review of Earth and Planetary Sciences* 38.1, pp. 551–575. DOI: 10.1146/annurev-earth-040809-152438.

Floberghagen, R., Fehringer, M., Lamarre, D., Muzi, D., Frommknecht, B., Steiger, C., Piñeiro, J., and Costa, A. da (2011). "Mission design, operation and exploitation of the gravity field and steady-state ocean circulation explorer mission". *Journal of Geodesy* 85.11, pp. 749–758. DOI: 10.1007/s00190-011-0498-3.

Forsberg, R. and Tscherning, C. C. (1981). "The use of height data in gravity field approximation by collocation". *Journal of Geophysical Research: Solid Earth* 86.B9, pp. 7843–7854. DOI: 10.1029/JB086iB09p07843.

Fourier, J.-B. J. (1822). *Théorie analytique de la chaleur*. Chez Firmin Didot, père et fils.

Fretwell, P., Pritchard, H. D., Vaughan, D. G., Bamber, J. L., Barrand, N. E., Bell, R., Bianchi, C., Bingham, R. G., Blankenship, D. D., Casassa, G., Catania, G., Callens, D., Conway, H., Cook, A. J., Corr, H. F. J., Damaske, D., Damm, V., Ferraccioli, F., Forsberg, R., Fujita, S., Gim, Y., Gogineni, P., Griggs, J. A., Hindmarsh, R. C. A., Holmlund, P., Holt, J. W., Jacobel, R. W., Jenkins, A., Jokat, W., Jordan, T., King, E. C., Kohler, J., Krabill, W., Riger-Kusk, M., Langley, K. A., Leitchenkov, G., Leuschen, C., Luyendyk, B. P., Matsuoka, K., Mouginot, J., Nitsche, F. O., Nogi, Y., Nost, O. A., Popov, S. V., Rignot, E., Rippin, D. M., Rivera, A., Roberts, J., Ross, N., Siegert, M. J., Smith, A. M., Steinhage, D., Studinger, M., Sun, B., Tinto, B. K., Welch, B. C., Wilson, D., Young, D. A., Xiangbin, C., and Zirizzotti, A. (2013). "Bedmap2: improved ice bed, surface and thickness datasets for Antarctica". *The Cryosphere* 6, pp. 4305–4361. DOI: 10.5194/tc-7-375-2013.

Geissler, W. H., Sodoudi, F., and Kind, R. (2010). "Thickness of the central and eastern European lithosphere as seen by S receiver functions". *Geophysical Journal International* 181.2, pp. 604–634. DOI: 10.1111/j.1365-246X.2010.04548.x.

Gerya, T. (2010). *Introduction to Numerical Geodynamic Modelling*. Cambridge University Press. ISBN: 9780521887540. DOI: 10.1201/9781482234213.

Ghiorso, M. S., Hirschmann, M. M., Reiners, P. W., and Kress III, V. C. (2002). "The pMELTS: A revision of MELTS for improved calculation of phase relations and major element partitioning related to partial melting of the mantle to 3 GPa". *Geochemistry, Geophysics, Geosystems* 3.5, pp. 1–35. DOI: 10.1029/2001GC000217.

GOCE-ESA (2014). GO CONS GCF 2 TIM R5 *datasheet*. ESA and Graz University of Technology, Institute for Theoretical and Satellite Geodesy and University of Bonn, Institute of Geodesy and Geoinformation and TU München, Institute of Astronomical and Physical Geodesy. URL: https://earth.esa.int/

documents/10174/1604019/GO_CONS_EGM_GCF_2_TIM_R5_DataSheet.pdf.

Gosnold, W. D. (2011). *Global Heat Flow Database*. Provided by the University of North Dakota, interim custodian. International Heat Flow Commission of the International Association of Seismology and Physics of the Earth's Interior (IASPEI). URL: https://engineering.und.edu/research/global-heat-flow-database/.

Grad, M. and Tiira, T. (2012). "Moho depth of the European Plate from teleseismic receiver functions". *Journal of Seismology* 16.2, pp. 95–105. DOI: 10.1007/s10950-011-9251-x.

Grad, M., Tiira, T., and ESC Working Group (2009). "The Moho depth map of the European Plate". *Geophysical Journal International* 176.1, pp. 279–292. DOI: 10.1111/j.1365-246X.2008.03919.x.

Griffin, W. L., O'Reilly, S. Y., Afonso, J. C., Begg, G. C., O'Reilly, S. Y., Afonso, J. C., and Begg, G. C. (2009). "The composition and evolution of lithospheric mantle: A re-evaluation and its tectonic implications". *Journal of Petrology* 50.7, pp. 1185–1204. DOI: 10.1093/petrology/egn033.

Grombein, T., Seitz, K., and Heck, B. (2013). "Optimized formulas for the gravitational field of a tesseroid". *Journal of Geodesy* 87.7, pp. 645–660. DOI: 10.1007/s00190-013-0636-1.

Grombein, T., Seitz, K., and Heck, B. (2016). "The Rock–Water–Ice Topographic Gravity Field Model RWI_TOPO_2015 and Its Comparison to a Conventional Rock-Equivalent Version". *Surveys in Geophysics* 37.5, pp. 937–976. ISSN: 1573-0956. DOI: 10.1007/s10712-016-9376-0. URL: https://doi.org/10.1007/s10712-016-9376-0.

Guerri, M., Cammarano, F., and Connolly, J. A. D. (2015). "Effects of chemical composition, water and temperature on physical properties of continental crust: COMPOSITION EFFECTS ON CRUST PROPERTIES". *Geochemistry, Geophysics, Geosystems* 16.7, pp. 2431–2449. DOI: 10.1002/2015GC005819.

Hackney, R. I. and Featherstone, W. E. (2003). "Geodetic versus geophysical perspectives of the 'gravity anomaly'". *Geophysical Journal International* 154.1, pp. 35–43. DOI: 10.1046/j.1365-246X.2003.01941.x.

Hammer, S. (1963). "Deep Gravity Interpretation by Stripping". *Geophysics* 28.3, pp. 369–378. DOI: 10.1190/1.1439186.

Hasterok, D. and Chapman, D. S. (2008). "Global Heat Flow: A New Database and a New Approach". In: AGU Fall Meeting Abstracts.

Hasterok, D. and Chapman, D. S. (2011). "Heat production and geotherms for the continental lithosphere". *Earth and Planetary Science Letters* 307.1-2, pp. 59–70. DOI: 10.1016/j.epsl.2011.04.034.

Hasterok, D. and Gard, M. (2016). "Utilizing thermal isostasy to estimate sublithospheric heat flow and anomalous crustal radioactivity". *Earth and Planetary Science Letters* 450, pp. 197–207. DOI: 10.1016/j.epsl.2016.06.037.

Hasterok, D., Gard, M., and Webb, J. (2017). "On the radiogenic heat production of metamorphic, igneous, and sedimentary rocks". *Geoscience Frontiers*. ISSN: 1674-9871. DOI: 10.1016/j.gsf.2017.10.012.

Hasterok, D. and Webb, J. (2017). "On the radiogenic heat production of igneous rocks". *Geoscience Frontiers* 8.5, pp. 919–940. DOI: 10.1016/j.gsf.2017.03.006.

Hauck, S. A., Phillips, R. J., and Hofmeister, A. M. (1999). "Variable conductivity: Effects on the thermal structure of subducting slabs". *Geophysical Research Letters* 26.21, pp. 3257–3260. DOI: 10.1029/1999GL010831.

Hayford, J. F. and Bowie, W. (1912). "The Effect of Topography and Isostatic Compensation Upon the Intensity of Gravity". *US Department of Commerce Special Publication* 10.

Heck, B. and Seitz, K. (2007). "A comparison of the tesseroid, prism and point-mass approaches for mass reductions in gravity field modelling". *Journal of Geodesy* 81.2, pp. 121–136. DOI: 10.1007/s00190-006-0094-0.

Hinze, W. J. (2003). "Bouguer reduction density, why 2.67?" *Geophysics* 68.5, pp. 1559–1560. DOI: 10.1190/1.1620629.

Hinze, W. J., Frese, R. R. B. von, and Saad, A. H. (2013). *Gravity and Magnetic Exploration: Principles, Practices, and Applications*. Cambridge University Press. DOI: 10.1017/CBO9780511843129.

Hinze, W. J., Aiken, C., Brozena, J., Coakley, B., Dater, D., Flanagan, G., Forsberg, R., Hildenbrand, T., Keller, G. R., Kellogg, J., Kucks, R., Li, X., Mainville, A., Morin, R., Pilkington, M., Plouff, D., Ravat, D., Roman, D., Urrutia-fucugauchi, J., Webring, M., Winester, D., and Marc, V. (2005). "New standards for reducing gravity data : The North American gravity database". 70.4, pp. 25–32. DOI: 10.1190/1.1988183.

Hirt, C., Marti, U., Bürki, B., and Featherstone, W. E. (2010). "Assessment of EGM2008 in Europe using accurate astrogeodetic vertical deflections and omission error estimates from SRTM/DTM2006.0 residual terrain model data". *Journal of Geophysical Research* 115.B10, B10404. DOI: 10.1029/2009JB007057.

Hirt, C. and Kuhn, M. (2014). "Band-limited topographic mass distribution generates full-spectrum gravity field: Gravity forward modeling in the spectral and spatial domains revisited". *Journal of Geophysical Research: Solid Earth* 119.4, pp. 3646–3661. DOI: 10.1002/2013JB010900.

Hirt, C. and Kuhn, M. (2017). "Convergence and divergence in spherical harmonic series of the gravitational field generated by high-resolution planetary

topography—A case study for the Moon". *Journal of Geophysical Research: Planets* 122.8, pp. 1727–1746. DOI: 10.1002/2017JE005298.

Hirt, C., Kuhn, M., Featherstone, W. E., and Gtötl, F. (2012). "Topographic/isostatic evaluation of new-generation GOCE gravity field models". *Journal of Geophysical Research: Solid Earth* 117.5, pp. 1–16. DOI: 10.1029/2011JB008878.

Hirt, C. and Rexer, M. (2015a). *Earth2014 1 arcmin global topography and relief models – readme-file V1.1*. URL: http://ddfe.curtin.edu.au/gravitymodels/Earth2014/readme_earth2014.dat.

Hirt, C. and Rexer, M. (2015b). "Earth2014: 1 arc-min shape, topography, bedrock and ice-sheet models - Available as gridded data and degree-10,800 spherical harmonics". *International Journal of Applied Earth Observation and Geoinformation* 39, pp. 103–112. DOI: 10.1016/j.jag.2015.03.001.

Hirt, C., Yang, M., Kuhn, M., Bucha, B., Kurzmann, A., and Pail, R. (2019). "SRTM2gravity: An Ultrahigh Resolution Global Model of Gravimetric Terrain Corrections". *Geophysical Research Letters* 46.9, pp. 4618–4627. DOI: 10.1029/2019GL082521.

Hofmann-Wellenhof, B. and Moritz, H. (2006). *Physical Geodesy*. Springer Vienna. ISBN: 978-3-211-33544-4. DOI: 10.1007/978-3-211-33545-1.

Hofmeister, A. M. (1999). "Mantle Values of Thermal Conductivity and the Geotherm from Phonon Lifetimes". *Science* 283.5408, pp. 1699–1706. DOI: 10.1126/science.283.5408.1699.

Holland, T. J. B. and Powell, R. (1998). "An internally consistent thermodynamic data set for phases of petrological interest". *Journal of Metamorphic Geology* 16.3, pp. 309–343. DOI: 10.1111/j.1525-1314.1998.00140.x.

Horváth, F., Musitz, B., Balázs, A., Végh, A., Uhrin, A., Nádor, A., Koroknai, B., Pap, N., Tóth, T., and Wórum, G. (2015). "Evolution of the Pannonian basin and its geothermal resources". *Geothermics* 53, pp. 328–352. DOI: 10.1016/j.geothermics.2014.07.009.

Hu, X. and Jekeli, C. (2015). "A numerical comparison of spherical, spheroidal and ellipsoidal harmonic gravitational field models for small non-spherical bodies: examples for the Martian moons". *Journal of Geodesy* 89.2, pp. 159–177. DOI: 10.1007/s00190-014-0769-x.

Huang, Y., Chubakov, V., Mantovani, F., Rudnick, R. L., and McDonough, W. F. (2013). "A reference Earth model for the heat-producing elements and associated geoneutrino flux". *Geochemistry, Geophysics, Geosystems* 14.6, pp. 2003–2029. DOI: 10.1002/ggge.20129. eprint: 1301.0365.

Jarvis, A., Reuter, H. I., Nelson, A., Guevara, E., et al. (2008). *Hole-filled SRTM for the globe Version 4*. Available from the CGIAR-SXI SRTM 90m database. URL: http://srtm.csi.cgiar.org.

Jaupart, C. and Mareschal, J.-C. (2003). "Constraints on Crustal Heat Production from Heat Flow Data". In: *Treatise on Geochemistry*. Ed. by H. D. Holland and K. K. Turekian. Oxford: Pergamon, pp. 65–84. ISBN: 978-0-08-043751-4. DOI: 10.1016/B0-08-043751-6/03017-6.

Jaupart, C., Mareschal, J. C., and Iarotsky, L. (2016). "Radiogenic heat production in the continental crust". *Lithos* 262, pp. 398–427. DOI: 10.1016/j.lithos.2016.07.017.

Jokinen, J. and Kukkonen, I. T. (1999). "Random modelling of the lithospheric thermal regime: Forward simulations applied in uncertainty analysis". *Tectonophysics* 306.3-4, pp. 277–292. DOI: 10.1016/S0040-1951(99)00061-X.

Jones, A. G., Plomerova, J., Korja, T., Sodoudi, F., and Spakman, W. (2010). "Europe from the bottom up: A statistical examination of the central and northern European lithosphere-asthenosphere boundary from comparing seismological and electromagnetic observations". *Lithos* 120.1-2, pp. 14–29. DOI: 10.1016/j.lithos.2010.07.013.

Kaban, M. K., Schwintzer, P., and Reigber, C. (2004). "A new isostatic model of the lithosphere and gravity field". *Journal of Geodesy* 78.6, pp. 368–385. DOI: 10.1007/s00190-004-0401-6.

Kaban, M. K., Tesauro, M., and Cloetingh, S. (2010). "An integrated gravity model for Europe's crust and upper mantle". *Earth and Planetary Science Letters* 296.3-4, pp. 195–209. DOI: 10.1016/j.epsl.2010.04.041.

Kaban, M. K., Tesauro, M., Mooney, W. D., and Cloetingh, S. A. P. L. (2014). "Density, temperature, and composition of the North American lithosphere—New insights from a joint analysis of seismic, gravity, and mineral physics data: 1. Density structure of the crust and upper mantle". *Geochemistry, Geophysics, Geosystems* 15.12, pp. 4781–4807. DOI: 10.1002/2014GC005483.

Kennett, B. L. N., Engdahl, E. R., and Buland, R. (1995). "Constraints on seismic velocities in the Earth from traveltimes". *Geophysical Journal International* 122, pp. 108–124. DOI: 10.1111/j.1365-246X.1995.tb03540.x.

Kirby, J. F. (2014). "Estimation of the effective elastic thickness of the lithosphere using inverse spectral methods: The state of the art". *Tectonophysics* 631, pp. 87–116. DOI: https://doi.org/10.1016/j.tecto.2014.04.021.

Kontoghiorghes, E. (2005). *Handbook of Parallel Computing and Statistics*. CRC Press. ISBN: 9780429118647. DOI: 10.1201/9781420028683.

Kuhn, M. and Featherstone, W. E. (2005). "Construction of a Synthetic Earth Gravity Model by Forward Gravity Modelling". In: *A Window on the Future of Geodesy*. Ed. by F. Sansò. Vol. 128, pp. 350–355. ISBN: 9783540274322. DOI: 10.1007/3-540-27432-4_60.

Kvas, A., Mayer-Gürr, T., Krauß, S., Brockmann, J., Schubert, T., Schuh, W.-D., Pail, R., Gruber, T., Jäggi, A., and Meyer, U. (2019a). *The satellite-only gravity*

field model GOCO06s (dataset). GFZ Data Services. DOI: 10.5880/ICGEM.2019.002.

Kvas, A., Mayer-Gürr, T., Krauss, S., Brockmann, J., Schubert, T., Schuh, W.-D., Pail, R., Gruber, T., Jäggi, A., and Meyer, U. (2019b). "The satellite-only gravity field model GOCO06s". In: EGU General Assembly 2019 conference abstracts. DOI: 10.13140/RG.2.2.14101.99047.

LaFehr, T. R. and Nabighian, M. N. (2012). *Fundamentals of Gravity Exploration*. Society of Exploration Geophysicists. DOI: 10.1190/1.9781560803058.

Laske, G., Masters, G., Ma, Z., and Pasyanos, M. (2012). "CRUST1. 0: An updated global model of Earth's crust". In: EGU2012-3743-1. EGU General Assembly 2012 conference abstracts.

Laske, G. and Masters, T. G. (1997). "A global digital map of sediment thickness". *Eos Trans. AGU* 78, F483. URL: http://igppweb.ucsd.edu/~gabi/sediment.html.

Lee, W. H. and Uyeda, S. (1965). "Review of heat flow data". In: *Terrestrial heat flow*. Vol. 8. American Geophysical Union, pp. 87–190. DOI: 10.1029/GM008p0087.

Li, H., Fang, J., and Braitenberg, C. (2017). "Lithosphere density structure beneath the eastern margin of the Tibetan Plateau and its surrounding areas derived from GOCE gradients data". *Geodesy and Geodynamics* 8.3, pp. 147–154.

Limberger, J., Wees, J. D. van, Tesauro, M., Smit, J., Bonté, D., Békési, E., Pluymaekers, M., Struijk, M., Vrijlandt, M., Beekman, F., and Cloetingh, S. (2018). "Refining the thermal structure of the European lithosphere by inversion of subsurface temperature data". *Global and Planetary Change* 171, pp. 18–47. DOI: 10.1016/j.gloplacha.2018.07.009.

Liu, K., Hao, T., Yang, H., Wen, B., Hu, W., He, E., and Xu, Y. (2018). "3D gravity anomaly separation method taking into account the gravity response of the inhomogeneous mantle". *Journal of Asian Earth Sciences* 163, pp. 212–223. DOI: 10.1016/j.jseaes.2018.06.006.

Majorowicz, J. and Wybraniec, S. (2011). "New terrestrial heat flow map of Europe after regional paleoclimatic correction application". *International Journal of Earth Sciences* 100.4, pp. 881–887. DOI: 10.1007/s00531-010-0526-1.

Mareschal, J.-C. and Jaupart, C. (2013). "Radiogenic heat production, thermal regime and evolution of continental crust". *Tectonophysics* 609, pp. 524–534. ISSN: 0040-1951. DOI: 10.1016/j.tecto.2012.12.001.

Mariani, P., Braitenberg, C., and Ussami, N. (2013). "Explaining the thick crust in Paraná basin, Brazil, with satellite GOCE gravity observations". *Journal of South American Earth Sciences* 45, pp. 209–223. ISSN: 0895-9811. DOI: 10.1016/j.jsames.2013.03.008.

Martinec, Z. (1994). "The Minimum Depth of Compensation of Topographic Masses". *Geophysical Journal International* 117.2, pp. 545–554. DOI: 10.1111/j.1365-246X.1994.tb03951.x.

Mather, B., McLaren, S., Taylor, D., Roy, S., and Moresi, L. (2018). "Variations and controls on crustal thermal regimes in Southeastern Australia". *Tectonophysics* 723, pp. 261–276. DOI: https://doi.org/10.1016/j.tecto.2017.12.015.

Mazur, S., Mikolajczak, M., Krzywiec, P., Malinowski, M., Lewandowski, M., and Buffenmyer, V. (2016). "Pomeranian Caledonides, NW Poland — A collisional suture or thin-skinned fold-and-thrust belt?" *Tectonophysics* 692, pp. 29–43. ISSN: 0040-1951. DOI: 10.1016/j.tecto.2016.06.017.

McKenzie, D. and Fairhead, D. (1997). "Estimates of the effective elastic thickness of the continental lithosphere from Bouguer and free air gravity anomalies". *Journal of Geophysical Research: Solid Earth* 102.B12, pp. 27523–27552. DOI: 10.1029/97JB02481.

Meurers, B. (2017). "Chapter 2 - The Physical Meaning of Bouguer Anomalies—General Aspects Revisited". In: *Understanding the Bouguer Anomaly*. Ed. by R. Pašteka, J. Mikuška, and B. Meurers, pp. 13–30. ISBN: 978-0-12-812913-5. DOI: https://doi.org/10.1016/B978-0-12-812913-5.00001-4.

Mikuška, J., Marušiak, I., Pašteka, R., and Pohánka, V. (2007). "Estimation of gravitational effect of crust/mantle boundary based on CRUST 2.0 model". In: *SEG Technical Program Expanded Abstracts 2007*, pp. 800–804. DOI: 10.1190/1.2792532.

Mikuška, J., Pašteka, R., and Marušiak, I. (2006). "Estimation of distant relief effect in gravimetry". *GEOPHYSICS* 71.6, J59–J69. DOI: 10.1190/1.2338333.

Molinari, I. and Morelli, A. (2011). "EPcrust: A reference crustal model for the European Plate". *Geophysical Journal International* 185.1, pp. 352–364. DOI: 10.1111/j.1365-246X.2011.04940.x.

Montagner, J.-P. and Kennett, B. L. N. (1996). "How to reconcile body-wave and normal-mode reference earth models". *Geophysical Journal International* 125.1, pp. 229–248. DOI: 10.1111/j.1365-246X.1996.tb06548.x.

Montagner, J.-P. and Anderson, D. L. (1989). "Constrained reference mantle model". *Physics of the Earth and Planetary Interiors* 58.2-3, pp. 205–227. DOI: 10.1016/0031-9201(89)90055-1.

Mooney, W. D. (2015). "Crust and Lithospheric Structure - Global Crustal Structure". In: *Treatise on Geophysics*. Ed. by G. Schubert. Second Edition. Oxford: Elsevier, pp. 339–390. ISBN: 978-0-444-53803-1. DOI: 10.1016/B978-0-444-53802-4.00010-5.

Mooney, W. D. and Kaban, M. K. (2010). "The North American upper mantle: Density, composition, and evolution". *Journal of Geophysical Research: Solid Earth* 115.B12. DOI: 10.1029/2010JB000866.

Mooney, W. D., Laske, G., and Masters, T. G. (1998). "CRUST 5.1: A global crustal model at 5° × 5°". *Journal of Geophysical Research: Solid Earth* 103.B1, pp. 727–747. DOI: 10.1029/97JB02122.

Moresi, L. and Mather, B. (Mar. 15, 2019a). *litho1pt0, a pPython interface to the Crust1.0 dataset and the lithospheric part of the Litho1.0 dataset*. URL: https://pypi.org/project/litho1pt0/.

Moresi, L. and Mather, B. (2019b). "Stripy: A Python module for (constrained) triangulation in Cartesian coordinates and on a sphere." *Journal of Open Source Software* 4.38, p. 1410. DOI: 10.21105/joss.01410.

Moresi, L., Mather, B., Soler, S., and Smith, A. (2019). *Stripy 1.0.2, 2D spherical and Cartesian triangulation toolkit using tripack, stripack, srfpack and ssrfpack*. DOI: 10.5281/zenodo.3247000.

Moritz, H. (1980a). *Advanced physical geodesy*. Wichmann. ISBN: 9780856261954.

Moritz, H. (1980b). "Geodetic reference system 1980". *Bulletin géodésique* 54.3, pp. 395–405. DOI: 10.1007/BF02521480.

Moritz, H. (1990). *The Figure of the Earth: Theoretical Geodesy and the Earth's Interior*. Wichmann. ISBN: 9783879072200.

Moritz, H. (2000). "Geodetic Reference System 1980". *Journal of Geodesy* 74.1, pp. 128–133. DOI: 10.1007/s001900050278.

Mosegaard, K. and Tarantola, A. (1995). "Monte Carlo sampling of solutions to inverse problems". *Journal of Geophysical Research: Solid Earth* 100.B7, pp. 12431–12447. DOI: 10.1029/94JB03097.

Nagy, D., Papp, G., and Benedek, J. (2000). "The gravitational potential and its derivatives for the prism". *Journal of Geodesy* 74.7, pp. 552–560. DOI: 10.1007/s001900000116.

Nagy, D., Papp, G., and Benedek, J. (2002). "Corrections to "The gravitational potential and its derivatives for the prism"". *Journal of Geodesy* 76.8, pp. 475–475. DOI: 10.1007/s00190-002-0264-7.

Novák, P. and Grafarend, E. W. (2006). "The effect of topographical and atmospheric masses on spaceborne gravimetric and gradiometric data". *Studia Geophysica et Geodaetica* 50.4, pp. 549–582. DOI: 10.1007/s11200-006-0035-7.

O'Reilly, S. Y. and Griffin, W. L. (2013). "Moho vs crust-mantle boundary: Evolution of an idea". *Tectonophysics* 609, pp. 535–546. DOI: 10.1016/j.tecto.2012.12.031.

Oldenburg, D. W. (1974). "The Inversion and Interpretation of Gravity Anomalies". *Geophysics* 39.4, pp. 526–536. DOI: 10.1190/1.1440444.

Pail, R., Goiginger, H., Schuh, W.-D., Höck, E., Brockmann, J. M., Fecher, T., Gruber, T., Mayer-Gürr, T., Kusche, J., Jäggi, A., and Rieser, D. (2010). "Combined satellite gravity field model GOCO01S derived from GOCE and GRACE". *Geophysical Research Letters* 37.20. DOI: 10.1029/2010GL044906.

Pail, R., Bruinsma, S., Migliaccio, F., Förste, C., Goiginger, H., Schuh, W.-D., Höck, E., Reguzzoni, M., Brockmann, J. M., Abrikosov, O., Veicherts, M., Fecher, T., Mayrhofer, R., Krasbutter, I., Sansò, F., and Tscherning, C. C. (2011). "First GOCE gravity field models derived by three different approaches". *Journal of Geodesy* 85.11, p. 819. ISSN: 1432-1394. DOI: 10.1007/s00190-011-0467-x.

Parker, R. L. (1973). "The Rapid Calculation of Potential Anomalies". *Geophysical Journal International* 31.4, pp. 447–455. DOI: 10.1111/j.1365-246X.1973.tb06513.x.

Pastorutti, A. and Braitenberg, C. (2017). "Geothermal estimates from GOCE data alone: assessment of feasibility and first results". In: *European Geosciences Union General Assembly 2017*, p. 15930.

Pastorutti, A. and Braitenberg, C. (2018). "Constraining the continental crust heat production with a gravimetric Moho". In: *European Geosciences Union General Assembly 2018*, p. 7739.

Pastorutti, A. and Braitenberg, C. (2019). "A geothermal application for GOCE satellite gravity data: modelling the crustal heat production and lithospheric temperature field in Central Europe". *Geophysical Journal International* 219.2, pp. 1008–1031. DOI: 10.1093/gji/ggz344.

Pastorutti, A., Braitenberg, C., and Pail, R. (2019a). "Uncertainity of satellite–gravity–derived Moho estimates: Contribution of data reductions". In: *Living Planet Symposium 2019*. ESA living planet symposium. (poster presentation).

Pastorutti, A., Braitenberg, C., Pivetta, T., and Mariani, P. (2016). "Goce and future gravity missions for geothermal energy exploitation". In: *European Space Agency, (Special Publication) ESA SP*. ESA living planet symposium. Vol. SP-740.

Pastorutti, A., Pail, R., and Braitenberg, C. (2019b). "Error Characteristics of Satellite-only Global Gravity Models after Solid Earth Data Reductions". In: *27th IUGG General Assembly*. 27th IUGG General Assembly. (poster presentation). International Union of Geodesy and Geophysics.

Pastorutti, A., Pail, R., and Braitenberg, C. (2019c). "Uncertainty budget of solid Earth data reductions to global gravity models". In: *European Geosciences Union General Assembly 2019*.

Pasyanos, M. E. (2005). "A variable resolution surface wave dispersion study of Eurasia, North Africa, and surrounding regions". *Journal of Geophysical Research: Solid Earth* 110.B12. DOI: 10.1029/2005JB003749.

Pasyanos, M. E., Masters, T. G., Laske, G., and Ma, Z. (2014). "LITHO1.0: An updated crust and lithospheric model of the Earth". *Journal of Geophysical Research: Solid Earth* 119.3, pp. 2153–2173. DOI: 10.1002/2013JB010626.

Patankar, S. (1980). *Numerical Heat Transfer and Fluid Flow*. CRC Press. ISBN: 9781482234213. DOI: 10.1017/CBO9780511809101.

Pavlis, N. K., Holmes, S. A., Kenyon, S. C., and Factor, J. K. (2012). "The development and evaluation of the Earth Gravitational Model 2008 (EGM2008)". *Journal of Geophysical Research: Solid Earth* 117.B4. DOI: 10.1029/2011JB008916.

Pebay, P. P. (2008). *Formulas for robust, one-pass parallel computation of covariances and arbitrary-order statistical moments.* Tech. rep. Sandia National Laboratories. URL: https://prod-ng.sandia.gov/techlib-noauth/access-control.cgi/2008/086212.pdf.

Peral, M., Fernàndez, M., and Torne, M. (2018). "Resolution test of GOCE satellite data applied to density anomalies at crustal and upper mantle levels". *Geologica Acta* 16.1, pp. 93–105. DOI: 10.1344/GeologicaActa2018.16.1.6.

Peterson, P. (2009). "F2PY: a tool for connecting Fortran and Python programs". *International Journal of Computational Science and Engineering* 4.4, p. 296. DOI: 10.1504/ijcse.2009.029165.

Phillips, R. J. and Lambeck, K. (1980). "Gravity fields of the terrestrial planets: Long-wavelength anomalies and tectonics". *Reviews of Geophysics* 18.1, p. 27. DOI: 10.1029/RG018i001p00027.

Plomerová, J. and Babuška, V. (2010). "Long memory of mantle lithosphere fabric — European LAB constrained from seismic anisotropy". *Lithos* 120.1. The lithosphere/asthenosphere boundary: Nature, formation and evolution, pp. 131–143. ISSN: 0024-4937. DOI: 10.1016/j.lithos.2010.01.008.

Pollack, H. N., Hurter, S. J., and Johnson, J. R. (1993). "Heat flow from the Earth's interior: Analysis of the global data set". *Reviews of Geophysics* 31.3, pp. 267–280. ISSN: 1944-9208. DOI: 10.1029/93RG01249.

Priestley, K. and McKenzie, D. (2006). "The thermal structure of the lithosphere from shear wave velocities". *Earth and Planetary Science Letters* 244.1-2, pp. 285–301. DOI: 10.1016/j.epsl.2006.01.008.

Przybycin, A. M., Scheck-Wenderoth, M., and Schneider, M. (2015). "The 3D conductive thermal field of the North Alpine Foreland Basin: influence of the deep structure and the adjacent European Alps". *Geothermal Energy* 3.1, p. 17. ISSN: 2195-9706. DOI: 10.1186/s40517-015-0038-0.

Rapp, R. H. (1982). "Degree variances of the Earth's potential, topography and its isostatic compensation". *Bulletin géodésique* 56.2, pp. 84–94. DOI: 10.1007/BF02525594.

Reguzzoni, M. and Sampietro, D. (2015). "GEMMA: An Earth crustal model based on GOCE satellite data". *International Journal of Applied Earth Observation and Geoinformation* 35, pp. 31–43. DOI: 10.1016/j.jag.2014.04.002.

Reguzzoni, M., Sampietro, D., and Sansò, F. (2013). "Global moho from the combination of the CRUST2.0 model and GOCE data". *Geophysical Journal International* 195.1, pp. 222–237. DOI: 10.1093/gji/ggt247.

Revil, A. (2000). "Thermal conductivity of unconsolidated sediments with geophysical applications". *Journal of Geophysical Research: Solid Earth* 105.B7, pp. 16749–16768. DOI: 10.1029/2000JB900043.

Rexer, M., Hirt, C., Claessens, S., and Tenzer, R. (2016). "Layer-Based Modelling of the Earth's Gravitational Potential up to 10-km Scale in Spherical Harmonics in Spherical and Ellipsoidal Approximation". *Surveys in Geophysics* 37.6, pp. 1035–1074. DOI: 10.1007/s10712-016-9382-2.

Root, B. C., Ebbing, J., Wal, W. van der, England, R. W., and Vermeersen, L. L. (2017). "Comparing gravity-based to seismic-derived lithosphere densities: A case study of the British Isles and surrounding areas". *Geophysical Journal International* 208.3, pp. 1796–1810. DOI: 10.1093/gji/ggw483.

Root, B. C., Novák, P., Dirkx, D., Kaban, M., Wal, W. van der, and Vermeersen, L. L. (2015). "On a spectral method for forward gravity field modelling". *Journal of Geodynamics* 97, pp. 22–30. DOI: 10.1016/j.jog.2016.02.008.

Rudnick, R. L. and Gao, S. (2003). "Composition of the continental crust". In: *Treatise on Geochemistry*. Ed. by H. D. Holland and K. K. Turekian. Vol. 3, pp. 1–64. ISBN: 978-0-08-043751-4.

Rummel, R., Rapp, R. H., Sünkel, H., and Tscherning, C. C. (1988). *Comparisons of global topographic/isostatic models to the Earth's observed gravity field*. Tech. rep. 388. Columbus, Ohio: Department of Geodetic Science and Surveying, Ohio State University.

Saad, Y. and Schultz, M. H. (1986). "GMRES: A Generalized Minimal Residual Algorithm for Solving Nonsymmetric Linear Systems". *SIAM Journal on Scientific and Statistical Computing* 7.3, pp. 856–869. DOI: 10.1137/0907058.

Schaeffer, A. J. and Lebedev, S. (2013). "Global shear speed structure of the upper mantle and transition zone". *Geophysical Journal International* 194.1, pp. 417–449. DOI: 10.1093/gji/ggt095.

Scheck-Wenderoth, M., Cacace, M., Maystrenko, Y. P., Cherubini, Y., Noack, V., Kaiser, B. O., Sippel, J., and Björn, L. (2014). "Models of heat transport in the Central European Basin System: Effective mechanisms at different scales". *Marine and Petroleum Geology* 55, pp. 315–331. ISSN: 0264-8172. DOI: 10.1016/j.marpetgeo.2014.03.009.

Schön, J. (2011). *Physical Properties of Rocks: A Workbook*. Handbook of Petroleum Exploration and Production. Elsevier Science. ISBN: 9780444537973.

Sebera, J., Haagmans, R., Floberghagen, R., and Ebbing, J. (2018). "Gravity Spectra from the Density Distribution of Earth's Uppermost 435 km". *Surveys in Geophysics* 39.2, pp. 227–244. DOI: 10.1007/s10712-017-9445-z.

Sheriff, R. E. (2002). *Encyclopedic Dictionary of Applied Geophysics*. Society of Exploration Geophysicists. ISBN: 9781560802969. DOI: 10.1190/1.9781560802969.

Sibson, R. (1981). “A brief description of natural neighbor interpolation”. In: *Interpreting Multivariate Data*. Ed. by V. Barnet. Wiley. Chap. 2, pp. 21–36.

Simmons, N. A., Myers, S. C., Johannesson, G., and Matzel, E. (2012). “LLNL-G3Dv3: Global P wave tomography model for improved regional and teleseismic travel time prediction”. *Journal of Geophysical Research: Solid Earth* 117.B10. DOI: 10.1029/2012JB009525.

Simmons, N. A., Forte, A. M., Boschi, L., and Grand, S. P. (2010). “GyPSuM: A joint tomographic model of mantle density and seismic wave speeds”. *Journal of Geophysical Research: Solid Earth* 115.12, pp. 1–24. DOI: 10.1029/2010JB007631.

Sjöberg, L. E. (2013). “On the isostatic gravity anomaly and disturbance and their applications to vening meinesz-moritz gravimetric inverse problem”. *Geophysical Journal International* 193.3, pp. 1277–1282. DOI: 10.1093/gji/ggt008.

Sjöberg, L. and Bagherbandi, M. (2011). “A method of estimating the Moho density contrast with a tentative application of EGM08 and CRUST2.0”. *Acta Geophysica* 59, pp. 502–525. DOI: 10.2478/s11600-011-0004-6.

Smith, G. (1985). *Numerical Solution of Partial Differential Equations: Finite Difference Methods*. Oxford Applied Mathematics. Clarendon Press. ISBN: 9780198596509.

Smith, N. and van der Walt, S. (2015). “A better default colormap for Matplotlib”. In: *SciPy2015*.

Sneeuw, N. (1994). “Global spherical harmonic analysis by least-squares and numerical quadrature methods in historical perspective”. *Geophysical Journal International* 118.3, pp. 707–716. DOI: 10.1111/j.1365-246X.1994.tb03995.x.

Starostenko, V., Janik, T., Yegorova, T., Czuba, W., Środa, P., Lysynchuk, D., Aizberg, R., Garetsky, R., Karataev, G., Gribik, Y., Farfuliak, L., Kolomiyets, K., Omelchenko, V., Komminaho, K., Tiira, T., Gryn, D., Guterch, A., Legostaeva, O., Thybo, H., and Tolkunov, A. (2018). “Lithospheric structure along wide-angle seismic profile GEORIFT 2013 in Pripyat-Dnieper-Donets Basin (Belarus and Ukraine)”. *Geophysical Journal International* 212.3, pp. 1932–1962. DOI: 10.1093/gji/ggx509.

Steffen, R., Strykowski, G., and Lund, B. (2017). “High-resolution Moho model for Greenland from EIGEN-6C4 gravity data”. *Tectonophysics* 706-707, pp. 206–220. DOI: 10.1016/j.tecto.2017.04.014.

Steinberger, B. and Becker, T. W. (2016). “A comparison of lithospheric thickness models”. *Tectonophysics*, pp. 1–14. DOI: 10.1016/j.tecto.2016.08.001.

Stüwe, K. (2007). *Geodynamics of the lithosphere. Quantitative description of geological problems*. Springer Science. ISBN: 9783540712367.

Sun, W. and Sjöberg, L. E. (2001). "Convergence and optimal truncation of binomial expansions used in isostatic compensations and terrain corrections". *Journal of Geodesy* 74.9, pp. 627–636. DOI: 10.1007/s001900000125.

Szwillus, W., Afonso, J. C., Ebbing, J., and Mooney, W. D. (2019). "Global Crustal Thickness and Velocity Structure From Geostatistical Analysis of Seismic Data". *Journal of Geophysical Research: Solid Earth* 124.2, pp. 1626–1652. DOI: 10.1029/2018JB016593.

Szwillus, W., Ebbing, J., and Holzrichter, N. (2016). "Importance of far-field topographic and isostatic corrections for regional density modelling". *Geophysical Journal International* 207.1, pp. 274–287. DOI: 10.1093/gji/ggw270.

Tărăpoancă, M., Bertotti, G., Maţenco, L., Dinu, C., and Cloetingh, S. A. P. L. (2003). "Architecture of the Focşani Depression: A 13 km deep basin in the Carpathians bend zone (Romania)". *Tectonics* 22.6. DOI: 10.1029/2002TC001486.

Tenzer, R. and Chen, W. (2014). "Regional gravity inversion of crustal thickness beneath the Tibetan plateau". *Earth Science Informatics* 7.4, pp. 65–276. DOI: 10.1007/s12145-014-0146-6.

Tenzer, R. and Chen, W. (2019). "Mantle and sub-lithosphere mantle gravity maps from the LITHO1.0 global lithospheric model". *Earth-Science Reviews* 194, pp. 38–56. DOI: 10.1016/j.earscirev.2019.05.001.

Tenzer, R., Chen, W., Tsoulis, D., Bagherbandi, M., Sjöberg, L. E., Novák, P., and Jin, S. (2015). "Analysis of the Refined CRUST1.0Crustal Model and its Gravity Field". *Surveys in Geophysics* 36.1, pp. 139–165. DOI: 10.1007/s10712-014-9299-6.

Tenzer, R., Gladkikh, V., Novák, P., and Vajda, P. (2012a). "Spatial and Spectral Analysis of Refined Gravity Data for Modelling the Crust-Mantle Interface and Mantle-Lithosphere Structure". *Surveys in Geophysics* 33.5, pp. 817–839. DOI: 10.1007/s10712-012-9173-3.

Tenzer, R., Hamayun, K., and Vajda, P. (2009a). "Global maps of the CRUST 2.0 crustal components stripped gravity disturbances". *Journal of Geophysical Research: Solid Earth* 114.5, pp. 1–10. DOI: 10.1029/2008JB006016.

Tenzer, R., Hamayun, Novák, P., Gladkikh, V., and Vajda, P. (2012b). "Global Crust-Mantle Density Contrast Estimated from EGM2008, DTM2008, CRUST2.0, and ICE-5G". *Pure and Applied Geophysics* 169.9, pp. 1663–1678. DOI: 10.1007/s00024-011-0410-3.

Tenzer, R., Vajda, P., and Hamayun (2009b). "Global atmospheric effects on the gravity field quantities". *Contributions to Geophysics and Geodesy* 39.3, pp. 221–236.

Tesauro, M., Kaban, M. K., and Cloetingh, S. A. P. L. (2008). "EuCRUST-07: A new reference model for the European crust". *Geophysical Research Letters* 35.5, pp. 1–5. DOI: 10.1029/2007GL032244.

Tesauro, M., Kaban, M. K., and Cloetingh, S. A. (2009). "A new thermal and rheological model of the European lithosphere". *Tectonophysics* 476.3–4, pp. 478–495. ISSN: 0040-1951. DOI: 10.1016/j.tecto.2009.07.022.

Tscherning, C. and Sünkel, H. (1981). "A method for the construction of spheroidal mass distributions consistent with the harmonic part of the Earth's gravity potential". *Manuscripta Geodaetica* 6, pp. 131–156.

Tsoulis, D. (2012). "Analytical computation of the full gravity tensor of a homogeneous arbitrarily shaped polyhedral source using line integrals". *Geophysics* 77.2, F1–F11. DOI: 10.1190/geo2010-0334.1.

Turcotte, D. and Schubert, G. (1982). *Geodynamics: Application of Continuum Physics to Geological Problems*. Wiley. ISBN: 9780471060185.

Turcotte, D. and Schubert, G. (2014). *Geodynamics*. 3rd ed. Cambridge University Press. DOI: 10.1017/CBO9780511843.

Uieda, L. (2017). *Tesseroids v1.2.1: Forward modeling of gravitational fields in spherical coordinates*. DOI: 10.5281/zenodo.582366.

Uieda, L., Barbosa, V. C. F., and Braitenberg, C. (2016). "Tesseroids: Forward-modeling gravitational fields in spherical coordinates". *Geophysics* 81.5, F41–F48. DOI: 10.1190/geo2015-0204.1.

Uieda, L. and Barbosa, V. C. (2017). "Fast nonlinear gravity inversion in spherical coordinates with application to the South AmericanMoho". *Geophysical Journal International* 208.1, pp. 162–176. DOI: 10.1093/gji/ggw390.

Vajda, P., Ellmann, A., Meurers, B., Vaníček, P., Novák, P., and Tenzer, R. (2008). "Global ellipsoid-referenced topographic, bathymetric and stripping corrections to gravity disturbance". *Studia Geophysica et Geodaetica* 52.1, pp. 19–34. DOI: 10.1007/s11200-008-0003-5.

Vajda, P., Vaníček, P., and Meurers, B. (2006). "A new physical foundation for anomalous gravity". *Studia Geophysica et Geodaetica* 50.2, pp. 189–216. DOI: 10.1007/s11200-006-0012-1.

Vajda, P., Vaníček, P., Novák, P., Tenzer, R., and Ellmann, A. (2007). "Secondary indirect effects in gravity anomaly data inversion or interpretation". *Journal of Geophysical Research: Solid Earth* 112.6, pp. 1–11. DOI: 10.1029/2006JB004470.

Van der Meijde, M., Julià, J., and Assumpção, M. (2013). "Gravity derived Moho for South America". *Tectonophysics* 609, pp. 456–467. DOI: 10.1016/j.tecto.2013.03.023.

van der Meijde, M., Pail, R., Bingham, R., and Floberghagen, R. (2015). "GOCE data, models, and applications: a review". *International Journal of Applied Earth Observation and Geoinformation* 35, Part A. ESA GOCE solid earth workshop, 16-17 October 2012, pp. 4–15. DOI: 10.1016/j.jag.2013.10.001.

van der Meijde, M. and Pail, R. (2020). "Impact of Uncertainties of GOCE Gravity Model on Crustal Thickness Estimates". *Geophysical Journal International*. DOI: 10.1093/gji/ggaa073.

Vaníček, P., Novák, P., and Martinec, Z. (2001). "Geoid, topography, and the Bouguer plate or shell". *Journal of Geodesy* 75.4, pp. 214–215. DOI: 10.1007/s001900100165.

Vening Meinesz, F. A. (1931). "Une Nouvelle Méthode Pour la Réduction Isostatique Régionale de L'intensité de la Pesanteur". *Bulletin Géodésique* 29.1, pp. 33–51. DOI: 10.1007/BF03030038.

Vilà, M., Fernández, M., and Jiménez-Munt, I. (2010). "Radiogenic heat production variability of some common lithological groups and its significance to lithospheric thermal modeling". *Tectonophysics* 490.3–4, pp. 152–164. DOI: 10.1016/j.tecto.2010.05.003.

Watts, A. B. and Moore, J. D. (2017). "Flexural Isostasy: Constraints From Gravity and Topography Power Spectra". *Journal of Geophysical Research: Solid Earth* 122.10, pp. 8417–8430. DOI: 10.1002/2017JB014571.

Wedepohl, K. H. (1995). "The composition of the continental crust". *Geochimica et Cosmochimica Acta* 59.7, pp. 1217–1232. DOI: 10.1016/0016-7037(95)00038-2.

Wessel, P. (2009). "A general-purpose Green's function-based interpolator". *Computers & Geosciences* 35.6, pp. 1247–1254. ISSN: 0098-3004. DOI: 10.1016/j.cageo.2008.08.012.

Wessel, P. and Luis, J. F. (2017). "The GMT/MATLAB Toolbox". *Geochemistry, Geophysics, Geosystems* 18.2, pp. 811–823. DOI: 10.1002/2016GC006723.

Wessel, P., Smith, W. H. F., Scharroo, R., Luis, J., and Wobbe, F. (2013). "Generic Mapping Tools: Improved Version Released". *Eos, Transactions American Geophysical Union* 94.45, pp. 409–410. DOI: 10.1002/2013EO450001.

Wieczorek, M. A. (2007). "Gravity and topography of the terrestrial planets". In: *Treatise on geophysics*. Ed. by T. Spohn. Elsevier. Chap. 10, pp. 165–206. ISBN: 9780444535740.

Wieczorek, M. A., Meschede, M., Sales de Andrade, E., Oshchepkov, I., Xu, B., and Walker, A. (2018). *SHTOOLS: Version 4.3*. DOI: 10.5281/zenodo.1346663.

Wieczorek, M. A. and Meschede, M. (2018). "SHTools: Tools for Working with Spherical Harmonics". *Geochemistry, Geophysics, Geosystems* 19.8, pp. 2574–2592. DOI: 10.1029/2018GC007529.

Wieczorek, M. A. and Phillips, R. J. (1998). "Potential anomalies on a sphere: Applications to the thickness of the lunar crust". *Journal of Geophysical Research: Planets* 103.E1, pp. 1715–1724. DOI: 10.1029/97JE03136.

Wieczorek, M. A. and Simons, F. J. (2007). "Minimum-Variance Multitaper Spectral Estimation on the Sphere". *Journal of Fourier Analysis and Applications* 13.6, pp. 665–692. DOI: 10.1007/s00041-006-6904-1.

Wienecke, S., Braitenberg, C., and Götze, H.-J. (2007). "A new analytical solution for estimating flexural rigidity and application to the Andes". *Geophysical Journal International* 169, pp. 789–794. DOI: 10.1111/j.1365-246X.2007.3396.x.

Woodside, W. and Messmer, J. (1961). "Thermal conductivity of porous media". *Journal of Applied Physics* 32.9, pp. 1688–1699. DOI: 10.1063/1.1728419.

Xu, Y., Shankland, T. J., Linhardt, S., Rubie, D. C., Langenhorst, F., and Klasinski, K. (2004). "Thermal diffusivity and conductivity of olivine, wadsleyite and ringwoodite to 20 GPa and 1373 K". *Physics of the Earth and Planetary Interiors* 143.1-2, pp. 321–336. DOI: 10.1016/j.pepi.2004.03.005.

Yegorova, T. P. and Pavlenkova, G. A. (2015). "Velocity-density models of the Earth's crust and upper mantle from the quartz, Craton, and Kimberlite superlong seismic profiles". *Izvestiya, Physics of the Solid Earth* 51.2, pp. 250–267. ISSN: 1069-3513. DOI: 10.1134/S1069351315010048.

Zhao, G., Liu, J., Chen, B., Kaban, M., and Zheng, X. (2020). "Moho Beneath Tibet Based on a Joint Analysis of Gravity and Seismic Data". *Geochemistry, Geophysics, Geosystems* 21.2. DOI: 10.1029/2019GC008849.

List of Figures

List of Tables